AL-TR-89-092 AD:

Final Report
for the period
May 1986 to
April 1987

Characterization of Plasma Flow Through Magnetic Nozzles

February 1990

Authors:
R.A. Gerwin
G.J. Marklin
A.G. Sgro
A.H. Glasser

Los Alamos National Laboratory
P O Box 1663
Los Alamos NM 87545

RPL 69018

Approved for Public Release

Prepared for the: **Astronautics Laboratory (AFSC)**
Air Force Space Technology Center
Space Division, Air Force Systems Command
Edwards Air Force Base, CA 93523-5000

90 04 25 010

Best
Available
Copy

NOTICE

When U.S. Government drawings, specifications, or other data are used for any purpose other than a definitely related Government procurement operation, the fact that the Government may have formulated, furnished, or in any way supplied the said drawings, specifications, or other data, is not to be regarded by implication or otherwise, or in any way licensing the holder or any other person or corporation, or conveying any rights or permission to manufacture, use, or sell any patented invention that may be related thereto.
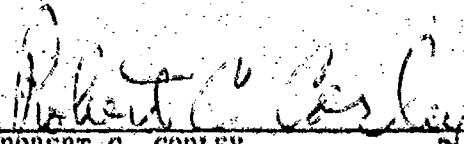
FOREWORD

This final report was submitted by Los Alamos National Laboratory, Los Alamos NM on completion of RPL 69018 for the Astronautics Laboratory (AFSC), Edwards Air Force Base, CA. AL Project Manager was Lt Tim Lawrence.

This report has been reviewed and is approved for release and distribution in accordance with the distribution statement on the cover and on the DD Form 1473.

TIMOTHY J. LAWRENCE, LT, USAF
Project Manager

CLARENCE J. C. COLEMAN, CAPT, USAF
Chief, Advanced Concepts Branch

FOR THE DIRECTOR

ROBERT C. CORLEY
Director, Astronautical Sciences
Division

REPORT DOCUMENTATION PAGE

Form Approved
OMB No. 0704-0188

1a. REPORT SECURITY CLASSIFICATION UNCLASSIFIED	1b. RESTRICTIVE MARKINGS

2a. SECURITY CLASSIFICATION AUTHORITY	3. DISTRIBUTION/AVAILABILITY OF REPORT
2b. DECLASSIFICATION/DOWNGRADING SCHEDULE	Approved for Public Release; Distribution is Unlimited

4. PERFORMING ORGANIZATION REPORT NUMBER(S)	5. MONITORING ORGANIZATION REPORT NUMBER(S) AL-TR-89-092

6a. NAME OF PERFORMING ORGANIZATION Los Alamos National Laboratory	6b. OFFICE SYMBOL (If applicable)	7a. NAME OF MONITORING ORGANIZATION Astronautics Laboratory (AFSC)

6c. ADDRESS (City, State, and ZIP Code) P.O. Box 1663 Los Alamos NM 87545	7b. ADDRESS (City, State, and ZIP Code) AL/LSVF Edwards AFB CA 93523-5000

8a. NAME OF FUNDING/SPONSORING ORGANIZATION	8b. OFFICE SYMBOL (If applicable)	9. PROCUREMENT INSTRUMENT IDENTIFICATION NUMBER RPL 69018

8c. ADDRESS (City, State, and ZIP Code)	10. SOURCE OF FUNDING NUMBERS			
	PROGRAM ELEMENT NO. 61102F	PROJECT NO. 5730	TASK NO. 00	WORK UNIT ACCESSION NO. FE

11. TITLE (Include Security Classification)
Characterization of Plasma Flow Through Magnetic Nozzles (U)

12. PERSONAL AUTHOR(S)
Gerwin, Richard A.; Marklin, George J.; Sgro, Anthony G.; Glasser, Alan H.

13a. TYPE OF REPORT Final	13b. TIME COVERED FROM 860501 TO 870430	14. DATE OF REPORT (Year, Month, Day) 9002	15. PAGE COUNT 172

16. SUPPLEMENTARY NOTATION

17. COSATI CODES			18. SUBJECT TERMS (Continue on reverse if necessary and identify by block number)
FIELD	GROUP	SUB-GROUP	rocket nozzles, magnetic nozzles, plasma dynamics, HEPS propulsion
20	03		
20	09		sub r sub p

19. ABSTRACT (Continue on reverse if necessary and identify by block number)

This report is an account of research undertaken to describe the steady, axisymmetric flow of plasmas through rocket nozzles, with attention directed to the use of magnetic fields for guiding or propelling the plasmas. The primary emphasis is on simply connected nozzles containing strictly longitudinal $(B_r, 0, B_z)$ magnetic fields to guide the plasma, with secondary consideration given to annular nozzles containing strictly azimuthal $(0, B_\theta, 0)$ magnetic fields to propel the plasma. The possibility and desirability of using hot plasma in a repetitive mode is discussed, and motivates our consideration of an extensive range of parameters. Although slightly ionized gases having low temperatures (a fracture of an eV) and low magnetic Reynolds numbers often are the objects of valid and useful research (for example, in connection with MHD generators, with MPD thrusters, and with arc heaters to provide sources of hot gas for expanding gas-dynamic flow fields), we have chosen to focus upon the effective and efficient interaction of substantial plasmas with guiding or driving magnetic fields. Thus, we focus primarily on highly ionized plasmas that are not dominated

20. DISTRIBUTION/AVAILABILITY OF ABSTRACT ☒ UNCLASSIFIED/UNLIMITED ☐ SAME AS RPT. ☐ DTIC USERS	21. ABSTRACT SECURITY CLASSIFICATION UNCLASSIFIED
22a. NAME OF RESPONSIBLE INDIVIDUAL TIMOTHY J. LAWRENCE, 1Lt, USAF	22b. TELEPHONE (Include Area Code) (805) 275-5640	22c. OFFICE SYMBOL AL/LSVF

DD Form 1473, JUN 86   Previous editions are obsolete.   SECURITY CLASSIFICATION OF THIS PAGE

AL-TR-89-092

Block 19.

by resistive dissipation. Some of the principal physics issues associated with these concepts are addressed, including the assumptions and limitations of the ideal MHD model, the magnitude and scaling of classical and anomalous transport losses and of radiation losses in hydrogen plasma during transit of plasma through the nozzle, and the transport-related detachment problem of how the plasma leaves the exit region of the nozzle. Moreover, a formalism is developed for treating the steady, axisymmetric MHD nozzle. Moreover, a formalism is developed for treating the steady, axisymmetric MHD flow of ideal through the nozzle; and a finite element code based upon the formalism is constructed with the capability to adapt a body-fitted coordinate system to arbitrary nozzle shapes. This code is validated by detailed comparison with experiment, and it provides benchmark results to which the results of other codes can be compared. Finally, the limitations of the present computational approach are pointed out, suggestions for further work free of these limitations are made, and an attempt to acquire and apply an independent 2-D MHD initial-value code is described.

We conclude with the impression that the use of plasmas for space vehicle propulsion is a natural and interesting application of plasmas that well deserves further study.

CONTENTS

APPENDICES

LIST OF TABLES

FORWARD

This report is an account of research undertaken to describe the steady, axisymmetric flow of plasmas through rocket nozzles, with attention directed to the use of magnetic fields for guiding or propelling the plasmas. The primary emphasis is on simply connected nozzles containing strictly longitudinal $(B_r, 0, B_z)$ magnetic fields to guide the plasma, with secondary consideration given to annular nozzles containing strictly azimuthal $(0, B_\theta, 0)$ magnetic fields to propel the plasma. The possibility and desirability of using hot plasmas in a repetitive pulsed mode is discussed, and motivates our consideration of an extensive range of parameters. Although slightly ionized gases having low temperatures (a fraction of an eV) and low magnetic Reynolds numbers often are the objects of valid and useful research (for example, in connection with MHD generators, with MPD thrusters, and with arc heaters to provide sources of hot gas for expanding gas-dynamic flow fields), we have chosen to focus upon the effective and efficient interaction of substantial plasmas with guiding or driving magnetic fields. Thus, we focus primarily on highly ionized plasmas that are not dominated by resistive dissipation. Some of the principal physics issues associated with these concepts are addressed, including the assumptions and limitations of the ideal MHD model, the magnitude and scaling of classical and anomalous transport losses and of radiation losses in hydrogen plasma during transit of plasma through the nozzle; and the transport-related detachment problem of how the plasma leaves the exit region of the nozzle. Moreover, a formalism is developed for treating the steady, axisymmetric MHD flow of ideal plasma through the nozzle; and a finite element code based upon the formalism is constructed with the capability to adapt a body-fitted coordinate system to arbitrary nozzle shapes. This code is validated by detailed comparison with experiment, and it provides benchmark results to which the results of other codes can be compared. Finally, the limitations of the present computational approach are pointed out, suggestions for further work free of these limitations are made, and an attempt to acquire and apply an independent 2-D MHD initial-value code is described.

We conclude with the impression that the use of plasmas for space vehicle propulsion is a natural and interesting application of plasmas that well deserves further study.

EXECUTIVE SUMMARY

The thrust of a conventional rocket engine is obtained by allowing a gas under pressure to be expelled through a nozzle. By operating at higher temperatures to gain more specific impulse and concomitantly a bigger payload mass fraction, the propulsive gas ultimately becomes partially or fully ionized, and one is then led to consider the flow of plasma through a nozzle (plasma propulsion). In such a scheme, the presence of a properly shaped longitudinal magnetic guide field can serve to confine the plasma pressure in the transverse direction, as well as to reduce the cross-field transport of charged particles and thermal energy to the surrounding walls. We shall refer to this configuration as a "meridional magnetic nozzle," and this concept is the primary focus of this report. In another scheme of interest, which is the basis of coaxial plasma guns and MPD thrusters, it is possible to accelerate plasma through the nozzle by primarily using internal magnetic forces derived from transverse magnetic fields rather than using thermal energy. We shall refer to the latter scheme as the "azimuthal magnetic nozzle."

In more detail, rocket missions may be characterized (regardless of the mass of the space vehicle) by the velocity increments of the vehicle that are required to attain the necessary mission orbits, or to transfer from one orbit to another. The rocket momentum balance equation then shows that in order to realize a significant mass payload fraction, the exhaust velocity of the propulsive gas relative to the vehicle, V_e, cannot be too much smaller than the required vehicle velocity increments. On the other hand, the goal of efficient engine performance (high thrust per unit power) dictates that the fuel exhaust velocity not be unnecessarily large either. These two basic goals, high-mass-payload fraction and efficient utilization of engine power, tend to define a desirable window of operation for the exhaust velocities (sometimes characterized in terms of specific impulse). This, in turn, helps to determine the relative merits of various proposed rocket fuels and associated systems. Since the velocity increments for near-term solar system missions (near-Earth and terrestrial planet missions) generally fall in the range of 0.5 to 1.0×10^6 cm/s, (depending partly upon the flexibility desired in the choice and timing of transfer orbits) one is led to consider temperatures of the fuel gas in the fraction of an eV to few eV range (Hydrogen). [An excellent systematic and detailed account of the orbits and velocity increments of interest may be found in The Foundations of Astrodynamics by Archie E. Roy; Macmillan, NY (1965).] Temperatures in this range can correspond to a significant ionization fraction and concomitantly useful electrical conductivity of the propulsive gas, to the point where the concepts of magnetic force either guiding or propelling plasmas become of interest for rocket propulsion. Finally, if the condition $\beta \sim 1$ is invoked as defining the least magnetic field strength for which significant magnetic confinement of plasma pressure is feasible (where "β" is the ratio of internal plasma pressure to external magnetic pressure), then an additional relationship among the plasma parameters is provided. This value of beta proves to be relevant for azimuthal nozzles also (see Appendix D).

It is possible, in principle, to further improve the situation described above, with regard to efficient fuel mass utilization and plasma-magnetic field interaction, by going to a repetitive-pulsed-power approach that employs very hot plasmas (hundreds of eV instead of a few eV). This would have to be managed without greatly increasing the time-average power consumption, by adjustment of the rep-rate and duty fraction, in order for the scheme to be credible in the near term. A detailed comparison between the steady-burn

and the repetitive-pulsed burn approaches is made in Appendix C. From this point of view, hot plasmas remain interesting candidates for vehicle propulsion. This motivates us to include temperatures in the 100 eV range, as well as in the 1 eV range, in the survey of Chapter 1.

In contrast, chemically driven rocket exhausts are operating at their upper limits of capability for the needed range of velocity increments, just because of the relatively modest amount of energy per atom available from chemical bonds. Consequently, such conventional schemes sometimes attain the required velocity increments by stages, with attendant mass penalties exacted on the payloads.

(It need not be invariably the case that higher specific impulse (I_{sp}) is desirable as described above. The actual requirements will depend jointly upon the scheduling details of a particular mission, and upon the engine-mass-power-utilization figure of merit. If, for example, a very high acceleration maneuver is called for during a transient phase of the mission, then a lower specific impulse will better serve the purpose during that phase of the mission, for a given figure of merit of this kind. Thus, if the figure of merit is taken to have a value of N megawatts per tonne, then the instantaneous vehicle acceleration may be expressed as

$$\text{Acceleration} \left[\frac{m}{s^2}\right] \approx N \times \frac{200\left[\frac{m}{s}\right]}{I_{sp}[s]} \frac{M_{Engine}}{M_{Total}},$$

where $I_{sp} \equiv V_e/g$, where M_{Engine} is the instantaneous mass of the engine utilized for this phase of the mission (including fuel), and M_{Total} is the total instantaneous mass of the vehicle. Thus, the vehicle acceleration is maximized by means of a small specific impulse coupled with a high fuel mass loss rate.)

In this report, the plasma flow through axisymmetric magnetic nozzle configurations is considered. Configurations containing either externally generated meridional magnetic fields or azimuthal magnetic fields are discussed, but the former receives the primary emphasis in this report. A mixed configuration containing both types of magnetic fields is also possible, with its own advantages and disadvantages, but is not discussed in this report.

No detailed consideration is given here to the production or sustainment of the heated plasma in the reservoir that feeds the meridional nozzle inlet, nor of the optimal heating mechanisms. Attention is restricted to the problem of producing a description of the flow of plasma through the nozzle. (But plasma heating in the azimuthal nozzle is considered in Appendices D and E.)

In Chapter 1, a scoping study is presented which describes conditions under which the plasma nozzle flow can be approximately regarded as an ideal magnetohydrodynamic (MHD) process. This point of view is motivated by the goal of effective and efficient employment of the guiding or driving magnetic fields acting upon substantial plasmas. The deviations from ideal MHD are associated with transport and radiation losses for which rough estimates are given, including the power loads on the walls of the nozzle. This prepares the way for Chapter II, the purpose of which is to describe the dynamical results of the ideal model (no transport losses, no radiative losses, no resistivity, no Hall effect in the plasma) in order to establish a perspective from which to view and measure the effects of the non-ideal processes. The ideal MHD situation is of interest in itself because it corresponds to parameter regimes in which the energetics of the flow are not at

all dominated by loss processes, and the plasma medium is efficiently utilized.

Some important results of the scoping study may be stated briefly as follows. A wide choice of plasma parameters is laid out for study, with ion number densities ranging from 10^{13} cm^{-3} to 10^{19} cm^{-3}, and plasma temperatures ranging from 1 eV to 100 eV (with occasional comments for 1 keV). For these densities and temperatures, the magnetic field is determined by our choice of the $\beta = 1$ condition, so as to provide the least magnetic field for which transverse plasma confinement by magnetic pressure is sensible. A table is set up, which provides the thermal pressures, thrust pressures, and thrust power densities for all of these cases, and which proves useful for future reference. For this set of parameters, it is then shown that the plasma may reasonably be regarded as fully ionized. The validity of the fluid-plasma model is then shown to rest upon the smallness of the Coulomb mean-free path λ and of the ion gyro-radius r_{ci} in comparison with nozzle dimensions. A table of values of λ and r_{ci} is laid out for reference. A condition for neglecting the Hall effect in the ideal MHD description of axisymmetric nozzle flow is then found to be that the ion gyro-radius should be small compared to nozzle dimensions, for both types of nozzles. (However, if there exists a low-beta region in the azimuthal nozzle, the condition for neglecting the Hall effect is found to be the smallness of the ion skin depth, c/ω_{pi}, compared to nozzle dimensions.)

We then go on to consider mass, heat, and radiation losses from the plasma while it is flowing through the nozzle. To the extent that they occur, such losses constitute undesirable inefficiencies in the utilization of plasmas for vehicle propulsion. Such losses also must be dealt with on board the vehicle, by finding benign ways to utilize or to dispose of the power discarded by the plasma, including, if necessary, the protection of materials from deterioration due to that power flux. Here, the "small" non-ideal terms must be retained in the plasma model, including the Hall and pressure terms in Ohm's law. For plasmas with temperatures near 1 eV, we find that classical resistive diffusion (radial mass transport) results in unacceptably large mass-loss fractions when the plasma beta is of order unity. However, we note that such losses can be reduced by working with much smaller values of "beta" instead of $\beta = 1$. (Therefore, further detailed studies at low beta for ~ 1 eV plasmas are recommended.) These observations apply both to the meridional nozzle configuration for all degrees of magnetization of the electrons ($\omega_{ce} \tau \gtrless \nu_{ei}$), and to the azimuthal nozzle when the electrons are un-magnetized ($\omega_{ce} < \nu_{ei}$). However, we note that when the electrons are magnetized, a different mechanism of lateral mass transport comes into play in the azimuthal nozzle wherein the Hall term rather than resistive diffusion determines radial mass transport. Concomitantly, it is found that when the electrons are magnetized in the azimuthal nozzle, mass transport can be reduced to small fractional losses by working under conditions in which the ion gyro-radius is small compared to nozzle radial dimensions, in this case the radial space between the inner and outer electrodes. (A table of electron and ion degrees of magnetization is provided for reference.)

With regard to radial heat transport, we find that thermal convection associated with classical resistive diffusion dominates classical heat conduction for plasmas near 1 eV. Again, the fractional losses of thermal energy are unacceptably large for $\beta = 1$, but can be reduced by working with low-beta plasmas. The wall heat loads from 1 eV plasmas (with $\beta = 1$) subject to classical transport are not more than a few megawatts per square meter (for a radius of one meter) in the range where the plasma model is reliable (ion densities up

to 10^{16} cm^{-3}). However, at temperatures of 10 eV and above, classical transport allows radial thermal fluxes of hundreds to thousands of MW/m^2 for ion densities exceeding 10^{17} cm^{-3}. (The standard plasma model remains reliable at much higher densities for $T \geq 10$ eV.) Thus, although the fractional thermal losses from conduction or convection are small at the higher temperatures, the absolute energy fluxes to the wall will be large, and may be cause for concern.

A possible source of non-classical transport that has received much attention in plasma physics is called Bohm diffusion. When the electrons are magnetized ($\omega_{ce} > \nu_{ei}$), a form of electrostatic turbulence in non-equilibrium plasmas can be generated and produces an anomalous collision rate for electrons leading to a non-classical diffusion process across the ambient magnetic field. Surprisingly, for all cases studied we found that Bohm losses dominated classical in only three significant cases, namely $n = 10^{15}, 10^{16}$ and 10^{17} cm^{-3}, all for $T = 100$ eV, producing thermal fluxes of 6.7, 21, and 67 MW/m^2 respectively. In all cases, the Bohm Reynolds numbers were much larger than unity, signifying small fractional losses.

With regard to radiation losses, the nature of the losses depends upon whether the plasma is optically thin or optically thick. In all but two of our standard cases (at 1 eV), the plasma may be regarded as optically thin. Moreover, bremsstrahlung rather than cyclotron radiation proves to be the primary form of radiant energy loss. We note that this form of energy loss depends upon an integral over the plasma volume, and therefore is not sensitive to adjustments of the plasma profile (for given bulk densities and temperatures). On the other hand, the possibility is suggested for exerting edge control on optically thick plasmas.

For general diffuse profiles, it is found that the optically thin bremsstrahlung wall loading in a chamber of 1 meter radius exceeds the wall loading from classical transport for temperatures equal to or larger than 10 eV and densities equal to or larger than 10^{16} cm^{-3}. The bremsstrahlung wall loading is also competitive with or larger than the dominant Bohm thermal fluxes for $n \gtrsim 10^{16}$ cm^{-3} for $T = 100$ eV. These radiation wall loads can exceed hundreds, or tens of thousands of megawatts per square meter at the higher densities considered here ($n = 10^{17} - 10^{18}$ cm^{-3}). However, it is important to note that the plasma propulsion scheme itself becomes questionable at such high densities because the fraction of initial thermal energy lost to radiation by a given element of plasma during its transit through the nozzle becomes large.

With regard to convective transport losses induced by nonlinear dynamical processes occurring over macroscopic distances, it was noted that there is as yet no generally accepted, definitive model of turbulent plasma flow through magnetic nozzles in which the plasma beta is of order unity and the magnetic Reynolds number is larger than unity. This is in contrast to the situation in compressible fluid dynamics wherein a set of sophisticated semi-empirical models has been built up in conjunction with experiments to provide practical models of boundary-layer flow and nozzle flow. Although we are aware of progress in this direction for plasmas of small magnetic Reynolds numbers and small beta values ($\ll 1$), we have chosen not to consider this parameter regime, but instead to focus upon significant Reynolds numbers and beta values that reflect the efficient interaction of substantial (hot) plasmas with the guiding or driving magnetic fields.

Within this context, we noted that highly conducting plasmas are most vulnerable to those dynamical processes that avoid the bending of magnetic field lines. Examples of such processes in the meridional magnetic nozzle are the Rayleigh-Taylor instability

with wave vectors in the azimuthal direction, and the Kelvin-Helmholtz instability, also with wave vectors in the azimuthal direction. The former instability can be driven by bad magnetic curvature in the nozzle entrance region, and the latter by the shear in the $\vec{E} \times \vec{B}$ velocity field that arises naturally in the plasma-wall sheath. (Note that the magnetized sheath is much thicker than the Debye length.) Neither of these instabilities relies for its existence upon the presence of axial flow through the meridional nozzle. In contrast, in the azimuthal magnetic nozzle both of these instabilities can exist with wave vectors in the axial direction without bending the magnetic field lines, and one would then expect fundamental interactions of these instabilities with the axial flow field. In this report, our detailed discussion is limited to these convective transport processes in the meridional magnetic nozzle. The influence of these processes on the operation of the azimuthal nozzle configuration is a subject that is strongly recommended for future research.

A quasilinear mixing-length model is constructed so as to provide estimates of "equivalent" axisymmetric convective transport arising from outward fluting of the outer plasma surface (since sharply bounded plasmas are subject to the most rapidly growing Rayleigh-Taylor modes). Various estimates of the boundary layer thickness are made, resulting in heat fluxes that are competitive with (or even stronger than) radiation wall fluxes, at temperatures in the range of $10 - -100$ eV and densities in the range of $10^{16} - -10^{18}$ cm^{-3}.

The plasma-sheath induced Kelvin-Helmholtz turbulence has been modeled in a recent 2D full particle simulation by Theilhaber and Birdsall. The Kelvin-Helmholtz vortices apparently do not contribute directly to cross-field plasma transport, but instead are seen to cascade to short wavelengths which ultimately produce Bohm diffusion of electrons. (The ions must follow, by quasi-neutrality.) Taken at face value, these simulations predict transport that scales very similarly to the Rayleigh-Taylor induced transport described above, but is about one order of magnitude smaller. However, we must remember that the simulation parameters were rather unrealistic, and that stronger transport may yet come out of a more realistic simulation of Kelvin-Helmholtz turbulence in the magnetized plasma sheath.

The manner in which plasma exits the nozzle appears to be a critical issue requiring further study. For the meridional nozzle, plasma constrained to axisymmetric flow will experience a resistive drag as it tries to axially detach itself from the radially diverging magnetic field lines. This drag will be transmitted to the vehicle through the magnetic field coils. We call this the "detachment problem." Such an effect could be prevented if the downstream electron temperature drop predicted by the simple model of isentropic flow were sufficient to practically decouple the plasma from the magnetic field. However, electron parallel thermal conduction would tend to counter the downstream temperature drop, and it also constitutes an inefficiency in the propulsive process. These two counter-acting effects (including the possibility of electron-ion recombination) should be studied quantitatively with an axisymmetric non-ideal MHD simulation. In the 100 eV range, parallel thermal conduction was found to be a problem for all densities below 10^{17} cm^{-3}, and in the 10 eV range for all densities below 10^{18} cm^{-3}. It is important to include this effect when modeling the performance of the meridional nozzle configuration. Moreover, non-axisymmetric effects may be important in determining how plasma exits the nozzle. Flute instabilities (Raleigh-Taylor instabilities) may provide an additional channel by which a resistive plasma can escape axially from the radially diverging magnetic field

and should be studied with a 3-D resistive MHD simulation. An approximate estimate of the resistive drag of the fields on the plasma for axisymmetric steady flow is made in Chap. I. The preliminary conclusion is that the resistive drag force is practically always of the same order as the ideal thrust (for magnetic Reynold's numbers larger than unity), and is therefore a critical issue that must be addressed. If nozzle input conditions could be arranged to have either a field-free plasma core contained by an external layer of magnetic field, or an internal plasmoid separated from the external magnetic guide field by a magnetic separatrix, then the necessity to deal with the detachment problem can be obviated.

In the case of the azimuthal magnetic nozzle, a related inefficiency may occur in the exit flow. If the exiting plasma remains highly conducting, it may convect azimuthal magnetic field out into the exhaust. This is also a detachment problem and it signifies wasted magnetic energy (ultimately dissipated as heat in the exhaust plasma) that has not contributed to momentum transfer. Again, the effect could be prevented either by a sufficiently rapid downstream drop in the electron temperature or by arranging to have the magnetic field become very small near the exit.

In Chapter II, analytical and numerical procedures are developed for computing ideal MHD steady axisymmetric flows, for given input conditions at the reservoir-nozzle transition. A code to carry out such procedures has been developed by Marklin for meridional magnetic nozzles, and it performs a "direct method" search for the steady-flow, in contrast to an "initial-value" approach. The latter would presumably settle down to the final state by means of simulated dissipative dynamical processes. The result of this work can serve well as an independent check on limiting cases of more general simulations (time-dependent, with azimuthal and meridional magnetic fields, with non-uniform input conditions, and with non-ideal MHD properties). Marklin's code has been successfully validated by a detailed comparison with experimental observations on ordinary nozzle flow. That comparison is presented in Chapter II. Also in Chapter II, the important point is clearly demonstrated that in order to properly model the ideal MHD physics of the meridional magnetic nozzle, it is essential to include the transition from the plasma reservoir to the nozzle entrance.

The first half of our one-year contract period (at a level of 0.8 man-years) was used for performing work described in Chapter I, and, as so far described, in Chapter II. The second half was used as follows.

By numerically experimenting (in Chap. II) with a number of nozzle configurations possessing varying degrees of magnetic-pressure-balance of diffuse transverse plasma pressure gradients, the conclusion was gradually arrived at that the "direct solution" method of steady magnetized flow problems in general axisymmetric geometry is computationally delicate. Although the method works well (as shown in Chap. II) for uniform input conditions (implying wall-confined plasma pressure), it would need to be carefully modified in order to handle the more general case of transverse magnetic confinement of plasma pressure. The reasons for this are discussed in Chap. II. The difficulty is that, in magnetized nozzle flow with magnetically confined plasma pressure, the elliptic and hyperbolic flow regions are configured in a complicated and non-standard manner, due to the presence of three characteristic speeds instead of just one. Finally, in order to supplement the computations carried out for the case of wall-confined plasma with magnetized flow, Chap. II concludes with a semi-analytic treatment of nozzle flow with

magnetically-confined plasma pressure using a sharp-boundary model. A nozzle "stuffing condition" thereby is uncovered in which too much magnetic flux can block the steady flow of plasma through the nozzle throat if the parameters are not properly chosen.

For the reasons just stated, employment of time-dependent (initial-value) simulations was therefore deemed to be a superior computational approach to the steady flow solution, as well as providing access to possible un-steady features of MHD nozzle flow. A brief comparative discussion of such considerations is provided in Chapter III.

Consonant with these conclusions, we spent considerable time and effort to acquire and become familiar with the use of a time-dependent, two-dimensional, axi-symmetric, non-ideal MHD simulation. This simulation includes dissipative plasma features such as resistivity, viscosity, and thermal conduction, and also has provision for including the Hall effect. It is most important to note that the configurations and boundary conditions treatable by this code are not restricted, in principle, to straight cylindrical geometry, but instead can possess arbitrary axi-symmetric shapes. Moreover, the code can treat free boundaries, which would be important in the simulations of flows separated or confined away from the wall by magnetic pressure. Thus this particular code is highly relevant to the realistic plasma propulsion problem. A brief description of the code and an example of its ability to simulate plasmoid propagation is provided by Glasser in Chapter IV. However, neither sufficient time nor personnel were available within our allotted AFAL contract to properly modify and systematically apply this simulation so as to study systematically a variety of examples of non-ideal MHD nozzle flow. Our present opinion is that this particular simulation is no longer the best one to use, because it does not take proper advantage of modern FORTRAN and Supercomputer capabilities, making the code unnecessarily awkward to apply and tedious to modify. We believe that it now would be best to write a new code tailored specifically for the purposes of MHD nozzle flow.

Finally, Chap. V summarizes the contents of this report, compares the various loss processes, and makes recommendations for further work.

I. CONDITIONS FOR MAGNETIC NOZZLE FLOW AS AN IDEAL MHD PROCESS, AND WALL LOADING FROM PLASMA LOSS PROCESSES

Introduction and Preliminary Parameter Survey

This chapter has the purpose of providing an overview of the physics important for steady plasma flow through magnetic nozzles. Two basic types of axisymmetric magnetic configurations are discussed, those containing only meridional magnetic fields and those containing only azimuthal magnetic fields.

Plasma nozzle flows for a large range of sample plasma parameters are considered here, with temperatures T ranging from 1 eV (envisioned to be characteristic of steady-state burns) to 100 eV (envisioned to be characteristic of repetitive pulsed burns). (Each pulse of hot plasma is envisioned to achieve a state of steady flow during the pulse. Start-up and termination transients are not considered here.) The magnetic field B and the plasma pressure $P = 2nT$ (assuming equal electron and ion temperatures for simplicity here) are assumed to be coupled by the condition $\beta = 1$, where $\beta = 2nT/(B^2/2\mu_0)$ ideally represents the ratio of internal plasma pressure to external magnetic pressure. (Sometime, we shall simply employ a local beta.) The density n is taken to range from $10^{13} cm^{-3}$ to $10^{19} cm^{-3}$, except for an upper cut-off point (in the briefly considered 1 keV range) determined jointly by the $\beta = 1$ condition and a (somewhat arbitrary) practical upper limit of 30 Tesla imposed on the magnetic field strength. The corresponding magnetic pressure is about 5000 atmospheres, which the magnetic coils would have to support under tension. These sorts of field strengths are at the upper limits of presently envisioned future tokamak experiments in magnetic fusion energy devices.

In addition, parameter values that invalidate the fluid-plasma model are flagged, and are different for the meridional and azimuthal magnetic nozzles. Moreover, high densities and low temperatures are flagged for which basic, conventional plasma physics assumptions are invalid. For all of these parameters, the quasineutrality assumption, $|n_e - n_i| \ll n_e$ is valid because the Debye length, $\lambda_D = (\frac{T}{4\pi ne^2})^{1/2}$, is short compared to dimensions of interest, and the electron and ion plasma periods $\omega_{pe,i}^{-1} = (\frac{4\pi ne^2}{m_{e,i}})^{-1/2}$, are short compared to times of interest.

For each set of parameters, a set of relevant Reynolds numbers and time scales is evaluated for hydrogen plasma, leading to estimates of fractional energy losses, both thermal and radiative, and corresponding estimates of power densities loading the walls of the nozzle. In addition, the thrust pressure and thrust power density are provided for each case. In the absence of generally accepted definitive models for turbulent MHD boundary layers, several provisional models are utilized to estimate the thermal transport.

Finally, with regard to radiation losses over the range of parameters considered, it is important to distinguish between optically thin and optically thick plasmas. The length scale for which this distinction is drawn in this report is taken (somewhat arbitrarily) as 10 cm.

In the following table, Table I.1, we present the magnetic field strengths and magnetic pressures for $\beta = 1$ plasmas, for a range of densities and temperatures assumed to be present in the throat of the nozzle. Approximate formulas are also presented (in the quasi-1D approximation) for the corresponding thrust pressure and thrust power density, both referred to the area of the throat of the nozzle for convenience. For thermal throat

TABLE 1.1 Magnetic Fields and Pressures for "$\beta = 1$" Hydrogen Plasmas

(B_0 in Tesla: $P_0 = \frac{B_0^2}{2\mu_0}$: Throat Pressure (thermal) in psi)

$T[eV]$	1	10	100	1000
$n[cm^{-3}]=$				
10^{13}	2.83×10^{-3} [Tesla]	8.94×10^{-3}	2.83×10^{-2} x	8.94×10^{-2} x
	4.62×10^{-4} [psi]	4.62×10^{-3}	4.62×10^{-2}	4.62×10^{-1}
10^{14}	8.94×10^{-3}	2.83×10^{-2}	8.94×10^{-2} x	2.83×10^{-1} x
	4.62×10^{-3}	4.62×10^{-2}	4.62×10^{-1}	4.62
10^{15}	2.83×10^{-2}	8.94×10^{-2}	2.83×10^{-1}	8.94×10^{-1} x
	4.62×10^{-2}	4.62×10^{-1}	4.62	46.2
10^{16}	8.94×10^{-2}	2.83×10^{-1}	8.94×10^{-1}	2.83 x
	4.62×10^{-1}	4.62	46.2	462
10^{17}	2.83×10^{-1} x	8.94×10^{-1}	2.83	8.94
	4.62	46.2	462	$4,620$
10^{18}	8.94×10^{-1} x	2.83	8.94	28.3
	46.2	462	$4,620$	$46,200$
10^{19}	2.83 x	8.94	28.3	$(89.4\ Tesla)$
	462	$4,620$	$46,200$	

Note: (See Appendix A)

a. Thrust Pressure refered to area of throat is $\frac{T}{A_0} \approx 3P_0$

b. Thrust Power Density refered to area of throat is $\frac{P}{A_0} \left[\frac{MW}{m^2} \right] \approx 400 \times P_0[psi] \times T_0^{1/2}[eV]$

c. Cases marked "x" lie outside of the standard fluid-plasma model ($\ell n\Lambda \gg 1$ is required. see Table 1.2: and x also flags values of mean-free-path larger than 10^2 cm: thus mean-free-path $\lesssim 10^2$ cm is imposed. see Table 1.5)

pressures exceeding 10 psi, one sees that tremendous instantaneous power densities are involved. (Note that "thermal pressure" in the nozzle throat is distinct from "thrust pressure" referred to the area of the throat.)

This is followed by Table I.2, which presents values of "$\ell n\Lambda$" for the same range of densities and temperatures. When $\ell n\Lambda \gg 1$, conventional plasma theory can be used. This is known as the "weakly coupled" plasma model, wherein the average Coulombic interaction energy of a particle is small compared to its average (random) kinetic energy. At high densities and low temperatures, this model breaks down and the plasma tends to become "strongly coupled," describable only by much more complicated and less understood models. Such cases will not be considered here, and are marked with "x" in the tables.

TABLE I.2 Values of $\ell n\Lambda$ (Ref. 2)

$T[eV]$	1	10	100	1000
$n[cm^{-3}] = 10^{13}$	8.45	11.9	14.95	17.25
10^{14}	7.3	10.75	13.80	16.10
10^{15}	6.15	9.60	12.65	14.95
10^{16}	5.00	8.45	11.50	13.80
10^{17}	3.85 x	7.30	10.35	12.65
10^{18}	2.70 x	6.15	9.20	11.50
10^{19}	1.55 x	5.00	8.05	10.35

$T < 50\ eV: \quad \ell n\Lambda = 23.4 - 1.15\ log n + 3.45\ log T$
$T > 50\ eV: \quad \ell n\Lambda = 25.3 - 1.15\ log n + 2.3\ log T$

A. Neglect of Charge-Neutral Collisions, and Validity of the Fluid Model

1. The Role of Charge-Neutral Collisions. A partially ionized gas may, for some purposes, be regarded as fully ionized. To make this point, we shall examine elastic scattering cross sections and collision frequencies for electrons on neutral monatomic hydrogen compared with those for electrons scattering from hydrogen ions. (Throughout this chapter, only hydrogen plasma is considered, both for simplicity and because larger specific impulse is more easily achieved with the less massive ions. Also, temperatures in

the 1 eV to 10^3 eV range are considered, subject to the validity of the fluid-plasma model as mentioned above.)

Burke and Smith[1] calculate the scattering cross section of electrons on neutral hydrogen atoms at energies between 1 and 20 eV. They find the cross section σ_{eH} ranges from near 10^{-14} cm^2 below $5eV$ down to near 10^{-15} cm^2 above $10eV$. The enhanced cross section at lower energies is associated with the "electron affinity" of H wherein the incident electron is temporarily captured to produce a meta-stable H^- ion. At higher energies, the scattering cross section is essentially geometrical (including the effect of the wave function of the incident electron in addition to the "size" of the atom).

The momentum-transfer cross section for Coulomb scattering of electrons on hydrogen ions can be simply calculated from the characteristic length $r_{ei} = (e^2/T)$ (in cgs units) where T is the electron temperature in energy units. The distance of approach of the electron to the H^+ ion, r_{ei}, is where the representative electron with kinetic energy T begins to feel the Coulomb potential of the H^+ ions and thus begins to have its orbit altered. The scattering cross section is then estimated as $\sigma_{ei} = \pi r_{ei}^2 \ell n \Lambda$, where the Coulomb logarithm, $\ell n \Lambda$, is appended to account for the cumulative effects of multiple small-angle scatterings.[2] For situations of interest in this report, $\ell n \Lambda \approx 10$, and the momentum-transfer cross section for Coulomb scattering of electrons by H^+ ions becomes

$$\sigma_{ei}[cm^2] \approx 0.64 \times \frac{10^{-12}}{T^2_{(eV)}}.$$

For temperatures not greater than $10eV$, we see that the cross-section for Coulomb scattering dominates the cross-section for electron-neutral scattering.

Although this result is suggestive, it is really necessary to compare the collision frequencies for these two kinds of scattering, rather than the cross-sections. This comparison is especially necessary for high temperature plasmas, the particles of which have small Coulomb-scattering cross-sections. The Coulomb collision frequency for momentum transfer of electrons with ions can be estimated approximately as

$$\nu_{ei} \approx n_i \sigma_{ei} v_e$$

where n_i is the ion density and v_e is the electron thermal velocity, $v_e[cm/s] \approx 5.7 \times 10^7 T^{1/2}_{(eV)}$ using $m_e \approx 1 \times 10^{-27}$ gm for the electron mass. . (A more accurate expression for ν_{ei} is used later in this chapter.[3]) Thus

$$\nu_{ei}[s^{-1}] \approx 3.6 \times 10^{-5} \frac{n_i(cm^{-3})}{T^{3/2}_{(eV)}}$$

(To clarify our notation, we emphasize that ν_{ei} is here used to represent a momentum transfer rate, so that ν_{ei}^{-1} does not represent the electron-ion energy equipartition time.)

In order to estimate the electron-neutral collision frequency arising from elastic scattering, and to compare it with the electron-ion momentum-transfer collision frequency, we shall need to know the degree of ionization. Assuming that the atomic rates are fast

enough to maintain a local equilibrium state at each point in the flow field, we have from Reif, Chapter 9,[3-a]

$$\frac{\xi^2}{1-\xi} = \frac{1}{n_0} \left(\frac{m_e T}{2\pi\hbar^2}\right)^{3/2} e^{-\frac{\epsilon_0}{T}}$$

where $\xi = \frac{n_i}{n_0} = \frac{n_e}{n_0}$ is the degree of ionization referred to the total density $n_H + n_i = n_0$, n_H is the residual density of neutral monatomic hydrogen, T is the local temperature in energy units, and $\epsilon_0 = 13.6 eV$ is the ionization energy of hydrogen from its ground state. Also, $\hbar = h/2\pi$ where h is Planck's constant, and m_e is the mass of an electron.

(If the atomic rates are slow in comparison to the transit time of plasma through the nozzle, it is better to think of this formula as describing the quasi-equilibrium reservoir plasma. Then, this pre-nozzle ionization will tend to be maintained in the flow, and is better described in the flow by non-equilibrium models[3-b].)

The above relation can be conveniently rewritten as

$$\frac{n_i}{n_H} = \frac{1}{n_i} f(T)$$

where $f(T) = \left(\frac{m_e T}{2\pi\hbar^2}\right)^{3/2} e^{-\epsilon_0/T}$. Thus, for a specified ion density and temperature, the ratio (n_i/n_H) is known, and the equilibrium degree of ionization in hydrogen follows from $\xi = (n_i/n_H)/(1+(n_i/n_H))$. The degree of ionization is given in Table I.3 for a large range of densities and temperatures. One sees that the plasma is practically fully ionized in most cases, except for those cases already ruled out as being beyond the scope of the standard plasma model.

The ratio of the electron-atom collision frequency to the electron-ion collision frequency can be written as

$$\frac{\nu_{eH}}{\nu_{ei}} = \frac{n_H \sigma_{eH} v_e}{n_i \sigma_{ei} v_e} = \frac{n_H}{n_i} \frac{\sigma_{eH}}{\sigma_{ei}}.$$

This ratio is listed in Table I.4, where we used nominal values, $\sigma_{eH} = 10^{-14}$ cm^2 at $T = 1$ eV, $\sigma_{eH} = 10^{-15}$ cm^2 for $T \gtrsim 10$ eV. One sees that the electron-atom collision frequency is always negligible for all cases within the scope of the model. Since, according to Ref. (4), σ_{iH} is of the same order as σ_{eH}, and σ_{ii} is of the same order as σ_{ei}, one sees that the ion-atom collision frequency is also negligible against the ion-ion collision frequency.

We shall therefore neglect ion-neutral and electron-neutral collisions in this report. We nevertheless remark that as the temperature in the plasma decreases near a material surface, the degree of ionization drops exponentially (ξ^2 is proportional to exp $(-\epsilon_0/T)$) so that charge-neutral collisions ought to become prominent in edge layers. Impurity ions released from the wall will also contribute to the Coulomb-collision rates of electrons and hydrogen ions in edge layers, but these processes are not considered in this report.

2. The Limitations of the Fluid Model. Continuing with our examination of the conditions required for invoking convenient idealizations of flowing plasmas, we now ask when the fluid model of such a plasma is valid. Quite generally, fluid models are validated by a "localizing effect," the effect of which is that a local group of particles retains its

TABLE I.3 The Equilibrium Degree of Ionization

TABLE I.3 The Equilibrium Degree of Ionization
of Hydrogen Plasma $(\frac{n_i}{n_i+n_H})$
(In the tables, "n" represents the number density of ions.

$T[eV]$	1	10	100	1000
$n[cm^{-3}] = \quad 10^{13}$	0.997	1.000	1.000	1.000
10^{14}	0.974	1.000	1.000	1.000
10^{15}	0.788	1.000	1.000	1.000
10^{16}	0.271	1.000	1.000	1.000
10^{17}	0.036 ˣ	1.000	1.000	1.000
10^{18}	0.004 ˣ	1.000	1.000	1.000
10^{19}	0.0004ˣ	0.9996	1.000	1.000

group identity during a dynamical time of interest, and is not dispersed by random kinetic motions of the individual particles during this time. For an ordinary fluid composed of particles having a collisional mean-free path λ, undergoing a dynamical process having a characteristic time scale $\frac{L}{V}$, where L is a characteristic macroscopic length and V is a typical macroscopic fluid velocity, one can easily show (invoking the diffusivity $D = \lambda v_{th} = \lambda^2 \nu$ where v_{th} is the thermal velocity of the particles and ν is the collision frequency of an average particle) that the dispersal time is long compared to $\frac{L}{V}$ provided that $\frac{L}{\lambda} \gg 1$ (assuming that V is on the order of the thermal velocity of the particles). Accordingly, we list values of the electron mean-free path, $\lambda = \frac{v_e}{\nu_{ei}}$, in Table I.5 below (in Sec. I.B). The ion-mean-free path will be about the same[2] provided that the electron and ion temperatures are close. (In this scoping chapter, we assume a single temperature for simplicity.) Cases in which the mean free path (along the meridional magnetic field) exceeds 10^2 cm are flagged, because the fluid model of the plasma flow through the meridional magnetic nozzle then becomes suspect, and should be replaced with a kinetic model. Only cases accessible to a fluid treatment will be considered in this report.

With regard to the azimuthal magnetic nozzle, a large mean-free path along $\vec{B}$ is not particularly significant or detrimental for the fluid model of axisymmetric flow because $\vec{B}$ is in the ignorable (azimuthal) direction. Instead, the localizing agent relevant to (r, z) fluid motions is the ion gyro-radius, r_{ci}. (The symbol r_{ci} historically stands for "ion cyclotron radius." It is defined by $r_{ci} = v_i/\omega_{ci}$, where v_i is the ion thermal velocity and

TABLE I.4 The equilibrium ratio of electron-atom collision frequency to electron-ion collision frequency for hydrogen plasma.
(The electron-atom scattering cross-section was assigned nominal values $\sigma_{eH} = 10^{-14}\ cm^2$ for $T = 1\ eV$, $\sigma_{eH} = 10^{-15}\ cm^2$ for $T \geq 10\ eV$.)

$T[eV]$	1	10	100	1000
$n[cm^{-3}] = 10^{13}$	4.2×10^{-5}	6.4×10^{-11}	6.0×10^{-11}	1.7×10^{-10}
10^{14}	4.2×10^{-4}	6.4×10^{-10}	6.0×10^{-10}	1.7×10^{-9}
10^{15}	4.2×10^{-3}	6.4×10^{-9}	6.0×10^{-9}	1.7×10^{-8}
10^{16}	4.2×10^{-2}	6.4×10^{-8}	6.0×10^{-8}	1.7×10^{-7}
10^{17}	4.2×10^{-1}ˣ	6.4×10^{-7}	6.0×10^{-7}	1.7×10^{-6}
10^{18}	4.2 ˣ	6.4×10^{-6}	6.0×10^{-6}	1.7×10^{-5}
10^{19}	4.2×10 ˣ	6.4×10^{-5}	6.0×10^{-5}	1.7×10^{-4}

$\omega_{ci} = (eB/m_i c)_{cgs}$, is the ion gyro-frequency in the magnetic field B.) Now, one can invoke the ion collisional diffusivity across the magnetic field, $D = r_{ci}^2 \nu_{ii}$, where ν_{ii} is the ion-ion Coulomb collision frequency. Then, repeating the same argument as for the mean-free-path case above, one finds that the dispersal time for the minor cross-section of a ring-shaped (annular) group of ions to spread out in the (r, z) plane will be long compared to $\frac{L}{V}$ provided that $(\frac{L}{r_{ci}})(\frac{\omega_{ci}}{\nu_{ii}}) \gg 1$ (again assuming that V is on the order of or larger than the thermal velocity of the ion particles). Thus, it is required, at least, that $\frac{L}{r_{ci}} \gg 1$. (A supporting condition is that there should be many ion gyro-periods between collisions of an average ion, $\omega_{ci} > \nu_{ii}$.) Accordingly, we also list values of the hydrogen-ion gyro-radius in Table I.5. It appears that r_{ci} is a comfortably small scale length in all but the lowest density cases. We emphasize that the marginally worrisome value, $r_{ci} \approx 5$ cm, obtained for $n = 10^{13}$ cm^{-3} in Table I.5, is a cause for concern in fluid-plasma modeling of both types of magnetic nozzles, meridional and azimuthal, if their transverse dimensions are not much larger than 5 cm.

We also note that when $\lambda < r_{ci}$, the condition for validity of the fluid model again reverts to the condition that $\frac{L}{\lambda} \gg 1$. Here, we note that mean free path scattering for

TABLE 1.5 Values of Mean-Free Path (λ) in cm, and Ion-Gyro-Radius (r_{ci}) in cm, (for a $Z = 1$ Hydrogen Plasma.)

T [eV]	1	10	100	1000
n [cm^{-3}] =				
10^{13}	$\lambda = 1.60 \times 10^{-1}$ [cm] $r_{ci} = 5.30$ [cm]	1.60×10 5.30	1.60×10^3 x 5.30	1.60×10^5 x 5.30
10^{14}	1.60×10^{-2} 1.68	1.60 1.68	1.60×10^2 x 1.68	1.6×10^4 x 1.68
10^{15}	1.60×10^{-3} 5.30×10^{-1}	1.60×10^{-1} 5.30×10^{-1}	1.60×10 5.30×10^{-1}	1.60×10^3 x 5.30×10^{-1}
10^{16}	1.60×10^{-4} 1.68×10^{-1}	1.60×10^{-2} 1.68×10^{-1}	1.60 1.68×10^{-1}	1.60×10^2 x 1.68×10^{-1}
10^{17}	1.60×10^{-5} x 5.30×10^{-2}	1.60×10^{-3} 5.30×10^{-2}	1.60×10^{-1} 5.30×10^{-2}	1.60×10 5.30×10^{-2}
10^{18}	1.60×10^{-6} x 1.68×10^{-2}	1.60×10^{-4} 1.68×10^{-2}	1.60×10^{-2} 1.68×10^{-2}	1.60 1.68×10^{-2}
10^{19}	1.60×10^{-7} x 5.30×10^{-3}	1.60×10^{-5} 5.30×10^{-3}	1.60×10^{-3} 5.30×10^{-3}	(89 $Tesla$)

Note:

a. λ [cm] $\approx 1.6 \times 10^{12} \dfrac{T^2_{[eV]}}{n_{[cm^{-3}]}}$ (At high temperatures. "x" flags values of λ larger than 1 meter.)

b. r_{ci} [cm] $\approx 1.5 \times 10^2 \dfrac{T^{1/2}_{[eV]}}{B_{[Gauss]}}$

c. $\dfrac{\nu_{ii}}{\nu_{\perp}} \approx \dfrac{\lambda}{r_{ci}}$

d. The large ion gyro-radius at $T = 1$ eV for $n = 10^{13} - 10^{15}$ cm^{-3} is not physically significant because the ions are un-magnetized at 1 eV.

15

$\lambda < r_{ci}$ occurs in all directions (especially across $\vec{B}$) and thus can affect, in principle, the validity of the fluid model for both types of magnetic nozzles. However, Table I.5 shows that whenever $\lambda < r_{ci}$ does occur, the length scale for λ is, in fact, comfortably small compared to envisioned nozzle dimensions. Therefore, the value of λ is a concern only when it is large and thereby affects the validity of fluid modeling of the meridional magnetic nozzle.

Finally, we note that Appendix D addresses the notion that $\beta \sim 1$ is a reasonable relation to invoke for the scoping study of azimuthal magnetic nozzles as well as meridional magnetic nozzles; and we mention that the limitations of the single-temperature assumption for azimuthal nozzles are addressed in Appendix E in which the degree of electron heating is estimated for these devices.

B. Neglect of the Hall Effect in Ideal MHD

The often-neglected Hall term in Ohm's law is (in MKS units)

$$\frac{1}{ne}\vec{J} \times \vec{B}$$

Usually, one compares this to the $\vec{V} \times \vec{B}$ term in Ohms law,

$$\vec{E} + \vec{V} \times \vec{B} = \frac{1}{ne}\vec{J} \times \vec{B} + \eta\vec{J} - \frac{1}{ne}\nabla P_e$$

Here

V = fluid or plasma velocity

B = magnetic field strength

n = particle number density

J = current density

E = electric field

P_e = electron pressure

η = resistivity of plasma

The fluid momentum equation is used to estimate $\vec{J} \times \vec{B}$. The transverse (cross-field) component of conducting fluid momentum balance in axi-symmetric steady flow is

$$\rho(\vec{V} \cdot \nabla\vec{V}) \cdot \hat{\tau} + (\nabla P) \cdot \hat{\tau} = \vec{J} \times \vec{B} \cdot \hat{\tau}$$

where P is the total pressure of electrons and ions, $\rho = nm_i$ is the mass density, and where $\hat{\tau}$ is a unit vector in the relevant transverse or cross-field direction. Thus, $\hat{\tau}$ is in the radial-like direction for meridional magnetic fields ($\vec{J} \times \vec{B} = J_\theta B_z \hat{r}$) and $\hat{\tau}$ has components in the radial and axial directions for azimuthal magnetic fields ($\vec{J} \times \vec{B} = J_r B_\theta \hat{z} - J_z B_\theta \hat{r}$). Here, we are referring to cylindrical coordinates (r, θ, z), and unit vectors $\hat{r}$ and $\hat{z}$ in the radial and axial directions respectively.

If we assume that transonic flow is characteristic of the configuration, then both terms on the *lhs* of the momentum equation are comparable, and we estimate that

$$\left| \vec{J} \times \vec{B} \right| \sim \frac{P}{\ell_\perp} \sim \frac{nm_i v_i^2}{\ell_\perp}$$

where $\ell_\perp$ is a characteristic cross-field dimension of the flow configuration ($\ell_\perp$ is the smaller of the cylindrical radius and the radius of curvature of a representative streamline), and v_i is the ion thermal velocity, which is comparable to the sonic speed in the plasma.[*] The desired inequality for neglect of the Hall term,

$$\left| \vec{V} \times \vec{B} \right| \gg \frac{1}{ne} \left| \vec{J} \times \vec{B} \right|,$$

together with the transonic estimate, $V \sim v_i$, then leads immediately to the condition

$$1 \gg \left(\frac{v_i}{\omega_{ci} \ell_\perp} \right)$$

where $\omega_{ci} = (eB/m_i)_{MKS}$ is the ion gyro-frequency.

In other words, the above considerations lead to the condition that the representative ion gyro radius, $r_{ci} \equiv (v_i/\omega_{ci})$, should be small compared to the characteristic cross-field dimensions of the configuration, as a requirement that the Hall term should be ignorable in a model that describes the ideal dynamical properties of the highly conducting fluid. This argument as given above is certainly reasonable for azimuthal magnetic nozzles in which the dominant flow is across the magnetic field so that $\vec{V} \times \vec{B}$ is a dominant term.

However, in the case of plasma flow through meridional magnetic nozzles, the above argument and conclusion must be re-examined and reconstructed, because the flow (which is indeed transonic) is parallel to the magnetic field, $\vec{V} \times \vec{B} \equiv 0$ in ideal MHD (see Appendix A) so that the basic desired inequality, $|\vec{V} \times \vec{B}| \gg \frac{1}{ne}|\vec{J} \times \vec{B}|$, makes no sense in the meridional case.

Thus, we reconsider the meridional magnetic field configuration. Knowing that the flow is parallel to $\vec{B}$ and is transonic in ideal MHD, we ask what is the effect of the Hall term on the distortion of this flow. In thermally-driven flow which is practically parallel to $\vec{B}$, there is no inconsistency in arranging to have all meridional magnetic field lines held at the same electric potential. In fact, the electric field perpendicular to $\vec{B}$ must vanish in ideal MHD with purely parallel flow, because the field lines are immersed in a highly conducting fluid. Assuming this to be the case with the Hall effect present, the Ohm's law including the Hall term (but neglecting the resistive and diamagnetic terms) becomes simply

$$\vec{V}_\perp \times \vec{B} \equiv \frac{1}{ne} \vec{J} \times \vec{B}$$

---

[*] The transonic character of the flow for azimuthal magnetic nozzles follows from Appendix D in which it is argued that the ion-beta value ought to be near unity because of the manner in which the plasma is created.

17

where the Hall-induced velocity increment, $\vec{V}_\perp$, is in the azimuthal direction as dictated by $\vec{J}_0 \times \vec{B}$.

Thus, if all meridional magnetic field lines are held at the same electric potential, the main effect of the Hall term is to induce a small rotational motion of the plasma. To see how small this rotational motion really is, we re-write the above equation as

$$|V_\theta| = \frac{1}{neB}\left|\vec{J}\times\vec{B}\right|,$$

and use the transverse momentum equation as before to provide the estimate of $|\vec{J}\times\vec{B}|$ given above, which is still valid. The outcome of this exercise is simply that

$$\frac{|V_\theta|}{v_i} \sim \frac{r_{ci}}{\ell_\perp},$$

which implies that the rotational motion will be negligible in comparison with the transonic (parallel) flow provided that the ion gyro-radius is small compared to the transverse dimensions of the nozzle.

$$r_{ci} \ll \ell_\perp$$

This is the same condition we found earlier for neglecting the Hall term, but now derived in a manner that recognizes explicitly that in the meridional case, the basic plasma flow is parallel to $\vec{B}$. This small ion-gyro-radius requirement will generally be satisfied in cases of interest. (See Table I.5.)

As a final remark on the meridional configuration, we observe that $(ne)^{-1}(\vec{J}\times\vec{B})$, as estimated above, is on the same order as the electron diamagnetic term in Ohm's law, $(ne)^{-1}\nabla P_e$, for comparable electron and ion temperatures. Thus, the condition for neglecting the electron pressure gradient (diamagnetic term) in Ohm's law is essentially the same as the condition required to neglect the Hall term, namely, $r_{ci} \ll \ell_\perp$. Including either of these terms has the effect of producing only a slight azimuthal twist to the fluid streamlines.

Finally, as a check and to illustrate a certain point, we reconsider the azimuthal magnetic field configuration. Here, the accelerated flow is primarily axial due to the $(\vec{J}_r \times \vec{B}_\theta)$ force. In this case, a direct comparison of the $|\vec{V}\times\vec{B}|$ term in Ohm's law to the often neglected Hall term can be made in a straight forward manner. Referring to the axial cross-field component of the fluid momentum equation written down at the beginning of this section, and using convenient cgs units in this case, the rhs is $\frac{1}{c}(\vec{J}\times\vec{B})\cdot\hat{r}$. Since, along a streamline, $\frac{V_r}{V_z} \sim \frac{\Delta r}{\Delta z}$, the inertial term on the lhs can be estimated by $(\rho V^2/\ell_z)$ where ℓ_z is a characteristic axial length of the azimuthal magnetic nozzle. This term sufficiently represents the lhs of the axial momentum equation since it will be comparable to the axial pressure gradient term in transonic flow. (Since $\beta \sim 1$ (see Appendix D), transonic and trans-Alfvénic flows are essentially the same condition.) Since the flow is characteristically trans-Alfvénic (see Appendix B), we can estimate as follows.

$$\frac{1}{c}\left|\vec{J}\times\vec{B}\right| \sim \frac{\rho C_A^2}{\ell_z}$$

18

Here, C_A^2 is the square of the Alfvén speed, given by

$$C_A^2 = B_\theta^2/(4\pi\rho)$$

in cgs units. In Ohm's law, the desired inequality for neglecting the Hall term (in cgs units) is

$$\frac{1}{c}\left|\vec{V} \times \vec{B}\right| \gg \frac{1}{nec}\left|\vec{J} \times \vec{B}\right|.$$

Using the above estimate for $\frac{1}{c}|\vec{J} \times \vec{B}|$, and the characteristic trans-Alfvénic flow velocity, $V \sim C_A$, the magnetic field cancels out and the inequality is easily reduced to

$$\ell_z \gg \frac{c}{\omega_{pi}},$$

where $\omega_{pi} = (4\pi ne^2/m_i)^{1/2}$ is the ion plasma frequency expressed in cgs format and c is the speed of light. The above derivation is valid as it stands if conditions in the azimuthal magnetic nozzle happen to be "low beta," i.e. $\beta \ll 1$. Then, the characteristic length that needs to be small in order to neglect the Hall effect in ideal MHD modeling is (c/ω_{pi}) rather than the ion gyro-radius.

But $\frac{c}{\omega_{pi} r_{ci}} = \frac{1}{\sqrt{\beta_i}} \approx 1$, provided that the ion beta, $\beta_i = 8\pi nT_i/B^2$, is of order unity, as it should be for azimuthal magnetic nozzles (see Appendix D). Thus, we are again led to the condition of a small ion gyro-radius, $\ell_z \gg r_{ci}$, in order to neglect the Hall term. One can generally expect this condition to be well satisfied. Here, it is important to remark that although the small ion-gyroradius condition is a reasonable general assumption, particular devices may contain localized regions in the axisymmetric flow that entail sharp gradients, comparable to r_{ci} (or smaller), within which the Hall effect may play an important role. Flows that develop local asymmetries are also subject to this effect.

Morozov and co-workers[5-a,5-b] have discussed some aspects of steady axisymmetric MHD flow with account of the Hall effect. Mathematically, they find that the ideal MHD equations including the Hall term are not well-posed and that the equations to be solved are, therefore, vulnerable to instabilities. Moreover, they find that the equations do become well-posed and computationally robust provided sufficient resistive diffusion is added to the model by including the $\eta\vec{J}$ term in Ohm's law. The computational results[5-b] show that the Hall term induces the formation of strong localized plasma currents at certain characteristic positions on both cathode and anode, suggesting that the Hall effect may be related to electrode erosion in azimuthal magnetic nozzles.

It needs to be remarked here that the order of the Hall term compared to remaining terms in Ohm's law is similar to the order of certain components of the ion magneto-viscosity tensor compared to remaining terms in the fluid momentum equation.[2] Therefore, a proper computational treatment of the Hall effect may also require the incorporation of the correct ion viscosity tensor in the computational models. This point is often ignored because the Hall term by itself constitutes a simple addition to ideal MHD, whereas it is much more difficult to construct computational tools containing the full Braginskii viscosity tensor. Ref. 5-b does not seem to have included both effects at the same time in the computational model.

C. General Conditions for Relatively Small Losses from the Flowing Plasma

1. Transport Losses.

a. Mass Transport.   First, consider cross-field (radial) mass transport of plasma. To the extent that it occurs, this process represents an inefficiency of the guiding (meridional) or driving (azimuthal) magnetic fields, and it allows hot plasma to approach the walls. Both mass transport and heat transport may occur either as the result of Coulomb collisions of plasma particles (e.g. of electrons with ions), or as the result of convective motions induced by instabilities and/or turbulence. The latter possibility will be discussed in later sections. In this section, we limit the discussion to collisional transport.

The reader is cautioned that Hall and pressure terms in Ohm's law must be retained at the outset in this discussion. The previous section (I-B) showed only that such terms are small within the context of ideal MHD, but here, we are considering "small" non-ideal effects.

We shall take Ohm's law, and vector-multiply it with the magnetic field $\vec{B}$, retaining all terms. Ohm's law reads (conveniently in cgs units),[*]

$$\vec{E} + \frac{1}{c}\vec{V} \times \vec{B} = \eta\vec{J} + \frac{\vec{J} \times \vec{B}}{nec} - \frac{\nabla P_e}{ne} \qquad (I.1)$$

After taking the cross-product of this equation with $\vec{B}$ and dividing by B^2, we consider the radial component (or its generalization to axisymmetric geometry). The result can be written as follows.

$$\left(\vec{V}_\perp - \vec{V}_B\right)_r = -\eta\frac{c^2}{B^2}\left(\rho\vec{V}\cdot\nabla\vec{V} + \nabla P\right)_r + \frac{\vec{J}_{\perp r}}{ne} + \frac{c}{neB^2}(\nabla P_e \times \vec{B})_r \qquad (I.2)$$

Here, we have utilized the fluid momentum equation to replace $\vec{J} \times \vec{B}$ in the resistive term. The notation "$\perp$" means perpendicular to the magnetic field $\vec{B}$, and $\vec{V}_B$ represents the guiding center drift velocity (which can also be regarded as the velocity of the magnetic field lines), $\vec{V}_B \equiv c\vec{E} \times \vec{B}/B^2$ with $\vec{E}$ being the electric field in the plasma. Moreover, n is the plasma ion number density, and P is the total pressure of electrons and ions, $P = P_e + P_i$. Also, in cgs units, "c" is the speed of light in (cm/s).

CASE I: THE MERIDIONAL MAGNETIC NOZZLE $[\vec{B} = (B_r, 0, B_z)]$

In the case of the meridional magnetic nozzle with axisymmetric flow, there are no "radial" currents in the plasma, and there is only a "radial" component of the transverse electron pressure gradient. [Gradients parallel to $\vec{B}$ make no contribution to Eq. (I.2).] Therefore, the last two terms of Eq. (I.2) vanish. Moreover, because the azimuthal electric field, E_θ, vanishes in a steady state with axisymmetry, and because $B_\theta \equiv 0$ in the configuration, the $\vec{E} \times \vec{B}$ drift has no "radial" component. Therefore, Eq. (I.2) reduces to

$$V_{\perp r} = -\eta\frac{c^2}{B^2}(\rho\vec{V}\cdot\nabla\vec{V} + \nabla P)_r \qquad (I.3)$$

---

[*] The neglected thermal force terms do not change the essence of the discussion or the qualitative conclusions, but including them would considerably complicate the presentation. See Appendix F.

Thus, plasma resistivity allows "radial" slippage of plasma across the magnetic field, said slippage being driven by pressure gradients and inertial forces. In transonic flow through the nozzle, $V \sim v_i$, these two driving terms will initially have the same sign and the same order of magnitude.[*] (Here, $V = V_{\parallel}$ is the dominant component of flow velocity and v_i is the ion thermal velocity.) However, for long thin nozzles, the "radial" fluid inertial term $\frac{\rho V_{\parallel}^2}{R_c}$, will be dominated by the "radial" pressure gradient. (Here R_c represents the radius of curvature of magnetic field lines.) This is also true for general nozzle shapes in which the radius of curvature in the meridional plane is larger than the nozzle radius near the throat.

For the purpose of making a simple estimate, the inertial term will now be neglected, and the temperatures will be assumed uniform. Neither of these assumptions will change the order of magnitude of the result—nor the scaling properties.

Then, upon multiplication of (I.3) by the plasma density n, we find

$$nV_{\perp r} = -\eta c^2 \frac{n(T_e + T_i)}{B^2} \frac{\partial n}{\partial r}, \qquad (I.4)$$

where T_e and T_i are the electron and ion temperatures respectively. Introducing the local plasma beta by $\beta = 8\pi n(T_e + T_i)/B^2$, Eq. (I.4) reads

$$nV_{\perp r} = -\frac{1}{2}\left(\frac{c^2}{4\pi}\eta\right)\beta\frac{\partial n}{\partial r}. \qquad (I.5)$$

We see that this equation has the form of Fick's law for diffusion, $\vec{\Gamma} = -D\nabla n$, where $\vec{\Gamma}$ is the particle flux, and the particle diffusivity is

$$D_{part} = \frac{1}{2}D_\eta\beta. \qquad (I.6)$$

Here, the resistive diffusivity, D_η, in cgs units is given by

$$D_\eta\left(\frac{cm^2}{s}\right) = \frac{c^2}{4\pi}\eta, \qquad (I.7)$$

with $\eta(sec)$ being the plasma resistivity in cgs units.

Since we are limiting the discussion to $\beta \approx 1$, we shall take (I.6) in the form

$$D_{part} = \frac{1}{2}D_\eta. \qquad (I.8)$$

However, we emphasize that, for low densities and low temperatures, one could probably afford to reduce the particle diffusivity D_{part} by lowering the plasma beta with the use of stronger magnetic fields. (See Table I.1.)

---

[*] That is, in the upstream portion of the nozzle where the streamlines are convex to the outside, the inertial and pressure terms both force the plasma radially outwards. Further downstream in the throat and exit regions, the inertial term acts radially inwards, opposite the pressure term.

In order to estimate a time scale for mass loss by resistive diffusion, we shall simply divide the number of ions present per unit axial length by their loss rate from the "radial" diffusive flux, $D_{part}\frac{\partial n}{\partial r}$, per unit axial length. The result is

$$t_{part} = \frac{\langle n \rangle \pi r^2}{\left(D_{part}\frac{\partial n}{\partial r}\right) 2\pi r} = \frac{1}{D_\eta} \frac{r\langle n \rangle}{\left(\frac{\partial n}{\partial r}\right)}, \tag{I.9}$$

where $\langle n \rangle$ is the average density in the nozzle cross-section. For a parabolic density profile that has $n(a) = 0$ as the generic example of a general diffuse profile, this expression becomes

$$t_{part} \approx \frac{a^2}{4 D_\eta} \tag{I.10}$$

where "a" represents the characteristic radial dimension of the nozzle.

Next, we shall compare the characteristic loss time (I.10) with the characteristic transit time through the nozzle. Assuming transonic flow, we shall estimate the latter by

$$t_z = \frac{\ell_z}{v_i} \tag{I.11}$$

where ℓ_z represents the length of the nozzle, and $v_i \equiv \left(\frac{2T_i}{m_i}\right)^{1/2}$ represents the ion thermal velocity. Here, we note that v_i is close enough to C_s, the speed of sound, to be used for these rough estimates.

The ratio of (I.10) to (I.11) is

$$\frac{t_{part}}{t_z} = \frac{1}{4} \frac{R_\eta}{A}. \tag{I.12}$$

where the magnetic Reynold's number, R_η, has been defined as (with $v_i \approx V$ in the transonic flow)

$$R_\eta = \frac{a v_i}{D_\eta}, \tag{I.13}$$

and the aspect ratio of the nozzle, A, has been defined as

$$A = \frac{\ell_z}{a} \tag{I.14}$$

To avoid radial loss of plasma, the desired condition is $t_{part} \gg t_z$. We therefore see that large magnetic Reynolds numbers are required in order to avoid substantial radial mass loss of plasma during transit through the meridional nozzle, for $\beta = 1$. More generally, we shall have

$$\frac{t_{part}}{t_z} = \frac{1}{4} \frac{R_\eta}{\beta A}, \tag{I.15}$$

which illustrates that moderate values of R_η could be acceptable provided that the investment can be made in coil mass and power supplies required to increase the magnetic field strength and thereby reduce β.

TABLE I.6 Values of Magnetic Reynolds Number,
vs. Temperature for two values of
Nozzle radius a. ($\ell n\Lambda = 10$ assumed)

$T[eV] =$	1	10	100	1000
$a = 10\ cm$:	1.6	160	1.6×10^4	1.6×10^6
$a = 100\ cm$:	16	1600	1.6×10^5	1.6×10^7

Note: In tables such as this, we shall usually maintain only two-significant-figure accuracy.

Values of the magnetic Reynolds number are given in Table I.6, for values of nozzle radius $a = 10\ cm$ and $a = 10^2\ cm$. Because of the way Coulomb collisions act to produce electrical conductivity in plasmas, the magnetic Reynolds number proves to be independent of the density of plasma. (To obtain the results in this table, we took $T_e = T_i$ and used $v_i(cm/s) = 1.3 \times 10^6\ T^{1/2}(eV)$, $D_\eta = \frac{c^2}{4\pi}\eta$, and $\eta^{-1} = \sigma(s^{-1}) = 0.9 \times 10^{13}T^{3/2}(eV)$ for $\ell n\Lambda \approx 10$. [2])

It is important to add the following remark in connection with the Table. For beta values near unity, and nozzle aspect ratios near 10, the numbers in this Table must be divided by 40 [see Eq. (I.12)] in order to properly assess the losses due to radial resistive diffusion of plasma.* We see that plasmas of 10 eV temperature or higher appear to be quite satisfactory in this regard. However, the 1 eV plasmas are clearly not satisfactory for unity-beta-values, and should be operated at sufficiently high magnetic fields that the correspondingly lower beta value reduces the resistive transport of plasma to reasonable values. (This remark applies for general diffuse profiles, but does not apply to the "field-free core" version of the sharp-boundary profile (for which beta effectively must be unity) advocated later in order to overcome the "detachment problem.")

The Detachment Problem

At this point, it is appropriate to consider the "detachment problem" of how the plasma exits the meridional magnetic nozzle, because the axisymmetric description of this process depends on the extent of resistive transport of plasma across the magnetic field. We have just seen that large values of R_η (or $\beta^{-1}R_\eta$) prevent cross field resistive transport of plasma, but this condition of large magnetic Reynolds numbers is not desirable for general diffuse profiles in the final phase of axial transit. This is because if the plasma were highly conducting, it would then have to follow the radially diverging magnetic field lines back around the field coils where it would ultimately deposit its momentum onto the vehicle, thereby negating the thrust.

---

* However, Fig. 1-b indicates that it may be more accurate to replace A by $\frac{1}{2}A$ in making these estimates.

23

An exit plasma with a diffuse profile and with a small value of R_η, on the other hand, could use its inertia to coast axially across the radially diverging field lines, and thus avoid this "hang-up." The results of the quasi-1-D model of isentropic flow shown in Fig. 1 suggest that the strong downstream temperature drop, with the associated drop in electrical conductivity ($\sigma \sim T^{3/2}$), might actually allow this detachment to take place. Here, it is important to note that, in order for this to work, the input value of R_η should be only moderately large, otherwise the exit value of R_η would still be too large to allow cross-field transport. (That is, if $R_\eta (input) = 10^6$ and $R_\eta (exit) = 10^{-3} R_\eta (input)$, then one would still have a highly conducting plasma at the exit.)

However, real plasmas are not isentropic. The large parallel (to $\vec{B}$) thermal conductivity of the electrons must be taken into consideration here. This effect, precluded by the isentropic model, will tend to maintain a high electron temperature (and a high electrical conductivity) at the nozzle exit, thereby exacerbating the detachment problem. An axisymmetric MHD simulation with transport capabilities is required, in principal, to provide quantitative answers to the combined influences of parallel thermal conduction and rate of divergence of field lines at the nozzle exit on the detachment process in particular cases. Nevertheless, an approximate calculation that we perform below indicates that the effect of parallel electron thermal conduction can be suppressed for some reasonable parameter values.

For a time scale to transfer a substantial amount of heat from the hot upstream plasma to the cold downstream plasma by means of parallel electron thermal conduction, we take the following estimate,

$$t_{e\parallel} \sim \ell_z^2 / D_\parallel^e ,$$

where[2] the parallel electron thermal diffusivity is

$$D_\parallel^e = \frac{3}{2} \frac{v_e^2}{\nu_{ei}},$$

with

$$v_e = (2 T_e/m_e)^{1/2}, \quad \text{and} \quad \nu_{ei} = \tau_e^{-1} = \frac{ne^2}{m_e\sigma},$$

$$\sigma(s^{-1}) = 0.9 \times 10^{13} T_e^{3/2}(eV) \text{for} \quad \ell n \Lambda \approx 10.$$

For the axial transit time, we use

$$t_z = \ell_z / v_i$$

with $v_i = (2T_i/m_i)^{1/2}$ being the ion thermal velocity (which is close enough to C_s). We use m_i for hydrogen, set $T_e = T_i$ for simplicity, and thus find

$$\frac{t_{e\parallel}}{t_z} \approx 0.60 \times 10^{-14} \frac{\ell_z(cm)n(cm^{-3})}{T^2_{(eV)}} \tag{1.16}$$

It is reasonable to regard the parameters in this expression as being evaluated at the "halfway point," that is, in the throat region of the nozzle. In order for electron parallel

TABLE I.7 Values of $(t_{e\parallel}/t_z)$ for $\ell_z = 10^2\ cm$

$T[eV] =$	1	10	100
$n(cm^{-3}) = 10^{13}$	6	6×10^{-2}	6×10^{-4}
10^{14}	60	0.60	6×10^{-3}
10^{15}	600	6	6×10^{-2}
10^{16}	6000	60	0.60

thermal conduction to be unimportant, we require $t_{e\parallel} \gg t_z$. Values of $t_{e\parallel}/t_z$ are given in Table I.7, for $\ell_z = 10^2\ cm$.

From this, we conclude that there is a range of moderate upstream temperatures and fairly high densities wherein the effect of parallel electron thermal conduction downstream can be mitigated. Of course, the viable range of operating temperatures can be increased by the employment of longer nozzles. However, in the 100 eV range of temperatures, it appears that the effect of downstream electron thermal conduction will be a major concern except at very high densities.

It is important to mitigate the parallel electron thermal conduction for another reason besides that of allowing detachment of plasma at the exit. This other reason is that heat conducted rapidly downstream is wasted since it cannot contribute to the development of thrust, and hence represents an inefficiency. At the higher temperatures, more specific impulse is realized (see Appendix C for the pulsed power approach to the use of hot plasmas), but then the detachment problem and the issue of efficiency must be scrutinized. A trade-off study is indicated, and is best performed by means of a 2-D MHD simulation with transport capabilities. (Of course, such a simulation is reliable only when the Coulomb-collisional mean-free path along $\vec{B}$ is short compared to the length of the nozzle. See Table I.5.)

To indicate the importance of the detachment problem, we shall now make a rough estimate of the magnitude and scaling of the exit velocity. We shall assume that the parameters are such that electron thermal conduction is not a major problem. The possibility then arises that the axial inertia developed by the plasma within the nozzle will enable the plasma to coast resistively across the radially diverging magnetic fields at the exit. Such a possibility is brought about by the rapid drop in plasma temperature (hence a drop in electrical conductivity) as the plasma expands through the downstream side of the nozzle.

Let us focus our attention on the temporal behavior of an annular element of plasma as it follows an annular meridional magnetic flux tube out to where the field lines turn

25

around and start to go back around the outside of the field coils. We shall take an iterative approach that, in the first instance regards the plasma as highly conducting, but in the next instance calculates certain effects due to finite resistivity. The physics of the detachment process that we shall explore consists of the axial cross-field velocity of plasma, as allowed by the presence of resistivity, and as driven by the axially-directed centrifugal force on the plasma when the plasma (as a good conductor) attempts to turn around and follow the field lines back towards the vehicle.

The derivation is as follows. The azimuthal component of the complete Ohm's law (including Hall and diamagnetic terms) for the case of steady axisymmetric flow is simply (MKS units)

$$-V_r B_z + V_z B_r = \eta J_\theta. \tag{I.17}$$

In the exit region of radially diverging magnetic fields, $B_z \lesssim B_r$. In fact, we shall concentrate on the region near the maximum axial extension of a field line where $B_z \ll B_r$. Therefore, Eq. (I.17) shall be taken approximately as

$$V_z B_r = \eta J_\theta \tag{I.18}$$

At this point, we shall reduce the model to construct a simple physical picture of what is going on. Consider a strip of resistive metal, having resistivity η and density ρ, infinitely extended in the y-direction (representing the azimuthal direction θ), with a small thickness Δ_z in the z-direction, and arbitrary height L_x in the x direction (representing the radial direction r). Imagine that this strip of resistive metal is being pulled across a magnetic field B_x (representing B_r) by a steady external force acting in the z direction. Let F_z represent that external force, per unit (x,y) area. We shall identify F_z shortly. Moreover we shall take the electric field $E_y = 0$, because $E_\theta = 0$. Observe that the axial magnetic force acting on this resistive metal strip, per unit (x,y) area, is then

$$(\vec{J} \times \vec{B})_z \Delta_z = -J_y B_x \Delta_z = -\frac{1}{\eta} V_z B_x^2 \Delta_z, \tag{I.19}$$

which is opposite to the direction of motion caused by the force F_z. (Here, we have invoked Eq. (I.18) for $J_\theta = J_y$.) The equation of motion of this strip may now be written as follows noting that $\rho \Delta_z$ is the mass per unit (x,y) area,

$$(\rho \Delta_z) \frac{dV_z}{dt} = F_z - V_z \frac{B_x^2 \Delta_z}{\eta}. \tag{I.20}$$

The solution of this equation has the form of an exponential approach to a final steady velocity. That is

$$V_z = V_{z(final)}(1 - e^{-\frac{t}{t_{exp}}}). \tag{I.21}$$

The time scale to approach the final velocity proves to be given by

$$t_{exp} = \frac{D_{\eta(exit)}}{C_{A(exit)}^2}. \tag{I.22}$$

26

As an equivalent expression, one can also write

$$t_{exp} = \left(\frac{t_A}{R_\eta^{(A)}} \right)_{exit} \qquad (I.22-a)$$

where t_A is a radial Alfvén time, and $R_\eta^{(A)}$ is a magnetic Reynolds number that is defined using the Alfvén speed. Here, the resistive diffusivity, $D_\eta = \frac{\eta}{\mu_0}$, and the Alfvén speed, $C_A = (B_x^2/\mu_0\rho)^{1/2}$, are evaluated in the exit region of the nozzle. The time scale for this transient phase can be fairly short. As an example, consider the following moderate parameters that might characterize the hydrogen plasma in an exit region: $n \approx 10^{13} \ cm^{-3}$, $T \approx 1 \ eV$, $B \approx 100$ Gauss. Then, the transient phase lasts a time $t_{exp} \approx 2 \times 10^{-7}$ sec. The final axial velocity quickly becomes relevant for $t \gtrsim t_{exp}$, and is given by

$$V_{z(final)} = \frac{F_z D_\eta}{\Delta_z (B_x^2/\mu_0)} \qquad (I.23)$$

At this point, we arrive at a crucial feature of our model. We now identify the applied force density as the centrifugal force density exerted on the plasma as it tries to follow the field line "around the bend." This is the process whereby the axial plasma inertia induces the plasma to coast resistively in the axial direction across the radially diverging magnetic field.

$$\frac{F_z}{\Delta_z} = \left(\rho \frac{V_\parallel^2}{R_c} \right)_{exit} \qquad (I.24)$$

Here, ρ and $V_\parallel = V_e$ are the exit values of density and flow velocity as computed in the ideal MHD model (see Appendix A), and $R_c \gtrsim a$ is the representative radius of curvature of a magnetic field line evaluated at its farthest axial extension. After substituting (I.24) into (I.23), one finds

$$\frac{V_{z(final)}}{V_\parallel} = \left(\frac{V_\parallel^2}{C_A'^2} \right)_{exit} \left(\frac{D_\eta}{R_c V_\parallel} \right)_{exit} \qquad (I.25)$$

Now, it can be demonstrated that, to order of magnitude,

$$\left(\frac{V_\parallel^2}{C_A'^2} \right)_{exit} \sim \frac{A_e}{A_0} \beta_0 \qquad (I.26)$$

where A_e and A_0 are the areas of the nozzle exit and the nozzle throat respectively and β_0 is the value of the plasma beta in the throat of the nozzle. Therefore, to order of magnitude, we can write (I.25) as

$$V_{z(final)} \sim \left[\frac{A_e}{A_0} \frac{\beta_0}{R_{\eta(exit)}} \right] V_\parallel, \qquad (I.27)$$

where we have defined a magnetic Reynolds number in the exit region by $R_{\eta(exit)} \equiv (R_c V_\parallel / D_\eta)_{exit}$.

Note that this model cannot be applied for arbitrarily small Reynolds numbers, $R_\eta \to 0$, because then the transient phase would last for an arbitrarily long time, [see Eq. (I.22)], and thereby preclude consideration of the final asymptotic velocity. The qualitative conclusion from (I.27) is that axial plasma inertia can indeed axially drive the plasma resistively across the radially diverging magnetic fields, even with a velocity comparable to $V_\parallel$, provided that the magnetic Reynolds number in the exit region is not too large compared to unity, and provided also that the beta value in the throat of the nozzle is not too small.

So far, this result seems encouraging. It appears that if one can arrange the upstream parameters so that the downstream magnetic Reynolds number is near unity, then detachment will occur with the actual (detached) exit velocity (specific impulse) maintained near the predictions of ideal flow. But further examination of this process leads us to a view which is not so sanguine.

To show why there is still cause for concern, note that, from (I.23) and (I.19), the magnetic-drag-force density is precisely equal in magnitude to the applied-force density, for times larger than the time for the transient phase. That is

$$ J_y B_x = \frac{F_z}{\Delta_z} = \left(\rho \frac{V_\parallel^2}{R_c} \right)_{exit} \tag{I.28} $$

This is an axial drag force density (force per unit volume) exerted on the plasma by the magnetic fields (and ultimately transferred to the magnetic field coils on the vehicle). To get the total drag force, we must multiply the expression in (I.28) by a volume associated with the exit region of the nozzle.* This volume has to be on the order of $(A_e R_c)$, where A_e is the area of the nozzle exit and R_c is a representative radius of curvature of a diverging magnetic field line. We conclude from Eq. (I.28) that the total resistive drag force is given, therefore, to order of magnitude, by

$$ (\vec{J} \times \vec{B})_z (A_e R_c) \sim (\rho V_\parallel^2)_{exit} A_e = (\rho V_\parallel A)_{exit} V_{\parallel(exit)} = \dot{M} V_{\parallel(exit)} \tag{I.29} $$

Thus, although we have made no attempt to ascertain the exact numerical factors here, the above calculation indicates that the resistive drag force will be roughly the same as the ideally-calculated thrust, in our iterative model.

This qualitative argument suggests that, within the axisymmetric flow model, resistive detachment of plasma does not really solve the detachment problem, because the intended thrust will be substantially cancelled by the resistive drag on the plasma by the nozzle magnetic fields—no matter what value is achieved by the magnetic Reynolds number (within the validity of the model). This qualitative argument needs to be checked quantitatively by use of a 2-D resistive MHD simulation.

Three possibilities for really solving the detachment problem are as follows.

i) Resistive Raleigh-Taylor Instability. Non-symmetric plasma motions induced by centrifugal forces (similar to the physics discussed above) might lead to more effective

---

* Throughout the "exit volume," there will be a distribution of magnitudes and directions of these forces, which will usually have both axial and radial components. But, point by point, the axial component of the applied-force density will be balanced by the axial component of the magnetic-force density.

detachment of plasma in the form of flute instabilities. 3-D resistive MHD simulations could address this process. A similar process at the nozzle entrance is considered in section d (convective transport) below.

ii) <u>Recombination.</u> At the low exit temperatures, recombination of electrons and ions could occur to the extent that the plasma would revert to neutral gas and be uncoupled from the magnetic fields. However, this process might well be jeopardized by the precipitous drop in plasma density on the downstream side of the throat. Quantitative calculations that address this possibility are indicated. A resistive 2-D MHD simulation with capabilities to model ionization and recombination (analogous to reactive fluid simulations) would be required.

iii) <u>Utilization of Sharp-Boundary Profiles.</u> If the nozzle input condition could be arranged so as to have a core of field-free plasma, transversely contained in pressure balance by an external layer of magnetic flux, then, to the extent that this condition can be maintained downstream, the necessity for solving the detachment problem becomes obviated. Instead of a field-free core plasma, one can also consider here a core plasmoid containing closed magnetic field lines, separated from the open-line magnetic guide field by a magnetic separatrix. An example of such is the Field Reversed Configuration for which axial translation has already been demonstrated.[6]
The condition required for maintaining a semblance of the sharp boundary profile downstream can be obtained from the observation that the initially separated plasma and magnetic guide field will inter-mix by resistive diffusion. Because this is a diffusive process (with $\beta \lesssim 1$ in the interface region), the diffusive mixing depth, Δ_η, can be estimated from the expression

$$\Delta_\eta = \sqrt{D_\eta t_z} \qquad (I.30)$$

where the axial transit time, $t_z \approx \ell_z/v_i$, is the time during which the core plasma is in resistive contact with the magnetic guide field at the nominally sharp boundary of separation.

The boundary will remain "sharp" provided $\frac{\Delta_\eta}{a_p} \ll 1$, where a_p is a typical radius of the plasma near the throat of the nozzle. Using Eq. (I.30) to examine this ratio of lengths, we find

$$\frac{\Delta_\eta}{a_p} = \sqrt{\frac{D_\eta}{a_p v_i} \frac{\ell_z}{a_p}} = \sqrt{\frac{A}{R_\eta}}. \qquad (I.31)$$

Thus in order for the sharp boundary configuration to be maintained during the time for an element of plasma to flow through the nozzle, it is necessary that the magnetic Reynolds number be large compared with the aspect ratio of the nozzle.

All of the plasma that becomes lost in the resistive mixing layer, Δ_η, will be subject to resistive drag at the nozzle exit, as discussed earlier, and will thereby detract from the ideal thrust within the model of axisymmetric flow. The risk of using this sharp boundary approach to solve the detachment problem is that the plasma then becomes vulnerable to Rayleigh-Taylor instabilities in the nozzle entrance region. See section d: "Convective Transport," below.

CASE II. THE AZIMUTHAL MAGNETIC NOZZLE $[\vec{B} = (0, B_\theta, 0)]$

For convenience, we repeat Eq. (I.2) in the form

$$n(V_{\perp r} - V_{Br}) = -\frac{1}{2} D_\eta \frac{n}{(B^2/8\pi)} \left(\rho \vec{V} \cdot \nabla V_r + \frac{\partial P}{\partial r} \right) + \frac{J_r}{e} - \frac{c}{eB} \frac{\partial P_e}{\partial z} \qquad (I.32)$$

where $D_\eta = \frac{c^2}{4\pi} \eta$ is the resistive diffusivity, $\vec{V}_B$ is the guiding center drift velocity, $\vec{V}_B = c\vec{E} \times \vec{B}/B^2$, and we are using cgs units. We shall explore the consequences of Eq. (I.32) for a coaxial configuration of length ℓ_z, radius r, and coaxial width Δ, with $\Delta \ll r$.

Now the magnetic field lines, $\vec{B} = B_\theta \hat{\theta}$, are quickly moving downstream, so that V_{Br} on the *lhs* of (I.32) is not a dominant drift of the field lines.*In fact, V_{Br} must vanish at the highly conducting inner and outer electrodes, because $E_z = 0$ at those electrode surfaces. Consequently, the *lhs* of (I.32) represents radial mass transport across a magnetic field which itself has no significant radial motion of field lines, especially at the electrode surfaces.

Now let us consider the driving terms for this radial mass transport in the azimuthal magnetic nozzle. Assuming that the ion beta value is of order unity (see Appendix D), and knowing that the axial flow is both transonic and trans-Alfvénic (see Appendix B), it can be demonstrated that the radial inertial portions of the D_η term are small compared to the radial pressure gradient portion, in the ratios $(r_{ci}/\ell_z)^2$ and $A^{-1}(r_{ci}/\ell_z)$, where $A = \frac{\ell_z}{\Delta}$ is the aspect ratio of the nozzle, with Δ being the radial space between the inner and outer electrodes. Thus, the ion gyro-radius is being assumed small compared to the axial scale length of the nozzle, an easily satisfied condition.

Thus, when the D_η term is the dominant term in Ohm's law, Eq. (I.32), the importance of radial mass transport depends upon the radial pressure gradient and can be examined just as for Case I. The result is that the characteristic time for radial loss of plasma particles, in the terms of the axial transit time, can be written as

$$\frac{t_{part}}{t_z} = \frac{1}{3} \frac{R_\eta}{\beta A} \qquad (I.33)$$

where R_η is the magnetic Reynolds number defined as

$$R_\eta = \frac{\Delta V_z}{D_\eta}, \qquad (I.34)$$

with the axial flow velocity V_z on the order of c_s or C_A. (As in Case I, this result [Eq. (I.33)] was obtained assuming uniform and equal species temperatures, and a parabolic

* That is, the input power (in MKS units now), W, corresponds to the Poynting vector $\mu_0^{-1} E_r B_\theta$ times the area $2\pi r \Delta$. This is equivalent to an axial flux of magnetic energy, $2(\frac{B_\theta^2}{2\mu_0} V_{Bz}) 2\pi r \Delta$, with half expended in filling the tube with magnetic energy and half doing work pushing the conducting plasma on ahead with velocity $V_{Bz} = E_r/B_\theta$. The velocity V_{Br} does not enter this picture, at least not in zero order.

density profile that vanishes at the inner and outer electrodes.) This result, Eq. (I.33), is practically the same as for the meridional configuration. Thus, when the resistive term dominates Ohm's law, radial mass transport can be reduced to a small effect by working at high magnetic Reynolds numbers, $R_\eta \gg A$.

However, the resistive term does not necessarily have to dominate Ohm's law in the azimuthal magnetic nozzle. It can be demonstrated that the ratio of the J_r term (the Hall term) to the D_η term in (I.32) has the following dependences,

$$\frac{(J_r/e)}{D_\eta \beta (\partial n/\partial r)} \sim A^{-1}\beta^{-1}\frac{\omega_{ce}}{\nu_{ei}}, \qquad (I.35)$$

where ω_{ce} is the electron gyro-frequency in the B_θ magnetic field, and ν_{ei} is the electron momentum-transfer collision frequency due to Coulomb collisions with the ions. Also, $A = \ell_z/\Delta$ is the aspect ratio of the nozzle, and β is the total plasma beta value due to the sum of the electron and ion pressures. From the result (I.35), we conclude that when the electrons are strongly magnetized, $\omega_{ce} \gg \nu_{ei}$, the Hall term can play a much more important role than resistive diffusion as regards radial mass transport.

We also note that the last term, the $(\partial P_e/\partial z)$ term, is of order β_e times the Hall term, where β_e is $(8\pi n T_e/B^2)$. From Appendices D and E, we can infer that $\beta_e \lesssim \beta_i \approx 1$.

In the Table I.8, we present values of the electron (ion) magnetization parameter assuming that $T_e = T_i$, and $\beta = 1$. Thus, for given n and T, Table I.1 provides a corresponding value of magnetic field. For ν_{ei} we use[2] $\nu_{ei} = ne^2/m_e\sigma$, with $\sigma \approx 10^{13}T_{eV}^{3/2}(s^{-1})$ for $\ell n \Lambda \approx 10$. This value is somewhat more accurate than the earlier expression derived in (I.A) and is sufficient for present purposes. For ω_{ce} we use $m_e \approx 1 \times 10^{-27}$ gm, $e \approx 4.8 \times 10^{-10}$ esu, $\omega_{ce} = eB/m_ec = 1.6 \times 10^7$ $B_{Gauss} = 1.6 \times 10^{11}B_{Tesla}$. Note that (ω_{ce}/ν_{ei}) scales as $T^2/n^{1/2}$ for fixed beta. (In both ν_{ei} and ω_{ce}, we took $m_e \approx 1 \times 10^{-27}$ gm.)

From Table I.8 and Eq. (I.35), we see that in the 1 eV range of temperatures, the electrons are essentially unmagnetized, so that resistive diffusion determines radial mass transport. However, at higher temperatures, the reverse is generally true. For example, in the 10 eV range, the electrons will be strongly magnetized for a large range of number densities. (Appendix E shows that for ions in the range of 10 eV energies, the electrons can be heated up to this temperature by equipartition.) We shall now examine the character of radial mass transport in the azimuthal magnetic nozzle when the parameters are such that the electrons are strongly magnetized.

We begin by assuming that the electrons are low-beta in order to get a simple picture. (Remarks addressing the $\beta_e \sim 1$ case will follow.) Then, the transport of plasma particles proves to be completely different for electrons and ions. Electrons are simply stuck to the axially-drifting B_θ field lines and convected downstream. On the other hand, in this reduced model, the radial ion transport is determined from Eq. (I.32) in the following form for strongly magnetized, low-beta electrons.

$$n(V_{ir} - V_{Br}) = \frac{J_r}{e}. \qquad (I.36)$$

Here, V_{ir} is the radial component of the fluid velocity of the plasma, which is practically the radial fluid velocity of the ions. Thus, the physics embodied in Eq. (I.36) is that

31

TABLE I.8 Values of $\frac{\omega_{ce}}{\nu_{ei}}$ $\left(\frac{\omega_{ci}}{\nu_{ii}}\right)$ for $T_e = T_i$ and $\beta = 1$ (hydrogen ions)

	$T[eV] =$ 1	10	100
$n\ (cm^{-3}) =\ 10^{13}$	1.97 (.065)	197 (6.50)	19,700 (650)
10^{14}	0.623 (.0206)	62.3 (2.06)	6,230 (206)
10^{15}	0.197 (.0065)	19.7 (.650)	1,970 (65.0)
10^{16}	0.062 (.0021)	6.23 (.206)	623 (20.6)
10^{17}		1.97 (.065)	197 (6.50)
10^{18}		0.623 (.0206)	62.3 (2.06)
10^{19}		0.197 (.0065)	19.7 (0.650)

* *Slight inaccuracies in this table result from our use of an approximate evaluation of ν_{ei}. However, ν_{ei} itself is only accurate, in principle, to order $(\ell n\Lambda)^{-1}$.*

the ions must carry all of the radial current across the magnetic field because the low-beta magnetized electrons are unable to do so. (This statement applies only to an axisymmetric idealized model of the discharge wherein localized arcs or spokes are not the principle mechanisms for determining current paths.)

The radial distance traversed by the ions in carrying the radial current is $V_r t_z$ where t_z is the axial transit time. Thus, if $V_r t_z$ is small compared with Δ, then radial mass transport will be a small effect in this case of strongly magnetized electrons. Setting $V_{\perp r} = J_r/ne$, using Ampere's law to express J_r in terms of B_θ, and using ℓ_z/C_A for t_z, we find that

$$\frac{V_r t_z}{\Delta} \approx \frac{c}{\omega_{pi}\Delta} \approx \frac{r_{ci}}{\Delta} \qquad (I.37)$$

for ion beta values near unity (Appendix D). (Here, ω_{pi} is the ion plasma frequency.)

Thus, the condition that radial mass transport should be a small effect, within the axisymmetric model of the coaxial azimuthal nozzle, reduces to the requirement that

$$\frac{r_{ci}}{\Delta} \ll 1, \qquad (I.38)$$

in the case of strongly magnetized, low-beta electrons. The ion gyro-radius should be small compared with the transverse dimensions of the plasma.

Now, if one returns to Eq. (I.32) allowing for finite β_e electrons, still strongly magnetized, one has

$$n(V_{\perp r} - V_{Br}) = \frac{J_r}{e} - \frac{c}{eB}\frac{\partial P_e}{\partial z}. \tag{I.39}$$

The meaning of the electron pressure term is that the axial non-uniformity of electron pressure causes a lack of cancellation of neighboring gyro-orbits (evident from the form $\frac{cT}{eB}\frac{\partial n}{\partial z}$) leading to a radial diamagnetic fluid velocity of the electrons. Including this term only changes the estimate of radial mass transport by a factor of order $|1 \pm \beta_e|$ depending on the direction of J_r. Hence, the requirement (I.38) is still the fundamental restriction for radial mass transport to be a small effect in azimuthal magnetic nozzles in which the electrons are strongly magnetized.

b. Heat Transport.

The preceeding account of radial mass transport from resistive diffusion exemplifies certain general features of diffusive transport. Given a transport process for a quantity Q (e.g. for Q representing mass, momentum, or thermal energy) having diffusivity D, one can find a representative time scale for loss of Q from the core plasma to the lateral wall of the nozzle as $t_D \sim a^2/D$, where "a" is a characteristic radial dimension of the nozzle. If the condition $t_D \gg t_z$ is satisfied, where $t_z = \ell_z/V_z$ signifies the axial transit time of an element of plasma moving with velocity V_z through a nozzle of length ℓ_z, then fractionally large transport losses of Q will not have had time to occur. This desired condition can be expressed as

$$\frac{t_z}{t_D} = \frac{A}{R_D} \ll 1 \tag{I.40}$$

where $A = \ell_z/a$ is the aspect ratio of the nozzle and $R_D = V_z a/D$ is the Reynolds number for the given transport process. Thus, the Reynolds number for heat transport should be much larger than the aspect ratio of the nozzle in order that radial heat loss should constitute a minor effect.

Although an element of plasma may lose only a small fraction of its initial thermal energy during axial transit, due to fulfillment of condition (I.40), the actual heat loading of the lateral walls may be considerable, depending upon the plasma parameters and nozzle dimensions. *Whether such heat loading is tolerable in particular cases must be assessed by engineers on the basis of the duration and number of burns required by a particular mission. This assessment must be self-consistent, since the duration and number of burns will also depend on the plasma parameters.*

In this report, fractional energy losses and concomitant heat loads on the walls will be estimated as consequences of choices of the plasma parameters, but no formal value judgements of the wall loads will be rendered here. A convenient framework for making such estimates can be developed as follows.

CASE I. MERIDIONAL MAGNETIC NOZZLE

Consider the ratio of the total lateral heat loss rate, $H_\perp$, to the total axial kinetic power flow through the throat of the nozzle, P_0. (From Appendix A, we note here that $P_0 \approx \frac{1}{4}P$ where P is the kinetic power flowing out of the nozzle exit.) We have

$$\frac{H_\perp}{P_0} = 2A\frac{D|\partial T/\partial r|_0}{\frac{1}{2}m_i V_0^3} \tag{I.41}$$

33

where D is the thermal diffusivity ($D = \kappa/n$, where κ is the thermal conductivity), $A = \ell_z/a$ is the aspect ratio of the nozzle, and V_0 is the flow speed through the throat of the nozzle. The particular expression for D will depend upon the parameters of the plasma, for example, upon the degree of magnetization of the electrons; and it will depend upon the behavior of the profiles of density and temperature near the walls. Here, we shall just work with a "representative" value of D. Note that, from Appendix A, in the throat region of the nozzle,

$$C_{s0}^2 = V_0^2 = \gamma \frac{T_e + T_i}{m_i} \approx 3 \frac{T}{m_i} \qquad (I.42)$$

for $T_e = T_i$ and $\gamma = \frac{5}{3}$.

Now, taking a parabolic temperature profile as the generic example of a general diffuse profile, one has

$$T = T_{(0)}(1 - r^2/a^2),$$

where $T_{(0)}$ is the value of T on the centerline. Then, applying Eq. (I.42) on the centerline, the square of the velocity of fluid through the throat is $V_0^2 = \frac{3T_{(0)}}{m_i}$, and one can then compute the ratio of lateral heat transport per particle to axial kinetic power per particle. The result is

$$\frac{D|\partial T/\partial r|_a}{\frac{1}{2}m_i V_0^3} = \frac{4}{3}\frac{D}{a}\frac{1}{V_0} = \frac{4}{3}\frac{1}{R_D} \qquad (I.43)$$

wherein the Reynolds number for this transport process in the throat region has been introduced in an obvious manner.

Using (I.43) in (I.41), we have

$$\frac{H_\perp}{P_0} = \frac{8}{3}\frac{A}{R_D}. \qquad (I.44)$$

This expression for the fractional loss of power due to radial heat transport is in qualitative agreement with the estimate of the time ratio (t_z/t_D) used to derive the desired condition (I.40).

In terms of the final kinetic power at the nozzle exit, P, Eq. (I.44) can be written as

$$H_\perp = \frac{2}{3}\frac{A}{R_D}P. \qquad (I.44a)$$

Thus, the fractional loss of heat relative to the exit thrust power is essentially (A/R_D).

To estimate the heat load on the lateral wall, we use Eq. (I.43) in the form

$$\kappa\left|\frac{\partial T}{\partial r}\right|_a = \frac{4}{3}\frac{1}{R_D}\frac{1}{2}m_i n_0 V_0^3 = \frac{4}{3}\frac{1}{R_D}\frac{M V_0^2}{2A_0} \quad \text{or}$$

$$\kappa\left|\frac{\partial T}{\partial r}\right|_a = \frac{4}{3}\frac{1}{R_D}\frac{P_0}{A_0} = \frac{1}{3}\frac{1}{R_D}\frac{P}{A_0} \qquad (I.45)$$

where n_0 is the number density of ions in the throat region of the nozzle, and where A_0 is the area of the nozzle throat.

Here, we recall that values of $\frac{P}{A_0}[\frac{MW}{m^2}]$ may be obtained from Table I.1, Note b, for many cases of $\beta = 1$ plasmas. Hence, an estimate of the heat load on the lateral wall in $[\frac{MW}{m^2}]$ can be obtained simply by estimating the relevant Reynolds number and dividing it into the exit thrust power density (defined in terms of the area of the throat). The Reynolds number is obtained by choosing a transport model, plasma parameters, and nozzle dimensions. We shall now carry out such a procedure. Although it is not necessary to use the Reynolds Number approach to calculate the lateral heat fluxes, this approach provides a convenient and natural way to connect these heat fluxes with the corresponding thrust power densities.

Classical plasma transport presents a lower bound for transport losses from plasmas. From Braginskii[2], there are two types of contributions to the electron heat flux when $\omega_{ce} \gg \nu_{ei}$,

$$\vec{q}_u^e = 0.71 n T_e \vec{u}_\parallel + \frac{3}{2}\frac{T_e}{(\omega_{ce}/\nu_{ec})}n(\hat{b}\times\vec{u}) \qquad ((I.46-a)$$

$$\vec{q}_T^e = -\kappa_\parallel^e \nabla_\parallel T_e - \kappa_\perp^e \nabla_\perp T_e - \frac{5}{2}\frac{cT_e}{eB}n(\hat{b}\times\nabla T_e) \qquad (I.46-b)$$

(where $\vec{u} \equiv \frac{1}{ne}\vec{J}$ with $\vec{J}$ being the current density); and there is a contribution from the ions when $\omega_{ci} \gg \nu_{ii}$,

$$\vec{q}^i = -\kappa_\parallel^i \nabla_\parallel T_i - \kappa_\perp^i \nabla_\perp T_i + \frac{5}{2}\frac{cT_i}{eB}n(\hat{b}\times\nabla T_i) \qquad (I.46-c)$$

where $\hat{b} \equiv \vec{B}/B$ and $\parallel$ and $\perp$ respectively refer to directions along and transverse to the local magnetic field $\vec{B}$. (Here we use cgs units.)

In these equations, to sufficient accuracy,

$$\kappa_\parallel^e \approx \frac{3}{2}n\frac{v_e^2}{\nu_{ei}} \qquad (I.47-a)$$

$$\kappa_\perp^e \approx \frac{5}{2}n\frac{v_e^2}{\nu_{ei}}\left(\frac{\nu_{ei}}{\omega_{ce}}\right)^2, \qquad (I.47-b)$$

and

$$\kappa_\parallel^i \approx 2n\frac{v_i^2}{\nu_{ii}} \qquad (I.47-c)$$

$$\kappa_\perp^i \approx n\frac{v_i^2}{\nu_{ii}}\left(\frac{\nu_{ii}}{\omega_{ci}}\right)^2 \qquad (I.47-d)$$

where $v_{e,i}^2 \equiv 2T_{e,i}/m_{e,i}$. In evaluating these quantities, we shall use[2] $\nu_{ei} = \frac{ne^2}{m_e\sigma}$, with $m_e = 0.9 \times 10^{-27}$ gm and $\sigma = 0.9 \times 10^{13}$ $T_{eV}^{3/2}$, for $\ell n \Lambda \approx 10$. We also note[2] that

$$\nu_{ii} = \nu_{ei}\left(\frac{T_e}{T_i}\right)^{3/2}\left(\frac{m_e}{2m_i}\right)^{1/2}.$$

In Eqs. (I.46), the $u_\parallel = J_\parallel / ne$ term vanishes for both configurations under consideration. Moreover, the $\hat{b} \times \nabla T$ terms can never contribute to "radial" cooling of plasma.[2] (In the meridional magnetic field case, this is so because ∇T has no azimuthal component. In the azimuthal magnetic field case, this is so because the coaxial metal electrode surfaces cannot support a substantial longitudinal temperature gradient.) Finally, it is important to remember that when either electrons or ions become un-magnetized ($\omega_{ce} \ll \nu_{ei}$ or $\omega_{ci} \ll \nu_{ii}$), thermal conduction in the unmagnetized species is isotropic and is determined by the Coulomb-collision mean free path, so that the expression for the heat flux $\vec{q}$ reduces to just the $\kappa_\parallel$ term for the unmagnetized species.

Therefore several cases of thermal transport must be distinguished depending upon the degrees of magnetization of electrons and ions (see Table I.8). When the electrons are un-magnetized, radial thermal conduction is determined only by the $\kappa_\parallel^e$ term, and the ions are unimportant.*

When the electrons are magnetized, electron radial thermal conduction results from the $\hat{b} \times \vec{u}$ term and the $\kappa_\perp^e$ term. It can be shown that the former is of order $(\frac{3}{5} \frac{1}{\beta_e})$ times the latter. Hence, the former ($\hat{b} \times \vec{u}$) contribution dominates electron thermal conduction when the electron beta is very small against unity. Moreover, when the ions are magnetized, ion radial thermal conduction is due just to the $\kappa_\perp^i$ term. Since the $\kappa_\perp^e$ term is of order $(m_e/m_i)^{1/2} \kappa_\perp^i$, we see that electron radial thermal conduction is generally small against the $\kappa_\perp^i$ contribution from the ions. (The exception is when $\beta_e \lesssim (m_e/m_i)^{1/2} \sim 2\%$, in which case the $\hat{b} \times \vec{u}$ thermo-magnetic term from the electrons is competitive with the $\kappa_\perp^i$ term from the ions. We shall ignore this possibility in the scoping study, but it should be monitored in a more detailed transport study.)

Finally, it is possible for some parameter ranges that the electrons are magnetized ($\omega_{ce} \gg \nu_{ei}$) but the ions are un-magnetized ($\omega_{ci} \ll \nu_{ii}$). In this case, the radial thermal conduction is dominated by $\kappa_\parallel^i$.

In general, we shall apply the magnetization parameters in Table I.8 to calculate the heat diffusion Reynolds number for the different regions mentioned above. In so doing, a characteristic radial distance "a" for the nozzle dimension must be assumed. We shall set $a = 100$ cm. It is a trivial matter to try any other value of "a", since R_D scales directly with "a". In this connection, we also note that for well-confined plasmas supported in pressure-balance by an external magnetic field, with a boundary-layer thickness Δ_r, as opposed to general diffuse profiles, the lateral transport fluxes will be larger, and the effective Reynolds numbers will be smaller, in the ratio (Δ_r/a). For R_D, we shall use

$$R_D = \frac{v_i a}{D} \tag{I.48}$$

where v_i is the ion thermal velocity (which is sufficiently close to C_s, the flow velocity in the throat). We note that with $m_e = 0.9 \times 10^{-27}$ gm and $m_i = 1840\, m_e$, the thermal velocities are given by $v_i(\frac{cm}{s}) \approx 1.4 \times 10^6\, T_{eV}^{1/2}$ and $v_e(\frac{cm}{s}) \approx 6.0 \times 10^7\, T_{(eV)}^{1/2}$.

---

* The exact transport coefficients depend in detail on the degrees of magnetization (ω_{ce}/ν_{ei}) and (ω_{ci}/ν_{ii}), and are very complicated.[2] In this scoping study, we ignore these details, but they must be calculated in any thorough transport study of any specified design.

For unmagnetized electrons, we have the dominant radial thermal diffusivity,

$$D = D_{\parallel}^e = \frac{3}{2}\frac{v_e^2}{\nu_{ei}} \approx 19 \times 10^{19}\frac{T_{(eV)}^{5/2}}{n(cm^{-3})}\left[\frac{cm^2}{s}\right]. \qquad (I.49-a)$$

For magnetized electrons but un-magnetized ions, and with $T_e = T_i$ assumed, we have

$$D = D_{\parallel}^i = D_{\parallel}^e\left(\frac{T_i}{T_e}\right)^{5/2}\sqrt{\frac{2m_e}{m_i}} = 0.03 \times D_{\parallel}^e. \qquad (I.49-b)$$

(Temperature ratios are important here, and (T_i/T_e) should be taken into account in a more detailed transport study.)

When both species are magnetized, we take

$$D = D_{\perp}^i = \frac{1}{2}\left(\frac{\nu_{ii}}{\omega_{ci}}\right)^2 D_{\parallel}^i \qquad (I.49-c)$$

and use Table I.8 to obtain the ion magnetization parameter.

To show how this works, we construct the table of radial thermal diffusivities here, Table I.9, for a $\beta = 1$ hydrogen plasma, showing the dominant thermal diffusivity for each set of parameters. Noting that there is also a thermal flux associated with radial mass transport, with an effective diffusivity $\frac{3}{2}D_\eta$ when $T_e = T_i = T$ and $\frac{1}{n}\frac{\partial n}{\partial r} \approx \frac{1}{T}\frac{\partial T}{\partial r}$, we also show $\frac{3}{2}D_\eta$ parenthetically when it exceeds the thermal diffusivity, D_{therm}.

In Table I.10, the Reynolds numbers corresponding to the thermal diffusivities in Table I.9 are displayed, for the radial length scale $a = 100$ cm. The fact that these Reynolds numbers are much larger than unity means that the heat transport losses are negligible in comparison with the thrust power; see Eq. (I.44-a). But note that the Reynolds numbers associated with $\frac{3}{2}D_\eta$ are much smaller in several cases, indicating that the thermal flux associated with mass transport can be important for $\beta = 1$ plasmas under some conditions.

In Table I.11, we shall apply Eq. (I.45). The thrust power density is taken from Table I.1 (footnote b), and the result is divided by three times the Reynolds number (using $a = 10^2$ cm) in order to obtain an estimate of the lateral heat flux according to the classical plasma transport model. The thermal flux associated with radial mass transport is shown parenthetically when it is larger than the heat flux from thermal conduction.

We see that, in most cases, the heat flux due to classical heat transport is less than $1(MW/m^2)$, and in only two cases does the heat flux exceed $100(MW/m^2)$. However, we note that the thermal flux due to radial mass transport is substantially larger in several cases, producing two additional cases in excess of 100 MW/m^2.

CASE II. AZIMUTHAL MAGNETIC NOZZLE

The parameter survey for this second configuration is not carried out here, but it must lead to results that are qualitatively like those of Case I for thermal conduction. The reason is that, according to Appendix D, the ion beta is of order unity, and concomitantly the flow through the nozzle will be both trans-Alfvénic and transonic. These were the fundamental assumptions that led to the results of Case I. Of course, the Reynolds number in Case II

TABLE I.9 Radial Thermal Diffusivities $\left(\frac{cm^2}{s}\right)$
from classical transport theory, D_{therm},
for a "beta $= 1$" hydrogen plasma with $T_e = T_i$.
Parenthetically is shown $\frac{3}{2}D_\eta$ when it exceeds D_{therm}.
[See Note (a).] $\ell n \Lambda = 10$ is assumed.

$T[eV] =$		1	10	100
$n[cm^{-3}] =$	10^{13}	$D^i_\parallel = 5.7 \times 10^5$ (1.2×10^7)	$D^i_\perp = 2.1 \times 10^6$	
	10^{14}	$D^e_\parallel = 1.9 \times 10^6$ (1.2×10^7)	$D^i_\perp = 2.1 \times 10^6$	
	10^{15}	$D^e_\parallel = 1.9 \times 10^5$ (1.2×10^7)	$D^i_\parallel = 1.8 \times 10^6$	$D^i_\perp = 6.7 \times 10^4$
	10^{16}	$D^e_\parallel = 1.9 \times 10^4$ (1.2×10^7)	$D^i_\parallel = 1.8 \times 10^5$ (3.8×10^5)	$D^i_\perp = 6.7 \times 10^4$
	10^{17}		$D^i_\parallel = 1.8 \times 10^4$ (3.8×10^5)	$D^i_\perp = 6.7 \times 10^4$
	10^{18}		$D^e_\parallel = 6.0 \times 10^4$ (3.8×10^5)	$D^i_\perp = 6.7 \times 10^4$
	10^{19}		$D^e_\parallel = 6.0 \times 10^3$ (3.8×10^5)	$D^i_\parallel = 5.7 \times 10^4$

Note:

a) The ratio of the thermal flux associated with mass transport to the heat flux from thermal conduction, for $\beta = 1$, $T_e = T_i = T$, is $(\frac{3}{2}D_\eta)/D_{therm}$, times $(\frac{T}{n})(\frac{\partial n}{\partial r} / \frac{\partial T}{\partial r})$.

b) The blank spaces lie outside of the fluid-plasma model, either because $\ell n \Lambda$ is too small (at low temperatures) or because the mean free path is too large (at high temperatures).

must be defined in terms of the coaxial spacing between the inner and outer electrodes, Δ. To the extent that Δ is closer to 10 cm than 10^2 cm, the Reynolds numbers will be smaller and the wall heat fluxes will be larger by a factor of ten.

TABLE I.10. Reynolds Numbers for the Thermal Diffusivities in Table I.9. (Here, $v_i(\frac{cm}{s}) = 1.4 \times 10^6\ T^{1/2}_{(eV)}$ and $a = 100\ cm$) (See Note.)

	$T[eV] =$	1	10	100
$n[cm^{-3}] =$	10^{13}	245 (11.6)	211	
	10^{14}	73.7 (11.6)	211	
	10^{15}	737 (11.6)	246	20,900
	10^{16}	7,370 (11.6)	2,460 (1,160)	20,900
	10^{17}		24,600 (1,160)	20,900
	10^{18}		7,380 (1,160)	20,900
	10^{19}		73,800 (1,160)	24,560

Note: Reynolds Numbers due to the thermal flux associated with radial mass transport are shown parenthetically when they are smaller than the Reynolds Numbers for the thermal diffusivities in Table I.9.

A qualitative difference with Case I as regards thermal conduction would arise in the event that $D^i_\perp$ is the dominant diffusivity when $\beta_e \sim 1$, but is no longer the dominant diffusivity when $\beta_e \lesssim \sqrt{m_e/m_i}$. Such situations could arise in energetic operation of coaxial plasma guns ($\sim 100\ eV$ ion energies) wherein the electrons do not have sufficient time to heat up to near the ion temperature (see Appendix E). This situation should be monitored in a more detailed transport study of the azimuthal magnetic nozzles. Finally, it is important to note that the thermal flux associated with radial mass transport should be considered in azimuthal magnetic nozzles. This will be quite different than in the meridional magnetic nozzle when the electrons are magnetized, as discussed in an earlier section on mass transport.

TABLE I.11. Estimates of Lateral Classical Heat Flux
and Thermal Flux due to Radial Mass Transport
in (MW/m^2), from a $\beta = 1$ Hydrogen Plasma for a
Nozzle with throat radius $a = 10^2$ cm.
(See Note.)

$T[eV]$	1	10	100
$n[cm^{-3}] = 10^{13}$	$2.5 \times 10^{-4}(\frac{MW}{m^2})$ (5.3×10^{-3})	9.2×10^{-3}	x
10^{14}	8.4×10^{-3} (5.3×10^{-2})	9.2×10^{-2}	x
10^{15}	8.4×10^{-3} (5.3×10^{-1})	7.9×10^{-1}	2.9×10^{-1}
10^{16}	8.4×10^{-3} (5.3)	7.9×10^{-1} (1.7)	2.9
10^{17}	x	7.9×10^{-1} (17)	29
10^{18}	x	26 (165)	290
10^{19}	x	26 (1650)	2500

Note: The thermal flux associated with radial mass transport is shown parenthetically when it exceeds the radial heat flux due to classical thermal conduction.

        c. Bohm Transport. When the electrons are magnetized ($\omega_{ce} > \nu_{ei}$), an additional channel for cross-field transport is provided by electrostatic turbulence. First discussed by David Bohm[7a] who proposed a diffusivity $D_{Bohm} = \frac{1}{16}\frac{cT}{eB}$, many subsequent attempts were made to explain the origin of such a diffusivity. Braginskii[2] (in his Chap. 3) provides a qualitative explanation with a dynamical basis, and finds $D_{Bohm} \sim \frac{cT}{eB}$. A more systematic and detailed explanation of Bohm diffusion has been set forth in the book by Ichimaru[7b]. He finds that when the electrons are magnetized, low frequency electrostatic turbulence across the magnetic field produces a diffusivity given by

(for strong electrostatic turbulence),

$$D_{Bohm} \approx \frac{1}{32\pi} \frac{c(T_e T_i)^{1/2}}{eB} \left(1 + \frac{T_i}{T_e}\right)^{3/2} \ell n \frac{m_i}{m_e}. \qquad (I.50)$$

The expression is valid when a certain parameter, α^*, is much larger than unity. The α^* parameter is given by

$$\alpha^* = \left(1 + \frac{T_e}{T_i}\right) \frac{\omega_{pe}^2}{\omega_{ce}^2}, \qquad (I.51)$$

where T_e and T_i are respectively the electron and ion temperatures, and ω_{pe} and ω_{ce} are respectively the electron plasma and cyclotron frequencies, $\omega_{pe} = (4\pi n e^2/m_e)^{1/2}$ and $\omega_{ce} = eB/m_e c$, in cgs units. If we assume that $T_e = T_i$, the condition $\alpha^* \gg 1$ cm be reduced to

$$v_i \ll c\sqrt{\frac{m_e}{2m_i}} \sqrt{\beta} \qquad (I.52)$$

where v_i is the ion thermal velocity, $\beta = 16\pi n T/B^2$ is the plasma's total beta, and c is the speed of light. For hydrogen plasma, this can be written as

$$T_{(eV)} \ll 10^5 \beta \ . \qquad (I.52 - a)$$

This condition will easily be satisfied for the cases under consideration in this report $(\beta \sim 1)$.

For hydrogen plasma, with $T_e = T_i$, the Bohm diffusivity in Eq. (I.50) becomes

$$D_{Bohm} \approx 0.2 \frac{cT}{eB} \qquad (I.53)$$

The Bohm diffusivity is tabulated for $\beta = 1$ hydrogen plasma with $T_e = T_i$ in Table I.12. It can be written in practical terms as

$$D_{Bohm} \left(\frac{cm^2}{s}\right) \approx 2 \times 10^3 \frac{T_{(eV)}}{B_{(Tesla)}}.$$

The magnetic field values utilized here for $\beta = 1$ plasmas are given in Table I.1.

The Bohm diffusivity has a meaning for both thermal and particle cross-field diffusivity. (Although the electrons are the formal participants in this process, the ions must leave the plasma at the same rate, to maintain overall charge neutrality.) We recall that the particle diffusivity due to classical Coulomb collisions was given by

$$D_{part} = \frac{1}{2}\beta D_\eta \qquad (I.54 - a)$$

where

$$D_\eta = \frac{c^2}{4\pi}\eta = \frac{c^2}{4\pi}\frac{4\pi\nu_{ei}}{\omega_{pe}^2} = \frac{c^2}{\omega_{pe}^2}\nu_{ei} = \frac{r_{ce}^2\nu_{ei}}{\beta_e}, \qquad (I.54 - b)$$

41

TABLE I.12. Values of Bohm Diffusivity ($\frac{cm^2}{s}$) for $\beta = 1$
Hydrogen Plasma (when electrons are magnetized, $\omega_{ce} \geq \nu_{ei}$)

	$T[eV]$	1	10	100
$n[cm^{-3}] =$	10^{13}	$7.0 \times 10^5 (\frac{cm^2}{s})$	2.2×10^6	x
	10^{14}		7.0×10^5	x
	10^{15}		2.2×10^5	7.0×10^5 * $[2.2MW/m^2]$
	10^{16}		7.0×10^4	2.2×10^5 * $[6.9 \ MW/m^2]$
	10^{17}	x	2.2×10^4	7.0×10^4
	10^{18}	x		2.2×10^4
	10^{19}	x		7.0×10^3

Note— Only the 100 eV cases marked (*) are significantly larger than the classical thermal diffusivities tabulated in Table I.9., by a factor of 10 for $n = 10^{15} \ cm^{-3}$, and a factor of 3 for $n = 10^{16} \ cm^{-3}$. The corresponding Bohm heat fluxes are listed parenthetically [ ] for conditions corresponding to Table (I.11).

with $\beta_e = 8\pi n T_e / B^2$, r_{ce} being the electron gyro-radius, $r_{ce} = v_e / \omega_{ce}$, and ν_{ei} is the classical Coulomb collision frequency of electrons with ions. Hence the classical cross-field particle diffusivity is

$$D_{part} = \frac{1}{2} \frac{\beta}{\beta_e} r_{ce}^2 \nu_{ei} = r_{ce}^2 \nu_{ei}, \qquad (I.54 - c)$$

for $T_e = T_i$. Let us compare this to the Bohm diffusivity interpreted in the context of particle diffusivity. From Eq. (I.53), we have

$$D_{Bohm} = 0.2 \frac{cT}{eB} = 0.1 \frac{v_e^2}{\omega_{ce}} = 0.1 r_{ce}^2 \omega_{ce}$$

The ratio of the latter to the former is

$$\frac{D_{Bohm}}{D_{part}} = 0.1 \frac{\omega_{ce}}{\nu_{ei}} \qquad (I.55)$$

which is 0.1 times the electron magnetization parameter. Hence, when the electron magnetization exceeds 10, one expects the electrostatic turbulent particle diffusion to exceed the classical value, associated with cross-field mass transport.

From the standpoint of cross-field particle transport, and neglecting profile effects, the magnetic Reynolds numbers given in Table I.6 will be therefore degraded roughly by the inverse of the factor $\frac{1}{20}(\frac{\omega_{ce}}{\nu_{ei}})$ when this factor is large compared to unity. (Note that the values of the magnetization parameters in Table I.8 are only approximate.) (Here, we have used $\beta = 1, T_e = T_i$, so $\beta_e = \frac{1}{2}$.) We present this information on the Bohm Reynolds number in the following table, based upon Table I.12. For this tabulation, we take $a = 10^2$ cm for the radius, and $v_i(\frac{cm}{s}) = 1.4 \times 10^6 \, T_{(eV)}^{1/2}$ for the ion thermal velocity as representative of the flow velocity through the nozzle.

To summarize the results of this section on Bohm transport, we see from Table I.12 that Bohm thermal diffusion only rarely competes with classical heat diffusion in the parameter ranges considered. Moreover, we observe from Table I.13 that the Reynolds number associated with Bohm diffusion is sufficiently large in all cases that fractional heat and mass losses from the plasma during flow through the nozzle are quite small. Note, however, that the lateral thermal flux associated with Bohm mass transport is comparable to the classical heat flux (where applicable) and greatly exceeds classical in two cases at 100 eV. (Compare Table I.13 with Table I.11.) We conclude that Bohm diffusion is generally unimportant in the parameter range considered here. However, it is important to qualify this conclusion with the reminder that the scale length for diffuse profile gradients was taken to be the nozzle radius (at the throat). For sharper gradients the effect of Bohm diffusion can be significantly larger as discussed in the following section under convective transport [(ii): The Kelvin-Helmholtz instability].

d. Convective Transport.

We have already discussed a form of axisymmetric convective thermal loss under Sec. (b), heat transport. There, classical resistive diffusion produced a radial macroscopic fluid velocity that convected thermal energy outwards. In this section, we go on to consider other heat loss processes that may be induced by non-axisymmetric fluid motions triggered by macroscopic instabilities. The most dangerous MHD-type (i.e. macroscopic) instabilities in a plasma are those that least bend the magnetic field lines, or that don't bend them at all. This is because energy is required to bend the magnetic field lines, and so such plasma motions tend to be stable. A well known example of a stable perturbation associated with field-line bending is the torsional Alfvén wave. An example orthogonal to the Alfvén wave is the flute perturbation. Flute-type perturbations are plasma motions that move the field lines perpendicular to themselves without bending them, or bending them the least amount possible. Magnetic configurations without magnetic shear are particularly susceptible to flute perturbations because then large volumes of magnetic flux can be coherently moved practically without bending. Neither the meridional nor the azimuthal magnetic nozzle possesses any magnetic shear, in the "pure" versions of these configurations.

These unstable flute perturbations prove to be driven jointly by adverse pressure gradients and "bad" field line curvature (e.g. hot plasma surrounded in equilibrium by field lines that are convex outwards). Known as "interchange instabilities," their behavior can be shown to very similar (almost identical) to instabilities of the Rayleigh-Taylor type. This analogy can be inferred from the equations set forth in Freidberg's discussion of

43

TABLE I.13. Values of Reynolds Number and Convective Thermal Flux

TABLE I.13. Values of Reynolds Number and Convective Thermal Flux
$(\ldots)$, in MW/m^2 for Transport due to
Bohm Diffusion in $\beta = 1$ Hydrogen Plasma
Assuming $T_e = T_i$ ($R_{Bohm} = \frac{a v_i}{D_{Bohm}}$ for $a = 10^2$ cm)

$T[eV]$		1	10	100
$n[cm^{-3}] =$	10^{13}	200	200 $(0.021 MW/m^2)$	x
	10^{14}		632 (0.067)	x
	10^{15}		2,000 (0.21)	2,000 (6.7)[a]
	10^{16}		6,320	6,320 (21)[a]
	10^{17}	x	20,000	20,000 (67)
	10^{18}	x		63,200 (210)
	10^{19}	x		200,000 (670)

Only cases where the electrons are magnetized ($\omega_{ce} > \nu_{ei}$) are meaningful for R_{Bohm}. For fixed beta, we note the scaling. $R_{Bohm} \sim \frac{n^{1/3}}{\beta^{1/3}}$, so that R_{Bohm} is independent of temperature and weakly dependent on plasma density in the above tabulation. The convective thermal flux is listed parenthetically (assuming a diffuse profile $n = n_0(1 - r^2/a^2)$) only for cases where $\omega_{ce}/\nu_{ei} \geq 10$ (see Table I.9). The expression tabulated is $9.6 \times 10^{-23} \times n(cm^{-3}) T_{(eV)} D_{Bohm}(\frac{cm^2}{s})[\frac{MW}{m^2}]$.

[a] Greatly exceeds classical thermal flux.

ideal MHD instabilities as based upon the principle of virtual work (the δW approach).[80] For this reason, such modes are often called "g-modes," in connection with gravitational instabilities.

In the azimuthal magnetic nozzle, another class of flute-type perturbations may also arise, driven by the free energy in a sheared axial flow field (consonant with a "no-slip" boundary condition on the lateral walls). [These are in addition to the Rayleigh-Taylor-

type flute modes that can be unstable (depending on the radial pressure profile) due to the bad magnetic curvature of B_θ at the outer coaxial electrode.] Such perturbations are closely related to the Kelvin-Helmholtz instability and to the shedding of vortices by airfoils.

Finally, we shall mention that Kelvin-Helmholtz type instabilities of flute parity can be induced by plasma-sheath effects, even in the absence of an externally-driven plasma flow field. Thus, these instabilities may even be relevant to the meridional magnetic nozzle although it has no zero-order flow in the azimuthal direction.

Both Rayleigh-Taylor and Kelvin-Helmholtz types of flute perturbations merit consideration here, because they both can lead to the formation of macroscopic eddies that convect plasma across the magnetic field.

In the absence of a definitive and generally accepted practical model of the turbulent MHD boundary layer for highly-conducting ($R_\eta \gtrsim 1$) high-beta ($\beta \sim 1$) plasmas, we shall consider here what can be said about the influence of the above instabilities on convective cross-field transport. (However, Demetriades has constructed a well-considered approach to the turbulent MHD boundary layer problem for low-beta plasmas having R_η small.[8-b])

In this connection, we observe that in a magnetized plasma having small ion gyro-radius, and with beta not large compared to unity, the presence of the magnetic field may be expected to lend some degree of rigidity to the plasma, so that the character of turbulence and convective transport in such a plasma may well be rather different from the turbulence and associated transport in a neutral gas.

i.) Instabilities of the Rayleigh-Taylor Type. The meridional magnetic nozzle must contain a transition section between the reservoir and the nozzle throat where the magnetic field lines and the streamlines are narrowing down, so that these lines appear convex to the outside. A core of hot plasma would tend to be unstable in this region of "bad curvature." Further downstream, in the throat section of the nozzle, the lines appear concave to the outside, appearing as a region of "good curvature" to the core of hot plasma. (For example, see Fig. 30.) Because the potential energy driving the instability, δW, consists of an integral over the entire plasma volume,[8a] the stability properties of the plasma on a given flux tube will depend upon the integrated curvature effect (good and bad) all along the field lines in that flux tube, as well as depending upon the radial pressure gradients in that flux tube. A similar problem has recently been formulated (but not solved) for the case of a plasma flowing along field lines in a tokamak,[8-c] for which the flowing plasma also samples alternating regions of good and bad curvature (on the inner and outer regions of the torus respectively).

In the present instance, we shall make a simple "worst-case" estimate of the possible effect of the flute mode instability in the transition region in order to indicate the importance of a more detailed and systematic examination of this effect. We emphasize that an instability of this kind in the transition region could have a destructive effect on the entire plasma reservoir if care is not exercised. (For example, it is well known that theta-pinches, neutrally stable along their length because of zero curvature, can be thrown sideways to the wall because of instabilities associated with the bad curvature of magnetic mirrors applied at the ends of the pinch.) We also note that sufficiently short wavelengths of the Rayleigh-Taylor instability can be partially stabilized by the presence of fluid viscosity. This effect will be treated in the summary section in Chap. V.

To proceed, we consider a simple model of an incompressible fluid, unstably stratified under gravity. (The effects of compressibility will be discussed shortly.) From Ref. (8-a), one can infer that the effective gravitational force is a centrifugal force induced by thermal motion along $\vec{B}$, which is given to order of magnitude by

$$g \approx v_i^2/R_c \qquad (I.56)$$

where v_i is the ion thermal velocity and R_c is the radius of curvature of a field line in the bad curvature region.[*] In the presence of subsonic parallel flow, $V_\parallel \lesssim v_i$, this expression will be modified by a term $V_\parallel^2/R_c$, but the order of magnitude and the scaling still will be correctly given by (I.56).

Furthermore, for flute modes (wherein the wave-vector lies across the shearless magnetic field), it is easy to show that the magnetic field effectively drops out of the dynamics.

Now, Chandrasekhar[8-d] has presented the solution for the Rayleigh-Taylor instability in a diffusely stratified medium (originally worked out by Lord Rayleigh). The growth rate, Γ, is found to be given approximately by

$$\Gamma \approx \sqrt{gQ} \qquad (I.57)$$

where Q^{-1} is the scale length of the unstably stratified medium. It is noteworthy in the exact formula that as wavelengths increasingly smaller than Q^{-1} are considered, the growth rate is <u>not</u> enhanced, but remains essentially as given by Eq. (I.57). Therefore, this configuration provides an answer that, in some sense, completes the result for the sharp boundary model of a heavy fluid superposed on a lighter fluid, for which the instability growth rate increases without limit for increasingly smaller wavelengths.

Let us now compare the growth time, of this instability to the transit time, $t_{B.C.}$, for an element of plasma to flow through the section of bad curvature. In so doing, we shall set

$$Q^{-1} = \Delta_r, \qquad (I.58)$$

where Δ_r is the representative radial scale length of the unstably stratified plasma profile in the bad curvature transition section. Let the axial length of the bad curvature section be $\ell_{B.C.}$, then

$$t_{B.C.} \approx \ell_{B.C.}/V_\parallel \qquad (I.59)$$

Then, the number of growth times available for this type of instability is given by (from Eq's. I.56–I.59)

$$\Gamma t_{B.C.} \approx \frac{v_i}{V_\parallel}\sqrt{\frac{\ell_{B.C.}}{R_c}}\sqrt{\frac{\ell_{B.C.}}{\Delta_r}} = \frac{v_i}{V_\parallel}\frac{\ell_{B.C.}}{R_c}\sqrt{\frac{R_c}{\Delta_r}} \qquad (I.60)$$

For flow that is approaching the transonic condition, $V_\parallel \lesssim v_i$, and with $\ell_{B.C.} \approx R_c$, and with a sufficiently diffuse profile so that $\Delta_r \lesssim R_c$, one would expect only a few

---

[*] From the general expression for the square of the complex eigenfrequency, $\omega^2 = \delta W/K$, where δW and K are the potential and kinetic energies associated with pressure driven modes, with uniform and equal temperatures one obtains $\omega^2 \approx -\left(\frac{2T}{m_i R_c}\right)\left|\frac{\nabla n}{n}\right|$, to order of magnitude.

Rayleigh-Taylor growth times to be available during transit through the bad curvature section. Moreover, since flute modes (and the closely related ballooning modes) of this gravitational type extend nonlocally along field lines, the destabilizing tendencies may be mitigated by the effects of good curvature sampled by the modes in the nozzle throat. This qualitative preliminary estimate of a benign result needs to be supplemented by detailed quantitative studies of the MHD stability properties of the plasma in the entrance region of the nozzle. (For example, we note that the speed-up of $V_\parallel$ towards v_i initially occurs in conjunction with a decrease in R_c, so that Eq. (I.60) contains counteracting factors that require sorting out by detailed computations in order to obtain the net result.)

However, for ideally well-confined plasmas, one could be dealing with a sharp-boundary profile in which a core plasma is supported in transverse pressure balance by an external magnetic field, so that $\Delta_r \ll R_c$. According to Eq. (I.60), this pure form of the magnetic nozzle concept may then be subject to a large number of instability growth times during plasma transit of the bad curvature section. Thus, it is relevant to consider the sharp boundary version of this instability. (But note that the Rayleigh-Taylor instability does not require a free boundary, but can also occur in a stratified profile contained within fixed boundaries.)

To this purpose, we consider a uniform, motionless, field-free, highly conducting plasma half-space in the region $x < 0$ with a sharp free boundary at the plane $x = 0$. To the right in the half-space $x > 0$, there is a uniform, shearless magnetic field B_z in the $\hat{z}$ direction. We study the most dangerous Rayleigh-Taylor instabilities (thus with wave vectors in the y-direction) induced by an equivalent gravitational field $g\hat{x}$ applied in the x-direction. We limit the analysis to incompressible motions (with compressibility effects discussed thereafter),

$$\nabla \cdot \delta\vec{V} = 0 \tag{I.61}$$

so that, within the plasma, the linearized mass continuity equation

$$-i\omega\delta\rho + \rho_0 \nabla \cdot \delta\vec{V} = 0 \tag{I.62}$$

implies no density perturbations,

$$\delta\rho = 0. \tag{I.63}$$

(Here, any quantity Q has been split into zero order and fluctuating parts, $Q = Q_0(x) + \delta Q$, with $\delta Q = q(x)\, exp\,[i(ky - \omega t)]$.) The linearized momentum equation reads, for $x < 0$,

$$-i\omega\rho_0\delta\vec{V} + \nabla\delta P = \hat{x}g\delta\rho = 0 \tag{I.64}$$

(where $\hat{x}$ is the unit vector in the x-direction), from which, with incompressibility,

$$\nabla^2\delta P = 0. \tag{I.65}$$

The solution of (I.65) that vanishes in the plasma as $x \to -\infty$ is

$$\delta P = \delta P_0 e^{kx} e^{i(ky - \omega t)}. \tag{I.66}$$

The total fluid pressure perturbation at the displaced boundary $x = \xi_x$, is then

$$(\delta P)_{tot.} = \delta P + \vec{\xi} \cdot \nabla P_0 = \delta P + \xi_x \rho_0 g, \tag{I.67}$$

47

where ξ_x is the normal displacement of the boundary and we have used the equilibrium pressure-balance condition in the gravitational field, $\nabla P_0 = \rho_0 g \hat{x}$.

To the right of $x = 0$, there is a uniform vacuum magnetic field B_{z0} in the equilibrium state; and the perturbation magnetic field satisfies $\nabla \cdot \delta \vec{B} = 0$ and $\nabla \times \delta \vec{B} = 0$. Hence there is a fluctuating magnetic scalar potential, $\delta \phi$, with

$$\delta \vec{B} = \nabla \delta \phi \qquad (I.68)$$

and with

$$\nabla^2 \delta \phi = 0. \qquad (I.69)$$

The solution of (I.69) having the form $f(x) e^{iky}$ is

$$\delta \phi = \delta \phi_0 e^{-kx} e^{i(ky - \omega t)}. \qquad (I.70)$$

Here, we have chosen the solution that vanishes at $x \to +\infty$. It is obvious from the form of (I.70) that

$$\delta B_z \equiv 0, \qquad (I.71)$$

so that the fluctuating magnetic pressure $(\vec{B}_0 \cdot \delta \vec{B})$ vanishes in the right half-space, $x > 0$. Therefore, by continuity of pressure, the pressure perturbation at $x = \xi_x$ given by Eq. (I.67) also must vanish.

$$\delta P = -\xi_x \rho_0 g \qquad (I.72)$$

Here, δP is to be evaluated at $x = 0$ to first order accuracy. Now, δP can be related to δV_x through Eq. (I.64),

$$\delta P = i \frac{\omega}{k} \rho_0 \delta V_x, \qquad (I.73)$$

and $\delta V_x(x = 0)$ is related to the boundary displacement ξ_x by

$$\delta V_x = -i\omega \xi_x. \qquad (I.74)$$

The use of (I.73) and (I.74) in (I.72) immediately produces the Rayleigh-Taylor dispersion relation,

$$\omega^2 = -gk, \qquad (I.75)$$

corresponding to the growth rate ($\omega = i\Gamma$),

$$\Gamma = \sqrt{gk}. \qquad (I.75 - a)$$

From what has been said earlier, we know that the growth rate does not increase without limit as k increases, but is maximized for

$$k \sim \Delta_r^{-1} \qquad (I.76)$$

where Δ_r is the width of the "sharp" boundary.

48

Taking $g \approx v_i^2/R_c$, and $k \approx \Delta_r^{-1}$, the above growth rate Eq. (I.75-a), can be estimated as

$$\Gamma \approx \frac{v_i}{R_c}\sqrt{\frac{R_c}{\Delta_r}} \qquad (I.77)$$

Thus, since $\Delta_r \ll R_c$, the instability growth time, Γ^{-1}, will be much shorter than the thermal transit time through the bad-curvature region, in the case of a "sharp" boundary profile. (For $t_{B.C.} = \ell_{B.C.}/V_\parallel$, we find $\Gamma t_{B.C.}$ from Eq. (1.77) agrees exactly with Eq. (1.60).)

The above problem can also be worked including the effect of compressibility, and solved exactly. It is thus found that the effect of compressibility is stabilizing, but only for modes with wave vectors small enough that

$$g \approx ks^2,$$

where s is the compressional communication speed across the magnetic field. (Hence, $s \sim v_i$ (ion thermal velocity) or C_A (Alfvén speed) for $\beta \approx 1$.) Taking $g \approx v_i^2/R_c$ and $s \approx v_i$, one finds compressibility is important for global modes such that $1 \approx kR_c$. For larger wavenumbers, $k \gg R_c^{-1}$, the incompressible model should remain valid.

The presence of such growing g-modes in the meridional magnetic nozzle opens a channel for quasi-linear radial fluxes of particles and heat due to "crinkling" of the originally axisymmetric plasma boundary, i.e. a form of "convective transport." Unlike turbulent transport in ordinary fluids, the convective transport in this case is due to the coherent activity of individual modes.

For example, the convective radial mass flux can be estimated as $\langle \delta\rho\delta V \rangle$, where the brackets signify an average over the azimuthal (y) direction. Here, we shall use a "mixing length" Ansatz. Since $\delta\rho = 0$ behind the "sharp" boundary in the core plasma, its value within the boundary layer itself (i.e. $\delta\rho$ at a fixed position, induced by a moving non-uniform profile) must be given by $\delta\rho \sim -\xi_x(d\rho_0/dx)$ where $(d\rho_0/dx)$ is the density gradient within the boundary layer. Also, within the boundary layer (assumed to move rigidly) we have $\delta V_r = -i\omega\xi_x$. Since this is a purely growing mode with $\omega = i\Gamma$, the quasilinear mass flux becomes

$$\langle \delta\rho\delta V \rangle = -\langle \xi_x^2 \rangle \Gamma(d\rho_0/dx). \qquad (I.78)$$

Using the mixing length estimate for the nonlinear saturation limit, $\xi_x \sim \Delta_r$, with $|d\rho_0/dx| \sim \rho_0/\Delta_r$, and using (1.77) for the growth rate, we find

$$\langle \delta\rho\delta V \rangle \sim (\rho_0 v_i)\sqrt{\frac{\Delta_r}{R_c}}. \qquad (I.79)$$

Also, Eq. (I.78), with $\xi_x \sim \Delta_r$ and Γ given by (1.77), is equivalent to a diffusive flux,

$$\langle \delta n\delta V \rangle = -D_{RT}dn_0/dx \qquad (I.80)$$

where the Rayleigh-Taylor-induced particle diffusivity is given by

$$D_{RT} = \left(\frac{\Delta_r}{R_c}\right)^{3/2}(R_c v_i) \qquad (I.81)$$

Thus, looking at the plasma from an axisymmetric point of view, there is an apparent radial mass flux in the bad curvature region, due to the development of short wave length g-mode instabilities, on the order of the ion thermal flux times a small number depending upon the thickness of the "sharp" boundary. Of course, Eq. (I.79) is valid only as long as $\Delta_r \ll R_c$.

The fraction of mass "lost" to the outside in this manner this manner, beyond the desired axisymmetric sharp boundary, during plasma transit through the bad curvature region may be estimated as follows. The rate of loss multiplied by the transit time (t_{BC}) gives the amount lost (per unit length), which is then compared with the amount present (per unit length).

$$f_{mass\ loss} \sim \frac{(\langle \delta\rho\delta V \rangle 2\pi r_{B.C.})t_{BC}}{\rho\pi r_{B.C.}^2} \sim 2 \left(\frac{v_i}{V_\parallel} \right) \left(\frac{\ell_{B.C.}}{r_{B.C.}} \right) \sqrt{\frac{\Delta_r}{R_c}} \qquad (I.82)$$

in which we have made use of Eq. (I.79). Here, $r_{B.C.}$ is the representative ordinary radius measured from the axis of symmetry at the section of bad curvature. Since (Δ_r/R_c) only enters by the one-half power, the original boundary of separation of plasma and field must be very thin indeed in order that the mass-loss fraction be small, since the remaining factors are of order unity. Thus, the loss of integrity of the desired sharp boundary in the form of crinkling, and the associated mass and heat transport (heat transport is discussed below) out of the core plasma, present serious issues deserving detailed computational study focused upon the entrance region of the nozzle.

In a similar manner, one can estimate an equivalent nonlinear heat flux due to these instabilities, in addition to the effective convection of heat associated with the nonlinear mass flux,

$$T_0\langle \delta n \delta V \rangle \equiv \frac{T_0}{m_i} \langle \delta\rho\delta V \rangle.$$

The heat flux itself is given by

$$n_0\langle \delta V \delta T \rangle = n_0\langle (-i\omega\xi_x) \left(-\xi_x \frac{dT_0}{dx} \right) \rangle = -n_0\Gamma\langle \xi_x^2 \rangle \frac{dT_0}{dx} \qquad (I.83)$$

where dT_0/dx is the zero-order temperature gradient in the boundary layer separating the plasma from the magnetic field. Comparing to Eq. (I.78), we see that the effective thermal diffusivity is identical to the effective mass diffusivity. Similarly, the fraction of heat lost by the effective thermal conduction mechanism in Eq. (I.83) proves to be the same as the mass-loss fraction of Eq. (I.82), to within a numerical factor.

Use of the expression for Γ in Eq. (I.83), with $k \sim \Delta_r^{-1}$, $\xi_x \sim \Delta_r$ and $|dT_0/dx| \sim T_0/\Delta_r$, yields a quasilinear radial heat flux (whether due to convection or conduction) on the order of

$$q_{RT} \sim (nTv_i) \left(\frac{\Delta_r}{R_c} \right)^{1/2} = 2 \times 10^{-15} \left(\frac{\Delta_r}{R_c} \right)^{1/2} n(cm^{-3})T_{(eV)}^{3/2} \left[\frac{MW}{m^3} \right] \qquad (I.83-a)$$

Thus, for $n = \frac{1}{2} \times 10^{15}\ cm^{-3}$ and $T = 1\ eV$, we have

$$q_{RT} \sim \left(\frac{\Delta_r}{R_c} \right)^{1/2} \left[\frac{MW}{m^3} \right], \qquad \text{and for} \qquad T = 100\ eV, \qquad q_{RT} \sim \left(\frac{\Delta_r}{R_c} \right)^{1/2} 10^3 \left[\frac{MW}{m^3} \right].$$

Thus, the higher temperature (and density) cases can produce very high heat loads, correspondingly larger than in these examples to the extent that $n(cm^{-3})/(1/2 \times 10^{15})$ is larger than unity. In any case, Eq. (1.83-a) can provide an estimate of such quasilinear heat fluxes. These estimates are not very sensitive to the sharpness of the plasma edge.

In summary, the meridional nozzle entrance region presents magnetic field lines of bad curvature to the plasma, which may then become susceptible to instabilities of the Rayleigh-Taylor type. These instabilities have rapid growth rates in sharp-boundary plasmas, with attendant serious consequences for heat and mass transport losses according to the simple quasi-linear estimates given above. In order to study these effects properly, 3D MHD simulations are required and are recommended. Note also that fluid viscosity can provide a stabilizing influence on the growth rates, as discussed in Chap. V. Finally, we also note that the azimuthal magnetic nozzle has bad magnetic curvature at the outer electrode, so that Rayleigh-Taylor type instabilities may occur there too. In this connection, it is worth noting that special diffuse pressure profiles in Z-Pinch geometry can be stable to these instabilities due to the effects of compressibility.[8a]

ii) Instabilities of the Kelvin-Helmholtz Type.

As in the preceeding section on the effects of the Rayleigh-Taylor instability, we address our remarks here primarily to the radial transport issues in the meridional magnetic nozzle. A recent pair of journal articles[8-e] has made the important point that the electrostatic sheath generated by a plasma, nominally at rest, in contact with a (floating-potential) wall in the presence of a shearless magnetic field parallel to the wall induces a Kelvin-Helmholtz instability just from the action of the sheared $\vec{E}_s \times \vec{B}$ drift velocity. Here, $\vec{E}_s$ refers to the radial space-charge field of the plasma sheath. This instability and its subsequent turbulence occur spontaneously, in the absence of an externally driven flow field. The ultimate source of free energy for this instability comes from the joint action of ionization and heating in the bulk plasma, which serves to charge up the wall leading to radial electric fields that produce the sheared $\vec{E} \times \vec{B}$ drift velocity. Thus, this situation is relevant to instabilities in the meridional magnetic nozzle (except for the limitations mentioned below) with wave-vectors in the azimuthal direction, consonant with the absence of externally driven azimuthal velocity in the pure form of this nozzle configuration.

Moreover, Theilhalber and Birdsall[8-e] found quasi-linear modeling to be inapplicable for the description of instability saturation and turbulence (in contrast to our discussion of the Rayleigh-Taylor instability in the preceeding section), because of the shedding of small-scale vortices away from the plasma sheath region. Instead, they found the boundary layer always to be in an unstable condition and always to be radiating small vortices away (as well as to retain large vortices which coalesced). The balance between the action of the instability and the shedding of the smaller vortices allowed the plasma sheath to maintain itself in a "turbulent steady state."

Here, we shall present a brief account of the Kelvin-Helmholtz simulations of Theilhaber and Birdsall and their implications for "anomalous" transport losses in the meridional magnetic nozzle. We remark that these instabilities and their consequent turbulent fluctuations are dangerous in the same way that the Rayleigh-Taylor fluctuations are dangerous; that is, *both types of fluctuations are able to take place without bending the magnetic field lines.*

Theilhaber and Birdsall have carried out and analyzed the results of 2D particle simulations in slab geometry. The simulations were electrostatic, the magnetic field was

uniform and shearless, with no curvature, particle electrons and ions were introduced in bulk and their orbits were exactly followed as influenced by the macroscopic electric fields until the particles reached the wall, at which they were absorbed. An explicit algorithm was used to advance the particle orbits on the electron gyro time scale. The dynamical processes studied were of the flute type; that is, there was no variation of any quantity in the direction along the magnetic field. Because of the limitations of the computer, only a few runs were performed, and some of the dimensionless parameters were unrealistic. For example, the electron plasma-frequency to the electron gyro-frequency was taken as $\omega_{pe}/\omega_{ce} = 0.182$. In reality the latter quantity should be much larger than unity since $\omega_{pe}/\omega_{ce} = (\beta_e^{1/2})(c/v_e)$, where $\beta_e = 8\pi n T_e/B^2$, c is the speed of light, and v_e is the electron thermal velocity. Thus, even at temperatures as high as 100 eV, the electron beta would have to be less than 10^{-4} in order for ω_{pe}/ω_{ce} to be less than unity. Nevertheless, this state-of-the-art simulation produced new and important physics results relevant to the behavior of bounded magneto-plasmas.

The linear instability of the self-consistent sheath can be understood from the observations from the simulations that the sheath thickness is about three ion-gyro-radii ($\Delta_s \sim 3r_{ci}$) and the sheath potential drop is about twice the ion temperature ($\phi_s \sim 2T_i/e$). Thus, the space charge electric field in the radial direction is $E_x \approx \phi_s/\Delta_s \approx (\frac{1}{3}v_i)(\frac{1}{c}B)$ where, $v_i = (2T_i/m_i)^{1/2}$ is the ion thermal velocity. (Ref. 8-e uses $v_i = (T_i/m_i)^{1/2}$.) Thus, the guiding center drift velocity is $V_0 = cE_x/B \approx \frac{1}{3}v_i$. The instability growth rate Γ must be proportional to (V_0/Δ_s), as these quantities are the only characteristic zero order quantities with the correct dimensional combination for the slow time scale, fluid-type growth rate. A numerical solution of the linearized equations yields

$$\Gamma \approx 0.04\omega_{ci} \approx 0.4V_0/\Delta_s, \qquad (I.84)$$

where ω_{ci} is the ion gyro-frequency. This maximum growth rate occurs at a flute-mode wavelength k_y^{-1} (in the y or θ direction) on the order of $k_y r_{ci} \approx 0.4$.

We now inquire whether such an instability can grow appreciably during plasma transit of the meridional magnetic nozzle. Taking the transit time t_z as $t_z \sim \ell_z/v_i$ where ℓ_z is the length of the nozzle and v_i is the ion thermal velocity, the number of growth times can be expressed as

$$\Gamma t_z = 0.04\frac{a}{r_{ci}}A \qquad (I.85)$$

where "a" is a characteristic radius of the nozzle and $A = \ell_z/a$ is the nozzle aspect ratio. Here, we have made use of Eq. (I.84) for Γ.

We see from Table I.5 that, for $\beta = 1$ hydrogen plasmas, the ion gyro-radius r_{ci} can be on the order of 1 cm for densities in the range of $10^{13} - 10^{15}$ cm^{-3}, and r_{ci} is even smaller at higher densities. Thus, for transverse dimensions on the order of $10 - 10^2$ cm and nozzle aspect ratios of 10, we find that the number of growth times can range from 4 to 40, or even larger at higher densities. Thus, the Kelvin-Helmholtz instability should be expected to be present, in the azimuthal direction in the meridional magnetic nozzle.

According to Ref. (8-e), the nonlinear turbulent state of this instability indeed contributed to cross-field transport of plasma, but *not directly by means of the coherent vortex structures*. The actual transport mechanism was found to be due to the concomitant existence of incoherent turbulence at short length scales, where it manifested itself as

Bohm transport. The Bohm transport allowed electrons to migrate from the interior to the outside of the large coherent vortex structures, and thence to the wall. Without the Bohm transport, the electrons would have remained trapped in the vortices. Measurements from the simulations gave the result (in cgs units),

$$D'_{Bohm} \approx 0.04 c T_i / e B. \qquad (I.86)$$

This Bohm diffusivity, D'_{Bohm}, is about one order of magnitude smaller than that given earlier in Eq. (I.53). However, it acts over a much sharper gradient, only a few r_{ci} wide. This leads to a radial cross-field mass transport of order

$$(nV)_x = D'_{Bohm} \frac{\partial n}{\partial x} \approx \frac{1}{25} \frac{c T_i}{e B} \frac{n}{3 r_{ci}} \approx \frac{1}{150} n v_i \qquad (I.87)$$

where $v_i = (2 T_i / m_i)^{1/2}$. Thus radial mass transport through the plasma sheath is some small fraction of the ion thermal flux.

The fraction of mass lost during axial transit at velocity $V_\parallel \sim v_i$ through the nozzle in this manner is clearly given by

$$f_{mass\ loss} \sim \frac{1}{150} \frac{n v_i 2 \pi a}{n \pi a^2} \frac{\ell_z}{v_i} = \frac{1}{75} A \qquad (I.88)$$

where $A = \ell_z / a$ is the aspect ratio of the nozzle. Clearly, for $A \lesssim 10$, the fraction of mass (and heat) lost in this manner should be negligible.

The actual transverse heat flux due to this kind of Bohm diffusion, q'_{Bohm}, is (using $\frac{1}{150} n T v_i$),

$$q'_{Bohm} \sim \frac{1}{150} \times 2 \times 10^{-15} n (cm^{-3}) T_{(eV)}^{3/2} \left[\frac{MW}{m^2} \right]. \qquad (I.89)$$

For $n = \frac{1}{2} \times 10^{15}\ cm^{-3}$ and $T = 1\ eV$, we have $q'_{Bohm} \sim \frac{1}{150} [\frac{MW}{m^2}]$, but for $T = 100\ eV$ we have $q'_{Bohm} \sim \frac{1}{150} \times 1000 [\frac{MW}{m^2}] \sim 6 [\frac{MW}{m^2}]$. Thus, these kinds of heat fluxes do not seem very serious due to the small numerical factor in front, except at much higher densities, $n(cm^{-3})/(1/2 \times 10^{15}) > 10^2$.

We conclude this sub-section on the Kelvin-Helmholtz instability with the remark that, although we have considered here only the meridional magnetic nozzle, the azimuthal magnetic nozzle also will be subject to such an instability and also in a manner that does not bend the field lines. To address this issue, the simulations of Ref. (8-e) then would have to be extended to include an externally driven plasma flow field, and removal of the "floating potential" assumption on the walls, since the walls are electrodes connected to an external driving circuit.

iii) Summary and Comments on Convective Transport. It was pointed out that the entrance region of the meridional magnetic nozzle has bad magnetic curvature and is therefore susceptible to flute instabilities of the Rayleigh-Taylor type, thus leading to stationary deformations in the azimuthal direction. For general diffuse profiles, it was estimated that probably only a few instability growth times would be available during transit of the entrance region, so that diffuse profile configurations

would probably be immune to the consequences of Rayleigh-Taylor instabilities. However, sharply defined plasma profiles with a free boundary would be vulnerable to the rapid growth of short wavelength instabilities with wavelengths on the order of the boundary layer thickness. Even pressure-gradient boundary layers that extend right up to the wall without a free surface are vulnerable to this instability when $\frac{\partial \rho}{\partial r} < 0$. The linear growth rate of such instabilities was estimated by Eq. (I.77), the quasilinear mass flux by Eq. (I.79), the fractional mass loss by (I.82), and the quasilinear heat flux by Eq. (I.83), and Eq. (I.83-a). These equations can be used in conjunction with Table I.1 to provide estimates of these losses and heat loading of the walls in association with conjectured examples of thrust pressure and thrust power, provided that one has an estimate of the boundary layer thickness. For the latter, one might consider the effect of classical resistive diffusion as expressed by Eq. (I.31), adapted to the region of bad curvature of aspect ratio $A_{B.C.}$. Then, the factor $\sqrt{\Delta_r/R_c}$ in the above equations becomes

$$\sqrt{\frac{\Delta_r}{r_{B.C.}}}\sqrt{\frac{r_{B.C.}}{R_c}} = \left(\frac{A_{B.C.}}{R_\eta}\right)^{1/4}\sqrt{\frac{r_{B.C.}}{R_c}},$$

where $r_{B.C.}$ is the ordinary nozzle radius in the region of bad curvature, and R_η is the magnetic Reynolds number in that region.

The determination of the boundary layer thickness by classical resistive diffusion assumes that the ion gyro-radius r_{ci} is much smaller than any characteristic length in the fluid model. However, in Table I.5, we see that many ($\beta = 1$) examples ($n \sim 10^{13} - 10^{15}$ cm^{-3}) have r_{ci} on the order of 1 cm which is not all that small. For situations in which r_{ci} exceeds the classical resistive layer thickness, i.e., when

$$\frac{r_{ci}}{r_{B.C.}} > \sqrt{\frac{A_{B.C.}}{R_\eta}},$$

then one should use r_{ci} as the thickness of the boundary layer if the ions are magnetized. For instance, from Table I.6, we see that for $T = 100$ eV, one can have $R_\eta > 10^5$, and from Table I.5 we see that $r_{ci} \sim 0.5$ cm for $n \sim 10^{15}$ cm^{-3}. Moreover, Table I.8 shows that the ions are magnetized for these parameters. Thus $\sqrt{\Delta_r/R_c} = \sqrt{r_{ci}/R_c}$. For $r_{ci} \sim 1$ cm and $R_c \sim 10^2$ cm, Eq. (I.77) becomes

$$\Gamma^{-1} \approx \frac{R_c}{v_i} \times 0.1$$

allowing on the order of ten Rayleigh-Taylor growth times in the entrance region. Eq. (I.82) for $V_\parallel \lesssim v_i$ and $\ell_{B.C.} \sim r_{B.C.}$ yields

$$f_{mass\ loss} \sim a\ few\ times\ 0.1.$$

The heat flux to the wall provided by Eq. (I.83-a) becomes

$$q_{RT} \sim 2 \times 10^{-16} n(cm^{-3}) T_{(eV)}^{3/2} \left[\frac{MW}{m^2}\right].$$

(I.89). The fractional mass loss appears to be negligible, and the heat loading of the lateral wall appears to be moderate except at high densities ($\gtrsim 10^{17}\ cm^{-3}$) and simultaneously high temperatures ($\sim 100\ eV$). The heat flux equation can be used in conjunction with Table I.1 to provide estimates of the wall loading in association with conjectured examples of thrust pressure and thrust pow. Caution is advised in the use of these results because they were obtained in simulations with unrealistic parameters. For example, Ichimaru[7a] assumed that $\alpha^* \gg 1$, equivalent to $\omega_{pe}^2/\omega_{ce}^2 \gg 1$ where $\omega_{pe} = (4\pi ne^2/m_e)^{1/2}$ is the electron plasma frequency; whereas the simulations in Ref. (8-e) used $\omega_{pe}^2/\omega_{ce}^2 \ll 1$. This discrepancy may account for the much smaller Bohm transport obtained by Ref. (8-e) in comparison with the theory of Ichimaru. It is an open question whether these results of Ref. (8-e) will remain valid in more realistic simulations or over a more extended range of parameters. In a simulation for which $\omega_{pe}^2 > \omega_{ce}^2$, it is conceivable that the Bohm diffusivity would agree with Ichimaru.

Finally, we remark that the azimuthal magnetic nozzle may well be vulnerable to both Rayleigh-Taylor and Kelvin-Helmholtz instabilities, as modified by the presence of externally driven axial flow, and electrodes not at a floating potential but connected to an external circuit. Such instabilities would consist of axisymmetric deformations in the axial direction, drifting axially. Their initiation and nonlinear behavior can be examined with time-dependent (i.e. initial value) 2-D MHD or particle simulations. The latter would be preferable in order to be able to monitor the stabilizing effects of finite Larmor radius ion orbits. Properties that are sensitive to this axial plasma translation are electrode resistivity, electrode surface roughness, plasma viscosity, and axial non-uniformity of the electrodes associated with nozzle shaping. These properties should be included in a realistic simulation, and in analytic modeling of the Rayleigh-Taylor and Kelvin-Helmholtz instabilities in the azimuthal nozzle.

The azimuthal magnetic nozzle may also be subject to non-axisymmetric instabilities as manifested in radial spokes or arcs. These depend heavily on the Hall effect. They have been studied, both analytically and in simulation, by Demetriades[8-f], primarily in connection with MHD generators. Such studies are valuable and should be continued and extended in their range of parameters.

2. Radiation Losses. The general condition for radiation losses to be relatively small may be stated as follows. The energy lost by radiation from a sample of plasma during the transit by that sample through the nozzle should be small compared with the energy content of the sample. This general condition has to be stated in two different ways, depending on whether the plasma is optically thin or optically thick. Also, as in the previous section on transport, one should monitor the radiation flux incident upon material boundaries.

In order to provide a survey of conditions under which plasmas are to be regarded as optically thin or optically thick, A. G. Sgro has utilized an opacity code built by Group T-4 at Los Alamos. This computer code calculates normalized absorptivities (Rosseland and Planck)[9-a,b;3-b] ($Ch.II$) in this case for hydrogen plasma. The Rosseland model assumes equilibrium which strictly applies to the equilibrium plasma envisioned in the reservoir of the meridional magnetic nozzle. However this should be at least indicative of the opacity of the plasma in the nozzle itself. A more complete physical description requires the solution of the equations of radiative transfer within the flow field, and that

kind of detailed investigation is beyond the scope of this report. Table I.14 displays the output of the Group T-4 opacity code in the form of Rosseland and Planck normalized absorptivities (in cm^2/gm) for various temperatures, $T_{(eV)}$, and various electron number densities, $n_e(cm^{-3})$, for each temperature. The corresponding optical thicknesses, L_{Ross} and L_{Planck} (in cm), are obtained with the aid of the mass density $\rho(gm/cm^3)$ in an obvious manner.

For plasmas with a temperature of one to a few eV, one sees from this table that electron densities above a few times 10^{18} cm^{-3} are becoming optically thick for transverse global dimensions larger than 10 cm. According to Table I.1, this transition occurs for thermal pressures above about 50 psi, in the neighborhood of 1 eV temperatures.

On the other hand, for plasma temperatures of 10 eV or higher, the plasmas remain optically thin (for transverse global dimensions less than about 10^2 cm) for electron densities up to about 10^{19} cm^{-3}, corresponding to thermal pressures up to at least several thousand psi. Such densities are within the assumed range of parameters of Table I.1.

Therefore, when estimating radiation losses, we always shall use the optically thin model for plasma temperatures of 10 eV or above; and also for 1 eV temperatures for densities below 10^{18} cm^{-3}. But we shall use the optically thick model of a surface radiator for densities above 10^{18} cm^{-3} for temperatures in the 1 eV range. The intermediate range of $n \sim 10^{18}$ cm^{-3}, $T \sim 1\,eV$, is more correctly treated by solving the equations of radiative transfer, but that undertaking is beyond the scope of this report.

Incidentally, one generally can ignore electron cyclotron radiation as a loss channel here, because, for the range of parameters considered (see Table I.1), the electron plasma frequency greatly exceeds the electron gyro-frequency, $\omega_{pe} \gg \omega_{ce}$. That is, radiation cannot propagate out of a plasma unless the radiation frequency exceeds the electron plasma frequency, and this is not the case for the electron cyclotron frequency or its low harmonics.

a. Optically Thin Case.

From Chapter 1 of Glasstone and Lovberg,[10] the power per unit volume from bremsstrahlung radiation in a Hydrogen plasma of density n and temperature T can be written as

$$P_{brem} \approx 2 \times 10^{-25} n^2(cm^{-3}) T^{1/2}(eV)\,[erg\ cm^{-3}\ s^{-1}]$$
$$= 2 \times 10^{-26} n^2(cm^{-3}) T^{1/2}(eV)\,[Watts\ m^{-3}] \qquad (I.90)$$

(In this preliminary survey, we ignore line radiation and impurity radiation.) For a characteristic distance r [meters] to a material surface from the center of the plasma, a rough estimate of the radiation power density P_{rad} incident on the surface is (by assuming roughly spherical symmetry),

$$P_{rad} \approx P_{brem}\frac{r(m)}{3} \approx \frac{2}{3} \times 10^{-26} n^2(cm^{-3}) T^{1/2}(eV)r(m)\,[Watts\ m^{-2}]. \qquad (I.91)$$

(Approximately the same relation is obtained without making the assumption of spherical symmetry. For aspect ratios $A = 1, 2, \ldots 5$, one finds respectively $\frac{1}{4}, \frac{1}{4}, \frac{5}{2.7}, \frac{5}{2.8}$, and $\frac{5}{2.9}$, for a cylindrical model. The spherical model for P_{rad} is adequate for this scoping study.)

In Table I.15 below, we tabulate the radiation power densities on the lateral wall according to Eq. (I.91), in units of MW/m^2, for $r = 1$ meter.

TABLE 1.14 Rosseland and Planck Means (cm^2/gm) for hydrogen plasma in thermodynamic equilibrium, and corresponding optical depths (cm). The information is organized under each temperature as:

n_e (cm⁻³)	Ross.(cm^2/gm)	L_{Ross}(cm)
ρ(gm/cm³)	Planck(cm^2/gm)	L_{Planck}(cm)

T=1.25 eV

n_e / ρ	Ross / Planck	L_{Ross} / L_{Planck}
1.91×10^{15} / 3.96×10^{-8}	4.77×10^{2} / 8.26×10^{4}	5.3×10^{4} / 3.0×10^{2}
5.18×10^{15} / 1.41×10^{-7}	1.12×10^{3} / 2.82×10^{5}	6.3×10^{3} / 2.5×10
1.40×10^{17} / 6.23×10^{-7}	2.20×10^{3} / 4.57×10^{5}	7.3×10^{2} / 3.5
3.83×10^{17} / 3.36×10^{-6}	3.72×10^{3} / 5.00×10^{5}	8.0×10 / 6.0×10^{-1}
1.04×10^{18} / 2.03×10^{-5}	5.95×10^{3} / 5.58×10^{5}	8.3 / 8.8×10^{-2}
2.83×10^{18} / 1.26×10^{-4}	9.76×10^{3} / 5.91×10^{5}	8.1×10^{-1} / 1.3×10^{-2}
7.69×10^{18} / 7.47×10^{-4}	1.70×10^{4} / 6.10×10^{5}	7.9×10^{-2} / 2.2×10^{-3}
2.09×10^{19} / 4.91×10^{-3}	3.20×10^{4} / 6.33×10^{5}	6.4×10^{-3} / 3.2×10^{-4}
5.69×10^{19} / 4.77×10^{-2}	6.92×10^{4} / 6.49×10^{5}	3.0×10^{-4} / 3.2×10^{-5}

T = 3 eV

n_e / ρ	Ross / Planck	L_{Ross} / L_{Planck}
1.42×10^{15} / 2.45×10^{-8}	3.26×10^{3} / 2.56×10^{4}	1.3×10^{2} / 1.6×10
3.87×10^{16} / 6.79×10^{-8}	9.94×10^{3} / 6.36×10^{4}	1.5×10 / 2.3
1.05×10^{15} / 1.89×10^{-7}	2.90×10^{4} / 1.56×10^{5}	1.8 / 3.4×10^{-1}

T=10 eV

n_e(cm⁻³) / ρ(gm/cm³)	Ross.(cm^2/gm) / Planck(cm^2/gm)	L_{Ross}(cm) / L_{Planck}(cm)
1.59×10^{17} / 2.66×10^{-7}	1.20 / 1.47×10	3.1×10^{6} / 2.6×10^{5}
4.32×10^{17} / 7.24×10^{-7}	2.13 / 2.96×10	6.5×10^{5} / 4.7×10^{4}
1.17×10^{18} / 1.97×10^{-6}	4.35 / 6.09×10	1.2×10^{5} / 8.3×10^{3}
3.19×10^{18} / 5.37×10^{-6}	9.98 / 1.38×10^{2}	1.9×10^{4} / 1.4×10^{3}
8.67×10^{18} / 1.47×10^{-5}	2.46×10 / 3.41×10^{2}	2.8×10^{3} / 2.0×10^{2}
2.36×10^{19} / 4.01×10^{-5}	6.29×10 / 8.97×10^{2}	4.0×10^{2} / 2.8×10
6.41×10^{19} / 1.10×10^{-4}	1.61×10^{2} / 2.32×10^{3}	5.6×10 / 3.9
1.74×10^{20} / 2.99×10^{-4}	4.13×10^{2} / 5.87×10^{3}	8.1 / 5.7×10^{-1}

T=20 eV

n_e / ρ	Ross / Planck	L_{Ross} / L_{Planck}
1.22×10^{18} / 2.04×10^{-6}	6.68×10^{-1} / 3.09	7.4×10^{5} / 1.6×10^{5}
3.32×10^{18} / 5.57×10^{-6}	9.42×10^{-1} / 7.40	1.9×10^{5} / 2.4×10^{4}
9.02×10^{18} / 1.52×10^{-5}	1.53 / 1.86×10	4.3×10^{4} / 3.6×10^{3}
2.45×10^{19} / 4.13×10^{-5}	2.85 / 4.87×10	8.5×10^{3} / 5.0×10^{2}
6.66×10^{19} / 1.28×10^{-4}	6.07 / 1.29×10^{2}	1.3×10^{3} / 6.1×10
1.81×10^{20} / 3.08×10^{-4}	1.42×10 / 3.39×10^{2}	2.3×10^{2} / 9.6
4.92×10^{20} / 8.41×10^{-4}	3.50×10 / 8.76×10^{2}	3.4×10 / 1.4

TABLE I.15. Bremsstrahlung Power Density (MW/m^2) on the Lateral Wall
Assuming a Characteristic Dimension of $r = 1\ meter$
**(For $T = 1\ eV$, $n = 10^{18}$, and $10^{19}\ cm^{-3}$, the "optically-thick"
model is used, in which case the edge temperature of
the plasma can be influenced by thermal control of the boundary walls.)**

	$T[eV]$	1	10	100
$n[cm^{-3}] =$	10^{13}	$6.7 \times 10^{-7}(\frac{MW}{m^2})$	2.1×10^{-6}	6.7×10^{-6}
	10^{14}	6.7×10^{-5}	2.1×10^{-4}	6.7×10^{-4}
	10^{15}	6.7×10^{-3}	2.1×10^{-2}	6.7×10^{-2}
	10^{16}	6.7×10^{-1}	2.1	6.7
	10^{17}	67.0	212	670.0
	10^{18}	(opt. thick)	2.1×10^4	6.7×10^4
	10^{19}	(opt. thick)	2.1×10^6	6.7×10^6

Comparing with Table I.11, we see that for T larger than or equal to 10 eV, the radiation wall loads exceed the heat wall loads for ion densities equal to or larger than $10^{16}\ cm^{-3}$. We see that for plasma densities upwards of $10^{17}\ cm^{-3}$, the bremsstrahlung power density incident upon a nearby (1 meter distant) wall will equal or exceed on the order of one to several hundred megawatts per square meter, far in excess of classical heat fluxes at the higher densities. However, such operating densities will be more or less precluded anyway by the necessity not to waste the initial thermal energy by radiating it from the plasma during its transit through the nozzle, see Eq. (I.97) below.

Having discussed the radiation flux loads incident on the boundaries in the optically thin case, we return to the more basic physics issue of the fractional amount of energy lost from the plasma by radiation during the plasma transit through the nozzle.

A characteristic time, t_{brem}, for energy loss by bremsstrahlung radiation from the plasma can be estimated from

$$t_{brem} = \frac{(\text{thermal energy per unit volume})_{es}}{(\text{radiation power per unit volume})_{es}} = 2.4 \times 10^{13} \frac{T_{(eV)}^{1/2}}{n_{(cm^{-3})}}\ [sec.] \qquad (I.92)$$

Comparing with Table I.11, we see that for T larger than or equal to 10 eV, the radiation wall loads exceed the heat wall loads for ion densities equal to or larger than 10^{16} cm^{-3}. We see that for plasma densities upwards of 10^{17} cm^{-3}, the bremsstrahlung power density incident upon a nearby (1 meter distant) wall will equal or exceed on the order of one to several hundred megawatts per square meter, far in excess of classical heat fluxes at the higher densities. However, such operating densities will be more or less precluded anyway by the necessity not to waste the initial thermal energy by radiating it from the plasma during its transit through the nozzle, see Eq. (I.97) below.

Having discussed the radiation flux loads incident on the boundaries in the optically thin case, we return to the more basic physics issue of the fractional amount of energy lost from the plasma by radiation during the plasma transit through the nozzle.

A characteristic time, t_{brem}, for energy loss by bremsstrahlung radiation from the plasma can be estimated from

$$t_{brem} = \frac{\text{(thermal energy per unit volume)}_{cgs}}{\text{(radiation power per unit volume)}_{cgs}} = 2.4 \times 10^{13} \frac{T_{(eV)}^{1/2}}{n(cm^{-3})} [sec.] \qquad (I.92)$$

The transit time through the nozzle is estimated as

$$t_z = \frac{\ell_z}{V} \approx \frac{\ell_z}{v_i} = \frac{\ell_z(cm)}{1.3 \times 10^6 T_{(eV)}^{1/2}(cm\ s^{-1})}. \qquad (I.93)$$

The ratio of these times is

$$\frac{t_{brem}}{t_z} \approx 3.1 \times 10^{10} \frac{T_{(eV)}}{n(cm^{-3})\ell_z(cm)}. \qquad (I.94)$$

The condition required for radiation losses to be fractionally small in the optically thin case is then

$$t_{brem} \gg t_z \qquad (I.95)$$

which can be reduced to

$$(n\ell_z)(cm^{-2}) \ll 3 \times 10^{10} T_{(eV)} \qquad (I.96)$$

For $\ell_z = 10^2$ cm, we thus, require

$$n(cm^{-3}) \ll 3 \times 10^{17} T_{(eV)}. \qquad (I.97)$$

with even lower limits for still larger axial lengths ℓ_z.

b. Optically Thick Case. An interesting contrast to the optically thin case is the optically thick plasma, generally denser and colder than the plasmas in the previous examples. In this case, the emitted plasma radiation is absorbed within the plasma volume, so that the plasma appears to be a surface radiator rather than a volume radiator.

Since the plasma is a surface radiator in the example considered here, with collisions assumed to be frequent enough to produce a local equilibrium, its radiative properties are

described by the power emitted per unit surface at the plasma edge, having temperature T_{edge}, as given by the Stefan-Boltzmann law,

$$P_{rad} = \sigma_{SB} T_{edge}^4 (^\circ K)[\text{Watts per } m^2] \qquad (I.98)$$

where the Stefan-Boltzmann constant, σ_{SB}, is

$$\sigma_{SB} = 5.7 \times 10^{-8}[\text{Watts } m^{-2}(^\circ K)^{-4}]. \qquad (I.99)$$

Since $1 \ eV \approx 10^{4\circ} K$, the surface density of radiated power also can be written as

$$P_{rad} \approx 6 \times 10^8 T_{edge}^4(eV)[\text{Watts } m^{-2}]. \qquad (I.100)$$

Thus, an edge temperature of 1 eV implies 600 MW/m^2 of radiation energy flux on the wall. The use of this formula assumes that $T_H^4 \ll T_{edge}^4$, where T_H is the temperature of the hot side of the wall next to the plasma. The use of this formula also assumes that the mean-free-path for photon absorption in the plasma is small compared to the temperature-gradient scale length in the plasma. When the optical absorpion length is not small compared to scale lengths in the plasma, the Stefan-Boltzmann law loses validity and one must solve the full radiative transfer equations.

Now, it is important to note that this loss process depends very sensitively on the edge temperature of the plasma and is independent of the plasma density as long as the optical absorption length is short. In contrast, the radiative loss from the optically thin plasma depends upon an integral over the bulk plasma, and is very sensitive to the plasma density. For this reason, bremsstrahlung radiation from an optically thin plasma and the associated power density on the wall will be hard to control by profile adjustments, for a given operating density in bulk. However, in the optically thick case, there is a possibility to control the radiative loss by controlling the edge temperature of the plasma. This thermal control problem in principle amounts to a detailed engineering calculation, but it can be scoped out schematically as follows.

Let the boundary wall have a thickness Δ. Let T_H be the temperature of the hot side of the wall. Let the temperature T_C on the cold side of the wall be maintained by a circulating coolant, or by a heat-pipe arrangement. Then, in the steady state, the temperature profile within the wall is linear, and the heat flux through the wall is given by

$$q_W = K_W \frac{(T_H - T_C)}{\Delta}, \qquad (I.101)$$

where K_W is the thermal conductivity of the wall material. (We assume for simplicity that K_W is practically independent of temperature.) Also, assuming that radiation dominates thermal conduction, then,

$$P_{rad} = q_W = \sigma_{SB} T_{edge}^4 \qquad (I.102)$$

where T_{edge} is the edge temperature of the plasma (not generally equal to the wall temperature). A specification of q_W then determines $(T_H - T_C)$, namely,

$$T_H = T_C + q_W \frac{\Delta}{K_W}. \qquad (I.103)$$

A specification of q_W also determines the edge temperature of the plasma from the Stefan-Boltzmann law, provided that radiation is the dominant loss process. This law then constitutes one of the boundary conditions for the plasma in the optically thick case.

For a given $P_{rad} = q_W$, the restriction that T_H should remain below the melting point of the wall material puts an upper limit on the wall thickness Δ. More detailed engineering calculations also would have to take into account the differential thermal expansion in a wall of given shape, together-with the associated strains and stresses, as well as the detailed engineering mechanisms that determine the temperature of the coolant T_C.

For example, given an engineering estimate of the heat flux that can be handled by the pumping of coolants or other means, q_W is given. Then, for a simple example with $T_H \leq T_{M.P.}$ (the melting point of the wall material) and assuming that $T_C \ll T_{M.P.}$, an upper limit to the wall thickness is determined from Eq. (I.101) as $\Delta = \kappa_W T_{M.P.}/q_W$. Moreover, from Eq. (I.102), one has $T_{edge} = (q_W/\sigma_{SB})^{1/4}$ which determines the edge temperature of the plasma. In practical terms, $T_{edge}(eV) = (q_W[W/m^2]/6 \times 10^8)^{1/4}$. Thus, considering plasma radiation incident upon a copper wall, assuming $q_W = 100\ MW/m^2 = 10^4\ W/cm^2$, $\kappa_W = 1\ cal\ cm/(cm^2\ s^\circ C) = 4\ watts/(cm^\circ C)$, and $T_{M.P.} = 10^{3\circ}C$, we find $\Delta \approx 0.4\ cm$ and $T_{edge} = 0.6\ eV$. For $q_W = 10\ MW/m^2$, we find $\Delta = 4\ cm$ and $T_{edge} = 0.34\ eV$. Thus, in this manner (admittedly oversimplified), one can attempt to exert some control over the radiation wall loadings and plasma edge temperatures, for the parameter regime of optically thick plasmas.

To continue our discussion of the optically thick case, we now want to write down the condition that ensures that the energy lost by surface (black body) radiation during the transit of the nozzle by a given portion of plasma is small relative to the thermal energy content of that portion of plasma. The characteristic time for loss of energy by this means from a spherical plasma element of radius r can be estimated as

$$t_{bb} \approx \frac{3}{2} \times \left[\frac{2nT}{\sigma_{SB} T_{edge}^4} \right]_{cgs} \frac{r(cm)}{3} \approx 2.7 \times 10^{-24} n(cm^{-3}) \frac{T(eV)}{T_{edge}^4 (eV)} r(cm)[sec.] \quad (I.104)$$

where T is the bulk plasma temperature and T_{edge} is the edge plasma temperature. (The result is almost the same for a cylindrical volume of plasma.) The transit time through the nozzle is $t_s \approx \frac{\ell_s}{v_t} \approx \frac{\ell_s(cm)}{1.3 \times 10^6 T_{(eV)}^{1/2}}$ [sec]. The ratio of these times is roughly

$$\frac{t_{bb}}{t_s} \approx 3.5 \times 10^{-18} \frac{n(cm^{-3}) T_{(eV)}^{3/2}}{A T_{edge}^4 (eV)}, \quad (I.105)$$

where $A = \frac{\ell_s}{r}$ is the aspect ratio of the nozzle. The condition that this ratio needs to exceed 1 can be written as an upper limit on the edge temperature of the plasma, namely

$$T_{edge}(eV) \lesssim 4 \times 10^{-5} \frac{n^{1/4}(cm^{-3}) T_{(eV)}^{3/8}}{A^{1/4}}. \quad (I.106)$$

Of course, the internal density n and internal temperature T are restricted here to correspond to optically thick conditions. This means that radiation transport distances

must be short compared to nozzle dimensions. The need for an upper limit on T_{edge} implies the need for an upper limit on the heat flux carried away at the boundary.

II. DEVELOPMENT AND APPLICATION OF A CODE FOR STEADY IDEAL MHD FLOW THROUGH MERIDIONAL MAGNETIC NOZZLES

A. The Basic Equations

In Appendix A, a brief derivation is given of the Bernoulli equation, and then its consequences for nozzle flow for the case of long, thin magnetic nozzles. In the present section, that treatment is augmented by a full 2D derivation of the procedure for determining self-consistently the transverse and longitudinal profiles of magnetic flux, mass density, velocity, and thermal energy (enthalpy).

We begin by writing down the Ideal MHD Equations for Steady Flow.

$$\rho \vec{V} \cdot \nabla \vec{V} + \nabla P = \vec{J} \times \vec{B} \qquad (II.1)$$

$$\vec{V} \cdot \nabla (P\rho^{-\gamma}) = 0 \qquad (II.2)$$

$$\nabla \cdot (\rho \vec{V}) = 0 \qquad (II.3)$$

$$\nabla \cdot \vec{B} = 0 \qquad (II.4)$$

$$\nabla \times (\vec{V} \times \vec{B}) = 0 \qquad (II.5)$$

In the following treatment θ refers to the ignorable azimuthal coordinate, and r refers to the radial distance from the axis of symmetry. Assuming axisymmetry and $V_\theta = B_\theta = 0$, Eqs. (II.3) and (II.4) can be satisfied by defining

$$\rho \vec{V} = \nabla U \times \nabla \theta \quad \text{and} \qquad (II.6)$$

$$\vec{B} = \nabla \Psi \times \nabla \theta \qquad (II.7)$$

where U is the stream function for the mass flux and Ψ is the stream function for the magnetic flux. Plugging (II.6) and (II.7) into (II.5) gives

$$(\nabla U \times \nabla \Psi) \cdot \nabla \theta = 0$$

which implies that U and Ψ are functionally related, i.e., $\Psi = \Psi(U)$. This implies that $\vec{V}$ is parallel to $\vec{B}$ since

$$\vec{B} = \nabla \Psi \times \nabla \theta = \Psi' \nabla U \times \nabla \theta = \Psi' \rho \vec{V}. \qquad (II.8)$$

62

Using the identity $\vec{V} \cdot \nabla \vec{V} = \nabla \frac{V^2}{2} + (\nabla \times V) \times V$, Eq. (II.1) can be rewritten:

$$\rho \nabla \frac{V^2}{2} + \nabla P + (\nabla \times \vec{V}) \times \rho \vec{V} = \vec{J} \times \vec{B}. \qquad (II.9)$$

Equation (II.9) scalar-multiplied with $\vec{V}$ implies (since $\vec{V}$ is parallel to $\vec{B}$),

$$\rho \vec{V} \cdot \nabla \frac{V^2}{2} + \vec{V} \cdot \nabla P = 0,$$

which can be transformed into:

$$\vec{V} \cdot \nabla \left(\frac{V^2}{2} + \frac{\gamma}{\gamma - 1} \frac{P}{\rho} \right) = 0 \qquad (II.10)$$

using Eqs. (II.2) and (II.3).

Equations (II.2–4) and (II.10) can be solved analytically to show how everything varies along the streamlines relative to the throat of the nozzle. Taking $\gamma = 5/3$ and using $(\frac{\partial B}{\partial V})_0 = 0$ which defines the location of the throat, after a little algebra one can derive:

$$\frac{B}{B_0} = \frac{V}{V_0} \left[\frac{4}{3} - \frac{1}{3} \left(\frac{V}{V_0} \right)^2 \right]^{3/2} \qquad (II.11)$$

$$\frac{\rho}{\rho_0} = \left[\frac{4}{3} - \frac{1}{3} \left(\frac{V}{V_0} \right)^2 \right]^{3/2} \qquad (II.12)$$

$$\frac{P}{P_0} = \left[\frac{4}{3} - \frac{1}{3} \left(\frac{V}{V_0} \right)^2 \right]^{5/2} \qquad (II.13)$$

where $B_0(U)$, $V_0(U)$, $P_0(U)$ and $\rho_0(U)$ are the values at the throat of the nozzle which is also the Mach 1 surface $V_0 = C_0 = \sqrt{\frac{\gamma P_0}{\rho_0}}$. (See Appendix A for a demonstration that $V_0 = C_0$.)

Equation (II.11) can be inverted using the quartic formula:

$$\frac{V}{V_0} = \left[\sqrt{y} \pm \sqrt{\sqrt{4y^2 - 3 \left(\frac{B}{B_0} \right)^{2/3}} - y} \right]^{3/2} \qquad (II.14)$$

where

$$y = \frac{1}{2} \left[\sqrt{1 + \sqrt{1 - \left(\frac{B}{B_0} \right)^2}} + \sqrt{1 - \sqrt{1 - \left(\frac{B}{B_0} \right)^2}} \right]$$

and the $\pm$ sign is used for the super (sub) sonic part of the flow.

Equations (II.12), (II.13), and (II.14) express V, ρ, and P in terms of the magnetic field and they are plotted in Fig. (1a).

For a paraxial flux tube which is thin enough so that nothing varies over the radius, these equations give the complete solution to the MHD equations (II.1-5), the quasi-1-D solution. In addition, these equations (II.12-14) represent exact relations between the variables, along any streamline, for the full 2D problem. The positions of the streamlines themselves can be determined in the manner described below. For the moment, pretending we have paraxial flow, we show in Fig. (1b) a quasi-1-D solution for a nozzle formed by a paraxial flux tube produced by a single unit radius coil, for which $B/B_0 = (1 + z^2)^{-3/2}$.

For a full 2D nozzle configuration, radial profiles are determined by the perpendicular (cross-field) component of Eq. (II.9). In order to utilize that component, we first integrate Eqs. (II.2) and (II.10). That gives

$$\frac{V^2}{2} + \frac{\gamma}{\gamma - 1} \frac{P}{\rho} = H(U) \equiv \left(\frac{\gamma}{2} + \frac{\gamma}{\gamma - 1} \right) \frac{P_0(U)}{\rho_0(U)} \qquad (II.15)$$

and

$$P\rho^{-\gamma} = S(U) \equiv P_0(U)\rho_0(U)^{-\gamma}. \qquad (II.16)$$

Here, $H(U)$ is the enthalpy of the magneto-fluid, and $S(U)$ is closely related to the entropy density of the fluid.

Equation (II.16) can be used to express the pressure gradient as

$$\nabla P = \rho \nabla \left(\frac{\gamma}{\gamma - 1} \frac{P}{\rho} \right) - \frac{\rho^\gamma}{\gamma - 1} \nabla S. \qquad (II.17)$$

Combining this with Eq. (II.9) gives:

$$\rho \nabla H - \frac{1}{\gamma - 1} \rho^\gamma \nabla S + (\nabla \times \vec{V}) \times \rho \vec{V} = \vec{J} \times \vec{B} \qquad (II.18)$$

Then, using Eqs. (II.6) and (II.7) and the identity

$$\nabla \times (f \nabla g \times \nabla \theta) = -r^2 \left[\nabla \cdot \left(\frac{f \nabla g}{r^2} \right) \right] \nabla \theta$$

$$\left[\text{if } \frac{\partial f}{\partial \theta} = \frac{\partial g}{\partial \theta} = 0 \right],$$

it can be shown that

$$(\nabla \times \vec{V}) \times \rho \vec{V} = -\nabla \cdot \left(\frac{\nabla U}{\rho r^2} \right) \nabla U \qquad (II.19)$$

and

$$\vec{J} \times \vec{B} = -\nabla \cdot \left(\frac{\nabla \psi}{r^2} \right) \nabla \psi. \qquad (II.20)$$

Combining this with Eq. (II.18) yields:

$$\rho\nabla H - \frac{1}{\gamma-1}\rho^\gamma\nabla S - \nabla\cdot\left(\frac{\nabla U}{\rho r^2}\right)\nabla U + \nabla\cdot\left(\frac{\nabla\Psi}{r^2}\right)\nabla\Psi = 0, \qquad (II.21)$$

and since H, S and Ψ are functions of U, this reduces to the scalar equation:

$$\nabla\cdot\left(\frac{\nabla U}{\rho r^2}\right) - \Psi'\nabla\cdot\left(\frac{\Psi'\nabla U}{r^2}\right) - \rho H' + \frac{1}{\gamma-1}\rho^\gamma S' = 0 \qquad (II.22)$$

This is the master equation for obtaining the general solution to the MHD Eqs. (II.1-5), the full 2-D axisymmetric steady-state solution. It determines the stream function $U(r,z)$ in terms of the 3 arbitrary functions $\Psi(U)$, $H(U)$, and $S(U)$.

The density ρ must be expressed in terms of U, which can be done by using Eqs. (II.12) and (II.14) and noting that

$$\frac{B}{B_0} = \frac{\frac{|\nabla U|}{r}}{\left(\frac{|\nabla U|}{r}\right)_0} = \frac{\frac{|\nabla U|}{r}}{\left(\frac{|\nabla U|}{r}\right)_{\text{max along constant } U}} \qquad (II.23)$$

from Eq. (II.8).

Some additional insight can be obtained by using the identity $\vec{J}\times\vec{B} = \vec{B}\cdot\nabla\vec{B} - \nabla B^2/2$ to rewrite Eq. (II.1) as:

$$\rho\vec{V}\cdot\nabla\vec{V} + \nabla\left(P + \frac{B^2}{2}\right) = \vec{B}\cdot\nabla\vec{B} \qquad (II.24)$$

then, using $\vec{V} = V\hat{t}$, $\vec{B} = B\hat{t}$, $\hat{t}\cdot\nabla = \frac{\partial}{\partial s}$ and $\frac{\partial\hat{t}}{\partial s} = K\hat{n}$ where s is distance along the streamline, K is the curvature and $\hat{n}$ is the normal vector, Eq. (II.24) can be decomposed into tangential and normal components as follows:

$$\hat{t}: \quad \rho V\frac{\partial V}{\partial s} = -\frac{\partial P}{\partial s} \qquad (II.25)$$

$$\hat{n}: \quad (B^2 - \rho V^2)K = \frac{\partial}{\partial n}\left(P + \frac{B^2}{2}\right) \qquad (II.26)$$

Eq. (II.26) shows that wherever the streamlines are straight ($K = 0$) the pressure must be balanced by magnetic field pressure in the normal direction. It follows that in order to have magnetically confined, transversely non-uniform plasma pressure in the computational modeling of the meridional magnetic nozzle, the transition from the plasma reservoir to the nozzle entrance, with the attendant curved magnetic field lines, must be included in the equilibrium, and the reservoir must have a magnetic field with $\beta \approx 1$. (Here, β is the ratio of internal plasma pressure to external magnetic pressure.) The inclusion of the reservoir will require a body fitted coordinate system which conforms to the shape of the nozzle plus reservoir.

B. The Quasi 1-D Solution

The simplest solution to Eq. (II.22) would be an unmagnetized flow with no entropy or enthalpy transverse gradients (i.e. $\Psi' = H' = S' = 0$) in which case the problem reduces to

$$\nabla \cdot \left(\frac{\nabla U}{\rho r^2} \right) = 0$$

or

$$\Delta^* U = \nabla U \cdot \nabla \ell n \rho \tag{II.27}$$

where $\Delta^* = r^2 \nabla \cdot r^{-2} \nabla$. If the curvature of the throat is low enough so that $Kr \ll 1$ everywhere in the nozzle then the density will vary only along the streamlines and not across them. Then $\nabla U \cdot \nabla \rho = 0$ and Eq. (II.27) reduces to just $\Delta^* U = 0$ which is the same equation as for an incompressible potential flow through the same nozzle. This much simpler flow can be described by a stream function ψ and a velocity potential χ as:

$$\vec{v} = \nabla \psi \times \nabla \theta = \nabla \chi \tag{II.28}$$

where $\Delta^* \psi = 0$ and $\nabla^2 \chi = 0$. Since the general problem will have an approximately similar flow geometry, the functions ψ and χ make an ideal coordinate system for the general flow problem, as well as giving the exact solutions for the quasi 1-D case.

The components of II.28 are:

$$\psi_r = r \chi_z \tag{II.29a}$$

$$\psi_z = -r \chi_r \tag{II.29b}$$

which determines the functions $\psi(r, z)$ and $\chi(r, z)$. These equations may be inverted to give the inverse equations:

$$r_\chi = -r z_\psi \tag{II.30a}$$

$$z_\chi = r r_\psi \tag{II.30b}$$

which determines the inverse functions $r(\psi, \chi)$ and $z(\psi, \chi)$. They can be combined into a single second order equation by cross differentiating and eliminating z:

$$(r r_\psi)_\psi + \left(\frac{r_\chi}{r} \right)_\chi = 0 \tag{II.31}$$

or, if $s \cong r^2$:

$$s_{\psi\psi} + \left(\frac{s_\chi}{s} \right)_\chi = 0 \tag{II.32}$$

This equation can be solved analytically in the special case where separation of variables is possible. If $s(\psi, \chi) = s_1(\psi) s_2(\chi)$ then Eq. (II.32) can be separated into

$$\frac{d^2 s_1}{d\psi^2} = -2 \tag{II.33a}$$

and

$$\frac{1}{s_2} \frac{d}{d\chi} \left(\frac{1}{s_2} \frac{d s_2}{d\chi} \right) = 2 \tag{II.33b}$$

66

where the separation constant has been arbitrarily chosen equal to 2, which merely determines the scale of units for ψ and χ. These equations are easily solved giving

$$s(\psi, \chi) = (2\psi - \psi^2)\sec^2\chi$$

and hence the solutions for r and z are:

$$r(\psi, \chi) = (2\psi - \psi^2)^{1/2}\sec\chi \qquad (II.34a)$$

$$z(\psi, \chi) = (1 - \psi)\tan\chi. \qquad (II.34b)$$

With a little algebra these equations can be transformed into

$$\frac{r^2}{2\psi - \psi^2} - \frac{z^2}{(1 - \psi)^2} = 1 \qquad (II.35a)$$

and

$$\frac{r^2}{\sec^2\chi} + \frac{z^2}{\tan^2\chi} = 1 \qquad (II.35b)$$

which shows that the lines of constant ψ (for $\psi < 1$) are hyperbolas and the lines of constant χ (for $|\chi| < \pi/2$) are ellipses. Therefore Eqs. (II.34) can be used to describe a coordinate system in a hyperbolic nozzle with $0 \leq \psi \leq \psi_{max} < 1$ and $-\pi/2 < \chi < \pi/2$. They also give the solution to the quasi 1-D flow problem which is just $U = \psi$.

For more general geometries where separation of variables is not possible, Eq. II.32 must be solved using computational means. This quasilinear elliptic equation is solved numerically by integrating the finite-differenced version of

$$\ddot{s} + \nu\dot{s} = s_{\psi\psi} + (s_\chi/s)_\chi \qquad (II.36)$$

in time until a steady state is reached ($\dot{s} = 0$). The artificial time step is chosen small enough to satisfy the Courant condition

$$\Delta t \ll \left(\frac{1}{(\Delta\psi)^2} + \frac{1}{s_{min}(\Delta\chi)^2}\right)^{-1/2} \qquad (II.37)$$

and the numerical damping coefficient ν is chosen to maximize the convergence rate (typically $\nu \sim 4$.).

The solution of II.32 also requires specifying boundary conditions at $\psi = 0$ and ψ_{max} and at $\chi = 0$ and χ_{max}. At $\psi = 0$ we have $s = r^2 = 0$ and at $\psi = \psi_{max}$ we need $s = r^2 = r^2_{wall}(\chi)$. But $r_{wall}(\chi)$ is generally unknown. It is more desirable to specify $r_{wall}(z)$ or $r_{wall}(\ell)$ where ℓ is arclength along the wall. This requires an iteration which starts with a guess for $r_w(\chi)$ and then solves Eq. II.32. That solution can be used to calculate $\ell(\chi)$ and then $r_w(\ell)$ is used to get a new estimate for $r_w(\chi)$. This iteration usually converges in 20-50 steps providing the nozzle has $|dr_w/dz| \sim \infty$ everywhere. The boundary condition used at $\chi = 0$ and χ_{max} is simply that the streamlines be straight, ie.

$K = 0$ where K is the curvature. The symmetry condition $\frac{\partial s}{\partial \chi} = 0$ can instead be used at $\chi = 0$ if appropriate.

An approximate analytic solution to the inverse equations II.30 has been found and is valid wherever $Kr_{wall} \ll 1$:

$$r(\psi, \chi) = \left[\frac{2(\psi/\psi_{max})}{1 + \cos\phi} - \frac{\sin^2\phi(\psi/\psi_{max})^2}{(1 + \cos\phi)^2} \right]^{1/2} r_w(\ell) \qquad (II.38a)$$

$$z(\psi, \chi) = z_w(\ell) + \left(\frac{\sin\phi}{1 + \cos\phi} \right) \left(1 - \frac{\psi}{\psi_{max}} \right) r_w(\ell) \qquad (II.38b)$$

where $\phi(\ell) = \tan^{-1}(r'_w(\ell)/z'_w(\ell))$ and $\ell(\chi)$ is obtained by solving the ordinary differential equation:

$$\frac{d\ell}{d\chi} = \frac{r_w^2(\ell)}{1 + \cos\phi} \qquad (II.39)$$

This approximate solution is used as a starting guess for the iterative procedure described earlier.

A coordinate solution for the JPL nozzle[11] is shown in Fig. 2. This also shows the streamlines for the quasi 1-D flow in the JPL nozzle which is described by $U = \psi$.

C. The General 2-D Solution

1. Numerical Methods. The general solution to Eq. II.22 must be computed numerically. To allow for arbitrary geometry the (ψ, χ) coordinate system will be used with the domain ranging over $0 \leq \psi \leq \psi_{max}$ and $0 \leq \chi \leq \chi_{max}$. Here $\psi = 0$ is the z axis and $\psi = \psi_{max}$ is the wall, $\chi = 0$ is the entrance to the nozzle and $\chi = \chi_{max}$ is the exit. The boundary conditions to be applied are $U = 0$ at $\psi = 0$ and $U = U_{max}$ at $\psi = \psi_{max}$ (so $\vec{V} \cdot \hat{n} = 0$). At $\chi = 0$ the simplest condition is to require $\partial U/\partial \chi = 0$ which just means that the flow enters the nozzle normally (i.e. $\vec{V} \times \hat{n} = 0$). The boundary condition at $\chi = \chi_{max}$ is much more complicated and will depend on what type of problem is being solved, so the code is written to allow for an arbitrary boundary condition of the form $\partial U/\partial \chi = g$ where g may depend on U.

The stream function is expanded as

$$U(\psi, \chi) = U_0 + \sum_{i=1}^{N} a_i U_i + \sum_{i=1}^{M} b_i B_i \qquad (II.40)$$

where U_0 is the quasi 1-D solution satisfying the inhomogeneous boundary conditions. If the units of U are chosen so that $U_{max} = \psi_{max}$ then this is just $U_0 = \psi$. The $U_i(\psi, \chi)$ are a set of basis functions satisfying homogenous boundary conditions $U_i = 0$ at $\psi = 0$ and ψ_{max} and $\partial U_i/\partial \chi = 0$ at $\chi = 0$ and χ_{max}. The code uses bi-cubic B-splines with the stated boundary conditions, centered on each of the N mesh points. The $B_i(\psi, \chi)$ are a set of local basis functions which will control the boundary condition at the exit $\chi = \chi_{max}$. They must satisfy the same homogeneous boundary condition as the U_i at $\psi = 0$ and ψ_{max} (namely $B_i = 0$), but they will have an inhomogeneous boundary condition $\partial B_i/\partial \chi = 1$ at $\chi = \chi_{max}$. The code also uses bi-cubic B-splines with the stated boundary conditions

for the M b_i functions, but they are centered on "ghost" mesh points just beyond the exit and they only extend 1 cell length into the computational domain. Notice here that M is just the number of radial mesh points, and N is M times the number of axial mesh points.

This representation for $U(\psi, \chi)$ (Eq. II.40) is substituted into Eq. (II.22) and matrix elements are taken with each of the N U_i to get a system of N nonlinear algebraic equations depending on the N coefficients a_i and the M coefficients b_i. After integration by parts these equations take the form:

$$F_j(a_1, a_2, \ldots a_N, b_1, b_2, \ldots b_M) \equiv$$

$$\int \left[\left(\frac{1}{\rho} - (\Psi')^2 \right) \frac{\nabla U_j \cdot \nabla U}{r^2} - \left(\Psi' \Psi'' \frac{|\nabla U|^2}{r^2} + \rho H' - \frac{1}{\gamma - 1} \rho^\gamma S' \right) U_j \right] dr^3 = 0 \quad (II.41)$$

where $j = 1, 2, \ldots N$.

The integrals are done using a 4×4 point Gaussian quadrature rule on each cell and hence require the introduction of a 4X refinement in the mesh. This subgrid is unequally spaced according to the Gaussian quadrature convention which requires that the mesh points be located at the zeros of some appropriate Legendre polynomial.

If the b_i are known or if they can be expressed as functions of the a_i coefficients, then the system of equations in II.41 completely determine the solution. If the b_i are unknown, then these equations must be supplemented with M additional equations in order to determine the additional M unknowns.

The code solves for the unknown coefficients using the IMSL subroutine ZSPOW which applies a modified Newton's method to find the roots of a nonlinear system of equations. It typically uses $N = 9 \times 33$ mesh points and $M = 9$ boundary points and takes about 1 minute to find the solution on a Cray 1.

2. Unmagnetized Flow. The first set of solutions that will be discussed are cases of unmagnetized flow, which means $\Psi' = 0$. Without a magnetic field there is only one critical surface, the Mach-one surface, where the flow equations change character from elliptic to hyperbolic. The Mach-one surface is located at the point on each flux tube where the cross sectional area of the flux tube is a minimum. This is a choke point in the flow and must have $V_0 = C_0$, that is the flow speed must equal the sound speed at this point, which will also be referred to as the throat of the nozzle. The equations will be elliptic upstream of the throat and hyperbolic downstream of the throat. From Eq. (II.6) it can be seen that

$$\rho V = \frac{|\nabla U|}{r} \quad (II.42)$$

which shows that $\frac{|\nabla U|}{r}$ is the inverse area function for each flux tube. This means that the Mach-one surface is located by finding where $\frac{|\nabla U|}{r}$ is maximum. Since $V_0 = C_0$ at this point it follows that

$$\rho_0 V_0 = \rho_0 C_0 = \rho_0 \sqrt{\frac{\gamma P_0}{\rho_0}} = \sqrt{\gamma P_0 \rho_0}$$

thus, using II.42:

$$\gamma P_0 \rho_0 = \left(\frac{|\nabla U|^2}{r^2} \right)_{max \ along \ constant \ U} \quad (II.43)$$

Using equations II.15 and II.16, $P_0(U)$ and $\rho_0(U)$ can be related to the entropy and enthalpy functions $S(U)$ and $H(U)$ and II.43 can be rewritten as:

$$\left(\frac{|\nabla U|^2}{r^2}\right)_{max} = \gamma S(U)\left[\frac{2}{\gamma}\left(\frac{\gamma-1}{\gamma+1}\right)\frac{H(U)}{S(U)}\right]^{\frac{\gamma+1}{\gamma-1}}. \qquad (II.44)$$

This equation must be satisfied on the Mach-one surface and gives the extra conditions required to determine the boundary conditions at the exit of the nozzle. By requiring that Eq. (II.44) be satisfied at each of the M points where a longitudinal grid line intersects the Mach-one surface, a set of M additional equations are obtained which will suffice, together with Eq. (II.41), to determine the other M unknown coefficients $b_1, b_2 \ldots b_M$. The fact that the coefficients only adjust the boundary condition at the exit, while Eq. (II.44) must be satisfied at the Mach-one surface might at first glance seem to be a serious difficulty; but since the region between the Mach-one surface and the exit is hyperbolic, the information at the throat will be transferred along characteristics to the boundary where it is needed. It is to be expected that if any part of the region between the Mach-one surface and the exit were elliptic, this procedure wouldn't work. This procedure is the only one that has been developed and built into the code so far, so our "direct method" code for finding steady nozzle flow can only be applied to problems which are hyperbolic between the Mach-one surface and the exit. All unmagnetized nozzle flow problems are of this character, but many magnetized nozzle flows are not. This problem will be reexamined in later sections.

If the conditions in the reservoir are near equilibrium, meaning (in the absence of a magnetic field) no pressure or density gradients and negligible flow, then the entropy and enthalpy functions $S(U)$ and $H(U)$ will be constant, hence $S' = H' = 0$. This is the most likely situation to be encountered in a non-magnetic experiment and will be the main focus of this section. The compressibility of the gas will be assumed to be $\gamma = 5/3$, the appropriate value for a hydrogen plasma, unless otherwise noted.

Figure 3 shows the grid used for a hyperbolic nozzle with unit radius at the throat and a 45° opening half angle at each end. Every fourth line constitutes the coarse mesh, equally spaced in ψ and χ, on which the cubic splines are defined. The rest of the lines form the gaussian quadrature subgrid used for doing the integrals in Eq. (II.41). Fig. 4 shows the streamlines, which are almost the same as for quasi 1-D flow. Fig. 5 shows the inverse square area function $(\rho V)^2$, and Fig. 6 shows the same function plotted along streamlines. Fig. 5 also shows the location of the Mach-one surface. Fig. 7 shows a contour plot of the velocity and Fig. 8 shows the magnitude of the velocity plotted along the streamlines. Figs. 9 and 10 show the density, in contours and along streamlines.

Figure 11 shows the grid for the JPL nozzle[11] in units of inches. Fig. 12 shows the streamlines, Figs. 13 and 14 show $(\rho v)^2$, Figs. 15 and 16 show the density, and Figs. 17 and 18 show the pressure. Notice that there is a shock near the wall just downstream of the throat. The solution is not well resolved in this shock region since the code uses cubic splines which have a high degree of continuity and cannot represent a shock very accurately. The rest of the solution however should still be accurate. Fig. 19 shows contours of the Mach number. This calculation, like all others, used $\gamma = 5/3$. For purposes of comparison to experiment, the JPL nozzle was redone with $\gamma = 1.4$, the value for air. The solution was essentially identical to the $\gamma = 5/3$ case, but the Mach number contours were slightly different and are shown in Fig. 20. Fig. 20 also shows the data that was measured in

the JPL experiment which was done using air. The data was copied out of Ref. 11. The excellent agreement with experiment indicates that the code is working satisfactorily.

The next unmagnetized case to be examined has a pressure profile of the form $P_0 \sim (1 + \epsilon U)$ but still constant density, $\rho_0 = 1$. This corresponds to choosing $S(U)$ and $H(U) \sim (1 + \epsilon U)$. Since this assumes the existence of a pressure profile in the reservoir, the reservoir must be specially designed to allow for this. For example, it could consist of a set of nested concentric annular gas feeds run at different pressures.

Figures 21 and 22 show the streamlines for these nonuniform pressure cases. Fig. 21 has $\epsilon = -.02$ which makes the pressure drop near the wall. Fig. 22 has $\epsilon = .02$ which corresponds to increased pressure near the wall. The new feature in these solutions is the presence of vortices in the nozzle entrance region. These vortices can be understood by noting where the high and low pressure regions are as indicated in the figures, and observing that the gas flows from the high pressure regions to the low pressure regions. In these examples there are low pressure regions back in the reservoir as well as at the exit, so some of the gas flows back into the reservoir, creating the vortices. If the coefficient ϵ is increased in magnitude, the vortices just get bigger. In order to have a pressure profile (confined plasma) and still have radial equilibrium (no vortices) there must be a nonuniform magnetic field with the field pressure balancing the gas pressure. This situation will be addressed in the next sections.

3. Magnetized Flow. We now turn to the consideration of magnetized flows, the main purpose of this study. The magnetic field serves two essential purposes; confining the plasma so that it won't be in contact with the wall, and providing thermal insulation to reduce energy losses to the wall. First we shall consider a proportional field profile (magnetic flux density proportional to mass flux density), which provides insulation but not confinement, and we shall see how the introduction of a magnetic field significantly increases the mathematical complexity of the equilibrium. Next, a sharp boundary model will be considered which will allow us to examine situations with both confinement and insulation in a simple analytical manner, and thereby we will find a limit to the amount of flux that can be imbedded in a nozzle without quenching the steady flow of plasma. Finally, we shall discuss the general problem of finding an equilibrium with diffuse magnetic profiles and the complications encountered in a proper treatment of the boundary conditions.

a. **Proportional Field Case.** To get a proportional field profile we take $\Psi' = $ const. We will still assume equilibrium conditions in the reservoir and use $H' = S' = 0$. The major complication introduced by the magnetic field is that there are now three critical surfaces where the equilibrium equations change character from elliptic to hyperbolic[12,13]. The Mach-one surface where the flow velocity reaches the sound speed $V = C_s$ is still a critical surface, but there are now two more; the Alfvén surface where the flow speed reaches the Alfvén speed $V = C_A = B/\sqrt{\rho}$ and the cusp surface where it reaches the so called cusp speed $V = C^*$ where C^* is defined by

$$ C^* = \frac{C_s C_A}{\sqrt{C_s^2 + C_A^2}} \qquad (II.45) $$

There are two possible arrangements for the sequence of critical surfaces depending on the strength of the magnetic field as given by the constant Ψ'. To get a dimensionless measure of the field strength, we define $\alpha = \sqrt{\mu_0}\Psi'$ where ρ_0 is the density of the plasma at the

throat of the nozzle (this assumes MKSA units with $\mu_0 = 1$). Now $\Psi' = B/(\rho v)$ and at the throat of the nozzle $V_0 = C_{so}$ which implies that α is the ratio of the Alfvén speed to the sound speed at the throat of the nozzle: $\alpha = C_{AO}/C_{SO}$. Also, using $C_{SO} = (\gamma Po/\rho_0)^{1/2}$ it can be shown that the plasma beta at the throat is related to α by the formula $\beta_0 = 2/(\gamma\alpha^2)$.

The critical value for α is $\alpha = 1$. For $\alpha < 1$, (weak field) the Alfvén critical surface will occur before the Mach-one surface and the equations will be elliptic from the entrance ($V = 0$) up to the cusp surface ($V = C^*$), then hyperbolic from the cusp surface up to the Alfvén surface ($V = C_A$), then elliptic again from the Alfvén surface up to the Mach-one surface ($V = C_S$), and then hyperbolic again from the Mach-one surface to the exit. Since the region between the Mach-one surface and the exit is hyperbolic the same boundary conditions used for the unmagnetized case are still applicable and the same code can be used to solve this magnetized flow case. If $\alpha > 1$ (strong field) however, the situation is different. The Alfvén critical surface will occur after the Mach-one surface so the equilibrium equations will be elliptic from the entrance to the cusp surface, then hyperbolic up to the Mach-one surface at the throat, then elliptic up to the Alfvén surface and then hyperbolic from the Alfvén surface to the exit. Now the region between the Mach-one surface and the exit is part hyperbolic and part elliptic, so the boundary conditions are much harder to implement and a more sophisticated code would be needed to compute these equilibria, if they even exist.

The present code has been used to compute magnetized flows in meridional magnetic nozzles with α ranging from 0 up to .8. No flowing equilibria with α above .8 could be computed. Figures 23 through 36 show solutions for the hyperbolic nozzle and the JPL nozzle with $\alpha = .8$, which corresponds to a beta value at the throat of about 1.9. The most striking feature is that they look almost identical to the unmagnetized flows shown earlier. The only difference is that the magnetic field seems to stiffen the flow somewhat and make it closer to being one dimensional. This can be seen most clearly in Figs. 25, 29, 32, and 34. The radial variations in the flow variables are greatly reduced.

The fact that no solutions could be found for $\alpha > .8$ may be an indication that there are no solutions in at least part of this range because the code should have been able to find solutions up to $\alpha = 1$ if they existed. This is only an indication however and not a proof. Further investigations would be required to fully understand the physical issues behind such a limitation if it is real.

b. Sharp Boundary Model. The sharp boundary model consists of an unmagnetized flow surrounded by a vacuum field region between the plasma and the wall with a singular current and vorticity sheet at the interface. This is the simplest way to model a magnetically confined flow because the nozzle is divided into two separate regions, each having a very simple solution. The boundary condition that must be satisfied at the interface is just that the pressure of the vacuum field balance the plasma pressure, which would be known from the unmagnetized flow solution. If the radial width of the vacuum field region is $\delta(z)$ and the radius of the nozzle wall is $r_w(z)$ and if the vacuum region is thin enough so that $\delta(z) \ll r_w(z)$ everywhere, then the magnetic field will be given by

$$B(z) = \frac{\Psi}{2\pi r_w(z)\delta(z)} \qquad (II.46)$$

where Ψ is the amount of magnetic flux inside the nozzle. Equating the magnetic pressure

72

with the plasma pressure at the interface $P_w(z)$ one obtains (in MKSA units)

$$\frac{1}{2\mu_0}\left(\frac{\Psi}{2\pi r_w(z)\delta(z)}\right)^2 = P_w(z) \qquad (II.47)$$

which may be solved for $\delta(z)$ to get:

$$\delta(z) = \frac{\Psi}{2\pi r_w(z)\sqrt{2\mu_0 P_w(z)}}. \qquad (II.48)$$

An example of this type of solution is shown for the JPL nozzle in Fig. 37. The central unmagnetized flow solution is just copied from Fig. 12 and the pressure at the wall $P_w(z)$ from Fig. 18 is used in Eq. II.48 to compute $\delta(z)$ assuming that the amount of flux is as needed to make $\delta = .1$ inch at the entrance.

If the amount of flux in the vacuum region is increased, δ will increase until the inequality $\delta \ll r_w$ is no longer satisfied. An analytic treatment is still possible however, if a long thin approximation can be used. This would amount to assuming that $dr_w/dz \ll 1$ everywhere. In this case the magnetic field would be given by

$$B(z) = \frac{\Psi}{\pi(r_w^2(z) - r_I^2(z))} \qquad (II.49)$$

where $r_I(z)$ is the radius of the plasma-vacuum interface. Then Eq. II.47 would be modified to

$$\frac{\Psi}{\pi[r_w^2(z) - r_I^2(z)]} = \sqrt{2\mu_0 P_w(z)} \qquad (II.50)$$

which can be solved to give the location of the interface:

$$r_I^2(z) = r_w^2(z) - \frac{\Psi}{\pi\sqrt{2\mu_0 P_w(z)}}. \qquad (II.51)$$

Notice that for a given flow with some specific pressure $P_w(z)$, and some specific geometry $r_w(z)$, as the flux is increased the radius of the interface must decrease; but since it cannot be smaller than zero there will be a limit to the amount of flux that can be present in the nozzle without quenching the flow. The radius of the interface will always be smallest at the throat of the nozzle and if this value is equated to zero then Eq. II.51 gives for the flux limit

$$\Psi_{max} = \pi r_0^2 \sqrt{2\mu_0 P_0} \qquad (II.52)$$

where r_0 is the radius of the throat and P_0 is the pressure at the throat (which is related to the pressure in the reservoir by Eq. II.13). If the amount of flux exceeds this limit then the magnetic field will be too strong to allow any plasma to flow out of the reservoir and the nozzle will be shut off. This is sometimes referred to as "stuffing" the nozzle. Figure 38 shows a schematic representation of a nozzle which is close to being stuffed.

If the flux is below the stuffing limit given by Eq. II.52, then the sharp boundary equilibrium will always exist and one can infer that slightly diffuse equilibria that are

close to the sharp boundary profiles should also exist. Clearly then, an equilibrium nozzle flow with magnetically confined plasma should be possible, though not necessarily easy to compute if the profiles are diffused.

The flux limit in Eq. II.52 can also be expressed as a magnetic field limit in terms of the field at the throat B_0:

$$B_{0\ max} = \frac{\Psi_{max}}{\pi r_0^2} = \sqrt{2\mu_0 P_0} \qquad (II.53)$$

or in terms of the local beta at the throat β_0 as $\beta_{0\ min} = 1$. It is interesting to note that in the previous section with the constant field, no solutions could be found with $\beta_0 < 1.9$, which is close to the sharp boundary beta limit of 1.0; but it is unknown whether these two limits have any fundamental physical connection.

c. **Diffuse Field Profiles.** The general case of a diffuse field profile will have a very complicated arrangement of critical surfaces. Figure 39 shows one possibility for an equilibrium which is only slightly diffuse and still close to the sharp boundary model. The diagram is divided into 5 different regions labeled I through V. In region I, there is no magnetic field so the Alfvén speed and the cusp speed are zero. The pressure and hence the sound speed is high so the flow will be subsonic and the equilibrium will be elliptic, just as for any unmagnetized subsonic flow. In region II the magnetic field starts to build up, and the flow can enter the nozzle in this region subsonic and sub Alfvénic; but the cusp speed is always smaller than both characteristic velocities and the flow can enter the nozzle above the cusp speed, thus producing an equilibrium that is hyperbolic in this region. In region III, the cusp speed will reach a maximum and be larger than the entrance velocity of the fluid, so the fluid, so this region will be elliptic. In region IV the pressure is nearly zero so the sound speed and the cusp speed are almost zero, but the magnetic field and hence the Alfvén speed are high, so the flow velocity will be above the cusp and sound speeds, but below the Alfvén speed; so the equilibrium equations will be elliptic. [It is essentially just a vacuum field.] In region V the magnetic field is very small and the flow has crossed the Mach-one surface so it is supersonic and super-Alfvénic and this region is therefore hyperbolic. Table II.1 summarizes the relationships between the various velocities and the character of the equilibrium in the five different regions.

The difficulty with solving this type of problem numerically is now readily apparent. The region between the Mach-one surface and the exit is not purely hyperbolic; it has elliptic parts, and the division between the elliptic and hyperbolic parts cannot even be specified ahead of time. It must be found as part of the solution. Since the present code requires the region between the Mach-one surface and the exit to be hyperbolic, it should not be able to solve this type of problem. Several types of diffuse profile solutions were attempted with the code, but as expected it did not work. The code would not converge to a solution. One possible method of overcoming this problem would be to use a code based on a time-dependent method. The merits of this alternative approach will be discussed in Chapter III.

74

TABLE II.1. Dependence of the character of the PDE's describing Ideal MHD flow on the relationships amongst the several characteristic velocities and the fluid velocity. (Here C^* is the "cusp" speed.)

Region	Velocities	Character
I	$C^* < C_A < V < C_s$	elliptic
II	$C^* < V < C_s, C_A$	hyperbolic
III	$V < C^* < C_s, C_A$	elliptic
IV	$C^* < C_s < V < C_A$	elliptic
V	$C^* < C_s, C_A < V$	hyperbolic

III. COMPARISON OF THE DIRECT SOLUTION METHOD WITH THE INITIAL VALUE, TIME-DEPENDENT APPROACH TO COMPUTING THE MHD FLOW PROFILES IN THE NOZZLE

The complicated boundary conditions associated with the complex arrangement of critical surfaces discussed in the previous section can be mostly avoided by using a time-dependent initial-value approach. By introducing time dependence, and adding density and pressure evolution equations, there are no longer any boundary conditions to be satisfied at the Mach-one surface, hence Eq. (II.44) can be dropped. The only boundary conditions needed will be at the actual physical boundaries, namely; the walls, entrance, and the exit. The solution of general magnetized flows will still be a very complex numerical problem, however, because there will still be the different regions where the equations have different characteristics. Special numerical techniques will be required in the hyperbolic regions in order to insure numerical stability without introducing excessive numerical diffusivity. The proper treatment of time-dependent hyperbolic flows is still an area of active research and is beyond the scope of this study.

For problems requiring high resolution, it is also probably more efficient to solve the steady flow problem using a time dependent method. If M is the number of mesh points in each dimension, the computer time required to take one time step in a 2-D time dependent code would be proportional to M^2. The time step would be limited by numerical stability considerations (the Courant condition) to $1/M$ of the characteristic time (sonic or magnetosonic transit time), so if t_s (in units of the characteristic time), is the time it takes to reach a steady state (possibly including a steady level of fluctuations), then the time it would take to compute the steady state would be proportional to $t_s M^3$, compared to $M^6 = N^3$ for the direct method using a Newton iteration. In general, t_s may be a large

75

number, but, as a physical rather than a numerical quantity it is independent of M, so that for large enough M the time dependent method is always the faster computational method. The direct method would only be more efficient for problems where the number of mesh points (or spline functions) required for adequate resolution was small enough so that $M^6 < t_s M^3$ or $M < t_s^{1/3}$.

Another reason for employing the initial-value time-dependent computational model is that one may uncover unsteady processes that might actually occur but that would be inaccessible to a steady state computational model. The shedding of vortices by an airfoil is a well-known example. In the nozzle problem, vortices might be induced by plasma viscosity and a no-slip boundary condition, and would tend to be carried along by the flow. If present, such vortices would make a convective contribution to lateral heat and mass transfer. The presence of a meridional magnetic field would tend to inhibit such vortices since they would try to bend those field lines. However, the presence of a high plasma resistivity near the cold walls would allow the plasma to slip across the field lines. The balance between these two effects is a quantitative issue best resolved by a 2D time-dependent simulation with transport coefficients. Moreover, in the azimuthal magnetic nozzle, no line bending is available to inhibit the formation of such vortices.

IV. DESCRIPTION OF A 2D MHD INITIAL VALUE CODE

During the course of this work, one of the investigators (A. H. Glasser) acquired and learned to use an initial value 2D MHD simulation, originally constructed by J. Brackbill and R. Milroy,[14,15] with the following properties.

The single-fluid MHD equations are solved in two dimensions (r, z), retaining all three components of vector quantities. The equations include mass continuity; momentum (with scalar plasma pressure, magnetic forces, artificial viscosity $\sim 1\%$ of the parallel Braginskii viscosity to smooth the velocity profiles); separate electron and ion temperature equations including the effects of convection, Joule heating, viscous heating, and anisotropic thermal conduction in both species; and the generalized Ohm's law used within the context of quasi-neutrality and zero electron inertia. This Ohm's law includes anisotropic resistivity (classical plus anomalous), the Hall term, the diamagnetic drift contribution from the electron pressure gradient, and the classical "thermal force" contribution[2] to the electron-ion friction.

The simulated plasma was contained within a free-boundary separatrix, surrounded by a vacuum magnetic guide field outside of the separatrix. The vacuum magnetic field was found in terms of the positions and currents (time dependent) in external theta pinch coils. The vacuum solution was effected by solving Poisson's equation for the azimuthal component of the vector potential, A_θ.

The equations were solved on a Lagrangian mesh using an adaptive mesh algorithm for rezoning the mesh in order to concentrate the grid in regions of large current density to resolve regions having sharp gradients in the magnetic field. The motion of the free boundary separatrix was solved for self-consistently as part of the over-all time-dependent solution.

The simulation on a CRAY supercomputer of the formation, and translation-compression of a plasmoid known as the Field-Reversed Configuration is shown in Fig. 40, corresponding to the FRC experiments at Los Alamos. This process bears some

resemblance to the magnetic nozzle concept. The horizontal bars represent the positions of the theta pinch coils. The formation and motion of the plasmoid is clearly evident.

Because of the limited duration of the research period of this contract on the magnetic nozzle project and the limited amount of support allotted for personnel on this project (0.8 man-years), we were unable to expend the effort necessary to modify this code so as to perform a set of systematic runs more relevant to the magnetic nozzle concept. This situation was exacerbated by the cumbersome nature of the programming and structure of the code. We believe that recent improvements in FORTRAN and supercomputer capabilities will allow such simulations to be performed effectively and efficiently, using codes that are more amenable to trial modifications in boundary conditions and geometry.

V. SUMMARY, CONCLUSIONS, AND RECOMMENDATIONS

In Chapter I, we briefly reviewed the foundations of the ideal MHD model, and then made estimates of various losses from the plasma flowing through a meridional magnetic nozzle. A wide range of plasma parameters was considered, with maximum thermal pressures of $\sim$ 400 to 40,000 psi depending on the assumed temperature. Both fractional losses and absolute fluxes to the lateral wall were estimated for a $\beta = 1$ hydrogen plasma flowing through a nozzle with a characteristic radial dimension of one meter. The $\beta = 1$ condition was selected as representing the least magnetic field for which transverse pressure confinement of plasma is practical. The methods and results presented there are easily extendable in obvious ways to other values of β and other nozzle dimensions as desired. We also pointed out the importance of the MHD stability properties of the plasma in the transition region between the reservoir and the nozzle entrance, and of the plasma detachment problem at the nozzle exit. We recommend 2-D and 3-D initial value resistive MHD simulations to model those regions accurately.

Some specific results of the estimates of loss processes in hydrogen plasmas with $\beta = 1$ may be summarized as follows for the meridional magnetic nozzle with diffuse radial profiles. At temperatures near 1 eV, classical resistive cross field mass transport amounts to a significant (in fact, unacceptable) fractional loss of axially flowing plasma (see Table I.6 and remark following). This situation can be relieved by working at lower values of beta. (At temperatures of 10 eV and above, the mass-loss fraction is negligible even with $\beta = 1$.) Thus, we recommend detailed modeling of low-beta plasmas in the 1 eV range in the meridional nozzle configuration.

With regard to radial thermal losses, classical thermal diffusivities are dominated by thermal losses in association with classical resistive diffusion (radial mass transport) at 1 eV for all densities considered, and at 10 eV for densities of 10^{16} cm^{-3} or greater (see Table I.9). Moreover, these classical losses dominate the Bohm losses in all but three cases for all parameters considered (see Table I.12 and I.13 and compare with Table I.11). For plasmas near 1 eV, it is important to observe that the fractional thermal losses will be about the same as the fractional mass losses, and should be mitigated by working at lower values of beta. For radial nozzle dimensions on the order of one meter, the actual thermal power density on the wall due to classical transport amounts to only a few megawatts per square meter, at most, for densities up to 10^{16} cm^{-3}, but can be several hundred to several thousand MW/m^2 for densities exceeding 10^{17} cm^{-3} (see Table I.11).

Let us now compare these thermal conduction (and axisymmetric thermal convection) losses with the radiation losses assuming that the nozzle dimensions are on the order of one meter. We see from Table I.14 that all but two of our standard parameter cases may be treated as optically thin, the exceptions being $T = 1\ eV$ with $n = 10^{18}$ and $10^{19}\ cm^{-3}$. These two "optically thick" cases will not be discussed here because the edge conditions of the plasma itself will be influenced by the engineering approach to the management of the energy flux at the wall (see Chap. I-C, Sec. 2-b). In comparing the optically-thin bremsstrahlung radiation wall loading results (Table I.15) with the thermal wall loading results of Table I.11, we observe the following. At a temperature of 1 eV, the thermal wall loading is the larger for densities ranging from $10^{13} - 10^{16}\ cm^{-3}$, but it is, at most, a few megawatts per square meter. (Note that the <u>fractional</u> thermal losses due to axisymmetric convection (radial mass transport) from the $\beta = 1$ plasmas are large at $T = 1\ eV$.) At 1 eV, densities much larger than $10^{16}\ cm^{-3}$ ought also to be precluded by the restriction that the fractional energy loss from radiation be small [see Eq. (I.97)]. At 10 eV, for densities up to $10^{16}\ cm^{-3}$, radiation wall loading is less than or on the order of the thermal wall loading, and is at most a few MW/m^2. At densities greater than $10^{16}\ cm^{-3}$, at $T = 10\ eV$, radiation wall loading by far exceeds thermal wall loading and can amount to several hundred to millions of megawatts per square meter. However, at 10 eV, densities of $10^{18}\ cm^{-3}$ and higher ought to be precluded because the fractional energy loss from radiation would become large [see Eq. (I.97)]. The same qualitative statements apply at 100 eV (radiation wall loading $\lesssim$ thermal wall loading for $n \leq 10^{16}\ cm^{-3}$ and no more than a few MW/m^2), with very high radiation wall loads (several hundred to millions of MW/m^2) for densities above $10^{16}\ cm^{-3}$. Also, even if the power were available at 100 eV, densities ought to be kept less than $10^{19}\ cm^{-3}$ to keep the fractional radiation losses small.

Let us now compare the above losses with those induced by non-symmetrical plasma dynamics (convective transport) in the meridional magnetic nozzle as discussed in Chap. I-C, Sec. 1-d. First, it should be observed that these magneto-plasma models of "turbulent transport" are completely different from the conventional situation in turbulent pipe flow of ordinary compressible fluids wherein the turbulence is driven by the free energy in the axial flow field. In the meridional magnetic nozzle, azimuthal g-modes and azimuthal Kelvin-Helmholtz turbulence are not driven by the axial flow although they may be somewhat modified by it. (Conversely, in the azimuthal magnetic nozzle, the Kelvin-Helmholtz modes should be expected to be strongly coupled to the axial flow.) Both of the models we discussed earlier should be treated as provisional, in the case of g-modes because of the use of a non-rigorous quasi-linear "mixing length" construction, and in the case of the Kelvin-Helmholtz modes because of the employment of unrealistic parameters in the simulations of Theilhaber and Birdsall ($m_i/m_e = 40$, $\omega_{pe} \ll \omega_{ce}$). Moreover, the coupling of both types of instabilities to the axial flow field has yet to be elucidated for the types of plasmas considered here.

With these cautions in mind, we turn to the results of the "convective transport" investigations in Chap. I. With regard to "g-modes," we note from Eq. (I.82) that the fraction of mass (or thermal energy) lost is mostly dependent upon $(\Delta_r/R_c)^{1/2}$ where Δ_r is the thickness of the edge-plasma boundary layer and R_c is a macroscopic length scale (radius of curvature of a field line). Moreover, we note from Eq. (I.83-a) that the quasilinear heat flux is $2 \times 10^{-15}(\Delta_r/R_c)^{1/2}n(cm^{-3})T^{3/2}\ (eV)[MW/m^2]$, again dependent upon $(\Delta_r/R_c)^{1/2}$. We also recall that when (Δ_r/R_c) is of order unity, there are only a

few instability growth times available, but when $(\Delta_r/R_c) \ll 1$ there are many growth times available. Consequently, we shall concentrate on the "sharp boundary" case when $(\Delta_r/R_c) \ll 1$. In the low density regime, $10^{13} - 10^{15}\, cm^{-3}$, since $r_{ci} \sim 1\, cm$ (see Table I.5), and since the ions are magnetized at these densities for $10\, eV$ and above, one might expect the boundary layer thickness to be given by r_{ci}, so, for $R_c \sim 100\, cm$, we take $(\Delta_r/R_c)^{1/2} \sim 0.1$. (By restricting Δ_r and the g-mode wavelengths to be no smaller than r_{ci}, we are crudely taking into account the effect of "Finite Larmor Radius" stabilization [gyroviscosity].) In the high-density regime, $r_{ci} \ll 1\, cm$, and at $1\, eV$ where the ions are not magnetized, one might expect the classical resistive boundary layer behavior, so we take $(\Delta_r/R_c)^{1/2} \sim R_\eta^{-1/4}$ where R_η is the magnetic Reynolds number. Referring to Table I.6, we see that at $1\, eV$, $R_\eta^{-1/4} \sim 0.5$, producing a thick boundary layer and consequently only a few available instability growth times. Consequently, we do not expect the 1 eV plasmas to be vulnerable to transport from g-mode instabilities (they are already highly vulnerable to classical transport losses). On the other hand, 10 eV and 100 eV temperatures respectively yield $R_\eta^{-\frac{1}{4}} \approx 0.16$ and $R_\eta^{-\frac{1}{4}} \approx 0.05$. Thus, we see that in all 10 eV and 100 eV cases, for these rough estimates it is sufficient to take $(\Delta_r/R_c)^{1/2} \sim 0.1$. Having done so, we can expect fractional losses on the order of 10% from g-modes. The quasilinear heat fluxes themselves are given in the following table.

TABLE V.1. Quasilinear Heat Flow from Rayleigh Taylor Modes in $\beta = 1$ Hydrogen Plasmas for $(\Delta_r/R_c)^{1/2} = 0.1$

$$q_{R.T.} = 2 \times 10^{-16} n(cm^{-3}) T_{(eV)}^{3/2} [MW/m^2]$$

$T[eV]$	1	10	100
$n[cm^{-3}] = \quad 10^{13}$	--	$6.3 \times 10^{-2} (MW/m^2)$	x
10^{14}	--	6.3×10^{-1}	x
10^{15}	--	6.3	2.0×10^2
10^{16}	--	6.3×10	2.0×10^3
10^{17}	x	6.3×10^2	2.0×10^4
10^{18}	x	6.3×10^3	2.0×10^5
10^{19}	x	6.3×10^4	2.0×10^6

Note: Recall that "x" signifies a breakdown of the fluid-plasma model.

Comparing Table V.1 to Table I.15, we see that the g-mode induced thermal flux is more than competitive with the energy flux from radiation at 10 eV and 100 eV for densities of up to about 10^{18} cm^{-3} (where the thermal fluxes of several thousand to hundreds of thousands of MW/m^2 are produced). In view of this result, based upon a simple quasilinear model, we recommend quantitative resistive MHD modeling of MHD instabilities with nonlinear effects in the entrance region of the meridional magnetic nozzle.

One should remember here that even classical losses will increase at the edge of a sharply defined plasma with edge layer gradient lengths of order Δ_r, compared to what they would have been for a general diffuse profile. The increase will be on the order of a/Δ_r) where "a" is a characteristic radial dimension of the nozzle. In connection with g-modes, we are considering sharply bounded plasmas with $(a/\Delta_r) \sim 100$ as discussed above, so a fair comparison with classical transport requires that the edge thermal fluxes of Table I.11 be increased by this factor. Such a comparison is made in Table V.2.

TABLE V.2. Comparison of Classical and g-mode Induced Thermal Fluxes (MW/m^2) in a $\beta = 1$ Hydrogen Plasma with a Sharp Boundary $(\Delta_r = a/100)$, with $a = 100$ cm

$T[eV]$		10		100	
$n[cm^{-3}] =$ 10^{13}	9.2×10^{-1}	$6.3 \times 10^{-2}(\frac{MW}{m^2})$		x	x
10^{14}	9.2	6.3×10^{-1}		x	x
10^{15}	7.9×10	6.3		2.9×10^1	2.0×10^2
10^{16}	1.7×10^2	6.3×10		2.9×10^2	2.0×10^3
10^{17}	1.7×10^3	6.3×10^2		2.9×10^3	2.0×10^4
10^{18}	1.7×10^4	6.3×10^3		2.9×10^4	2.0×10^5
10^{19}	1.7×10^5	6.3×10^4		2.5×10^5	2.0×10^6
	classical	g-mode		classical	g-mode

It is interesting to see that the classical transport thermal flux slightly dominates at 10 eV but that the reverse is true at 100 eV.

The above discussion of g-mode-induced wall loading has not taken account of the reduction of the g-mode growth rate by the action of ion collisional viscosity. One would

expect fluid viscosity to have an appreciable stabilizing influence on the growth rate when the wave number becomes sufficiently large that

$$k^2 D_{vis} \approx \Gamma = \sqrt{gk},\qquad(V.1)$$

where D_{vis} is the ion viscous diffusivity (kinematic viscosity), and Γ is the g-mode growth rate. Making the substitutions $k \approx \Delta_r^{-1}$ where Δ_r is the thickness of the plasma-field boundary layer, $g = v_i^2/R_c$, where v_i is the ion thermal velocity, and obtaining D_{vis} from Braginskii[2] for the cases of un-magnetized ($\omega_{ci} < \nu_{ii}$) ions and magnetized ions ($\omega_{ci} > \nu_{ii}$), we find that Eq. (V.1) can be reduced respectively to

$$\frac{\Delta_r}{R_c} \approx \left(\frac{\lambda_{ii}}{R_c}\right)^{2/3}\qquad\text{(un-magnetized ions)},\qquad(V.2)$$

and

$$\frac{\Delta_r}{R_c} \approx \left(\frac{r_{ci}}{R_c}\right)^{2/3}\left(\frac{\omega_{ci}}{\nu_{ii}}\right)^{-2/3}\qquad\text{(magnetized ions)}.\qquad(V.3)$$

Here, ω_{ci} is the ion gyro-frequency, r_{ci} is the ion gyro-radius, ν_{ii} is the ion-ion Coulomb collision frequency for 90° deflections from cumulative small-angle scattering, and $\lambda_{ii} = v_i/\nu_{ii}$ is the ion mean-free path, and R_c is the radius of field line curvature in the bad curvature region of the meridional magnetic nozzle. We recall that the ion magnetization parameter is tabulated in Table I.8. The meaning of these equations is that they set lower limits on (Δ_r/R_c) below which the viscous damping of the g-modes becomes comparable to the mode-growth rate, but above which the neglect of viscosity is more or less valid.

From Table I.8, we find that the ions are un-magnetized at 1 eV, and from Table I.5 that the ion mean-free path is of order of 0.1 cm or smaller. Therefore, at $T = 1$ eV, our use of $\Delta_r \sim 1$ cm (with $R_c \sim 100$ cm) so that $\sqrt{\Delta_r/R_c} \approx 0.1$ is consonant with the neglect of ion viscosity in the study of the effects of g-modes [See Eq. (V.2).] However, only a few growth times are available at 1 eV so we have not considered this case in detail. The same reasoning for 1 eV is true at $T = 10$ eV for densities equal to or greater than 10^{15} cm^{-3}, so that viscosity can be neglected for $n \gtrsim 10^{15}$ cm^{-3} while using $(\Delta_r/R_c)^{1/2} \approx 0.1$. At $T = 10$ eV cm^{-3} and $n < 10^{15}$ cm^{-3}, even with viscosity incorrectly neglected the g-modes still are less important than classical transport.

On the other hand, at $T = 100$ eV, from Table I.8, the ions are magnetized at all but the highest density. Moreover, from Table I.5, for densities of 10^{15} cm^{-3} or higher, we see that the ion gyro-radius has $(r_{ci}/R_c) \lesssim .005$, for $R_c \approx 100$ cm. Hence $(r_{ci}/R_c)^{2/3} \approx 0.03$, and this number is reduced further by the factor $(\omega_{ci}/\nu_{ii})^{2/3} > 1$. [See Eq. (V.3).] Hence, we conclude that even in the case $T \approx 100$ eV, the lower limit on (Δ_r/R_c) can be brought down to about 0.01 so that $\sqrt{\Delta_r/R_c} \approx 0.1$ still provides a valid condition with which proceed without being overwhelmed by viscous damping.

Thus, our estimates of the effects of Rayleigh-Taylor instabilities, that neglected the action of ion viscosity, by and large should remain qualitatively valid. However, a detailed quantitative check of this qualitative assessment is recommended. Since the ion viscosity tensor is complicated, this will be a major project.

As regards the Kelvin-Helmholtz-induced Bohm transport simulated by Theilhaber and Birdsall, we note that it scales the same way as the g-mode-induced transport but is

smaller by an order of magnitude [for $(\Delta_r/R_c)^{1/2} = 0.1$, compare Eq. (I.83-a) with Eq. (I.89)]. Thus, it appears to be less important, but this conclusion is subject to the results of simulations with more realistic parameters.

In Chap. II, we set up the computational problem of ideal plasma-flow through a meridional magnetic nozzle, beginning with a quasi-1D formulation. Results for isentropic flow were shown for the variation of various fluid quantities along the streamlines. A formulation in full axisymmetric 2-D geometry was then set up in order to find the transverse distribution of the streamlines for specified input profiles at the reservoir-nozzle interface. Also, the importance of including this interface in the computation was emphasized. A finite element 2-D code for completely solving the steady isentropic flow problem was constructed, with provision for a body-fitted coordinate system to deal with arbitrary nozzle shapes (including the interface to the reservoir). The motivation for this approach, as opposed to the use of a straight cylindrical coordinate grid-for example, was to reduce the number of elementary functions needed to represent the flow pattern with high resolution. The code was tested on a case of un-magnetized flow by making detailed comparison with an experiment performed at the Jet Propulsion Laboratory, and the formulation and computational method was thus validated. Additional computations with this code on magnetized flow were attempted but were limited to wall-confined plasmas. The reasons for this limitation were found to originate in the complexity of the various critical surfaces (analogous to the Mach-one surface) in plasmas confined by magnetic pressure. (Even in the case of wall-confined plasmas, our code was unable to find a steady-flow solution with beta less than 1.9, although such solutions were found for slightly higher values of beta. The reason for this is not known.)

On the other hand, we were able to supplement the above-mentioned limitation to wall-confined plasma by analytically dealing with a field-free sharp-boundary plasma transversely confined by magnetic pressure. We showed how to make direct use of the un-magnetized flow solutions in this case, and we uncovered a "stuffing limit" that must be exceeded in order to keep the sharp boundary magnetic nozzle open. We recommend the examination of the MHD stability properties of such sharp-boundary flowing equilibria, and we also note that such equilibria are not subject to the detachment problem.

In order to solve the flow problem for diffuse plasma profiles transversely confined by magnetic pressure, we recommend the use of time-dependent (initial value) resistive MHD simulations, as opposed to "direct" solution of the steady flow problem. The initial-value approach will not be subject to the difficulties associated with the existence of several critical surfaces, and it will have access to unsteady flow phenomena if they should naturally and continually occur at large times.

We attempted to acquire and modify such a code for this purpose, but were unable to suitably modify and systematically apply the code within the restrictions of our 0.8 man-year effort.

Concluding with more general observations, it seems natural to use the plasmas produced at elevated temperatures to obtain higher nozzle exhaust velocities in the face of the limitations of chemical fuels (small amount of energy per atom available), and to thereby increase the payload capacity of space vehicles (provided that the requisite power sources to create and drive the plasmas are available). The meridional magnetic nozzle, based upon a reservoir of heated plasma, constitutes a conceptual approach to part of such a system. We also recommend further study for the azimuthal magnetic nozzle (not

82

limited to low magnetic Reynolds numbers), because this concept uses magnetic fields to drive the plasma and requires no special preparation of heated plasma in a reservoir. We refer the reader to the spontaneous heating process discussed in Appendix D, which naturally leads to beta-values of order unity and also thermally contributes to the drive. Finally, we observe that the plasma stability problems and concomitant inefficiencies to which these devices may be vulnerable can be ameliorated by the introduction of magnetic shear. The role of magnetic shear and the extent to which it would modify each of these concepts is a worthwhile research project.

REFERENCES

1. P. G. Burke and K. Smith, "The Low Energy Scattering of Electrons and Positrons by Hydrogen Atoms," *Rev. Modern Physics* **34**, (1962) 458.

2. S. I. Braginskii, "Transport Processes in a Plasma," **Reviews of Plasma Physics,** Vol. 1, Consultants Bureau, New York, 1965, Chap. 2.
   Lyman Spitzer, Jr., **Physics of Fully Ionized Gases,** Interscience Pub. Inc., New York, 1962.

3-a. F. Reif, *Fundamentals of Statistical and Thermal Physics,* McGraw Hill, 1965.

3-b. Ya B. Zel'dovich and Yu P. Raizer, *Physics of Shock Waves and High-Temperature Hydrodynamic Phenomena,* (Academic Press, New York, 1966).

4. K. Smith and A. H. Glasser, "Data Base of Cross Sections and Reaction Rates for Hydrogen Ion Sources," Los Alamos National Laboratory report LAUR-87-2736.

5-a. A. I. Morozov and L. S. Solov'ev, "Steady State Plasma Flow in a Magnetic Field," in **Review of Plasma Physics,** Vol. 8, edited by M. A. Leontovich, Consultants Bureau, New York, 1980, page 1.

5-b. K. V. Brushlinskii and A. I. Morozov, "Calculation of Two Dimensional Plasma Flows in Channels," in **Review of Plasma Physics,** Vol. 8, edited by M. A. Leontovich, Consultants Bureau, New York, 1980, page 105.

6. M. Tuszewski, "Field Reversed Configurations," *Nuc. Fusion* **28** (1988) 2033.

7-a. *Basic Principles of Plasma Physics* by S. Ichimaru, Chap. 11; W. A. Benjamin, Inc.; Reading, Mass., 1973.

7-b. D. Bohm, *The Characteristics of Electrical Discharges in Magnetic Fields,* (A. Guthrie and R. K. Wakerling, eds.) Chap. 2 (McGraw-Hill, NY, 1949).

8-a. J. P. Freidberg, "Ideal Magnetohydrodynamic Theory of Magnetic Fusion Systems," *Rev. Mod. Phys.* **54**, (1982) 801.

8-b. G. S. Argyropoulos, S. T. Demetriades, and K. Lackner, "Compressible Turbulent Magnetohydrodynamic Boundary Layers," *Phys. Fluids* **11** (1968) 2559.

8-c. A. Bhattacharjee, R. Iacono, J. L. Milovich, C. Paranicas, "Ballooning Stability of Axisymmetric Plasmas with Sheared Equilibrium Flows," *Phys. of Fluids B* **1** (1989) 2207.

8-d. S. Chandrasekhar, *Hydrodynamic and Hydromagnetic Stability,* Sec. 92, Oxford at the Clarendon Press, 1961.

8-e. K. Theilhaber and C. K. Birdsall, "Kelvin-Helmholtz Vortex Formation and Particle Transport in a Cross-Field Plasma sheath. I. Transient Behavior," *Phys. Fluids B* **1** (1989) 2244, and "Kelvin-Helmholtz Vortex Formation and Particle Transport in a Cross-Field Plasma Sheath II. Steady State," *Phys. Fluids B* **1** (1989) 2260.

8-f. S. T. Demetriades, "On the Magneto Aerothermal Instability," Paper AIAA-81-0248, presented at the 19th Aerospace Sciences Meeting, Am. Inst. Aero. Astro., Jan. 1981, St. Louis, Mo.

9-a. Arthur N. Cox, "Stellar Absorption Coefficients and Opacities," in **Stellar Structure**, Edited by Lawrence H. Aller and Dean B. McLaughlin, University of Chicago Press 1965, p. 197.

9-b. W. F. Huebner, A. L. Merts, N. H. Magee, Jr., M. F. Argo, Los Alamos report LA-6760-M (1977), Astrophysical Opacity Library.

10. S. Glasstone and R. H. Lovberg, **Controlled Thermonuclear Reactions**, D. Van Nostrand, Princeton, NJ, 1960.

11. R. F. Cuffel, L. H. Back, and P. F. Massier, "Transonic Flowfield in a Supersonic Nozzle with Small Throat Radius of Curvature," *AIAA* **7** (1969) 1364.

12. H. Grad, "Reducible Problems in Magneto-Fluid Dynamic Steady Flows," *Rev. Modern Phys.* **32** (1960) 830.

13. C. K. Chu, " Magnetohydrodynamic Nozzle Flow with Three Transitions," *Phys. Fluids* **5** (1962) 550.

14. R. D. Milroy and J. U. Brackbill, "Numerical Studies of a Field-Reversed Theta-Pinch Plasma," *Phys. Fluids* **25** (1982) 775.

15. R. D. Milroy and J. U. Brackbill, "Toroidal Magnetic Field Generation during Compact Toroid Formation in a Field-Reversed Theta Pinch and Conical Theta Pinch," *Phys. Fluids* **29** (1986) 1184.

16. K. F. McKenna, R. R. Bartsch, R. J. Commisso, C. Ekdahl, W. E. Quinn, and R. E. Siemon, *Physics of Fluids* **23** (1980) 1443.

17. J. C. Fernandez, C. W. Barnes, T. R. Jarboe, I. Henins, H. W. Hoida, P. L. Klingner, S. O. Knox, G. J. Marklin, and B. L. Wright, "Energy Confinement Studies in Spheromaks with Mesh Flux Conservers," *Nuc. Fusion* **28** (1988) 1555.

APPENDIX A
THE MERIDIONAL MAGNETIC NOZZLE

In this Appendix, we derive some basic results for axi-symmetric MHD steady flow, using the ideal MHD model (no transport effects, no Hall effect, no resistivity) in a configuration that contains no azimuthal magnetic field, and concomitantly no meridional currents in the plasma.

Ohm's law is

$$\vec{E} + \vec{V} \times \vec{B} = 0. \qquad (A-1)$$

In a steady-state configuration with azimuthal symmetry, $E_\theta \equiv 0$, and Eq. (A-1) becomes

$$-V_r B_z + V_z B_r = 0. \qquad (A-1a)$$

Thus the meridional component of the velocity field $\vec{V}_M$ is always lined up with the meridional magnetic field $\vec{B}_M \equiv \vec{B}$. We write this condition of parallel flow as

$$\vec{V}_M = \alpha \vec{B}_M. \qquad (A-2)$$

The factor α is generally not constant.

The mass-continuity equation

$$\nabla \cdot (\rho \vec{V}) = 0 \qquad (A-3)$$

then reduces to

$$\vec{V} \cdot \nabla(\alpha \rho) = 0 \qquad (A-4)$$

so that $(\alpha \rho)$ is constant along a streamline.[*] We denote this constant by C_1.

$$\alpha \rho = C_1. \qquad (A-5)$$

$$\frac{\rho V_M}{B_M} = \text{const. along a streamline.} \qquad (A-5a)$$

The momentum equation can be written as

$$\rho \left(\nabla \left(\frac{1}{2} V^2 \right) - \vec{V} \times \vec{\Omega} \right) + \nabla P = \vec{J} \times \vec{B}, \qquad (A-6)$$

where $\vec{\Omega} \equiv \nabla \times \vec{V}$ is the vorticity of the flow field.

Since Ampere's law is $\mu_0 \vec{J} = \nabla \times \vec{B} = \nabla \times \vec{B}_M$, $\vec{J}$ has only an azimuthal component. Consequently, the rhs of (A-6) has no non-zero azimuthal component, and the azimuthal component of (A-6) reads simply

$$-(\vec{V} \times \vec{\Omega}) \cdot \hat{\theta} = 0, \qquad (A-7)$$

_____

[*] Because of the assumed axisymmetry, there is no need to distinguish between $\vec{V}$ and $\vec{V}_M$ in the mass-continuity equation.

where $\hat{\theta}$ is a unit vector in the azimuthal direction. But, $-(V \times \Omega) \cdot \hat{\theta} = r^{-1}(\vec{V} \cdot \nabla)(rV_\theta)$. Consequently, (A-7) becomes

$$(\vec{V} \cdot \nabla)(rV_\theta) = 0 \qquad (A-8)$$

so that (rV_θ) is constant along a streamline. If we suppose that the plasma at the nozzle inlet is generated without rotation in the reservoir, then (A-8) implies

$$V_\theta \equiv 0 \qquad (A-9)$$

at every point in the flow field. Thus, $\vec{V}_M \equiv \vec{V}$.

We note in passing that, with $B_\theta \equiv 0$ and $V_\theta \equiv 0$, the azimuthal component of the curl of Ohm's law, $\nabla \times (\vec{V} \times \vec{B}) = 0$ is satisfied identically.

We now proceed to derive the Bernoulli equation from (A-6). We do this by taking the scalar product of (A-6) with $\rho^{-1}\vec{V}$. Since $\vec{V} = \vec{V}_M = \alpha\vec{B}_M$, and $\vec{B} \equiv \vec{B}_M$, the $(\vec{J} \times \vec{B})$ term on the rhs of (A-6) contributes nothing. Similarly, $\vec{V} \times \vec{\Omega}$ contributes nothing. Then $\rho^{-1}\vec{V} \cdot$ (A-6) reads

$$\vec{V} \cdot \nabla\left(\frac{1}{2}V^2\right) + \vec{V} \cdot \left(\frac{1}{\rho}\nabla P\right) = 0. \qquad (A-10)$$

(This equation appears formally the same as for the simple gas-dynamic nozzle because the magnetic field does not appear in it. However, the shape of the magnetic field lines has to be determined in a self-consistent manner with the flow field. That is, the $\vec{B}_M$ field cannot be taken as given.)

In ideal MHD, with no production or conduction of heat in the fluid, the flow is isentropic. This means that the pressure P and density ρ are related adiabatically along any streamline. Thus

$$P\rho^{-\gamma} = C_2 \qquad (A-11)$$

where C_2 is constant along a streamline, and γ is the adiabatic index. (To obtain concrete results, we shall choose $\gamma = 5/3$.)

Using (A-11), one can easily show that, along a streamline,

$$\vec{V} \cdot \left(\frac{1}{\rho}\nabla P\right) = \vec{V} \cdot \nabla\left(\frac{\gamma}{\gamma-1}\frac{P}{\rho}\right). \qquad (A-12)$$

Thus (A-10) becomes

$$\vec{V} \cdot \nabla\left(\frac{1}{2}V^2 + \frac{\gamma}{\gamma-1}\frac{P}{\rho}\right) = 0, \qquad (A-13)$$

which can be integrated along the streamline to give

$$\frac{1}{2}V^2 + \frac{\gamma}{\gamma-1}\frac{P}{\rho} = C_3 \qquad (A-14)$$

where C_3 is a constant along any streamline. Eq. (A-14) constitutes Bernoulli's law for the meridional magnetic nozzle. It demonstrates that the exhaust velocity that produces

the thrust is obtained at the expense of the thermal energy stored in the reservoir plasma. (The pressure term above is actually the enthalpy per unit mass, that is, $[\rho^{-1}\frac{P}{\gamma-1} + \rho^{-1}P]$, which represents the convected thermal energy per particle in plasma plus the work done per particle in volumetric changes of plasma.)

To complete our discussion of the meridional magnetic nozzle, we shall make use of the continuity and Bernoulli equations to obtain results for the flow velocity in the throat of the nozzle, for the thrust produced by the nozzle, and for the power required to produce that thrust, all in terms of given plasma parameters and the nozzle throat cross-sectional area.

For simplicity, let us consider a very thin (quasi-1D) tube of flow, of radius $r(z)$, containing the central streamline along the axis of symmetry, in which the z-coordinate represents distance along this particular streamline. The surface of this tube is assumed to be constituted of neighboring streamlines. Since $V_r = 0$ on the axis of symmetry, V_r will be very small throughout this thin central tube, so we shall set $V \approx V_z$. Then, by writing the mass continuity equation, $\nabla \cdot (\rho V) = 0$, in its integral form over this tube of flow, $\rho V_z \pi r^2 = \text{const.}$, and differentiating this result with respect to the z coordinate, it is easy to show that the following differential relation holds along the thin central tube.

$$\frac{1}{\rho}\left(\frac{d\rho}{dz}\right) + \frac{1}{V_z}\left(\frac{dV_z}{dz}\right) + \frac{2}{r}\left(\frac{dr}{dz}\right) = 0 \qquad (A-15)$$

Similarly, by differentiating the Bernoulli equation (A-14) with respect to Z, it is easily shown that

$$V_z\left(\frac{dV_z}{dz}\right) + \frac{C_s^2}{\rho}\left(\frac{d\rho}{dz}\right) = 0 \qquad (A-16)$$

where $C_s \equiv (\gamma P/\rho)^{1/2}$ constitutes the local speed of sound in the plasma. Then, by substituting for $\frac{1}{\rho}(\frac{d\rho}{dz})$ from Eq. (A-15), we can write Eq. (A-16) as follows.

$$\left(\frac{V_z^2}{C_s^2} - 1\right)\frac{1}{V_z}\left(\frac{dV_z}{dz}\right) = \frac{2}{r}\left(\frac{dr}{dz}\right). \qquad (A-17)$$

This fundamental relation provides insight into the local ratio of flow speed to sound speed in terms of the convergence or divergence of the streamlines. Eqs. (A-15, A-17) are known as the Hugoniot equations. Since $V_z > 0$ and $(dV_z/dz) > 0$ in the simplest picture of accelerated flow, we see from (A-17) that in the converging portion of the flow where $(dr/dz) < 0$, we must have $V_z^2 < C_s^2$. Conversely, in the diverging portion of the flow, $(dr/dz) > 0$ and $V_z^2 > C_s^2$. The throat of the nozzle is defined to be located where $(dr/dz) = 0$, and since the flow is accelerating axially even at this point, we must have $V_z^2 = C_s^2$ at the throat.

$$V_{z0}^2 = C_{s0}^2; \quad \text{(throat)}. \qquad (A-18)$$

This result is easily generalized for off-axis flux tubes.

By using result (A-17) back in (A-15), we find

$$\frac{1}{\rho}\left(\frac{d\rho}{dz}\right) + \frac{(V_z^2/C_s^2)}{(V_z^2/C_s^2)-1}\frac{2}{r}\left(\frac{dr}{dz}\right) = 0 \qquad (A-17a)$$

From the result derived above in (A-17), we found that, in accelerating flow, $\left(\frac{V^2}{C_s^2} - 1\right)$ always has the same sign as $\frac{dr}{dz}$. Therefore, the density ρ always decreases along the meridional magnetic nozzle, $(d\rho/dz) < 0$.

The fundamental result (A-18) allows a convenient expression to be obtained for the thrust of the meridional magnetic nozzle in terms of the plasma pressure in the throat (or in the reservoir) and the area of the throat. For these approximate estimates, the quasi-1D model of the nozzle will be invoked for simplicity and convenience.

The thrust acting upon the rocket in a steady state is given by

$$\mathbf{T} = \left(\frac{dM}{dt}\right) V_e \qquad (A-19)$$

where V_e is the exhaust velocity of plasma and (dM/dt) is the rate of loss of plasma mass from the rocket. In the quasi-1D approximation, one can write

$$\frac{dM}{dt} \approx \rho_0 V_0 A_0, \qquad (A-20)$$

where ρ_0 and V_0 are the density and velocity of plasma in the throat of the nozzle, and A_0 is the area of the throat. Now, if we accept $\gamma = 5/3$, then the Bernoulli law (A-14) can be written

$$\frac{1}{2} V^2 + \frac{3}{2} C_s^2 = \text{const.},$$

where $C_s^2 \equiv (\gamma P/\rho)$. From this Bernoulli relation and Eq. (A-18), one finds immediately that

$$V_0^2 = C_{S0}^2 = \frac{3}{4} C_{SR}^2 = \frac{1}{4} V_e^2, \qquad (A-21)$$

where C_{SR} represents the value of C_S back in the reservoir. Here, we have assumed a condition of zero pressure at the nozzle exit, so that $C_{ne} = 0$, and a condition of very low flow speed out of the reservoir, $V_R^2 \ll C_{SR}^2$.

Moreover, since the adiabatic relation between a change of P and a change of ρ is maintained (in ideal MHD) along the axial direction (in the quasi-1D approximation), one can relate the density and pressure of plasma in the throat to the density and pressure in the reservoir. Using this adiabatic relation and (A-21) we find

$$\frac{P_0}{\rho_0^\gamma} = \frac{P_R}{\rho_R^\gamma}, \quad \text{or}$$

$$\left(\frac{\rho_0}{\rho_R}\right)^{\gamma-1} = \frac{C_{S0}^2}{C_{SR}^2} = \frac{3}{4},$$

or,

$$\frac{\rho_0}{\rho_R} = \left(\frac{3}{4}\right)^{3/2} \approx 0.65 \approx 2/3. \qquad (A-22)$$

From this, and again from (A-21), it follows that

$$\frac{P_0}{P_R} = \frac{\rho_0 C_{S0}^2}{\rho_R C_{SR}^2} \approx \left(\frac{2}{3}\right) \times \left(\frac{3}{4}\right) \approx \frac{1}{2}. \qquad (A-23)$$

Thus, in the throat, the density has dropped to 2/3 of its input value, the pressure has dropped to half of its input value, and the temperature has dropped to 3/4 of its input value.

The thrust, from (A-19) and (A-20) may, therefore, be expressed as

$$\mathbf{T} = (A_0 \rho_0 V_0) V_e = (A_0 \rho_0 C_{S0})(2C_{S0}) = A_0 \times (2\rho_0 C_{S0}^2) = A_0 \times (2\gamma P_0),$$

or

$$\mathbf{T} = \frac{10}{3}(A_0 P_0) \approx \frac{5}{3}(A_0 P_R) \qquad (A-24)$$

for $\gamma = 5/3$. Thus, in the meridional magnetic nozzle, the thrust is a numerical factor times the plasma pressure times the throat area.

It is important to know the strength of the power source that is required to produce a given value of thrust. The required power may be found from the power expelled by the flowing plasma. Neglecting inefficiencies due to thermal conduction, radiation, viscosity, resistivity, and rotation, the expelled power in the exhaust is

$$\mathbf{P} = \left(A \times \frac{1}{2}\rho V^3\right)_e \qquad (A-25)$$

where the subscript "e" refers to downstream asymptotic values at the "exit." But, in steady state, $(A\rho V)_e = (A\rho V)_0$. Hence

$$\mathbf{P} = \frac{1}{2} A_0 \rho_0 V_0 V_e^2 = \frac{1}{2}\left(\frac{dM}{dt}\right) V_e^2, \qquad (A-26)$$

or, from (A-19),

$$\mathbf{P} = \frac{1}{2}\mathbf{T} V_e \qquad (A-26a)$$

With $\gamma = 5/3$, this becomes, in terms of throat values,

$$\mathbf{P} = \frac{10}{3}(A_0 P_0 C_{S0}) = \mathbf{T} C_{S0} = \left(\frac{10\sqrt{5}}{3\sqrt{3}}\right) A_0 \left(\frac{P_0^{3/2}}{\rho_0^{1/2}}\right), \qquad (A-26b)$$

where $C_{S0} = \left(\frac{10}{3}\frac{T_0}{m_i}\right)^{1/2}$, with T_0 being the plasma temperature in throat of the nozzle, and m_i the ion mass. Here, we have used (A-24) for $\mathbf{T}$ and (A-21) for V_e.

In terms of reservoir values, the power can also be written as

$$\mathbf{P} = \frac{5}{2\sqrt{3}}(A_0 P_R C_{SR}) = \left(\frac{5\sqrt{5}}{6}\right) A_0 \left(\frac{P_R^{3/2}}{\rho_R^{1/2}}\right). \qquad (A-26c)$$

To summarize the results for the meridional magnetic nozzle, Eq. (A-21) relates flow speeds to sound speeds, Eq. (A-24) gives the thrust, and Eq. (A-26) gives the required power. It is important to qualify this result for the thrust with the observation that it is contingent upon overcoming the "detachment problem." This critical problem is addressed in Sec. I-C.

APPENDIX B
THE AZIMUTHAL MAGNETIC NOZZLE

We turn now to the case of an azimuthal magnetic nozzle, where the meridional magnetic field vanishes, $B_M \equiv 0$. We shall always assume steady axisymmetric flow. This configuration contains only meridional currents.

The azimuthal component of Ohm's law, Eq. (A-1a), is satisfied identically now, so Eq. (A-2) no longer applies.

Since $\hat{\theta} \cdot (\vec{J} \times \vec{B}) = 0$ just as for the meridional nozzle, the azimuthal component of the momentum equation, (A-6), reduces to

$$-(\vec{V} \times \vec{\Omega}) \cdot \hat{\theta} = 0,$$

just as before. Here $\vec{\Omega} \equiv \nabla \times \vec{V}$. This result can therefore be written as

$$(\vec{V} \cdot \nabla)(rV_\theta) = 0$$

so that

$$(rV_\theta) = \text{const.}$$

along any streamline. We shall assume that the plasma is generated without rotation. Consequently, V_θ vanishes along all streamlines,

$$V_\theta = 0. \tag{$B-1$}$$

Next, let us consider the curl of Ohm's law,

$$\nabla \times (\vec{V} \times \vec{B}) = 0$$

This can be written as

$$-\vec{B}\nabla \cdot \vec{V} + \vec{B} \cdot \nabla \vec{V} - \vec{V} \cdot \nabla \vec{B} = 0. \tag{$B-2$}$$

From the continuity equation, the first term in (B-2) can be written as

$$-\vec{B}\nabla \cdot \vec{V} = \frac{\vec{B}}{\rho}\left(\vec{V} \cdot \nabla\right)\rho = \hat{\theta}\frac{B_\theta}{\rho}\left(\vec{V} \cdot \nabla\right)\rho$$

The second term in (B-2) can be written as

$$(\vec{B} \cdot \nabla)\vec{V} = (\vec{B}_\theta \cdot \nabla)\vec{V}_M = \frac{B_\theta}{r}V_r\frac{\partial \hat{r}}{\partial \theta} = \frac{B_\theta V_r}{r}\hat{\theta},$$

where $\hat{r}$ and $\hat{\theta}$ are unit vectors in the r and θ directions respectively. The third term in (B-2) can be written as

$$-(\vec{V}\cdot\nabla)\vec{B} = -(\vec{V}_M\cdot\nabla)(\hat{\theta}B_\theta) = -\hat{\theta}(\vec{V}\cdot\nabla)B_\theta$$

The sum of these three terms converts Eq. (B-2) to the following,

$$\frac{B_\theta}{\rho}(\vec{V}\cdot\nabla)\rho - \vec{V}\cdot\nabla B_\theta + \frac{B_\theta V_r}{r} = 0,$$

or, multiplying through by ρ,

$$(\rho B_\theta)\left(\frac{V_r}{r}\right) = \rho(\vec{V}\cdot\nabla)B_\theta - B_\theta(\vec{V}\cdot\nabla)\rho.$$

Finally, dividing through by ρ^2, one recognizes the rhs to be the derivative of a ratio, $\left(\frac{B_\theta}{\rho}\right)$. Thus,

$$\left(\frac{B_\theta}{\rho}\right)\left(\frac{V_r}{r}\right) = (\vec{V}\cdot\nabla)\left(\frac{B_\theta}{\rho}\right) \qquad (B-3)$$

Noting that

$$V_r \times \frac{1}{r} = V_r \frac{\partial}{\partial r}\ell n r = (\vec{V}\cdot\nabla)(\ell n r),$$

Eq. (B-3) can be transformed to the following,

$$(\vec{V}\cdot\nabla)\left[\ell n\left(\frac{B_\theta}{\rho}\right)\right] - (\vec{V}\cdot\nabla)[\ell n r] = 0,$$

or,

$$(\vec{V}\cdot\nabla)\left[\ell n\left(\frac{B_\theta}{r\rho}\right)\right] = 0.$$

The condition implied by this equation is that the quantity $(B_\theta/r\rho)$ is constant along a streamline.

$$\left(\frac{B_\theta}{r\rho}\right) = C_\theta = \text{const. along streamline.} \qquad (B-4)$$

At this point, we can begin to derive the Bernoulli equation for the azimuthal magnetic nozzle from the momentum equation (A-6). As before, we take the scalar product of $\rho^{-1}\vec{V}$ with (A-6). The resulting ℓhs is just as before, namely

$$\ell hs = (\vec{V}\cdot\nabla)\left(\frac{1}{2}V^2 + \frac{\gamma}{\gamma-1}\frac{P}{\rho}\right), \qquad (B-5)$$

The rhs is as follows,

$$rhs = \frac{1}{\rho}\vec{V}\cdot\vec{J}\times\vec{B}$$

91

We aim to transform the "rhs" into an integrable form.

Noting that $J_\theta \equiv 0$ in the azimuthal magnetic nozzle, and invoking azimuthal symmetry and $V_\theta \equiv 0$, together with Ampere's law, $\mu_0 \vec{J} = \nabla \times \vec{B}$, a straightforward calculation of "rhs" shows that

$$rhs = \frac{1}{\rho}\vec{V}\cdot\vec{J}\times\vec{B} = -\left(\frac{B_\theta}{\mu_0\rho r}\right)(\vec{V}\cdot\nabla)(rB_\theta).$$

But Eq. (B-4) states that $(B_\theta/\rho r)$ is constant along a streamline, so the above expression can immediately be written as follows.

$$rhs = -(\vec{V}\cdot\nabla)\left(\frac{B_\theta^2}{\mu_0\rho}\right) \qquad (B-6)$$

The differential form of the Bernoulli law is obtained by equating (B-5) and (B-6).

$$(\vec{V}\cdot\nabla)\left(\frac{1}{2}V^2 + \frac{\gamma}{\gamma-1}\frac{P}{\rho} + \frac{B_\theta^2}{\mu_0\rho}\right) = 0 \qquad (B-7)$$

Integrating along the streamline, we have the integral form of the "magnetic Bernoulli equation,"

$$\frac{1}{2}V^2 + \frac{\gamma}{\gamma-1}\frac{P}{\rho} + \frac{B_\theta^2}{\mu_0\rho} = C_4, \qquad (B-8)$$

or also,

$$\frac{1}{2}V^2 + \frac{1}{\gamma-1}C_S^2 + C_A^2 = C_4 \qquad (B-8a)$$

where C_4 is constant along the streamline, C_S is the local adiabatic sound speed, and C_A is the local Alfvén speed.

From this Bernoulli law, one can immediately observe that in order for the $(J_r B_\theta)$ magnetic forces to accelerate the flow, it is necessary that the quantity (B_θ^2/ρ) decreases along the streamline. From the point of view of magnetic body forces, the $(J_r B_\theta)$ magnetic force from the diverging current field accelerates the plasma in the axial direction. The diverging currents (which require an outer coaxial electrode) imply, from Ampere's law, that B_θ decreases in the downstream direction.

To complete our discussion of the azimuthal magnetic nozzle, we shall derive the Hugoniot equations for this azimuthal magnetic configuration, and shall use them to estimate the flow speed, thrust, and power of a coaxial magnetic nozzle.

With a coaxial nozzle in mind, we consider a thin annular tube of flow of radius $r(z)$ and radial thickness $\Delta(z)$ with $\Delta \ll r$. In the quasi 1-d approximation, the mass continuity equation can be written in its integral form over this tube as

$$\rho V 2\pi r \Delta = \text{const.}, \qquad (B-9)$$

that is, the above quantity does not vary in the flow direction. Here, V is the meridional flow velocity along the tube. Differentiating (B-9) with respect to z, the axial coordinate, we find

$$\frac{1}{\rho}\left(\frac{d\rho}{dz}\right) + \frac{1}{V}\left(\frac{dV}{dz}\right) + \frac{1}{(r\Delta)}\left(\frac{d(r\Delta)}{dz}\right) = 0. \qquad (B-10)$$

Next, we differentiate the Bernoulli equation (B-8) with respect to z, using the adiabatic relation between P and ρ along a streamline, $P = \text{const.} \times \rho^\gamma$. The resulting equation is easily found to be

$$V\left(\frac{dV}{dz}\right) + C_S^2 \frac{1}{\rho}\left(\frac{d\rho}{dz}\right) + 2C_A^2 \frac{1}{B_\theta}\left(\frac{dB_\theta}{dz}\right) - C_A^2 \frac{1}{\rho}\left(\frac{d\rho}{dz}\right) = 0, \qquad (B-11)$$

where the local speed of sound C_S and the local Alfvén speed C_A are given respectively by

$$C_S^2 \equiv \gamma \frac{P}{\rho}, \quad \text{and}$$

$$C_A^2 \equiv \frac{B_\theta^2}{\mu_0 \rho}.$$

Now, by differentiating Eq. (B-4) with respect to z, one easily finds

$$\frac{1}{B_\theta}\left(\frac{dB_\theta}{dz}\right) = \frac{1}{r}\left(\frac{dr}{dz}\right) + \frac{1}{\rho}\left(\frac{d\rho}{dz}\right) \qquad (B-12)$$

Then, by using (B-12) in (B-11), the latter becomes

$$V\left(\frac{dV}{dz}\right) + S^2 \frac{1}{\rho}\left(\frac{d\rho}{dz}\right) + 2C_A^2 \frac{1}{r}\left(\frac{dr}{dz}\right) = 0 \qquad (B-13)$$

where S is the local value of the fast magnetosonic speed, given by

$$S^2 \equiv C_S^2 + C_A^2$$

The use of (B-10) in (B-13) then yields

$$(V^2 - S^2)\frac{1}{V}\left(\frac{dV}{dz}\right) = C_S^2\left[\frac{1}{\Delta}\left(\frac{d\Delta}{dz}\right) + \frac{1}{r}\left(\frac{dr}{dz}\right)\right]$$
$$+ C_A^2\left[\frac{1}{\Delta}\left(\frac{d\Delta}{dz}\right) - \frac{1}{r}\left(\frac{dr}{dz}\right)\right], \qquad (B-14)$$

or, also,

$$(V^2 - S^2)\frac{1}{V}\left(\frac{dV}{dz}\right) = C_S^2 \frac{1}{(r\Delta)}\left(\frac{d}{dz}(r\Delta)\right) + C_A^2 \frac{1}{(\Delta/r)}\left(\frac{d}{dz}(\Delta/r)\right). \qquad (B-14a)$$

Equations (B-10, 12, 14) are the Hugoniot equations for the azimuthal magnetic nozzle.

At this point, it will be useful to distinguish two different geometrical versions of the coaxial azimuthal nozzle, namely,

    i. Proportional Radius, Variable thickness.
    ii. Variable Radius, Constant thickness.

(The practical difficulty is to find the right shapes so that the inner and outer boundaries constitute equipotential surfaces of electrodes. This constitutes a serious computational problem that we do not address in this report.)

Case i: $r(z) = r_0$, fixed. Thickness varies. For fixed radius of a flow tube of variable thickness, Eq. (B-14) reads

$$\left(\frac{V^2}{S^2} - 1\right)\frac{1}{V}\left(\frac{dV}{dz}\right) = \frac{1}{\Delta}\left(\frac{d\Delta}{dz}\right). \qquad (B-15)$$

Thus, for plasma to accelerate along the annular tube of flow, the channel width should be convergent ($\frac{d\Delta}{dz} < 0$) for $V^2 < S^2$, and divergent ($d\Delta/dz > 0$) for $V^2 > S^2$. At the throat itself, $V_0^2 = S_0^2$ and $(d\Delta/dz)_0 = 0$. Thus, there is a strong similarity here to the cases of gas-dynamic and meridional magnetic nozzles. The adiabatic sound speed is simply replaced by the fast magnetosonic velocity, but the constricted (annular) throat is conventional.

Substitution of Eq. (B-15) back into (B-10) yields

$$\frac{1}{\rho}\left(\frac{d\rho}{dz}\right) + \frac{(V^2/S^2)}{(V^2/S^2) - 1}\frac{1}{\Delta}\left(\frac{d\Delta}{dz}\right) = 0. \qquad (B-15a)$$

From what has been stated above, this equation demonstrates that, for a flow accelerating along the annular tube, the density $\rho(z)$ always decreases monotonically along the tube.

Case ii. $\Delta_z = \Delta_0$, fixed. Radius varies. Now Eq. (B-14) reads

$$(V^2 - S^2)\frac{1}{V}\left(\frac{dV}{dz}\right) = (C_S^2 - C_A^2)\frac{1}{r}\left(\frac{dr}{dz}\right). \qquad (B-16)$$

For fixed annular thickness of variable radius, we discern the possibility of "anomalous" behavior when $C_S^2 < C_A^2$.

For $C_S^2 \gg C_A^2$ (high-beta plasma), we see that acceleration of the plasma along the tube requires convergence ($\frac{dr}{dz} < 0$) when $V^2 < S^2$ and divergence ($\frac{dr}{dz} > 0$) when $V^2 > S^2$. At the throat, $V_0^2 = S_0^2$ with $(\frac{dr}{dz})_0 = 0$. Therefore, in the high-beta case, the throat appears to be "ordinary."

For $C_S^2 \ll C_A^2$ (cold plasma or low-beta plasma), we see that acceleration of plasma along the tube requires divergence when $V^2 < S^2$ and convergence when $V^2 > S^2$. Again, at the "throat," $V_0^2 = S_0^2$ with $(\frac{dr}{dz})_0 = 0$. Therefore, in the low-beta case, the throat appears to be anomalous. One could call it an "anti-throat."

Substitution of (B-16) back into (B-10) yields

$$\frac{1}{\rho}\left(\frac{d\rho}{dz}\right) + \frac{V^2 - 2C_A^2}{V^2 - S^2}\frac{1}{r}\left(\frac{dr}{dz}\right) = 0. \qquad (B-16a)$$

In the case of small magnetic field (negligible C_A), one finds from this that the density $\rho(z)$ decreases monotonically along the tube showing "ordinary" behavior.

In the case of cold plasma in strong magnetic field, the equation becomes (with $S^2 \approx C_A^2$),

$$\frac{1}{\rho}\left(\frac{d\rho}{dz}\right) + \frac{V^2 - 2C_A^2}{V^2 - C_A^2}\frac{1}{r}\left(\frac{dr}{dz}\right) = 0. \qquad (B - 16b)$$

From the preceeding remarks about Eq. (B-16), one reaches the following conclusions about the behavior of the density of cold plasma in a strong azimuthal field in a tube of constant annular thickness, by examining Eq. (B-16-b).

For $V^2 < C_A^2$, $\rho(z)$ decreases along the tube. (**Divergent radius**).
For $C_A^2 < V^2 < 2C_A^2$, $\rho(z)$ still decreases along the tube. (**Convergent radius**).
For $V^2 > 2C_A^2$, $\rho(z)$ increases along the tube. (**Convergent radius**).

Finally, we obtain expressions for the thrust and power from these azimuthal magnetic nozzles. For simplicity, we shall here assume cold plasma (hot enough to be highly conducting, but cold enough so that $C_S^2 \ll C_A^2$ everywhere). However, Appendix D will lead us to the conclusion that the neglected thermal contribution is about equal to the magnetic contribution, and has the same scaling as the magnetic contribution because $\beta \approx 1$. Consequently, the following formulas should be viewed as giving the correct scaling but an underestimate of the magnitudes (by about a factor of 2).

i) **Thrust and Power for the Annular Azimuthal Magnetic Nozzle of Constant Radius:**
Basic to this discussion is the Bernoulli law, Eq. (B-8-a). For cold plasma, it reads

$$\frac{1}{2}V^2 + C_A^2 = C_4 = \text{constant along the annular tube.}$$

Evaluating this equation at the nozzle receiver or reservoir end (R), at the throat (0), and at the nozzle exit end (e), we have

$$C_{AR}^2 = \frac{1}{2}V_0^2 + C_{A0}^2 = \frac{3}{2}C_{A0}^2 = \frac{1}{2}V_e^2, \qquad (B - 17)$$

in which we have set $V_0^2 = C_{A0}^2$ at the throat in accordance with Eq. (B-15), with $S^2 = C_S^2 + C_A^2 \approx C_A^2$. From (B-17), it follows that

$$C_{A0}^2 = \frac{2}{3}C_{AR}^2. \qquad (B - 18)$$

But, from Eq. (B-4), for the constant-radius annulus, we have the following relation along the tube.

$$B_\theta = \text{const.} \times \rho \qquad (B - 19)$$

Since $C_A^2 \equiv B_\theta^2/(\mu_0\rho)$, Eqs. (B-18) and (B-19) together imply that

$$\rho_0 = \frac{2}{3}\rho_R, \qquad (B - 20a)$$

and,

$$B_{\theta 0} = \frac{2}{3} B_{\theta R}. \qquad (B-20b)$$

Thus, both the mass density and the flux density at the throat have dropped to $\frac{2}{3}$ of their input values. To evaluate the thrust, we write, using (B-17) and (B-15),

$$
\begin{aligned}
\mathbf{T} &= \left(\frac{dM}{dt}\right) V_e \\
&= (\rho_0 V_0 A_0) V_e = (\rho_0 C_{A0})(\sqrt{3} C_{A0}) A_0 \\
&= \sqrt{3}(\rho_0 C_{A0}^2) A_0 = \sqrt{3} \frac{B_{\theta 0}^2}{\mu_0} A_0 \\
&= \left(\sqrt{3}\frac{4}{9}\right)\left(\frac{B_{\theta R}^2}{\mu_0}\right) A_0, \qquad (B-21)
\end{aligned}
$$

where $A_0 = 2\pi r_0 \Delta_0$ is the area of the annular throat of the nozzle, and in which Eq. (B-20-b) was invoked at the last step. But $B_{\theta R}$ is related to I, the input (gun) current applied to the electrodes, by Ampere's law, namely,

$$B_{\theta R} = \frac{\mu_0 I}{2\pi r_0}. \qquad (B-22)$$

Substitution of (B-22) into (B-21) yields (with $A_0 = 2\pi r_0 \Delta_0$),

$$\mathbf{T} = \left(\frac{2\sqrt{3}}{9\pi}\right)(\mu_0 I^2)\left(\frac{\Delta_0}{r_0}\right). \qquad (B-23)$$

We therefore find that the annular azimuthal nozzle of constant radius (variable thickness), using a cold-plasma as the working fluid, produces a thrust which depends only upon the square of the current and on the ratio of nozzle thickness to radius at the throat. Neither the plasma density nor any nozzle dimension by itself has any individual effect on the thrust.

To evaluate the power expelled by the nozzle, we write

$$\mathbf{P} = (\tfrac{1}{2}\rho V^3 A)_e = (\rho V A)_e(\tfrac{1}{2} V_e^2) = (\rho V A)_0(\tfrac{1}{2} V_e^2) = \frac{1}{2}\left(\frac{dM}{dt}\right) V_e^2. \qquad (B-24)$$

Since the thrust is $\mathbf{T} = (dM/dt) V_e$, the power can be written as

$$\mathbf{P} = \frac{1}{2}\mathbf{T} V_e. \qquad (B-25)$$

From (B-17), and Ampere's law,

$$V_e = \sqrt{2} C_{AR} = \frac{\sqrt{2} B_{\theta r}}{\mu_0^{1/2} \rho_R^{1/2}} = \frac{2^{1/2}}{\mu_0^{1/2} \rho_R^{1/2}} \frac{\mu_0 I}{2\pi r_0}. \qquad (B-26)$$

106

Using (B-23) for **T** and (B-26) for V_e, the power expressed by (B-25) becomes

$$\mathbf{P} = \left(\sqrt{\frac{3}{2}}\frac{1}{9\pi^2}\right)\mu_0^{3/2}\left(\frac{I^3}{\rho_R^{1/2}r_0}\right)\left(\frac{\Delta_0}{r_0}\right). \qquad (B-27)$$

Comparing Eq. (B-23) and (B-27), we see that the power requirement for a given thrust can be reduced simply by increasing r_0, the annulus radius, for fixed current and fixed (Δ_0/r_0).

The current-voltage relation for this type of annular azimuthal magnetic nozzle (fixed radius, variable thickness) can be obtained simply by recognizing that the expelled power can only come from the electrical power applied across the inner and outer electrodes.

$$\mathbf{P} = I\mathbf{V} \qquad (B-28)$$

Here **V** is the voltage applied across the electrodes. Equating (B-27) and (B-28), we have the following I, **V** relation.

$$\mathbf{V} = \left(\sqrt{\frac{3}{2}}\frac{1}{9\pi^2}\right)\mu_0^{3/2}\left(\frac{I^2}{\rho_R^{1/2}r_0}\right)\left(\frac{\Delta_0}{r_0}\right). \qquad (B-29)$$

Therefore, the nozzle electrical impedance is nonlinear and is proportional to current.

ii) Thrust and Power for the Annular Azimuthal Magnetic Nozzle of Constant Thickness: At the anti-throat where $dr/dz = 0$, we have shown that

$$V_0^2 = C_{A0}^2$$

given the cold plasma model. Moreover, from the Bernoulli equation (B-8a), we still have the following relations connecting the reservoir, throat, and exit points along the flow tube.

$$C_{A0}^2 = \frac{2}{3}C_{AR}^2$$

$$V_e^2 = 3C_{A0}^2 = 2C_{AR}^2.$$

Noting Eq. (B-4), that $B_\theta = \text{const.}\ r\rho$ along the flow tube, it can then be shown that

$$\frac{2}{3} = \frac{r_0^2\rho_0}{r_R^2\rho_R} = \frac{B_{\theta0}r_0}{B_{\theta R}r_R}.$$

Using the above relations, with $C_A^2 \equiv B_\theta^2/(\mu_0\rho)$, it is easy to show that the thrust is

$$\mathbf{T} = \left(\frac{dM}{dt}\right)V_e = \left(\frac{2\sqrt{3}}{9\pi}\right)\left(\frac{\Delta_0}{r_0}\right)(\mu_0 I^2), \qquad (B-30)$$

which is exactly the same as for the constant radius nozzle. Similarly, one can show that the required power is

$$\mathbf{P} = \frac{1}{2}\left(\frac{dM}{dt}\right)V_e^2 = \frac{1}{2}V_e\mathbf{T} = \left(\sqrt{\frac{3}{2}}\frac{1}{9\pi^2}\right)\left(\frac{\Delta_0}{r_0}\right)\left(\frac{\mu_0^{3/2}I^3}{\rho_R^{1/2}r_0}\right)\left(\frac{r_0}{r_R}\right). \qquad (B-31)$$

Comparing this with (B-27), we find that the power usage in the constant-thickness channel of variable radius is larger by (r_0/r_R) than that of the constant radius, variable-thickness channel.

APPENDIX C
COMPARISON OF PULSED AND
STEADY-STATE SYSTEMS

Because steady-state burns need to have their exhaust velocities near the vehicle velocity increment of the mission (ΔV) in order to realize substantial payload mass fractions without excessive power consumption, one is forced to consider plasmas with temperatures in the few eV range $(\Delta V \sim 10^6\ cm/s)$. In this case, the plasma conductivity does not produce a very tight coupling of the plasma and the magnetic fields, for either kind of magnetic nozzle.

However, it is possible at present to produce far hotter (or more energetic) plasmas (several hundred eV) in short pulses (theta pinch plasmas for meridional magnetic nozzles, and plasmas from pulsed coaxial plasma guns for azimuthal magnetic nozzles). The higher conductivities generated in such plasmas engender a more efficient coupling of the plasma to the magnetic fields. This consideration, as well as the higher payload obtainable with the use of hot plasmas, motivates the present comparison of the steady burn of a low temperature plasma with an alternative burn composed of many short pulses of hot plasma.

In making such a comparison meaningful, certain features need to be maintained the same in the two approaches. Therefore, we shall require that both approaches must produce the same velocity increment of the vehicle, and both approaches must operate with the same time-average power. The latter requirement reflects a general concern that because the instantaneous power depends upon the cube of the exhaust velocity, hot plasmas will be too demanding of presently conceivable power sources. These two conditions prove sufficient to determine the relative fuel mass utilization, burn time, energy store, and duty fraction of the hot pulsed plasma system.

For the repetitively pulsed approach, the total velocity increment, ΔV, is the sum of the increments produced in each pulse, that is

$$\Delta V = \sum_{i=1}^{i_f}(\Delta V)_i = \sum_{i=1}^{i_f}V_{e,p}\ln\frac{M_i}{\Delta_i}, \qquad (C-1)$$

where $V_{e,p}$ is the exhaust velocity of the pulsed plasma, M_i is the total mass of the vehicle after the ith pulse, and i_f is the number of pulses needed to produce the change of velocity

ΔV. The solution of the rocket equation was invoked in writing down Eq. (C-1). But this obviously leads to the result that

$$\Delta V = V_{e,p}\ell n\frac{M_0}{M_{\ell_f}} = V_{e,p}\ell n\frac{M_i}{M_{f,p}}, \qquad (C-2)$$

where M_i is the initial total mass of the vehicle and $M_{f,p}$ is the final total mass of the vehicle in the pulsed approach to the mission.

For the steady burn approach, we have

$$\Delta V = V_{e,s}\ell n\frac{M_i}{M_{f,s}} \qquad (C-3)$$

where $V_{e,s}$ is the exhaust velocity of the steady-state plasma, and $M_{f,s}$ is the final total mass of the vehicle in the steady-burn approach to the mission.

Since ΔV is assumed to be the same for both approaches, we can equate (C-2) and (C-3). The result can be expressed as follows.

$$\frac{M_i}{M_{f,p}} = \left(\frac{M_i}{M_{f,s}}\right)^{\sqrt{\frac{T_s}{T_p}}} \qquad (C-4)$$

Here, T_s and T_p are respectively the reservoir (pre-nozzle) temperatures of the steady and pulsed plasmas, and we have invoked the relation between exhaust velocities and pre-nozzle temperatures.

As an example, suppose that $\frac{M_i}{M_{f,s}} = 2$, and $\frac{T_s}{T_p} = 10^{-2}$. Then $\frac{M_i}{M_{f,p}} = 1.07$.

In this case, the steady burn was hypothesized to burn up 50% of the initial mass, but the pulsed approach correspondingly burned up only 6.5% of the initial mass. This effect is due to the hypothesized high temperature of the pulsed plasma. Thus, the pulsed hot plasma approach displays very efficient utilization of fuel mass.

What does the requirement of equal time-average powers imply about the relations between the operational burn times of the two approaches, $(\Delta t)_p$ and $(\Delta t)_s$; and what does it imply for the duty fraction of the repetitive pulses?

To answer these questions we write down the statement of equal time-average powers as

$$\frac{1}{2}(\dot{M})_s V_{e,s}^2 = \frac{1}{2}(\dot{M})_p V_{e,p}^2. \qquad (C-5)$$

Here, we have used the fact that the time-average of any instantaneous rate, $\dot{Q}$, is given by

$$\langle\dot{Q}\rangle = \dot{Q}\frac{\tau_{on}}{\tau} = \frac{\Delta Q}{\Delta t} = \frac{Q_i - Q_f}{\Delta t} \qquad (C-6)$$

where ΔQ is the amount of Q transferred during time Δt, and where (τ_{on}/τ) is the duty factor (the ratio of the "on" time to the total time $\tau = \tau_{on} + \tau_{off}$). Thus, the time-average power can be written as $(0.5\dot{M}V_{e,p}^2)\frac{\tau_{on}}{\tau} = 0.5(\dot{M})V_{e,p}^2$.

Replacing the exhaust velocities by their temperature equivalents, and again noting Eq. (C-6), we can write (C-5) as

$$\frac{M_i - M_{f,s}}{(\Delta t)_s} \frac{(\Delta t)_p}{M_i - M_{f,p}} = \frac{T_p}{T_s}. \qquad (C-7)$$

Noting (C-4), we can re-write (C-7) as follows.

$$\frac{(\Delta t)_p}{(\Delta t)_s} = \frac{T_p}{T_s} \frac{1 - \left(\frac{M_{f,s}}{M_i}\right)^{\sqrt{\frac{T_s}{T_p}}}}{1 - \frac{M_{f,s}}{M_i}} \qquad (C-8)$$

Again, as an example, consider $T_p = 100\ T_s$ and $M_{f,s} = 0.5\ M_i$. One finds $\frac{(\Delta t)_p}{(\Delta t)_s} = 13.4$. Thus, the operational burn time becomes somewhat longer in the repetitive-pulsed scheme. This is a simple consequence of the requirement that the time-average power remain small in the pulsed scheme. Note that the dilation of the burn time goes essentially as $\sqrt{T_p/T_s}$.

What about the required duty factor of the pulsed system? Returning to Eq. (C-5), we write it as

$$\frac{\dot{M}_s}{\dot{M}_p} \frac{T_s}{T_p} = \frac{\tau_{on}}{\tau} \qquad (C-9)$$

where $\dot{M}_p$ is the instantaneous mass flow rate during a pulse. But, for equal densities and equal areas, for example in the throats of the nozzles, this expression reduces to

$$\left(\frac{T_s}{T_p}\right)^{3/2} = \frac{\tau_{on}}{\tau}. \qquad (C-10)$$

Clearly, expression (C-10) is easily generalized to accommodate different densities and nozzle areas in the two schemes. Thus, if $T_p = 100\ T_s$ for the ratio of temperatures of pulsed and steady plasmas, then we have $\frac{\tau_{on}}{\tau} = 0.001$ for the duty factor. In this case, a millisecond pulse would be repeated once each second until the required ΔV is attained. For example, it has been demonstrated that theta pinch lifetimes from endloss are a few times the axial thermal transit time and are insensitive to the plasma beta and to the degree of collisionality.[16] Thus, a 100 meter theta pinch with a hydrogen plasma temperature of 100 eV would last for about one ms, if it were stabilized against "bad-curvature" instabilities associated with end effects. (Of course, one would either have to bend the pinch into a "U" shape, or else use a conical theta pinch.) Other kinds of hot pulsed plasmas could also be considered as the propelling plasma fuel, in the class known as compact tori (Field-reversed Configurations[6] and Spheromaks[17]).

In the foregoing discussion, it has been assumed for simplicity that the initial total mass of the vehicle is the same for the steady-state and pulsed schemes, even though the power sources and ancillary equipment will be quite different in the two cases. However, it is simple to generalize for different initial masses, $M_{i,s}$ and $M_{i,p}$. Now, Eq. (C-4) is replaced by

$$\frac{M_{i,p}}{M_{f,p}} = \left(\frac{M_{i,s}}{M_{f,s}}\right)^{\sqrt{T_s/T_p}}.$$

For example, with $T_p = 100T_s$ and $M_{i,s} = 2M_{f,s}$, the result that $(M_{i,p}/M_{f,p}) = 1.07$ still represents a tremendous improvement in mass utilization even though $M_{i,p}$ may be somewhat heavier than $M_{i,s}$. Looking further, we find that Eq. (C-8) is replaced by

$$\frac{(\Delta t)_p}{(\Delta t)_s} = \left(\frac{M_{i,p}}{M_{i,s}}\right)\left(\frac{T_p}{T_s}\right)\frac{1 - \left(\frac{M_{f,s}}{M_{i,s}}\right)^{\sqrt{T_s/T_p}}}{1 - \frac{M_{f,s}}{M_{i,s}}}.$$

Clearly, the nominal burn times, $(\Delta t)_p$ and $(\Delta t)_s$, will remain related essentially as before, for the example $T_p = 100T_s$ and $M_{i,s} = 2M_{f,s}$, provided that the initial total masses, $M_{i,p}$ and $M_{i,s}$, are at least comparable. Moreover, the required duty factor is still given by the relation (C-10), regardless of the initial masses.

In conclusion, the basic advantages and disadvantages of the repetitively pulsed burn scheme in comparison with the steady burn scheme may be summarized as follows. The pulsed hot plasma scheme affords far better fuel mass utilization, and far better coupling of plasma to magnetic fields in virtue of the higher plasma conductivity. However, the requirement of low time-average power utilization forces longer operational burn times for the pulsed system to achieve a given velocity increment, the burn time dilation factor being given roughly as $\sqrt{T_p/T_s}$. This longer operational burn time with the same time-average power utilization then implies that the initial on-board energy storage in the pulsed system must be larger by the same factor, $\sqrt{T_p/T_s}$, and it therefore puts a premium on the availability of high-energy-density storage (per unit volume and per unit mass). Moreover, other important issues arise, such as the reliability of repetitively pulsed, high-instantaneous-power systems; and the implications of longer burn times for the astrodynamic programming of the vehicle's mission.

APPENDIX D
ION HEATING PROCESSES IN AZIMUTHAL
MAGNETIC NOZZLES, AND THE ION BETA

For the meridional magnetic nozzle configuration, it has been assumed herein that the plasma reservoir is constructed and programmed in such a manner that the internal plasma pressure substantially balances the external magnetic pressure in the "radial" direction, and that this condition is at least approximately preserved downstream. If such an arrangement can be achieved, it constitutes the most efficient use of the applied magnetic field. In fact, experiments in magnetic fusion plasma physics have been carried out in which high-beta ($\beta \sim 1$) plasmas are routinely produced, such as in theta pinches, z-pinches, and field-reversed configurations. In virtue of their longitudinal magnetic fields, the first and the last of these (perhaps including modifications to improve configurational stability of the plasma) would naturally match onto the meridional magnetic nozzle. However, it is not obvious at first glance that the $\beta \sim 1$ condition also is to be expected in the orthogonal field example of coaxial plasma guns and the annular region of azimuthal magnetic nozzles.

We shall argue here that the $\beta \sim 1$ condition should indeed be expected for such devices, under ideal conditions. (Of course, the β-value is subject to reductions downstream from transport and radiation losses.)

The argument is as follows. In coaxial plasma guns and azimuthal magnetic nozzles, unlike the meridional nozzle-reservoir concept, a pre-existing reservoir of separately prepared hot plasma is not actually present. Instead, cold neutral gas is "continually" introduced into the tube during a "shot" or a "run", whereupon it is ionized (by plasma already there) and suddenly picked up by the applied fields and by Coulomb collisions with already-flowing plasma. For the case of short Coulomb-collision mean-free paths, one can draw an analogy to the situation of dropping sand on a conveyor belt. Newly-ionized ions suddenly appear (from neutrals "at rest"), and this introduction of added mass into the dynamical system corresponds to the appearance of sand dropped on the conveyor belt. Now, it is easy to show that the external forces maintaining the flow velocity (of sand or plasma) are, in fact, providing both macroscopic flow energy and heat energy (to the sand or plasma) at equal rates. Consequently, in the absence of losses, one finds that an initially cold, plasma-fluid element (in which ion mass continually becomes entrained) will have its flow energy and thermal energy about the same, $\frac{1}{2}\rho V^2 \approx \frac{P}{\gamma-1}$, at any later time. Since the flow energy corresponds to a characteristic flow velocity-squared given by $V^2 \approx C_A^2 + C_S^2$ near the throat of the azimuthal magnetic nozzle (see Appendix B)*, where $C_A^2 = B^2/(\mu_0\rho)$ and $C_S^2 = \gamma P/\rho$ are the squares of the Alfvén and sound speeds respectively, one immediately finds from $\frac{1}{2}\rho V^2 \approx \frac{P}{\gamma-1}$ that $\beta = 1.5$ for $\gamma = 5/3$. (We defined a local beta here by $\beta \equiv P/(B^2/2\mu_0)$.) Thus, $\beta \approx 1$ is a reasonable relation to use when considering collisional plasmas in azimuthal magnetic nozzles. Also, in the case of coaxial plasma guns, one can argue that the magnetic field drives plasmas at or near the Alfvén speed, leading again to the conclusion that $\beta \approx 1$.

For a plasma having long collisional mean free paths, $\lambda > r_{ci}$, the "β" argument for the azimuthal magnetic nozzle is different in detail from that given above, but the end result is essentially the same. For plasma ions of low collisionality, the argument is based upon the smallness of the ion gyro-radius in comparison with all nozzle dimensions, $r_{ci} \ll L$. Table 1.5 shows that this is probably a reasonable assumption for all but the lowest ion densities ($n = 10^{13}$ cm^{-3}). In such a case, one can show that the ion fluid axial velocity in steady flow is basically the sum of the (E_r/B_θ) drift velocity of the guiding centers of the ions, and the diamagnetic flow velocity associated with radial ion pressure gradients, $-\frac{1}{neB_\theta}\frac{\partial P_i}{\partial r}$. Here B_θ is the azimuthal magnetic field, and E_r is the radial electric field (or its generalization to axisymmetric configurations). The latter velocity arises from incomplete cancellation of neighboring ion gyro-orbits in the presence of radial non-uniformities of ion pressure. For the purpose of a simple plausibility argument, we shall now consider a plasma free of transverse non-uniformities. Then, the guiding-center drift velocity of the ions, $V_B = E_r/B_\theta$, also constitutes the ion fluid velocity. (The notation, V_B, means that one can also think of this velocity as the velocity of magnetic field lines.) If we now consider the orbit of a suddenly-ionized ion, initially at rest in crossed electric and magnetic fields, E_r and B_θ, we find the following. The ion orbit consists of a guiding center drift velocity given by $V_B = \frac{E_r}{B_\theta}$, and a circular gyration of the particle in the (r,z) plane about that

___
* Here, we invoked Appendix B which neglected mass entrainment in the flow. Thus, strictly speaking, we are assuming here that the entrainment process is limited to the region upstream of the throat. We believe that this conceptual detail, if altered, would not invalidate the qualitative conclusion that $\beta \sim 1$.

guiding center. Here, it is essential to note that the circular velocity of the ion about its guiding center, V_{ci}, has to be the same as the guiding center velocity, $V_{ci} = V_B$, because this is the only solution to the equation of motion of a charged particle in crossed $\vec{E}$ and $\vec{B}$ fields that allows the ion to be born at rest (or with a velocity small against V_B). The consequence of such an orbit is that the energy density associated with the longitudinal fluid velocity, $\frac{1}{2}nm_iV_B^2$, must be the same as the energy density of the "thermal" motion of the individual ions gyrating about their guiding centers. That is, the circular gyro-orbits of the ions about their guiding enters constitutes an effective thermal pressure of the plasma in the meridional plane (perpendicular to B_θ). Since according to Appendix B, the fluid flow velocity in the azimuthal magnetic nozzle is on the order of the fast magnetosonic speed (with $\gamma = 2$ for a collisionless plasma), we again conclude that β must be on the order of unity (subject to transport losses downstream).

The arguments above strictly apply to ion heating, because the process of plasma generation involves ion inertia being introduced (by ionization) into the moving electro dynamical system. Heating of the non-inertial electrons in the azimuthal magnetic nozzle must be treated from a different point of view. This is carried out in the following Appendix.

APPENDIX E
ELECTRON HEATING PROCESSES IN
AZIMUTHAL MAGNETIC NOZZLES

In discussing the meridional magnetic nozzle concept, we have assumed the existence of a reservoir of prepared hot plasma, in which electrons and ions of a given temperature are introduced at the input side of the nozzle and thence flow through it according to the rules of compressible MHD. However, coaxial plasma guns and azimuthal magnetic nozzles (MPD thrusters) do not work this way.

Therefore, this picture was modified in Appendix D, to take into account that the upstream source of plasma in azimuthal magnetic nozzles is really cold un-ionized gas. Conceptually, the latter constitutes a source of inertial mass which is "legislated" into the dynamical system consisting of ions and electric and magnetic fields. (The complicated ionization processes that mediate this conversion do not need to be considered in detail here, aside from the fact that they exist.) We then found that for either a small mean-free path for Coulomb collisions, or a small ion gyro-radius, the sudden interaction of ions initially at rest with the moving dynamical system actually constituted an ion heating mechanism leading to "beta" values of order unity.

Because of the tiny electron mass, this is not a realistic mechanism for electron heating in these azimuthal magnetic nozzle devices. Instead, one must look to equipartition (temperature relaxation) and Ohmic heating, which we now do in this Appendix.

The reason that the topic of electron heating is important here is that if the electron beta ($nT_e/(B^2/2\mu_0)$) is raised to the order of unity, then the electron pressure contributes significantly to the fast magneto-sonic speed, $C_A^2 + C_S^2$, and thereby increases the flow speed of the plasma through the nozzle compared to what it would have been with cold electrons.

I. ELECTRON HEATING BY TEMPERATURE EQUIPARTITION WITH THE IONS

First, let us consider thermal equipartition between cold electrons and hot ions due to Coulomb collisions between them. We shall calculate a time-scale for this process and then compare it to the transit time through the nozzle. In the absence of all other processes except this temperature relaxation (considering for simplicity a uniform two-temperature plasma at rest), the basic equations can be put in the form[2] of coupled ordinary differential equations in time for the evolution of the electron and ion temperatures, T_e and T_i,

$$\frac{dT_e}{dt} = -\nu(T_e - T_i) \qquad (E-1)$$

$$\frac{dT_i}{dt} = \nu(T_e - T_i), \qquad (E-2)$$

where the nominal equipartition rate, ν, is given by

$$\nu = 2\frac{m_e}{m_i}\frac{1}{\tau_e}, \qquad (E-3)$$

and τ_e^{-1} is the electron momentum transfer collision frequency, ν_{ei}, introduced in Chap. I., Sec. A. In the absence of density variations, ν depends upon the electron temperature as $\nu = \text{cons.} \times T_e^{-3/2}$. We shall express this dependence in the form

$$\nu = \nu_0 \frac{T_{e0}^{3/2}}{T_e^{3/2}} \qquad (E-4)$$

where ν_0 is a constant rate corresponding to conditions at the initial time, and T_{e0} is the initial (upstream) electron temperature.

An obvious result of Eqs. (E-1) and (E-2) is

$$T_e + T_i = \text{const.} \equiv T_+ = T_{e0} + T_{i0}, \qquad (E-5)$$

where T_{i0} is the initial ion temperature and T_+ is a constant. Next, defining a time-like variable χ, and normalized temperatures τ and τ_+ by

$$\chi \equiv 2\nu_0 t, \qquad (E-6)$$

$$\tau \equiv \frac{T_e}{T_{e0}}, \qquad (E-7)$$

and

$$\tau_+ \equiv \frac{1}{2}\frac{T_+}{T_{e0}}, \qquad (E-8)$$

Eq. (E-1) can be rewritten as follows.

$$\tau^{3/2}\frac{d\tau}{d\chi} = -(\tau - \tau_+) \qquad (E-9)$$

This is equivalent to the integral relation

$$\int_1^\tau \frac{\tau^{3/2} d\tau}{\tau_+ - \tau} = \chi. \qquad (E-10)$$

The integration can be accomplished in closed form, and the result is

$$2\left\{ -\frac{1}{3}\left[\tau^{3/2} - 1\right] - \tau_+\left[\tau^{1/2} - 1\right] + \tau_+^{3/2}\left[\operatorname{arctanh}\left(\frac{\tau^{1/2}}{\tau_+^{1/2}}\right) - \operatorname{arctanh}\left(\frac{1}{\tau_+^{1/2}}\right)\right]\right\} = \chi. \qquad (E-11)$$

This relation implicitly provides electron temperature as a function of time, $\tau(\chi)$, with τ_+ as a parameter.

The time-dependence of the electron temperature due to thermal equilibration with the ions is generally complicated as is apparent from Eq. (E-11). However, a simple result can be obtained when the ions are hot and the electrons are cold. Thus if $\tau_+ \gg 1$ ($\frac{1}{2}T_{i0} \gg T_{e0}$), and if $\tau_+ \gg \tau$ ($\frac{1}{2}T_{i0} \gg T_e$), one can expand the inverse hyperbolic tangents to fifth order in their small arguments. Then, after several cancellations, one finds

$$\frac{T_e^{5/2} - T_{e0}^{5/2}}{(\frac{1}{2}T_{i0})^{5/2}} \approx 5\frac{T_{e0}^{3/2}}{(\frac{1}{2}T_{i0})^{3/2}}(\nu_0 t). \qquad (E-12)$$

From this result, it is immediately clear that the effective equipartition rate, t_{eq}^{-1}, is given by

$$t_{eq}^{-1} \approx 5\left(\frac{T_{e0}}{\frac{1}{2}T_{i0}}\right)^{3/2}\nu_0, \qquad (E-13)$$

where, in hydrogen plasma with $\ell n \Lambda \approx 10$

$$\nu_0(s^{-1}) \equiv 2\frac{m_e}{m_i}\frac{1}{\tau_{e0}} \approx 2 \times 10^{-8}\frac{n(cm^{-3})}{T_{e0}^{3/2}(eV)}. \qquad (E-14)$$

It can be shown that, for hot ions and cold electrons, the final electron temperature is half of the initial ion temperature, independent of the initial electron temperature. At very large times, (E-11) reduces to

$$\ell n\left[\frac{2}{1 - (2T_e/T_{i0})^{1/2}}\right] \approx 2\left(\frac{2T_{e0}}{T_{i0}}\right)^{3/2}(\nu_0 t)$$

In the large time limit wherein $T_e \to \frac{1}{2}T_{i0}$, the time dependence of T_e is functionally different from (E-12), but still contains practically the same characteristic time scale. Thus, according to the time scale implied by (E-13), the equipartition rate is much smaller than ν_0 when the ions are much hotter than the electrons. The effective equipartition rate is obtained (except for a numerical factor) by replacing the initial electron temperature by half the initial ion temperature (which is also the final ion temperature).

105

Since $\beta \sim 1$, the plasma transit time through the nozzle can be estimated as

$$t_z = \frac{\ell_z}{v_i} \qquad (E-15)$$

where $v_i[\frac{cm}{s}] = 1.3 \times 10^6 T_i^{1/2}$ (eV) is the thermal velocity of a hydrogen ion, and ℓ_z $[cm]$ is the length of the azimuthal magnetic nozzle.

Now, using (E-13), (E-14), and (E-15), the number of equipartition times during a nozzle transit time can be expressed as (assuming $T_i \approx T_{i0}$),

$$\frac{t_z}{t_{eq}} \approx 2 \times 10^{-13} \frac{n(cm^{-3})\ell_z(cm)}{T_{i0}^2(eV)}. \qquad (E-16)$$

It is interesting that the number of equipartition times depends only on the ion temperature. As a working example, we take $\ell_z = 10^2$ cm. Then we have the tabulation listed below (Table E-1) for values of (t_z/t_{eq}).

TABLE E-1. The number of equipartition times during nozzle transit $\frac{t_z}{t_{eq}}$, for $\ell_z = 10^2$ cm.

	$T[eV]$	10	100
$n[cm^{-3}] =$	10^{13}	2	0.02
	10^{14}	20	0.20
	10^{15}	200	2.0

We conclude that the extent to which the electrons are brought up near the ion temperature by energy-transfer during Coulomb collisions with the ions depends very sensitively on the ion temperature. For 10 eV ions (Alfvèn speeds near 4×10^6 cm/s since $\beta \approx 1$), Table E-1 shows that equipartition is to be expected at all densities of interest to us. However, for 100 eV ions (Alfvèn speeds near 10^7 cm/s since $\beta \approx 1$), equipartition is achieved only at the higher densities.

II. ELECTRON HEATING BY RESISTIVE DISSIPATION

We now continue on to consider Ohmic heating of electrons in azimuthal magnetic nozzles. The equation describing this process contains the resistivity η, and the square of the current density J, and is[2]

$$\frac{3}{2} n \frac{dT_e}{dt} = \eta J^2 \approx D_\eta \frac{B_\theta^2}{\mu_0} \frac{1}{\ell^2} \qquad (E-17)$$

where n is the plasma density (assumed constant here), T_e is the electron temperature, where D_η is the instantaneous resistive diffusivity,

$$(D_\eta)_{MKS} = \frac{\eta}{\mu_0}\left(\frac{m^2}{s}\right), (D_\eta)_{cgs} = \frac{c^2}{4\pi}\eta\left(\frac{cm^2}{s}\right), \qquad (E-18)$$

with $\mu_0 = 4\pi \times 10^{-7}$ henries/meter, where $(B_\theta)_{MKS}$ is the azimuthal magnetic field in Tesla, and where ℓ (meters) is the characteristic length for spatial variations in B_θ. In writing the second equation in (E-17), we have used Ampere's law to estimate J in terms of B_θ. This type of heating relies upon randomization of electron momentum by collisions with the ions, rather than direct energy transfer during a collision. Electron-electron collisions subsequently incorporate the isotropized momentum into a Maxwellian distribution characterized by an electron temperature. Although temperature equilibration with the ions and resistive heating both occur simultaneously, we are considering them separately here in order to clarify the behavior of the individual processes.

Since D_η depends on electron temperature as $T_e^{-3/2}$, we shall write it as

$$D_\eta = D_\eta^0 \frac{T_{e0}^{3/2}}{T_e^{3/2}}, \qquad (E-19)$$

where "0" refers to initial (upstream) conditions. Then, defining a normalized time-like variable, χ, by

$$\chi = \frac{2}{3}D_\eta^0\frac{t}{\ell^2}, \qquad (E-20)$$

and a normalized temperature, τ, by

$$\tau = \frac{T_e}{T_{e0}}, \qquad (E-21)$$

we can write Eq. (E-17) as follows.

$$\tau^{3/2}\frac{d\tau}{d\chi} = \frac{1}{\beta_{e0}} \qquad (E-22)$$

Here, we have defined the initial electron beta by

$$\frac{1}{\beta_{e0}} = \frac{m_iC_A^2}{T_{e0}} = \frac{B_\theta^2}{\mu_0}\frac{1}{nT_{e0}}, \qquad (E-23)$$

where $C_A^2 \equiv \frac{B_\theta^2}{\mu_0 nm_i}$ is the Alfvén speed in MKS units. (The definition of β_e used here differs by a factor of 2 from the usual definition of beta. The present beta is half of the usual beta.)

The solution to Eq. (E-22) can conveniently be expressed in terms of a time-dependent electron beta, $\beta_e(t)$, with T_e replacing T_{e0} in the definition (E-23). The result is

$$\beta_e = \beta_{e0}\left[1 + \frac{5}{3}\frac{1}{\beta_{e0}}\frac{t}{\ell^2}D_\eta^0\right]^{2/5}. \qquad (E-24)$$

107

We immediately see that there can be no appreciable electron Ohmic heating unless the time t exceeds the time scale, t_0, where

$$t_0 = \frac{3}{5}\beta_{e0}\frac{\ell^2}{D_\eta^0}.\tag{E-25}$$

As an example, consider $\ell = 10^2 \ cm$, 1 eV electrons ($D_\eta^0 \approx 10^7 \frac{cm^2}{s}$), and an initial electron beta of 1%. Then $t_0 \approx 10^{-5}$ sec. (If $\ell = 10 \ cm$, then $t_0 = 10^{-7} \ sec.$)

Let us suppose that the transit time through the nozzle is of order t_0 or longer. Then we can neglect the "1" in (E-24), and can estimate the electron beta from

$$\beta_e = \beta_{e0}\left(\frac{5}{3}\frac{t}{\ell^2}\frac{D_\eta^0}{\beta_{e0}}\right)^{2/5} = \left(\frac{5}{3}\frac{t}{\ell^2}\beta_{e0}^{3/2}D_\eta^0\right)^{2/5}\tag{E-26}$$

But note that

$$\beta_{e0}^{3/2}D_\eta^0 = \left(\frac{T_{e0}}{m_iC_A^2}\right)^{3/2} \times \frac{const.}{T_{e0}^{3/2}}\tag{E-27}$$

Thus, the electron temperature cancels out, and we conclude that the electron beta achieved by Ohmic heating is practically independent of the initial electron temperature.

Now let us define an "Alfvén temperature" T_A by

$$m_iC_A^2 = T_A.\tag{E-28}$$

(Since the ion beta is of order unity by the arguments in Appendix D, we expect that $T_A \approx T_i$.) Then Eq. (E-27) becomes

$$\beta_{e0}^{3/2}D_\eta^0 = D_\eta^A\tag{E-29}$$

where D_η^A is the resistive diffusivity evaluated by replacing the electron temperature with the Alfvén temperature.

Now, equation (E-26) reads

$$\beta_e = \left(\frac{5}{3}\frac{t}{\ell^2}D_\eta^A\right)^{2/5}\tag{E-30}$$

for $t > t_0$. Because the Alfvén temperature is much larger than the initial or nominal electron temperature, we see that the effective resistive diffusivity that heats up the electrons is much smaller than we would have at first expected. It is essentially the resistive diffusivity obtained by replacing the electron temperature with the ion temperature (for ion beta ≈ 1), which is reminiscent of the way things worked for the temperature equilibration of cold electrons and hot ions. Insofar as the ion beta is indeed of order unity, we can conclude from (E-30) that the achieved electron beta will depend only on the ion temperature, plasma dimensions, and, of course, the elapsed time.

We now calculate some examples for β_e, and set $t = t_r = \ell_z/v_i$, on the order of the transit time through the nozzle when the ion beta is of order unity. As a working example, we shall take $\ell_z = 10^2$ cm. For the length, ℓ, we shall use the radial thickness of the annular magnetic nozzle $\ell = \Delta$, so that B_θ drops off significantly in the radial direction. This procedure assumes that appreciable axial as well as radial current flows in the plasma. If this is not the case, then the result below for β_e must be multiplied by a factor of $(\Delta^2/\ell_z^2)^{2/5} = A^{-4/5}$, where A is the aspect ratio of the nozzle.

Then, Eq. (E-30) becomes

$$\beta_e = \left(\frac{5}{3} \frac{\ell_z}{\Delta^2} \frac{D_\eta^A}{v_i} \right)^{2/5} .$$

Since, in cgs units, $\ell_z = \Delta^2$ numerically in the chosen example, we have (numerically),

$$\beta_e = \left(\frac{5}{3} \frac{D_\eta^A}{v_i} \right)^{2/5}_{cgs} ,$$

which reduces further (for $T_A = T_i$, $D_\eta^A(\frac{cm^2}{s}) \approx \frac{10^7}{T_i^{3/2}(eV)}$, and $v_i(\frac{cm}{s}) \approx 1.3 \times 10^6 T_i^{1/2}(eV)$) to

$$\beta_e = \left(\frac{5}{3} \times \frac{10}{T_i^2(eV)} \right)^{2/5} = \frac{3.0}{T_i^{4/5}(eV)} .$$

Then we have the following practical estimates.

$$T_i = 10 \ eV, \quad \beta_e = 0.48, \quad \beta_e(\text{actual}) = 0.96$$

$$T_i = 100 \ eV, \quad \beta_e = 0.075, \quad \beta_e(\text{actual}) = 0.15$$

Thus, we conclude, just as for the earlier equipartition study, that the final electron beta obtained by resistive heating depends sensitivity on the ion temperature. (If β_e (actual) is close to unity, it means that T_e is close to T_i.) Colder ions signify slower flow speeds (because $\beta_{ion} \sim 1$), and longer times available for Ohmic heating of the electrons. If the current density distribution is such that the factor $A^{-4/5}$ is necessary, then it must be concluded that for $A \gtrsim 10$, resistive heating of the electrons will be minor.

We may summarize the qualitative results of Appendix E by stating that the rates of equipartition and Ohmic dissipation are not as a rapid as one would have supposed based on the high Coulomb collisionality of cold electrons. Instead, these rates depend critically on the ion temperature. Equipartition and Ohmic dissipation should constitute effective electron heating mechanisms in azimuthal magnetic nozzles (MPD thrusters) when the flow velocities (Alfvén speeds) correspond to a lower range of energies ($\lesssim 10 \ eV$), but not when the flow velocities are in a range of higher energies ($\sim 100 \ eV$). Moreover, if the current is mostly radial, one suspects that resistive heating of electrons is always a small effect.

APPENDIX F
THE EFFECT OF THERMAL FORCE TERMS IN OHM'S LAW

The particular dependence of the Coulomb scattering cross section on the relative velocity of charged particles (before averaging over velocity), gives rise to a number of "extra" transport effects in a classical plasma.[2] We have already taken these extra terms into account in our discussion of thermal conduction in Chap. I. Here, we wish to examine the effects of such terms in Ohm's law in relation to the problem of cross-field mass transport.

The electron momentum equation divided by (ne) yields Ohm's law, in cgs units,

$$\vec{E} + \frac{1}{c}\vec{V} \times \vec{B} = \eta\vec{J} + \frac{\vec{J} \times \vec{B}}{nec} - \frac{\nabla P_e}{ne} + \frac{\vec{R}_T}{ne} = rhs \qquad (F-1)$$

where $\vec{R}_T$ is the thermal force term.[2]

In the case of un-magnetized electrons,

$$\frac{\vec{R}_T}{ne} = -0.71\frac{\nabla T_e}{e} \qquad (F-2)$$

When $P_e^{-1}\nabla P_e \approx T_e^{-1}\nabla T_e$, it is clear that such a term can produce no significant new qualitative effects beyond that already provided by the ∇P_e term. However, since it is on the same order as the ∇P_e term, the thermal force term must be included in a detailed study of mass transport in any situation that is influenced by the ∇P_e term. Here, however, we note that these two terms will have no influence at all on "radial" mass transport in the meridional magnetic nozzle, according to the arguments already expressed in Chap. I. Moreover, in the azimuthal magnetic nozzle with un-magnetized electrons, it can be shown that both of these terms are small compared to the resistive pressure-driven term (for radial transport) in the ratio (β/β_e) vs. $(A^{-1})(\omega_{ce}/\nu_{ei})$, with $(\omega_{ce}/\nu_{ei}) \ll 1$. The conclusion is that the thermal force terms are generally unimportant when the electrons are un-magnetized.

When the electrons are strongly magnetized, the thermal force term becomes

$$\frac{\vec{R}_T}{ne} = -0.71\frac{\nabla_\parallel T_e}{e} - 1.5\left(\frac{\omega_{ce}}{\nu_{ei}}\right)^{-1}\frac{\vec{B} \times \nabla T_e}{e}. \qquad (F-3)$$

To study mass transport, we crossed Ohm's law with $\vec{B}$ and multiplied through by (c/B^2). Then we examined the "radial" component. (Here, we also must multiply through by (-1) as in Chap. I.) The terms on the rhs of Eq. (F-1) then become

$$rhs = -4\pi\frac{D_\eta}{B^2}\frac{\partial P}{\partial r} + \frac{1}{ne}J_r + \frac{(\nabla P_e \times \vec{B})_r}{ne}\frac{c}{B^2} + 1.5\left(\frac{\nu_{ei}}{\omega_{ce}}\right)\left(\frac{\partial T}{\partial r}\right)\frac{c}{eB}, \qquad (F-4)$$

where $D_\eta = (c^2/4\pi)\eta$.

In the case of the meridional nozzle, only the first and last terms survive, and the last term is the thermal force. These two terms can be respectively shown to be in the ratio $\frac{1}{2}(\beta/\beta_i)$, where $\beta = \beta_e + \beta_i$. Thus, again no new qualitative effects are introduced by the thermal force, provided that the ion beta is of the same order of magnitude as the total beta. Nevertheless, it is interesting that the thermal force term is on the same order as the resistive pressure driven term when the electrons are magnetized. The thermal force therefore must be included in any detailed transport study of a specified meridional nozzle design when the electrons are magnetized.

In the case of the azimuthal magnetic nozzle, we have already seen that the Hall term, J_r, dominates the resistive pressure-driven term when the electrons are magnetized. Comparing the Hall term to the thermal force term, we easily find that they are in the ratio $1/(\omega_{ce}/\nu_{ei})^{-1} = (\omega_{ce}/\nu_{ei}) \gg 1$. Thus, when the electrons are magnetized, the thermal force term is much smaller than the Hall term and can be neglected in the study of radial mass transport in the azimuthal magnetic nozzle.

Here, we have considered only the extremes of un-magnetized electrons and strongly magnetized electrons. The exact situation where the degree of magnetization is arbitrary is very complicated, but all the formulas for $\vec{R}_T$ are known[2] and available for use in a study of radial mass transport.

LIST OF SYMBOLS AND DEFINITIONS
IN ORDER OF OCCURRENCE BEGINNING WITH CHAP. I

Symbol	Definition
T	plasma temperature
B	magnetic field
P	plasma pressure
n	ion-electron number density
β	$(2\mu_0 P/B^2)_{mks} = (8\pi P/B^2)_{cgs}$
μ_0	$4\pi \times 10^{-7}$ henries/meter (MKS)
n_e	electron number density
n_i	ion number density
λ_D	Debye length: $(T/4\pi n e^2)^{1/2}$ in cgs units
e	electron charge (4.8×10^{-10} esu or 1.6×10^{-19} Coulombs)
$\omega_{pe,i}$	electron (ion) plasma frequency: $(4\pi n e^2/m_{e,i})^{1/2}$ in cgs units
$m_{e,i}$	electron (ion) mass
Λ	$\lambda_D/(e^2/T)$ or $\lambda_D/(\text{De Broglie wavelength})$, where the latter is used for $T > 50$ eV.
H	hydrogen atom symbol
H^-	negative hydrogen ion symbol
r_{ei}	electron-ion distance within which electron orbit is significantly deflected by ion charge: (e^2/T)
H^+	positive hydrogen ion symbol
σ_{ei}	Coulomb scattering cross section (effective) for cumulative small-angle scattering of an electron leading to 90° deflection: $\pi r_{ei}^2 \ell n \Lambda$
ν_{ei}	electron momentum-transfer collision frequency for electron scattering by ions: $n_i \sigma_{ei} v_e$
$v_{e,i}$	electron (ion) thermal velocity: $(2T_{e,i}/m_{e,i})^{1/2}$
$T_{e,i}$	electron (ion) temperature
ξ	degree of ionization of plasma
n_H	neutral hydrogen atom number density
n_0	total number density: $n + n_H$
ϵ_0	ground state ionization energy of the hydrogen atom: 13.6 eV
h	Planck's constant
$\hbar$	$h/2\pi$

Symbol	Definition
ν_{eH}	electron-atom collision frequency
L	characteristic macroscopic length scale
V	characteristic fluid velocity
λ	collisional mean-free path
v_{th}	thermal velocity
D	diffusivity: λv_{th}
ν	collision frequency
r, z	cylindrical coordinates
$r_{ce,i}$	electron (ion) gyro-radius: $v_{e,i}/\omega_{ce,i}$
$\omega_{ce,i}$	electron (ion) gyro-frequency (cyclotron frequency): $(eB/m_{e,i}c)_{cgs}$
c	velocity of light in vacuum: 3×10^{10} cm/s
D	diffusivity: $r_{ci}^2 \nu_{ii}$
ν_{ii}	ion-ion Coulomb collision frequency
J	electric current density
η	plasma resistivity
$P_{e,i}$	electron (ion) pressure
E	electric field
ρ	plasma mass density: $m_i n$
$\hat{\tau}$	unit vector in the "radial" direction
$\hat{r}$	unit vector in the radial direction
θ	azimuthal angle coordinate
$\ell_{1,2}$	characteristic transverse (longitudinal) dimension
V_θ	azimuthal component of fluid (plasma) velocity
$C_{A,S}$	Alfvén (sound) speed: $(B^2/4\pi\rho)_{cgs}^{1/2}$ or $(\gamma P/\rho)^{1/2}$
γ	ratio of specific heats, usually taken as $\gamma = 5/3$.
B_θ	azimuthal magnetic field
$\beta_{e,i}$	electron (ion) beta: $(2\mu_0 P_{e,i}/B^2)_{MKS} = (8\pi P_{e,i}/B^2)_{cgs}$
$V_\perp$	fluid velocity component transverse to $\vec{B}$
V_B	guiding center drift velocity: $(\vec{E} \times \vec{B}/B^2)_{MKS} = (c\vec{E} \times \vec{B}/B^2)_{cgs}$
$J_\perp$	current density component transverse to $\vec{B}$
Γ	particle flux density: $n\vec{V}$
D_η	resistive diffusivity: $(\eta/\mu_0)_{MKS} = (c^2\eta/4\pi)_{cgs}$
D_{part}	particle diffusivity: $\frac{1}{2}\beta D_\eta$
t_{part}	characteristic time for particle loss transversely
a	radial dimension of nozzle
R_η	magnetic Reynolds number: $V_z a/D_\eta \approx v_z a/D_\eta$
V_z	axial component of fluid (plasma) velocity
A	nozzle aspect ratio: ℓ_z/a or ℓ_z/Δ
Δ	coaxial radial spacing of electrodes
σ	electrical conductivity of plasma: η^{-1}

113

Symbol	Definition
$t_{e\parallel}$	characterstic time for longitudinal electron thermal conduction
$D_\parallel^e$	thermal diffusivity for parallel electron thermal conduction
t_z	longitudinal (axial) transit time: $\frac{\ell_z}{V_z} \approx \frac{\ell_z}{v_i}$
V_r	radial component of fluid (plasma) velocity
$B_{r,z}$	radial (axial) component of magnetic field
$J_{\theta,r,z}$	azimuthal (radial, azial) component of current density
$E_{y,\theta}$	components of electric field
Δ_z	axial thickness of sample of resistive metal
t_{exp}	transient time for approach to asymptotic velocity
t_A	radial Alfvén time
$R_\eta^{(A)}$	magnetic Reynolds number defined using the Alvén speed
F_z	applied axial force (per unit area) acting upon sample of resistive metal
B_x	cartesian analog of radial component of magnetic field
$V_\parallel$	component of fluid (plasma) velocity parallel to $\vec{B}$
R_c	radius of curvature of magnetic field line in region of nozzle exit
$A_{e,0}$	area of nozzle exit (throat)
J_y	cartesian analog of azimuthal component of current density
β_0	value of β in nozzle throat
$\dot{M}$	rate of fuel mass loss from vehicle
Δ_η	resistive skin depth corresponding to time t_z
a_p	characteristic radius of plasma
t_D	characteristic time for diffusion across a characteristic radial dimension
R_D	Reynolds number associated with diffusivity D
$H_\perp$	lateral heat loss rate
$\mathbf{P_0}$	kinetic power in nozzle throat
$\mathbf{P}$	kinetic power in nozzle exit
V_0	fluid (plasma) velocity in nozzle throat
C_{so}	speed of sound in nozzle throat
$T_{(0)}$	plasma temperature on centerline in nozzle throat
$\kappa, \kappa_\parallel, \kappa_\perp, \kappa^{e,i}$	plasma thermal conductivities (along and across $\vec{B}$) and also for electrons (ions)

114

Symbol	Definition
$\vec{q}, \vec{q}_u, \vec{q}_T, \vec{q}^{\,e,i}$	heat fluxes
$\hat{b}$	unit vector along $\vec{B}$
$\vec{u}$	fluid velocity of electrons relative to ions: $\vec{J}/ne$
$D_{\parallel,\perp}, D^{e,i}$	thermal diffusivity along (across) $\vec{B}$ and also for electrons (ions)
D_{Bohm}	Bohm diffusivity: $0.2(cT/eB)_{cgs}$
α^*	$(1 + T_e/T_i)(\omega_{pe}^2/\omega_{ce}^2)$, parameter in connection with Bohm transport
R_{Bohm}	Reynolds number based upon D_{Bohm}
g	equivalent gravitational force
Γ	growth rate for Rayleigh-Taylor instability
Q	inverse scale length of unstably stratified medium
Δ_r	radial scale length of unstably stratified medium
$t_{B.C.}, \ell_{B.C.}$	transit time and longitudinal length scale of "bad curvature" entrance region of nozzle
$\delta V, \delta\rho, \ldots$	perturbations of velocity, mass density,..., associated with the Rayleigh Taylor instability
κ, ω	wave number and complex frequency of the Rayleigh-Taylor instability
ξ_x	normal boundary displacement due to the Rayleigh-Taylor instability
$P_0, \rho_0, \ldots$	unperturbed pressure, mass density, ... profiles subject to the Rayleigh-Taylor instability
s	compressional communication speed across the magnetic field direction
D_{RT}	equivalent diffusivity due to the Rayleigh-Taylor instability
$r_{B.C.}$	nozzle radius in the region of "bad curvature"
$R_{B.C.}$	field-line radius of curvature in "bad curvature" region
q_{RT}	quasilinear heat flux induced by Rayleigh-Taylor instability
E_r	radial space-charge electric field in the plasma sheath
ϕ_s	plasma sheath potential drop
Δ_s	plasma sheath thickness
V_0	guiding center drift velocity in the plasma sheath
k_y	wave number for flute modes induced by the Kelvin-Helmholtz instability
Γ	growth rate of the Kelvin-Helmholtz instability
D'_{Bohm}	simulation result for Bohm diffusion induced by the Kelvin-Helmholtz instability

115

Symbol	Definition
$f_{mass\ loss}$	mass loss fraction due to radial transport during axial transit of the nozzle
q'_{Bohm}	heat flux due to Bohm transport induced by the Kelvin-Helmholtz instability
L_{Ross}, L_{Planck}	Rosseland and Planck optical absorption lengths
P_{brem}	bremsstrahlung power per unit volume
P_{rad}	radiation surface power density on the wall
r	characteristic radial distance to the wall
t_{brem}	characteristic time for energy loss due to bremsstrahlung
T_{edge}	surface temperature of optically thick plasma
T_H	surface temperature of hot side of wall next to plasma
T_C	surface temperature of side of wall away from plasma
σ_{SB}	Stefan-Boltzmann constant for surface radiation
q_W	power flux through wall bounding optically thick plasma
K_W	thermal conductivity of wall bounding optically thick plasma
Δ	thickness of wall bounding optically thick plasma
t_{bb}	characteristic time for energy loss due to surface (Black Body) radiation
U	stream function for mass flux
Ψ	stream funtion for magnetic flux
Ψ'	$d\Psi/dU$
$B_0, V_0, \rho_0 \ldots$	values of magnetic field, velocity, density ... in the throat of the nozzle (Quasi 1 D)
C_0	speed of sound in the throat
$H(U)$	enthalpy
$S(U)$	entropy
B	in Chap. II only: $(B/\sqrt{\mu_0})_{MKS}$
$\hat{t}$	unit tangent vector along $\vec{B}$
$\hat{n}$	unit normal vector perpendicular to $\vec{B}$
s	distance measured along streamlines
K	curvature of a streamline
ψ, χ	stream function and velocity potential for the quasi-1D case
s	r^2, in the quasi-1D case
ν	artificial damping coefficient for solving the quasi-1D PDE using artificial time

116

Symbol	Definition
$r_I(z)$	radius of the plasma-field interface
$\phi(\ell)$	nozzle opening half-angle vs. distance along nozzle wall
$r_w(\ell), z_w(\ell)$	radial and axial coordinates of nozzle wall *vs.* distance along wall
$U_0(\psi, \chi)$	quasi 1-D solution for the mass flux
$U_i(\psi, \chi), B_i(\psi, \chi)$	basis functions for representing the general 2D solution
a_i, b_i	coefficients of the expansion of the solution in basis functions
ϵ	coefficient in the non-uniform pressure profile in the throat: $P_0 = const. \times (1 + \epsilon U)$
C^*	the "cusp" speed: $C_S C_A (C_S^2 + C_A^2)^{-1/2}$
α	a dimensionless measure of magnetic field strength: $\Psi'(U)\sqrt{\rho_0}$
$\delta(z)$	radial width of the vacuum field region in a sharply bounded plasma profile where $\delta(z) \ll r_w(z)$
$P_w(z)$	plasma pressure at the plasma-field interface
Ψ_{max}	the magnetic flux that "stuffs" the nozzle in the sharp-boundary profile
$B_{0\,max}$	the corresponding value of magnetic field strength in the nozzle throat
r_0	the nozzle radius at the throat
M	the number of mesh points in each dimension
t_s	the (normalized) time needed to reach a state of steady flow in the initial value approach, in units of a characterstic physical time
A_θ	azimuthal component of the magnetic vector potential
D_{vis}	viscous diffusivity (kinematic viscosity)
λ_{ii}	mean-free path for ion-ion Coulomb collisions
ν_{ii}	ion-ion Coulomb collision frequency
α	in the meridional nozzle: $\vec{V}_M = \alpha \vec{B}_M$
$\vec{V}_M, \vec{B}_M$	meridional components of fluid velocity and magnetic field
$\vec{\Omega}$	fluid vorticity
$\mathbf{T}$	thrust

Symbol	Definition
V_e	exit velocity of plasma
$C_{SR}, P_R, \ldots$	speed of sound, pressure ... in the reservoir
$\mathbf{P}$	power in the exhaust
S	fast magneto-sonic speed: $(C_S^2 + C_A'^2)^{1/2}$
r_R	radius of reservoir (i.e. at breech of coaxial gun or azimuthal nozzle)
ΔV	velocity increment of vehicle
$V_{e,p}$	exhaust velocity in pulsed system
M_ℓ	total mass of vehicle after ℓ^{th} pulse
$M_{i,f}$	initial (final) mass of vehicle
$T_{s,p}$	reservoir temperature in steady (pulsed) system
$V_{e,s}$	exhaust velocity in steady system
τ_{on}	the "on" time of a pulse
$\tau = \tau_{on} + \tau_{off}$	the total time for a pulse
$\dot{M}_{s,p}$	the instantaneous fuel mass flow rate in a steady (pulsed) system
$(\Delta t)_{s,p}$	nominal burn time for a steady (pulsed) system
ν	nominal rate for equilibration of electron and ion temperatures in the azimuthal nozzle
T_{eo}, T_{io}	initial temperatures prior to equilibration
t_{eq}^{-1}	effective equipartition rate
T_A	Alfvén temperature: $m_i C_A'^2$
D_η^A	resistive diffusivity evaluated using the Alfvén temperature instead of the electron temperature
t	time variable

LIST OF FIGURES

119

Fig. 18. Variation of pressure along streamlines for un-magnetized flow through JPL nozzle.

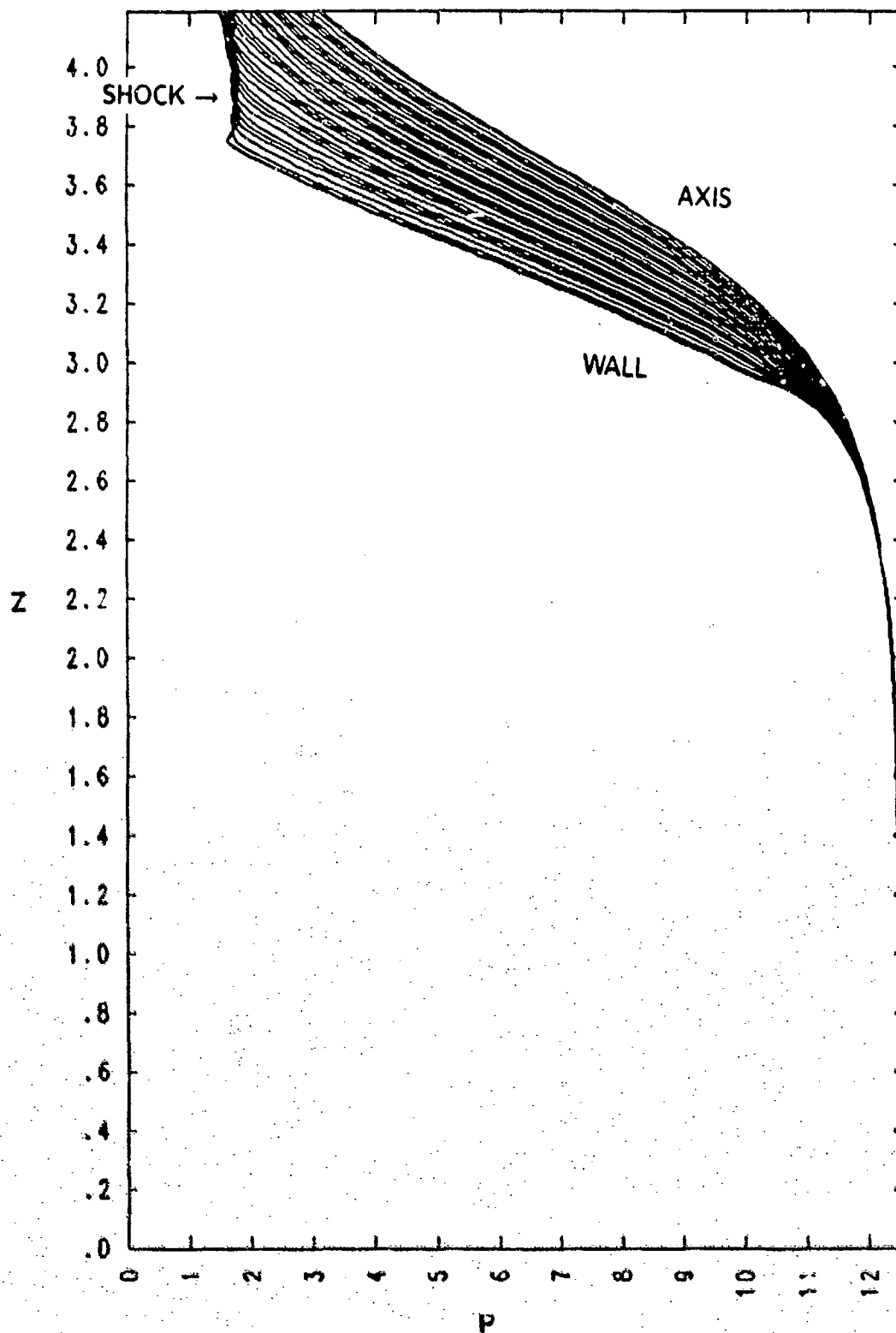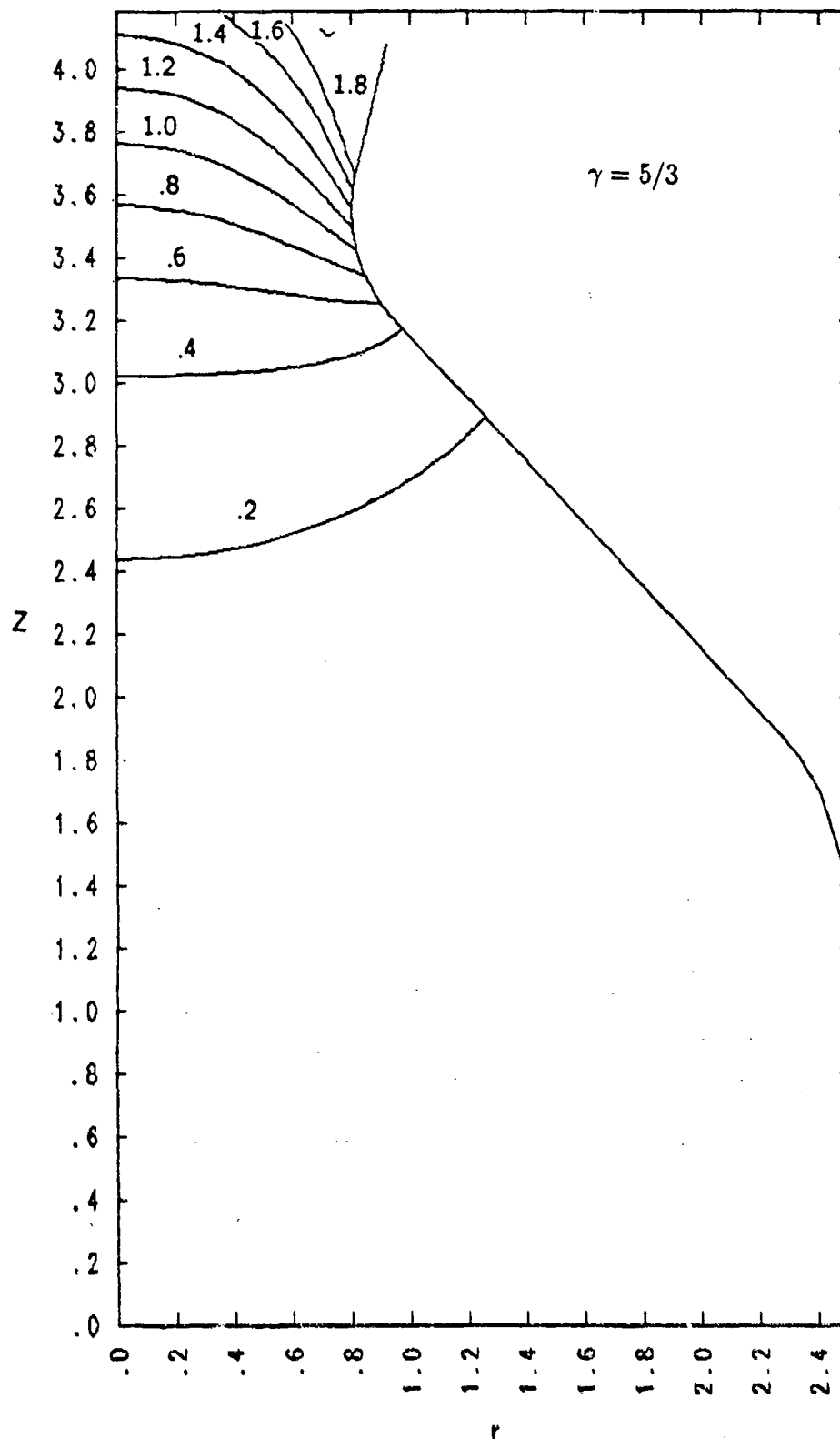Fig. 19. Contours of constant mach number (with $\gamma = 5/3$) for un-magnetized flow through JPL nozzle.

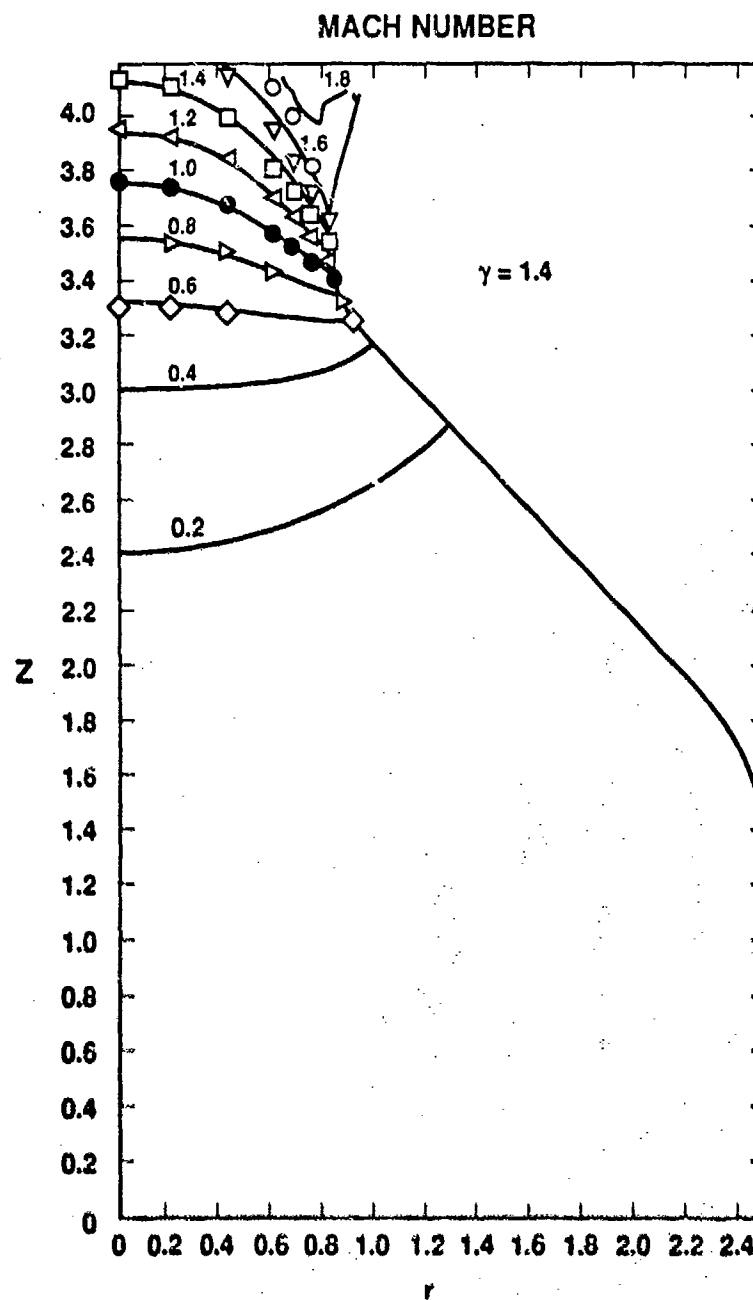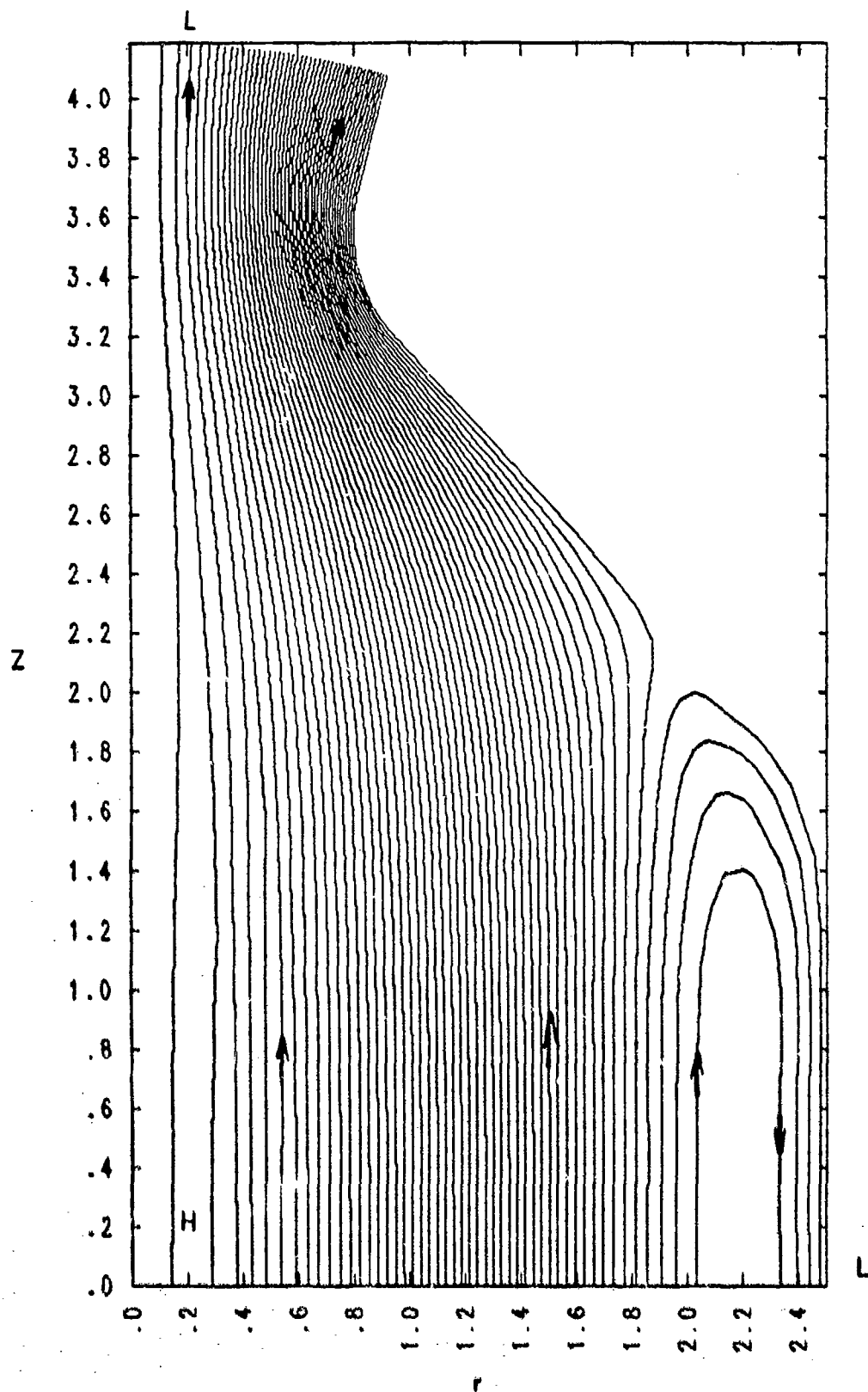Fig. 20. Contours of constant Mach number (with $\gamma = 1.4$) for un-magnetized flow through JPL nozzle.

Fig. 21. Streamlines in the JPL nozzle for the un-magnetized non-uniform pressure configuration, $P_0 \sim (1 + \epsilon U)$, with $\epsilon = -0.02$. Flow reversal at the nozzle entrance is induced by a non-uniform pressure profile in the reservoir.
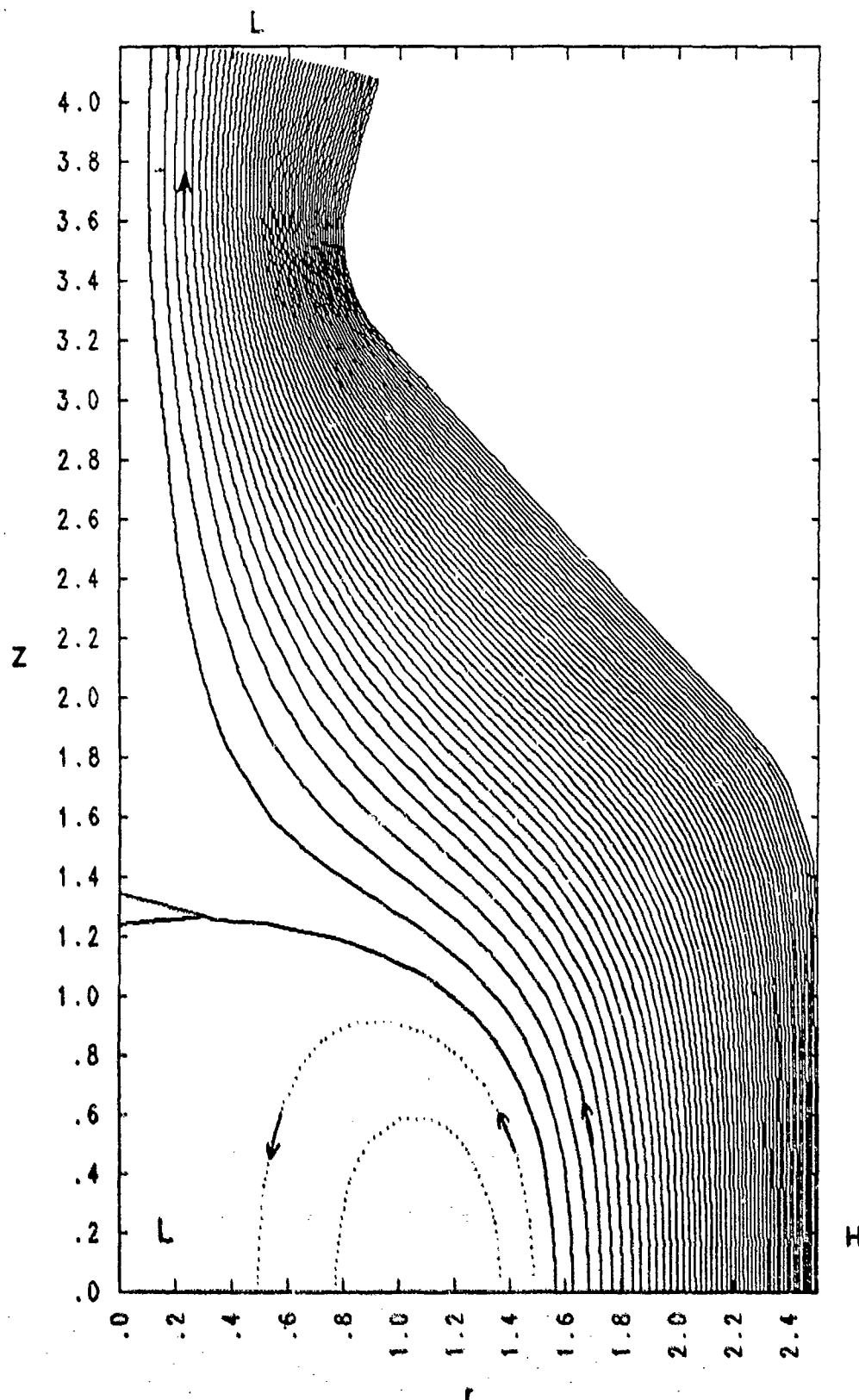
Fig. 22. Streamlines in the JPL nozzle for the un-magnetized non-uniform pressure configuration, $P_0(1 + \epsilon U)$, with $\epsilon = 0.02$. Flow reversal at the nozzle entrance is induced by a non-uniform pressure profile in the reservoir.

Fig. 23. Streamlines in the hyperbolic nozzle for magnetized flow with $\psi'(U) = $ const. and $\alpha = 0.8$ (Sec. II-C.3).

Fig. 24. Contours of constant $(\rho V)^2$ in the hyperbolic nozzle for magnetized flow with $\psi'(U) = $ const. and $\alpha = 0.8$ (Sec. II-C.3).

Fig. 25. Variation of $(\rho V)^2$ along streamlines in the hyperbolic nozzle for magnetized flow with $\psi'(U) = $ const. and $\alpha = 0.8$ (Sec. II-C.3).

Fig. 26. Contours of constant velocity in the hyperbolic nozzle for magnetized flow with $\psi'(U) = $ const. and $\alpha = 0.8$ (Sec. II-C.3).

Fig. 27. Variation of velocity along streamlines in the hyperbolic nozzle for magnetized flow with $\psi'(U) = $ const. and $\alpha = 0.8$ (Sec. II-C.3).

Fig. 28. Contours of constant density in the hyperbolic nozzle for magnetized flow with $\psi'(U) = $ const. and $\alpha = 0.8$ (Sec. II-C.3).

Fig. 29. Variation of density along streamlines in the hyperbolic nozzle for magnetized flow with $\psi'(U) = $ const. and $\alpha = 0.8$ (Sec. II-C.3).

Fig. 30. Streamlines in the JPL nozzle for magnetized flow with $\psi'(U) = $ const. and $\alpha = 0.8$ (Sec. II-C.3).

Fig. 31. Contours of constant $(\rho V)^2$ in the JPL nozzle for magnetized flow with $\psi'(U) = $ const. and $\alpha = 0.8$ (Sec. II-C.3).

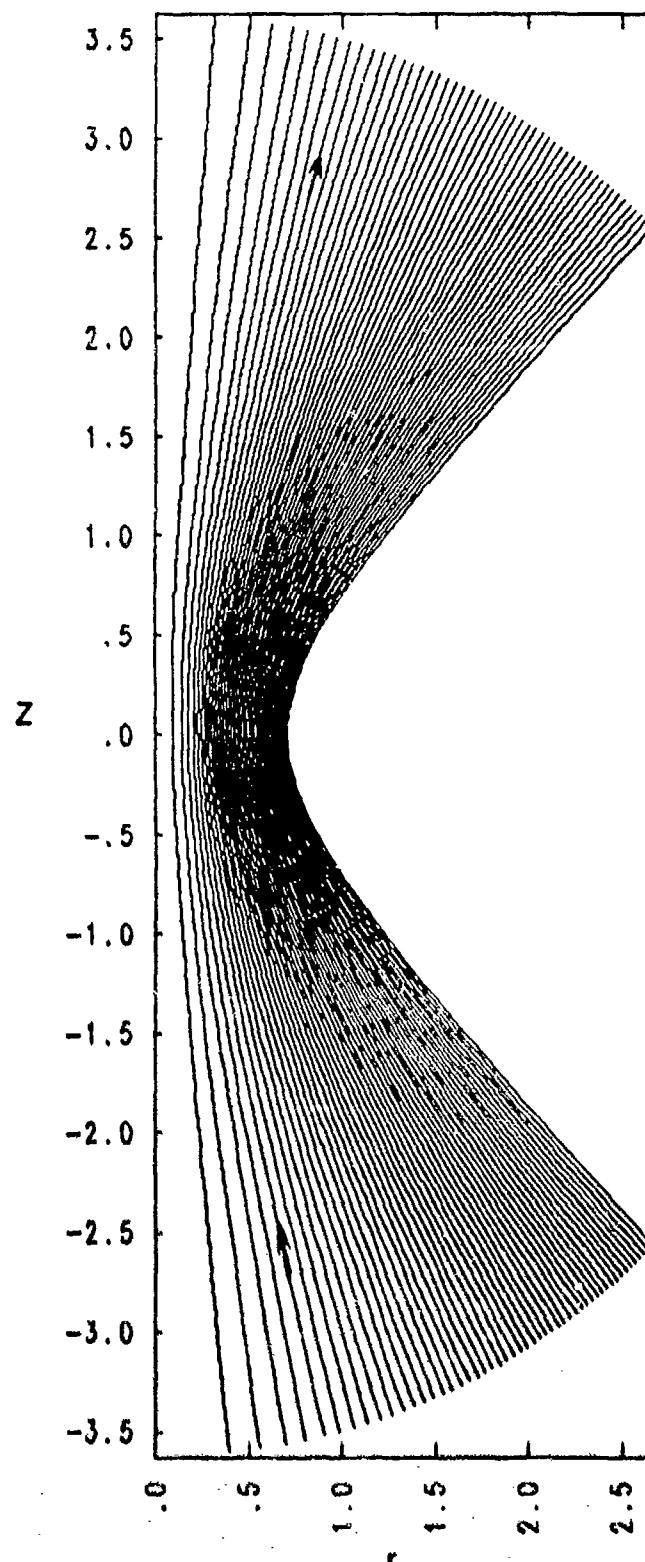Fig. 32. Variation of $(\rho V)^2$ along streamlines in the JPL nozzle for magnetized flow with $\psi'(U) = $ const. and $\alpha = 0.8$ (Sec. II-C.3).

Fig. 33. Contours of constant density in the JPL nozzle for magnetized flow with $\psi'(U) = $ const. and $\alpha = 0.8$ (Sec. II-C.3).

Fig. 34. Variation of density along streamlines in the JPL nozzle for magnetized flow with

Fig. 1-a. Functional dependence of Velocity V, Density ρ, and Pressure P, on Magnetic Field Strength B, along streamlines in the Meridional Magnetic Nozzle.

Fig. 1-b. Axial variation of fluid variables for a quasi-1D Meridional Magnetic Nozzle produced by a single-turn filamentary coil ($\frac{B}{B_0} = (1 + z^2)^{-3/2}$).
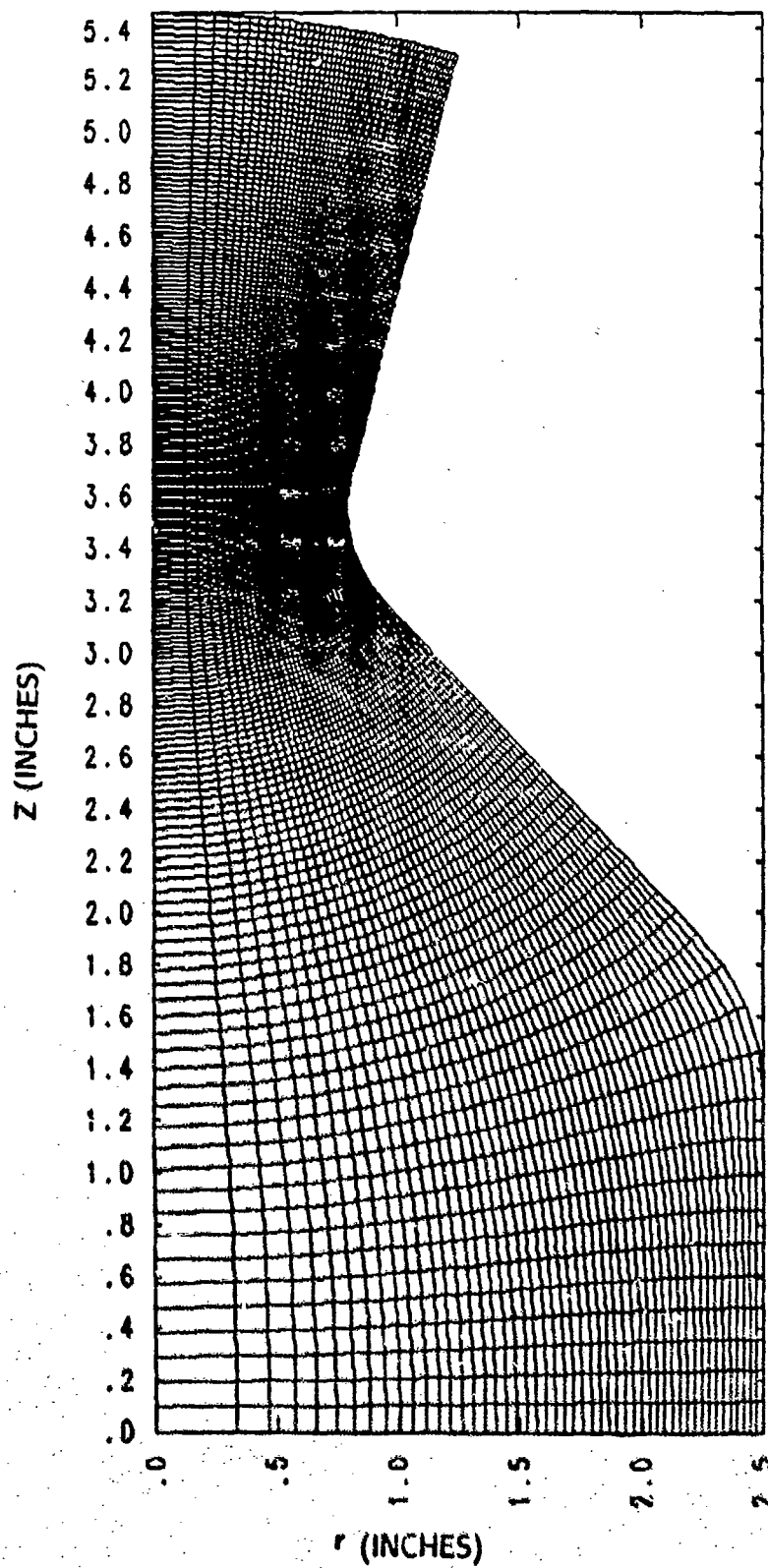
Fig. 2. A body-fitted coordinate system for the JPL nozzle (Ref. 11) computed by the method outlined in section II-B.
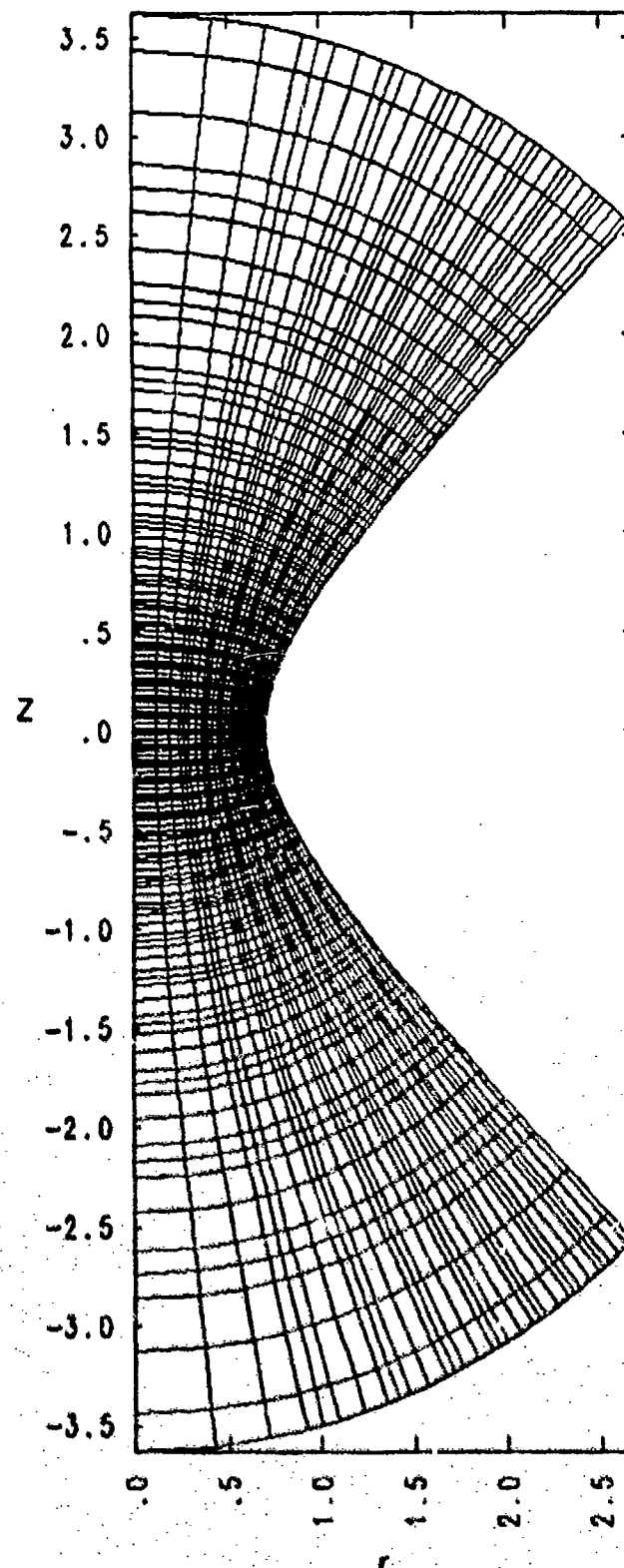
Fig. 3. Coordinate grid for hyperbolic nozzle with 45° opening half-angle at each end. Every fourth line constitutes the course grid, equally spaced in ψ and χ (see Sec. II-B). The remaining lines constitute the (unequally-spaced) Gaussian quadrature subgrid used to perform the integrals in Eq. (II.41) (see Sec. II-C).
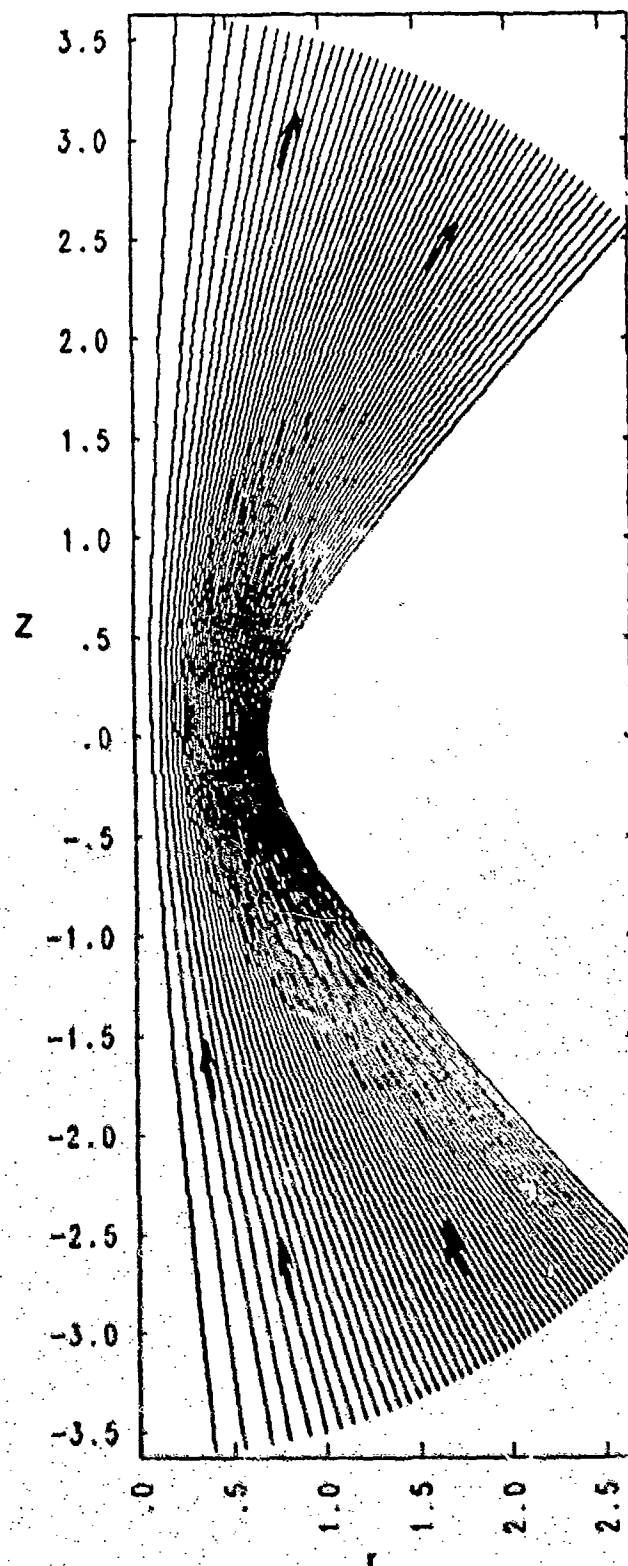
Fig. 4. Streamlines for un-magnetized flow through the hyperbolic nozzle of Fig. 3.
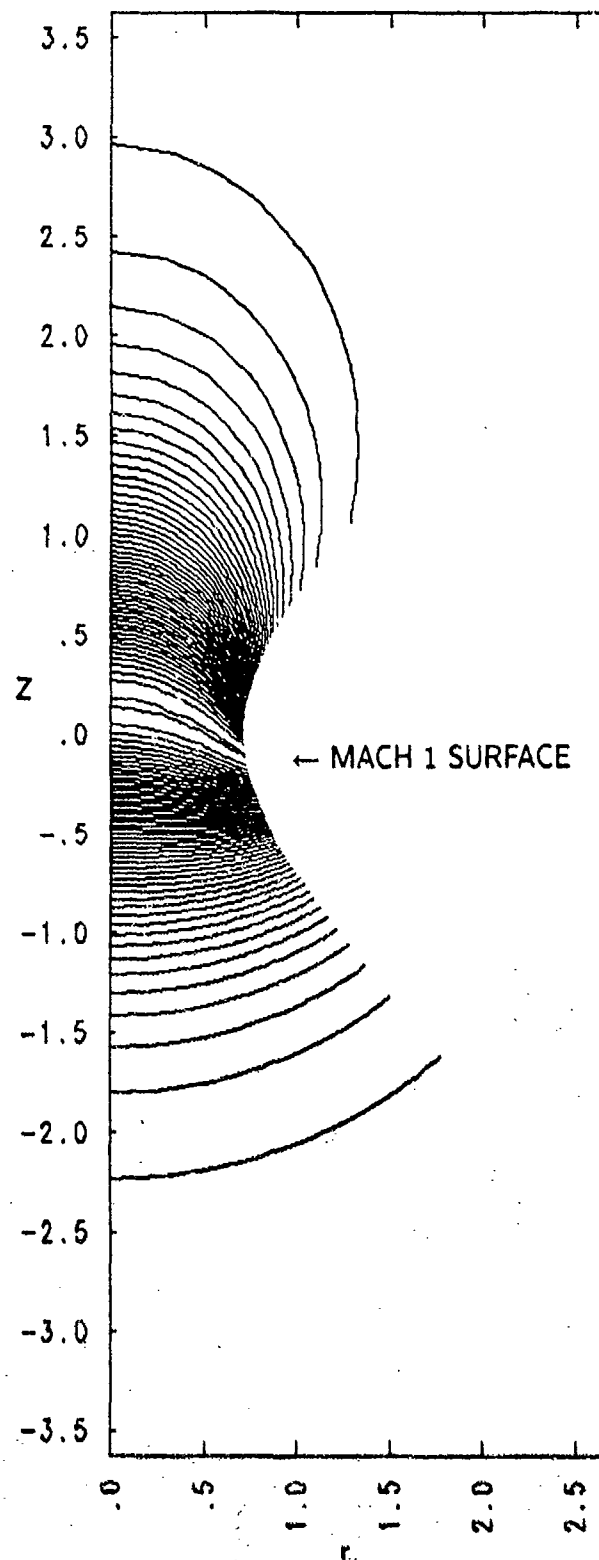
Fig. 5. Contours of constant $(\rho V)^2$ for un-magnetized flow through the hyperbolic nozzle of Fig. 3.
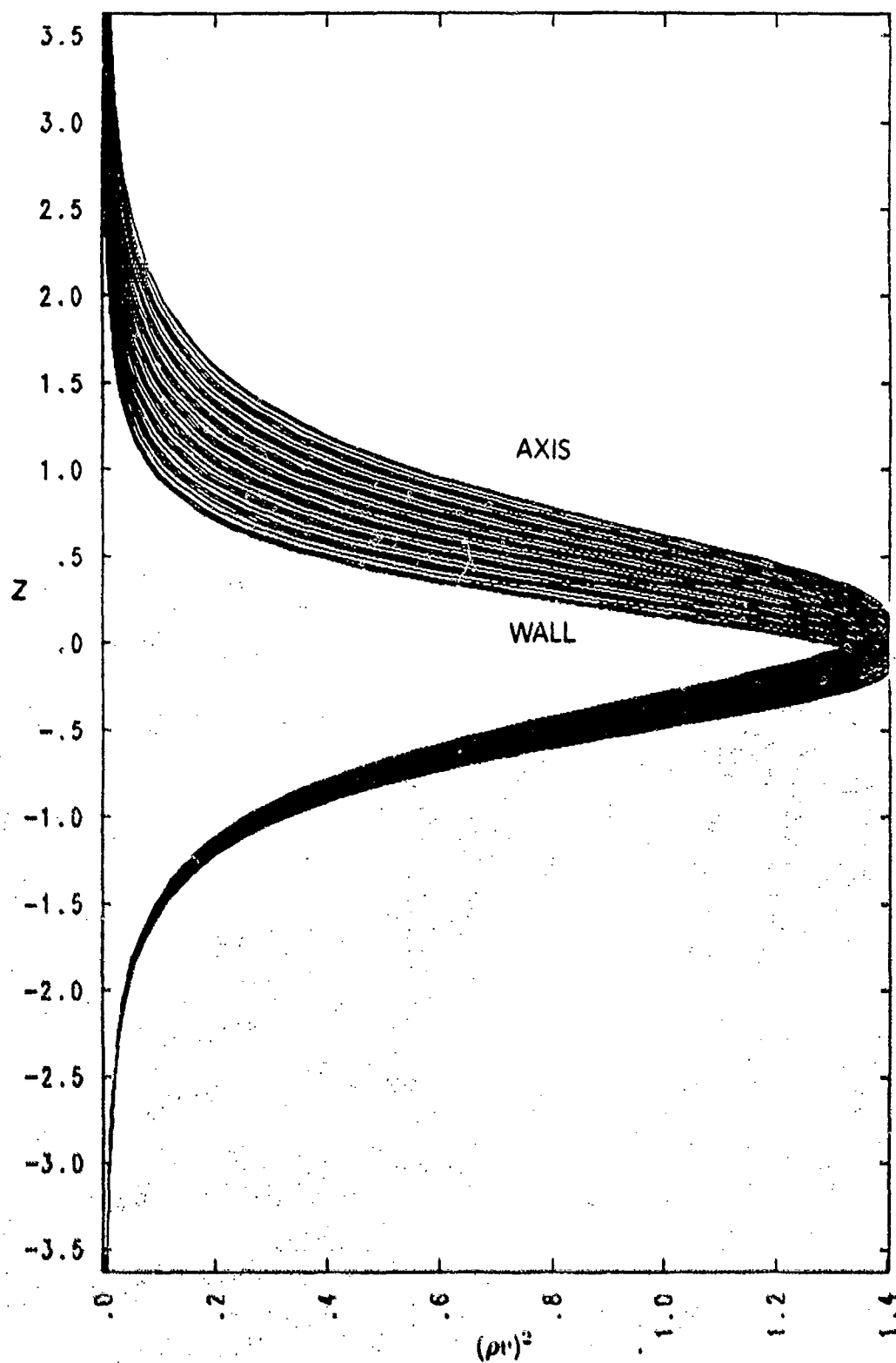
Fig. 6. Variation of $(\rho V')^2$ along streamlines for un-magnetized flow through the hyperbolic nozzle of Fig. 3.
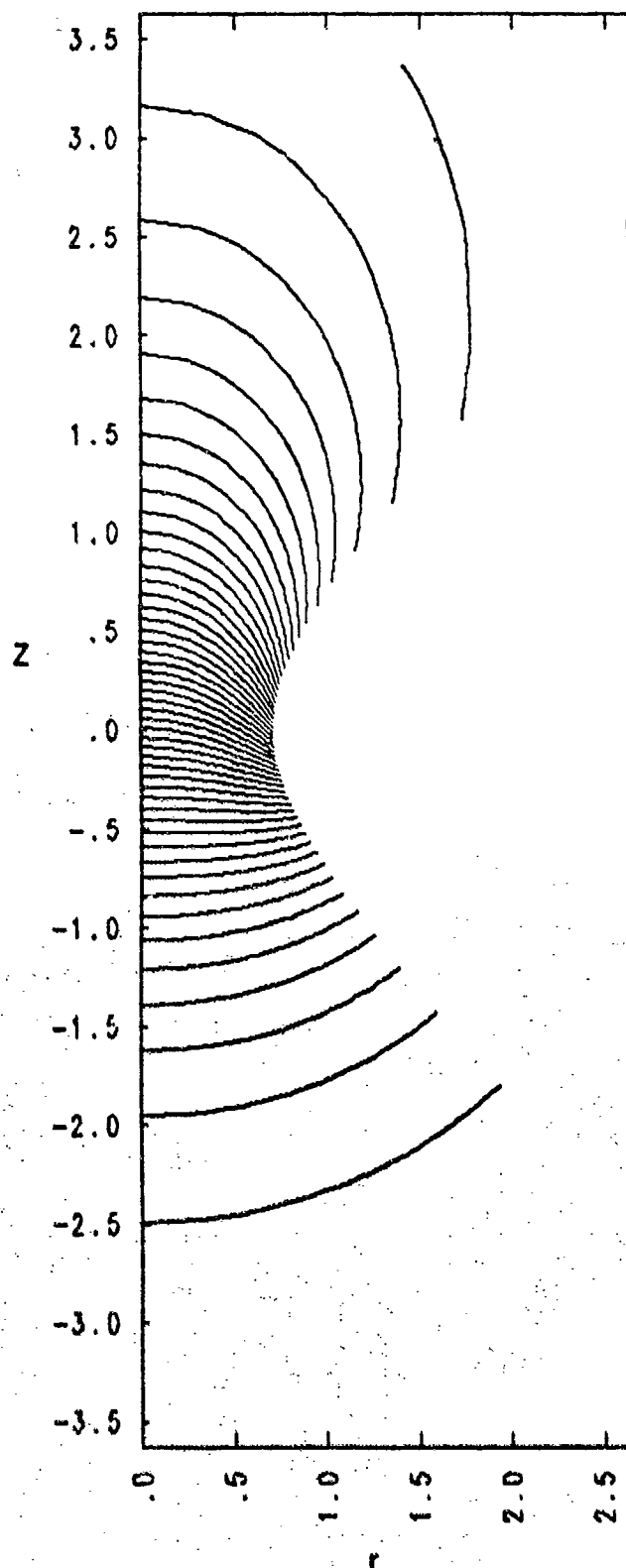
Fig. 7. Contours of cons.ant velocity for un-magnetized flow through the hyperbolic nozzle of
Fig. 3.
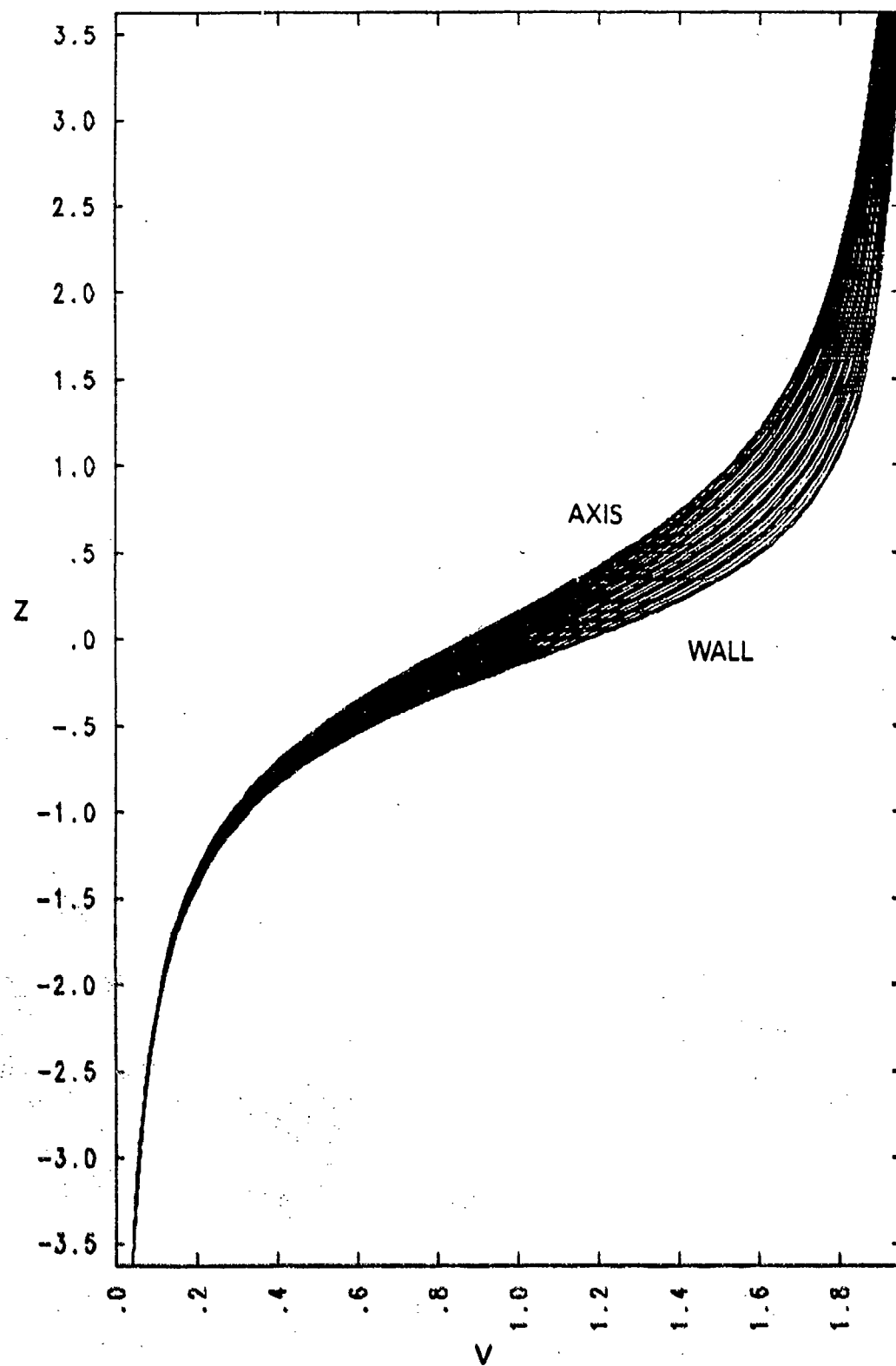
Fig. 8. Variation of velocity along streamlines for un-magnetized flow through the hyperbolic nozzle of Fig. 3.
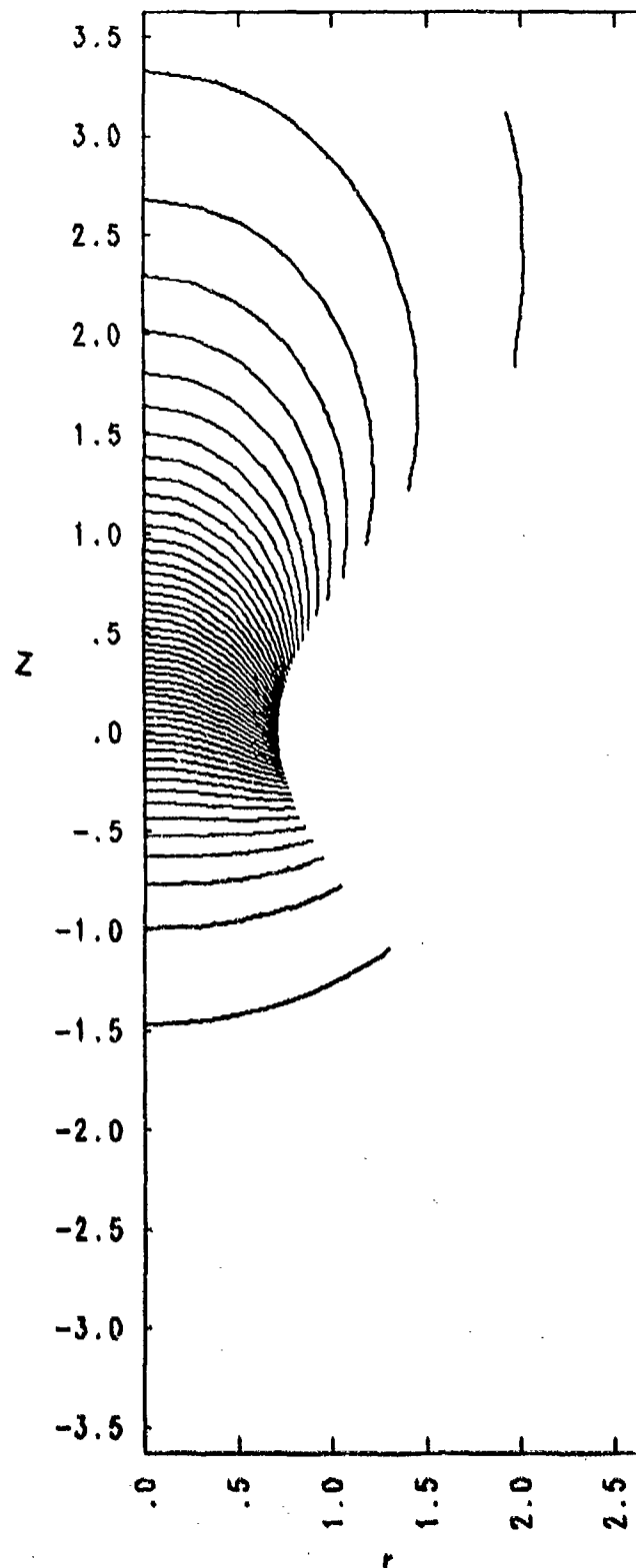
Fig. 9. Contours of constant density for un-magnetized flow through the hyperbolic nozzle of Fig. 3.
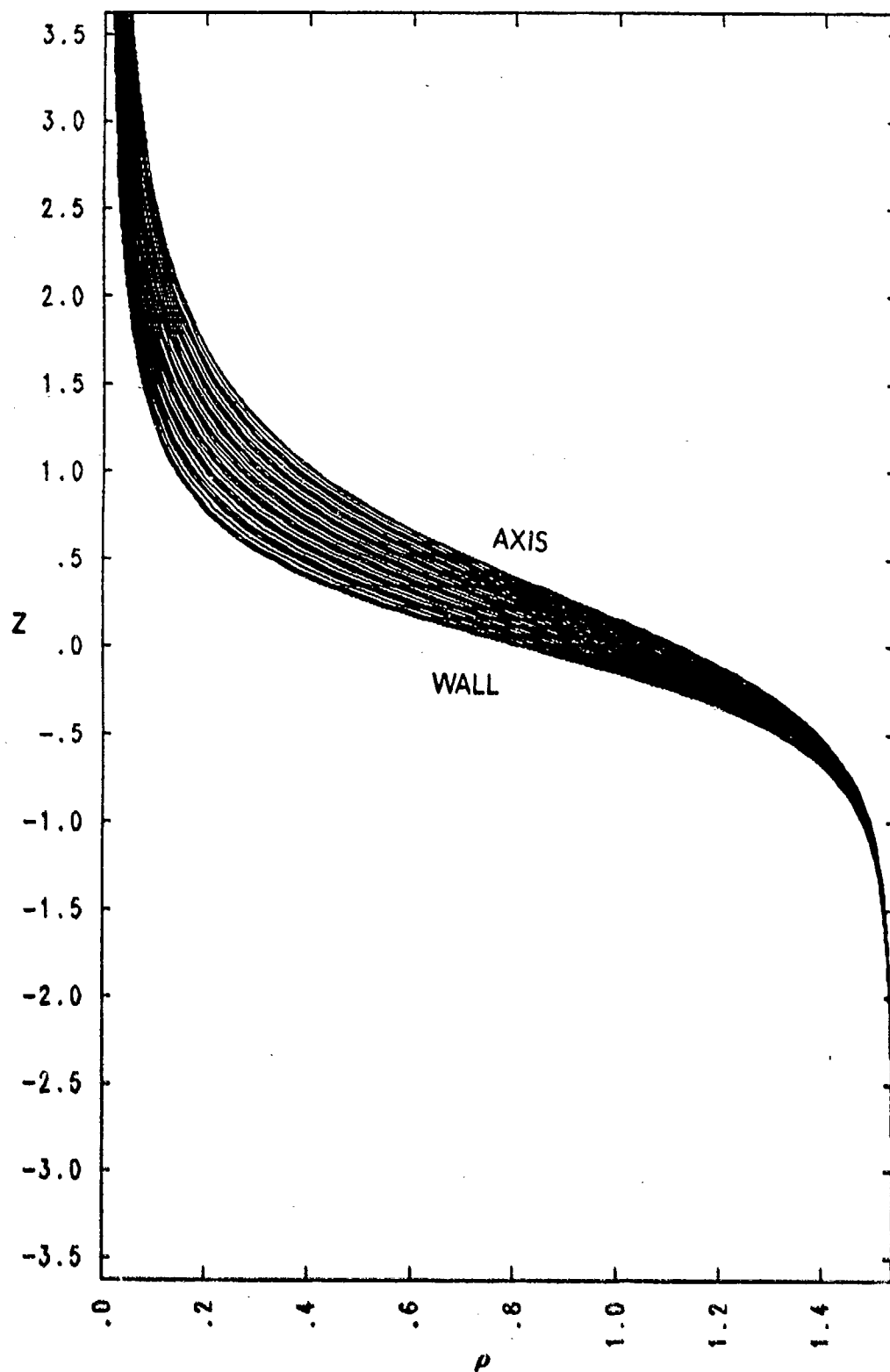
Fig. 10. Variation of density along streamlines for un-magnetized flow through the hyperbolic nozzle of Fig. 3.
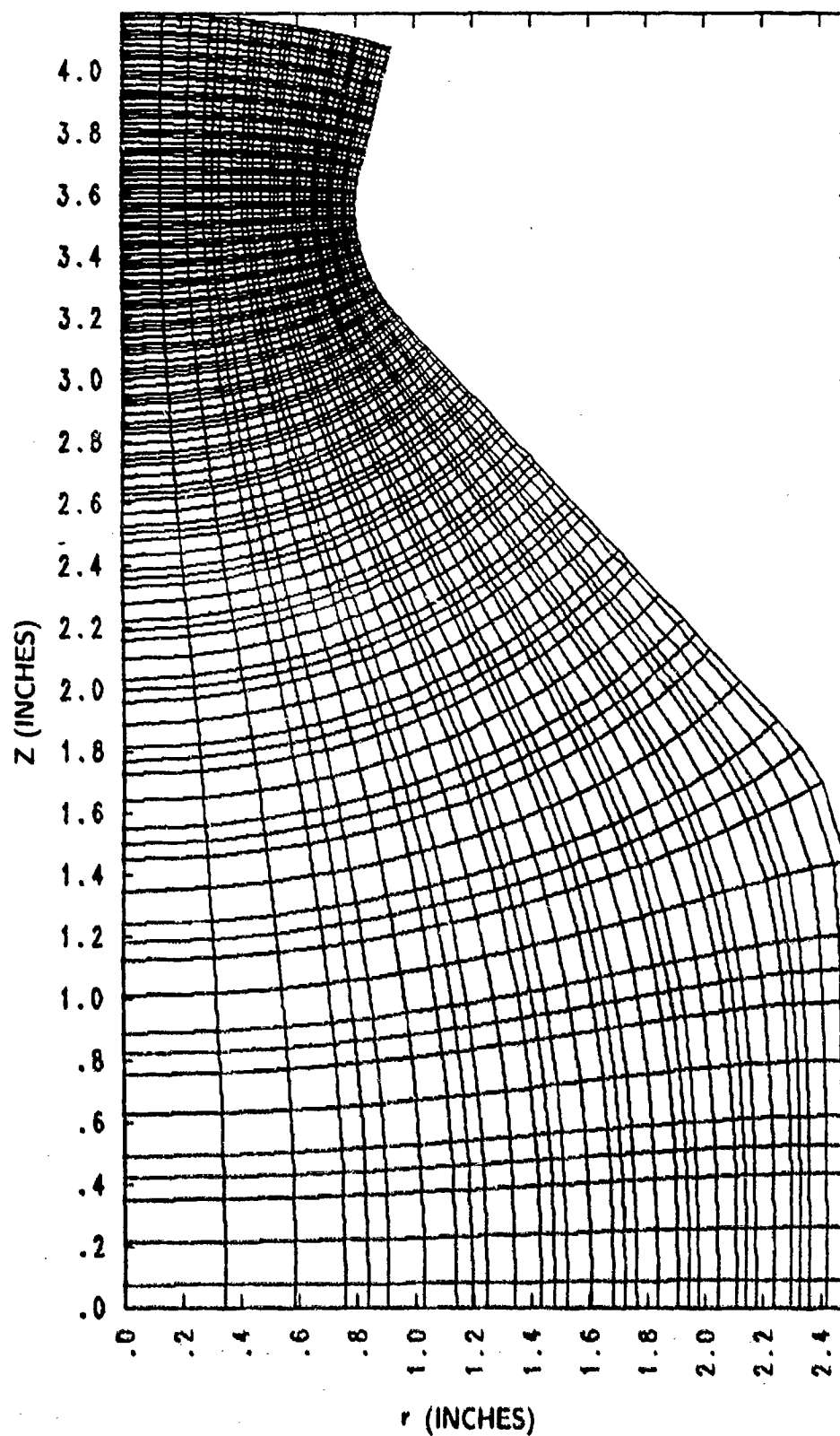
Fig. 11. Coordinate grid for JPL nozzle (Ref. 11) using the same scheme as in Fig. 3.
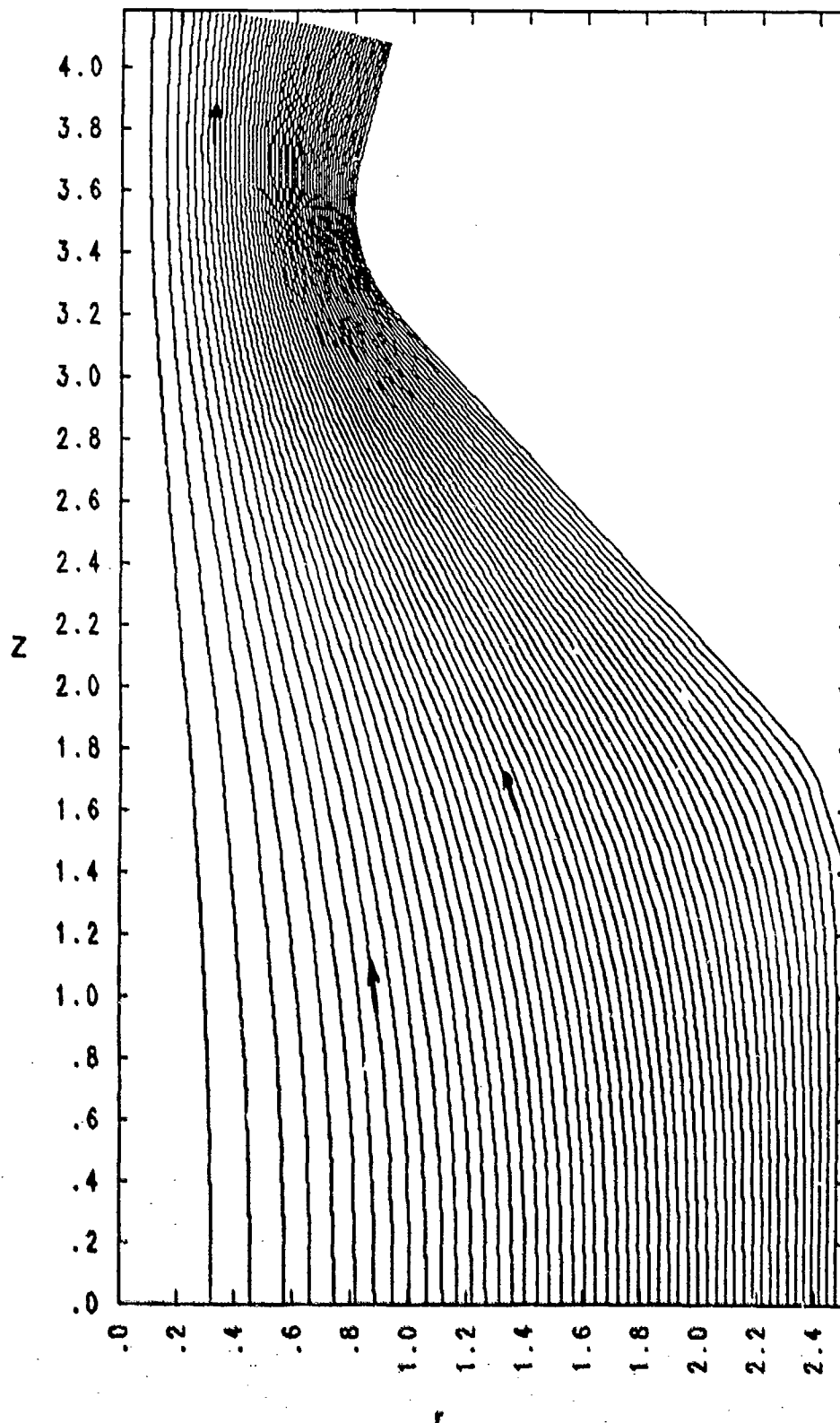
Fig. 12. Streamlines for un-magnetized flow through JPL nozzle.
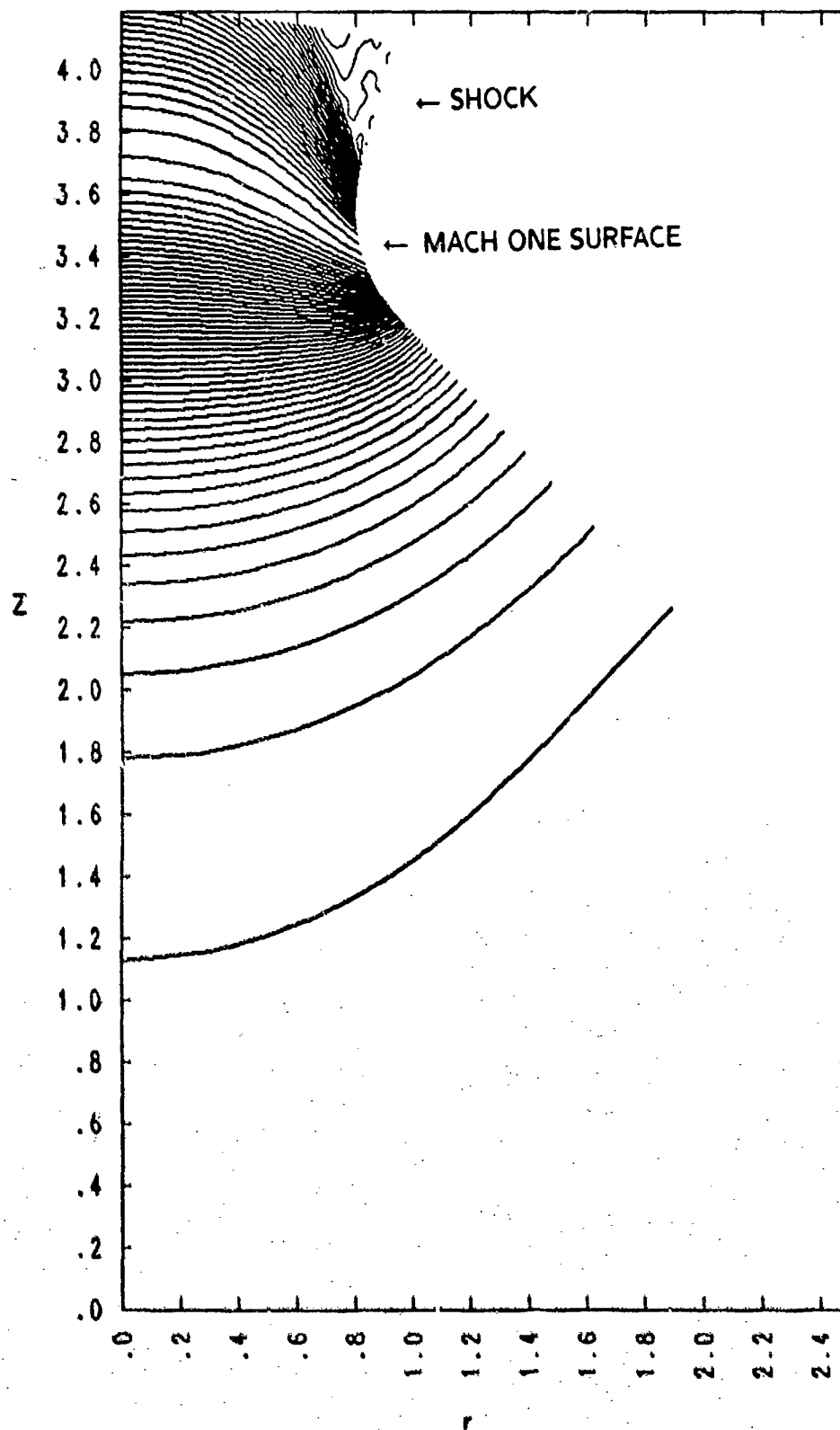
Fig. 13. Contours of constant $(\rho V)^2$ for un-magnetized flow through JPL nozzle.

136
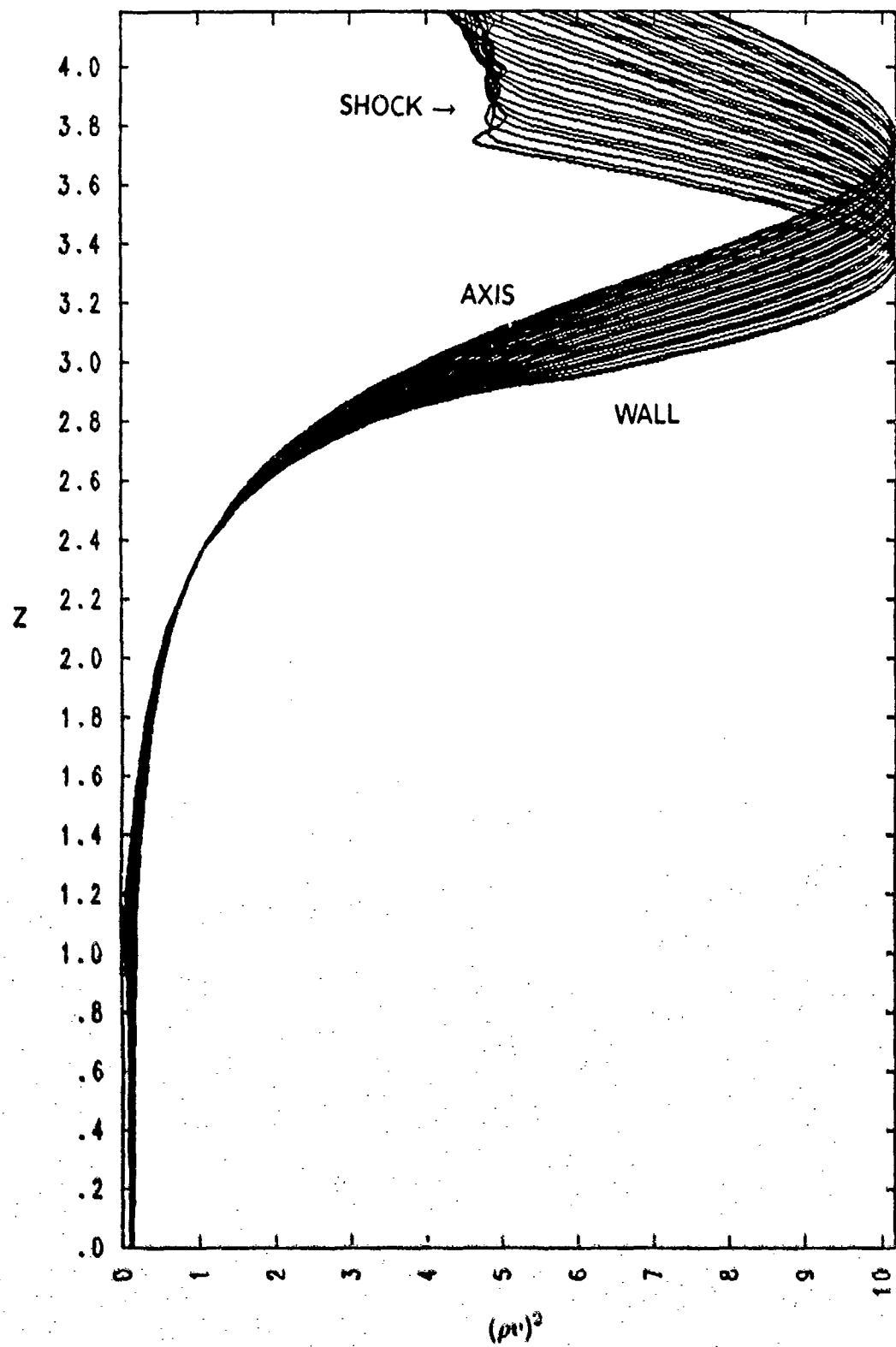
Fig. 14. Variation of $(\rho V')^2$ along streamlines for un-magnetized flow through JPL nozzle.

137
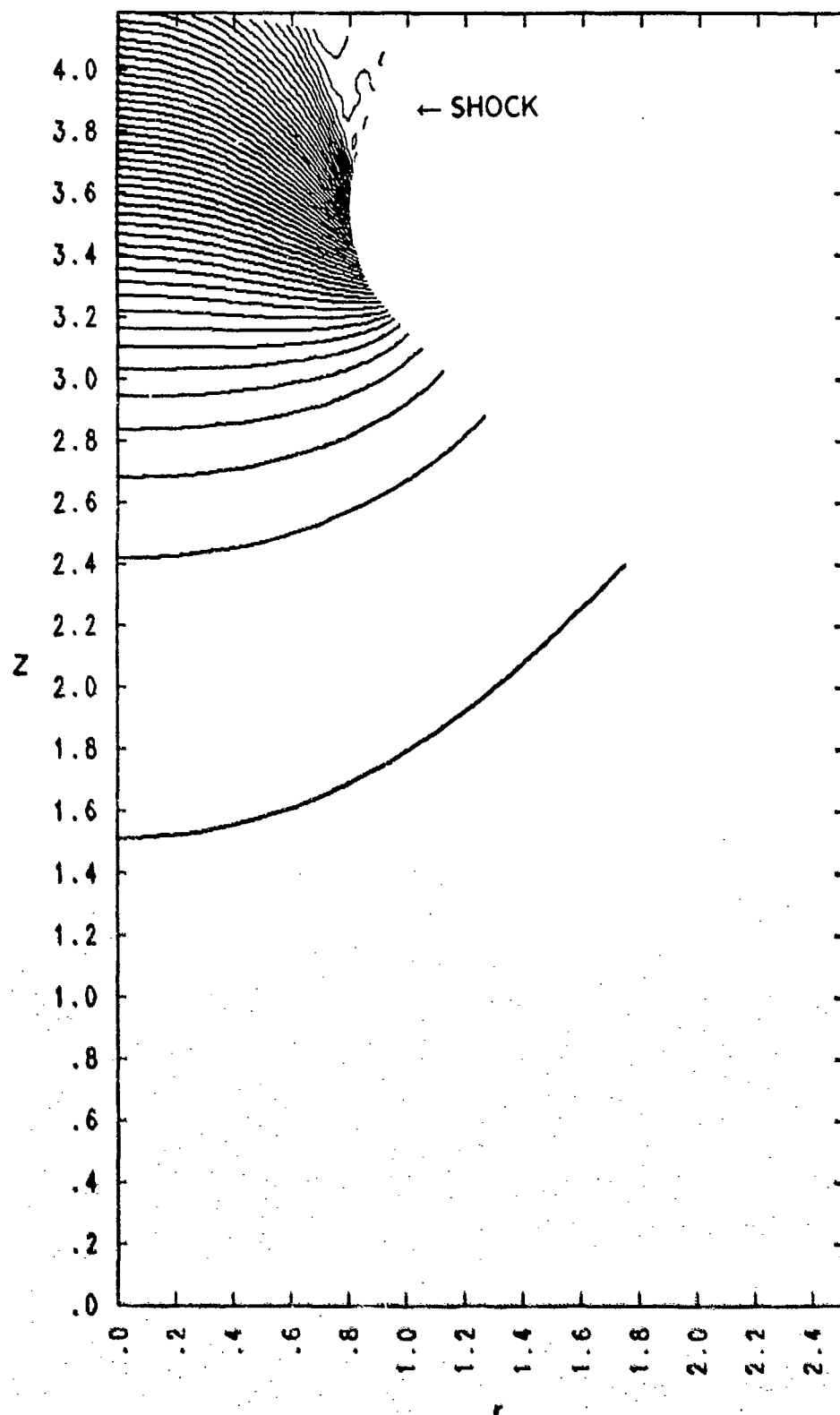
Fig. 15. Contours of constant density for un-magnetized flow through JPL nozzle.

138
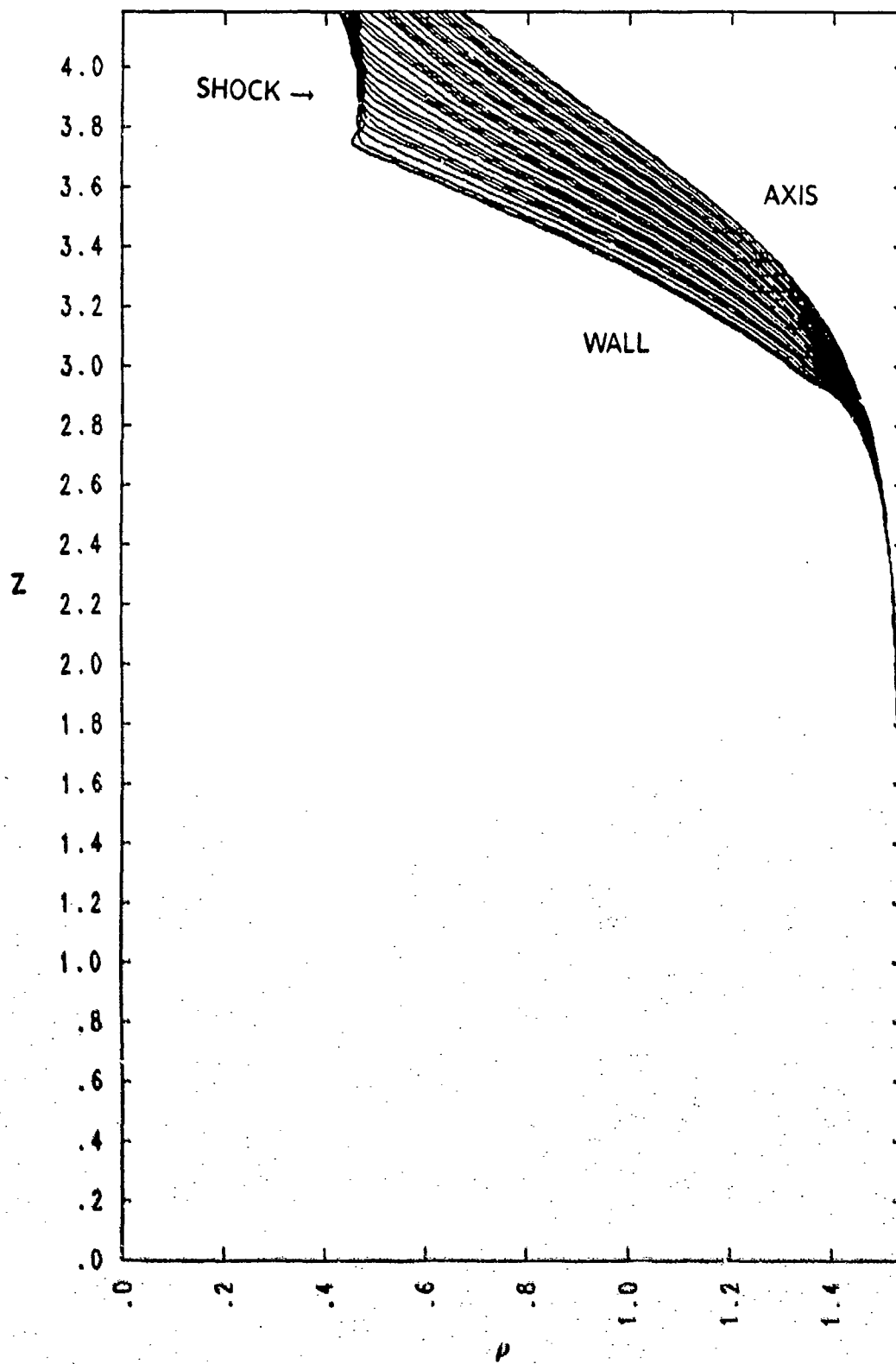
Fig. 16. Variation of density along streamlines for un-magnetized flow through JPL nozzle.
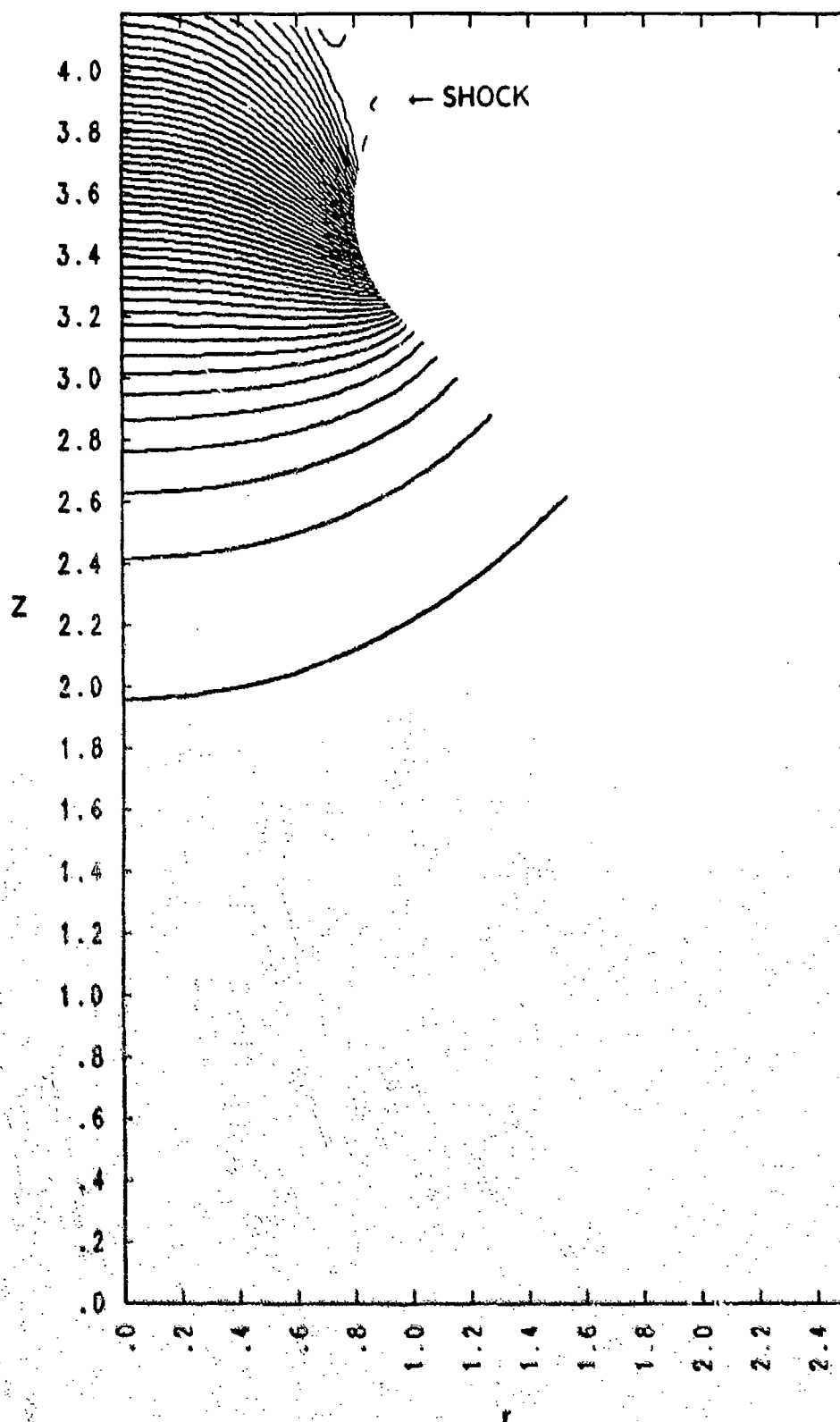
Fig. 17. Contours of constant pressure for un-magnetized flow through JPL nozzle.

Fig. 18. Variation of pressure along streamlines for un-magnetized flow through JPL nozzle.

Fig. 19. Contours of constant mach number (with $\gamma = 5/3$) for un-magnetized flow through JPL nozzle.

Fig. 20. Contours of constant Mach number (with $\gamma = 1.4$) for un-magnetized flow through JPL nozzle.

143

Fig. 21. Streamlines in the JPL nozzle for the un-magnetized non-uniform pressure configuration, $P_0 \sim (1 + \epsilon U)$, with $\epsilon = -0.02$. Flow reversal at the nozzle entrance is induced by a non-uniform pressure profile in the reservoir.

144

Fig. 22. Streamlines in the JPL nozzle for the un-magnetized non-uniform pressure configuration. $P_0(1+\epsilon U)$, with $\epsilon = 0.02$. Flow reversal at the nozzle entrance is induced by a non-uniform pressure profile in the reservoir.

Fig. 23. Streamlines in the hyperbolic nozzle for magnetized flow with $\psi'(\ell') = $ const. and $a = 0.8$
(Sec. II-C.3).

Fig. 24. Contours of constant $(\rho V')^2$ in the hyperbolic nozzle for magnetized flow with $\psi'(U) = $ const. and $\alpha = 0.8$ (Sec. II-C.3).
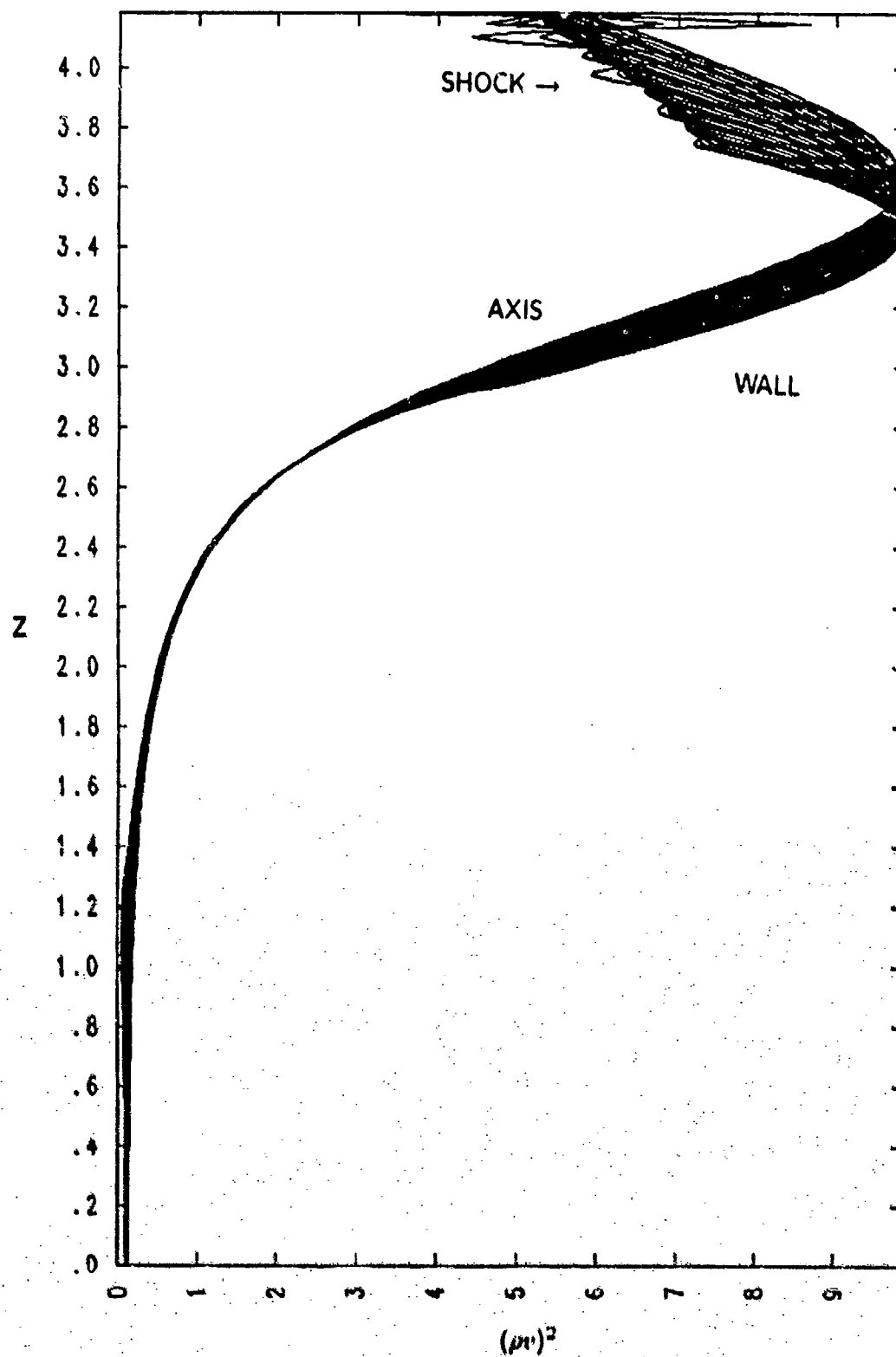
Fig. 25. Variation of $(\rho V)^2$ along streamlines in the hyperbolic nozzle for magnetized flow with $\psi'(U) = $ const. and $\alpha = 0.8$ (Sec. II-C.3).
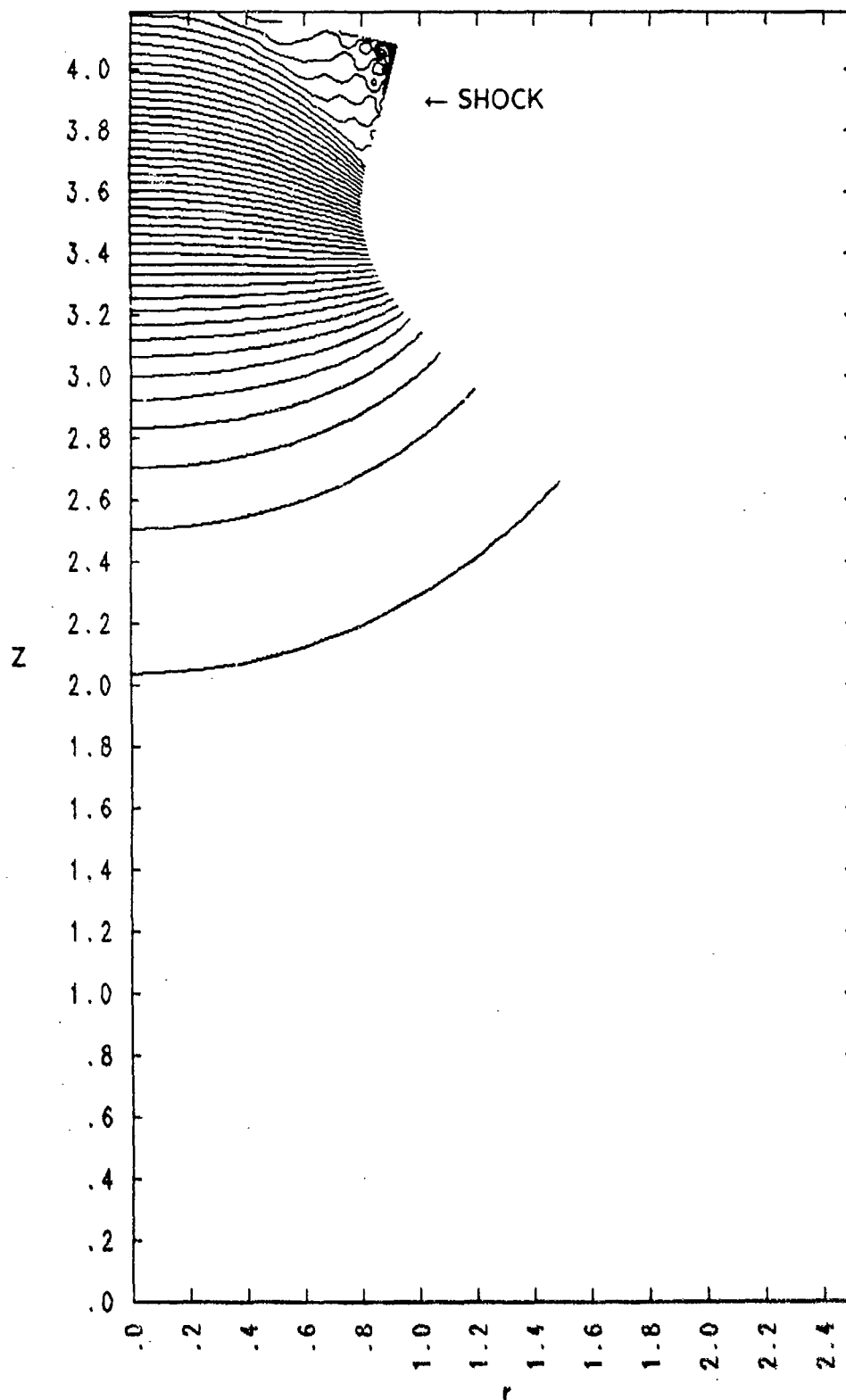
Fig. 26. Contours of constant velocity in the hyperbolic nozzle for magnetized flow with $\psi'(U) =$ const. and $\alpha = 0.8$ (Sec. II-C.3).
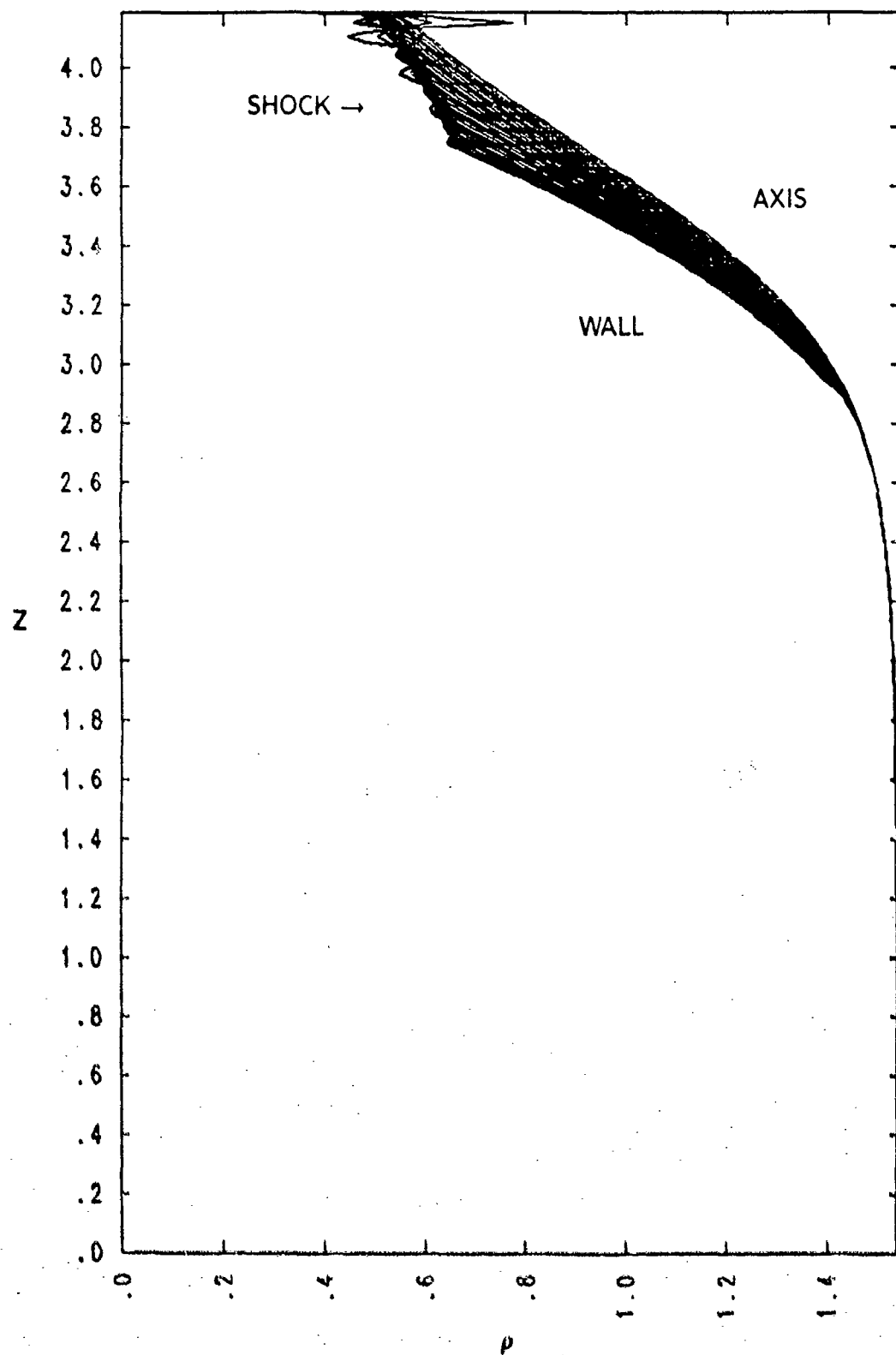
Fig. 27. Variation of velocity along streamlines in the hyperbolic nozzle for magnetized flow with $\psi'(U) = $ const. and $\alpha = 0.8$ (Sec. II-C.3).

Fig. 28. Contours of constant density in the hyperbolic nozzle for magnetized flow with $\psi'(U') = $ const. and $\alpha = 0.8$ (Sec. II-C.3).

Fig. 29. Variation of density along streamlines in the hyperbolic nozzle for magnetized flow with $\psi'(U) =$ const. and $\alpha = 0.8$ (Sec. II-C.3).
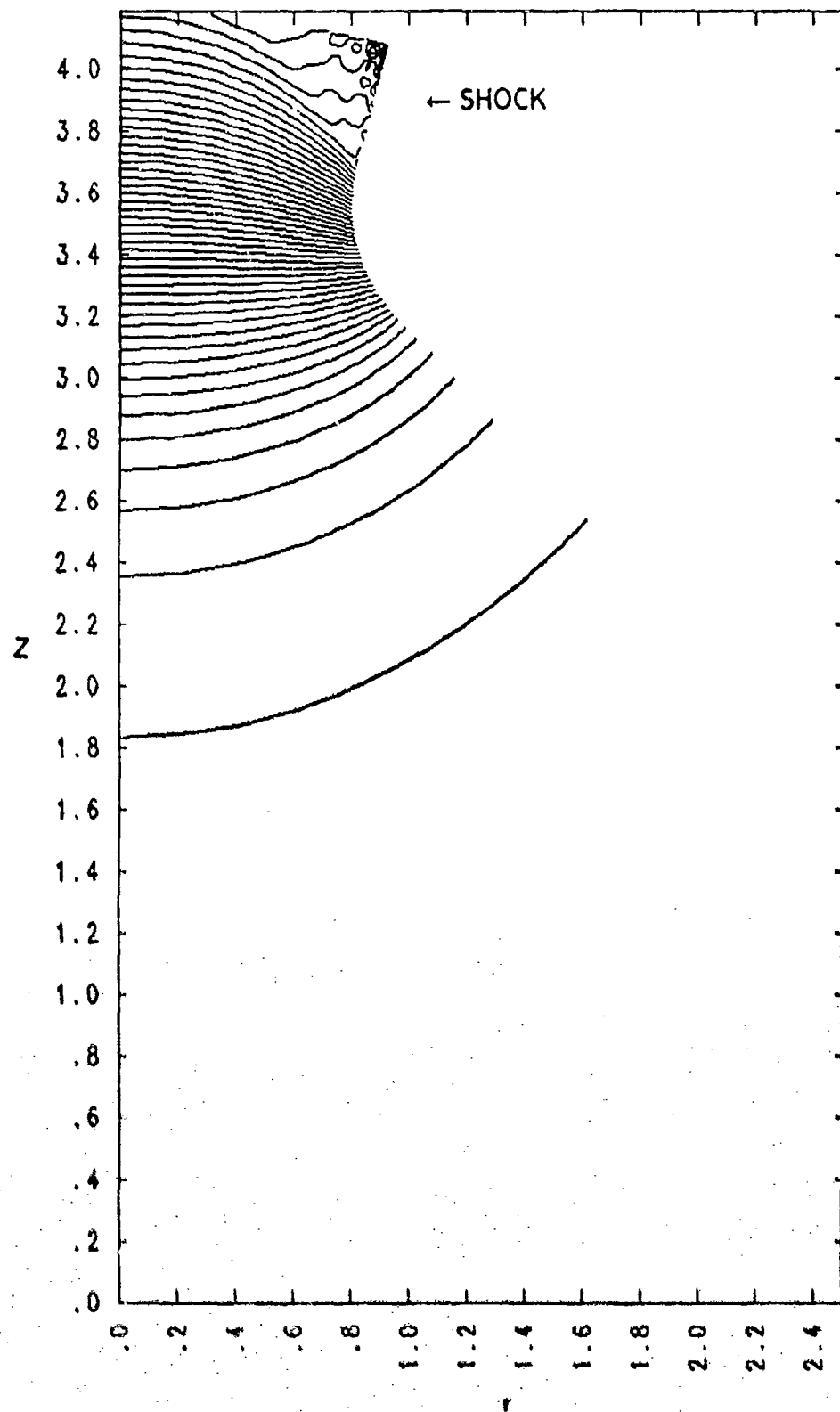
Fig. 30. Streamlines in the JPL nozzle for magnetized flow with $\psi'(l') = $ const. and $\alpha = 0.8$ (Sec. II-C.3).

153

Fig. 31. Contours of constant $(\rho V')^2$ in the JPL nozzle for magnetized flow with $\psi'(l') \simeq$ const. and $\alpha = 0.8$ (Sec. II-C.3).

Fig. 32. Variation of $(\rho I')^2$ along streamlines in the JPL nozzle for magnetized flow with $\zeta'(I') =$ const. and $\alpha = 0.8$ (Sec. II-C.3).

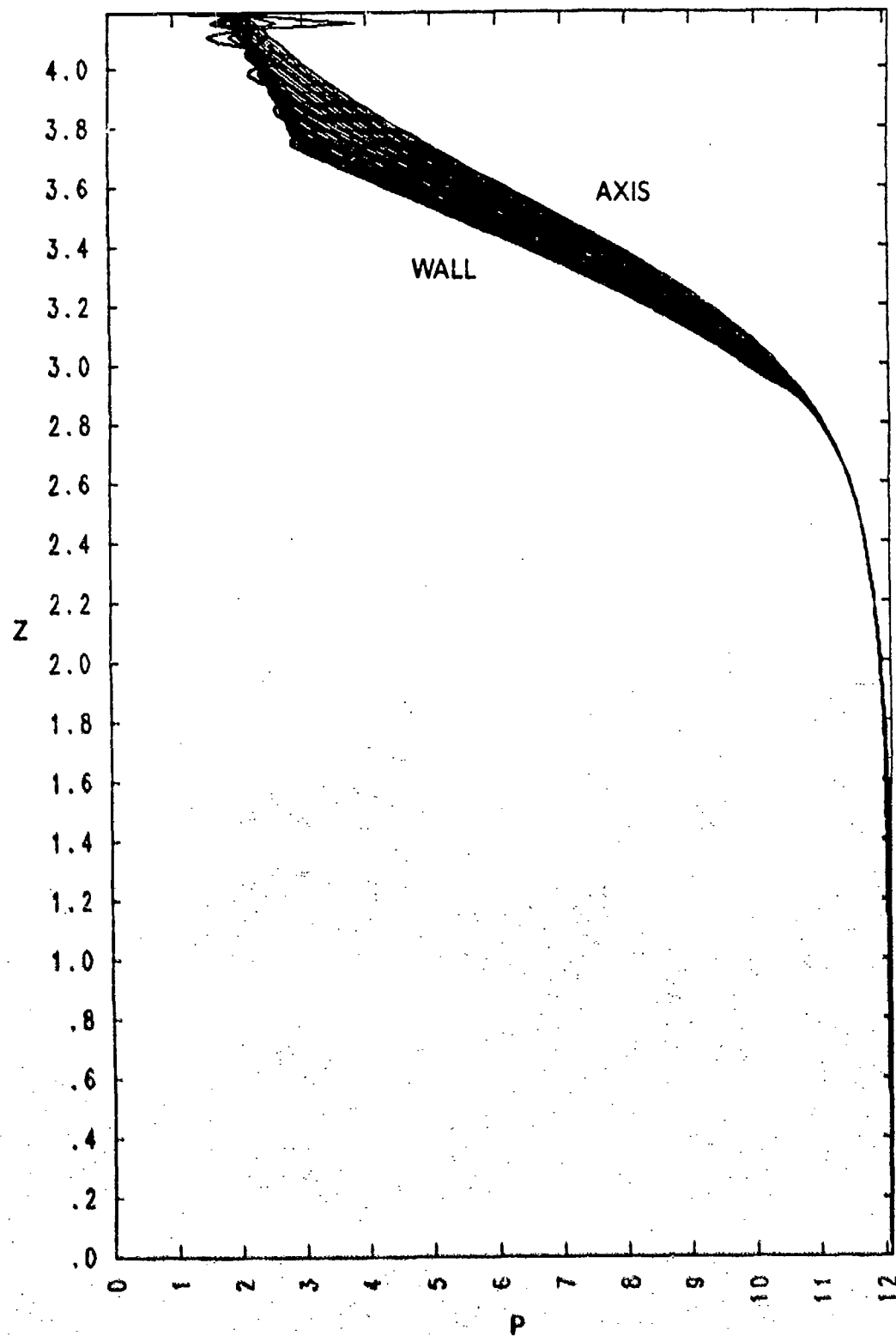Fig. 33. Contours of constant density in the JPL nozzle for magnetized flow with $\iota'(\iota') = \text{const.}$ and $\alpha = 0.8$ (Sec. II-C.3).

Fig. 34. Variation of density along streamlines in the JPL nozzle for magnetized flow with $\psi'(l')$ = const. and $\alpha = 0.8$ (Sec. II-C.3).
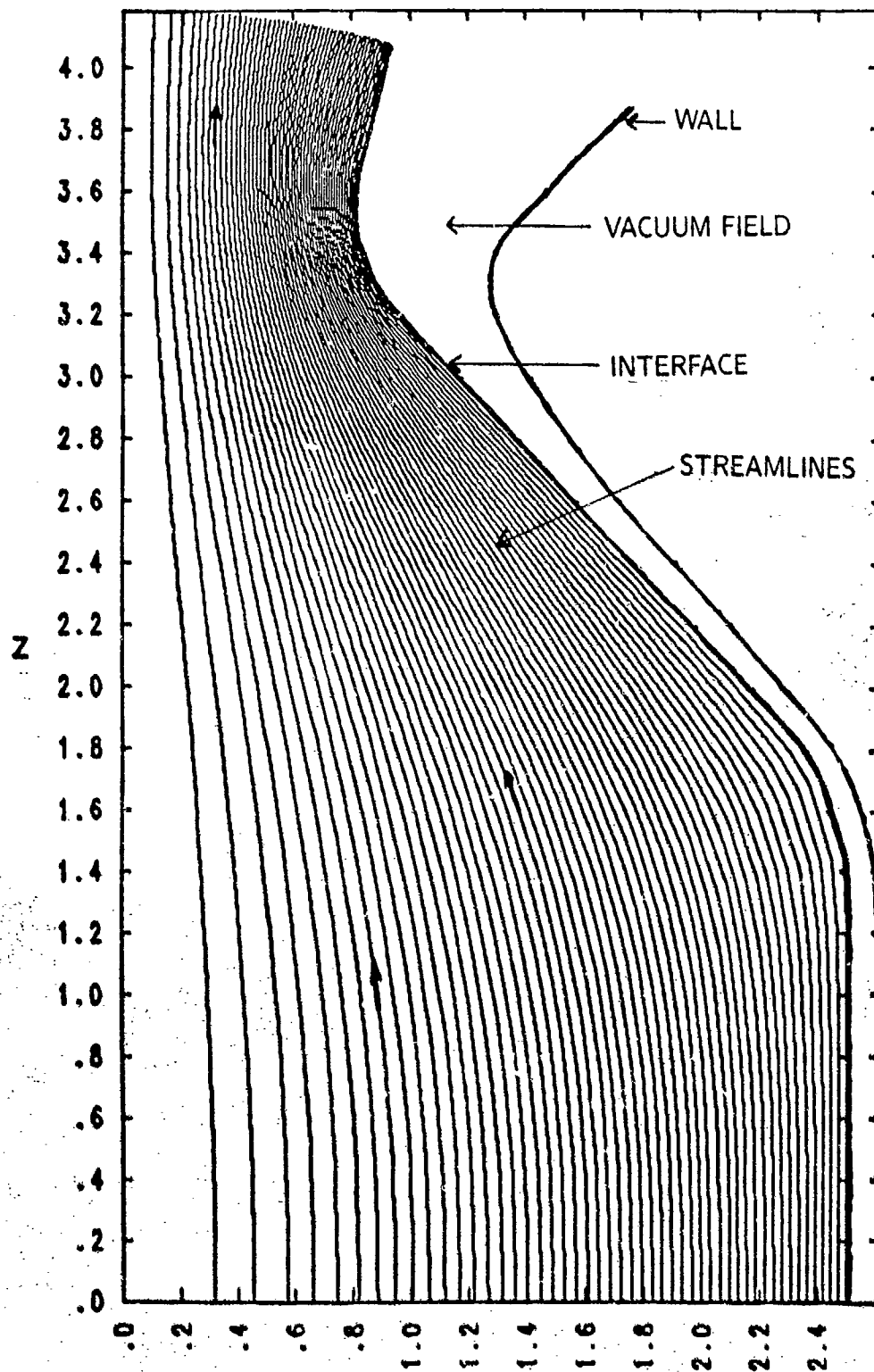
Fig. 35. Contours of constant pressure in the JPL nozzle for magnetized flow with $\psi'(U) = $ const. and $\alpha = 0.8$.

Fig. 36. Variation of pressure along streamlines in the JPL nozzle for magnetized flow with $v'(U)$ = const. and $\alpha = 0.8$.

Fig. 37. Example of a magnetically confined sharp boundary flow field in a meridional configuration similar to the JPL nozzle.

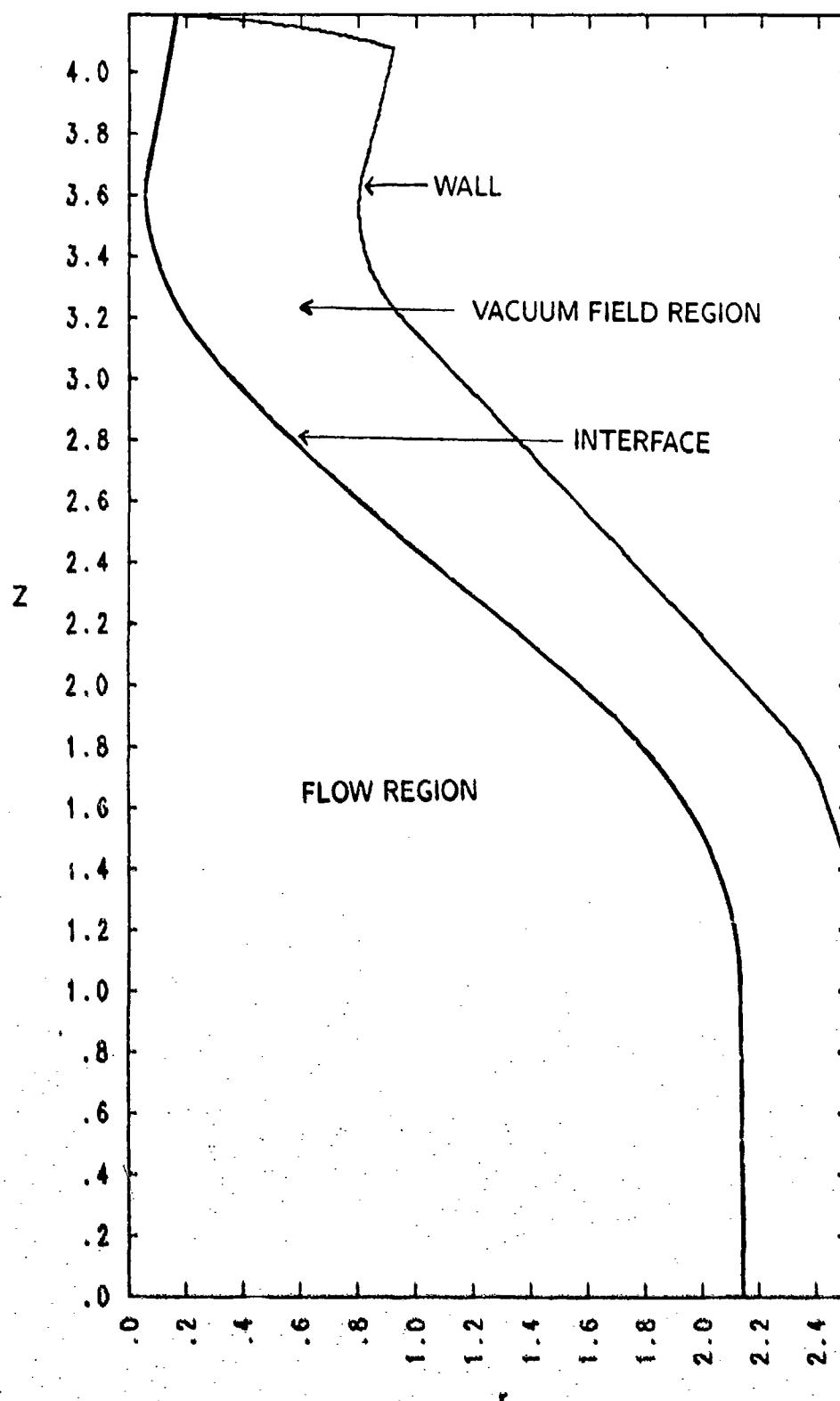Fig. 38. Example of a magnetically confined sharp boundary flow field in a meridional configuration near the "stuffing" limit.
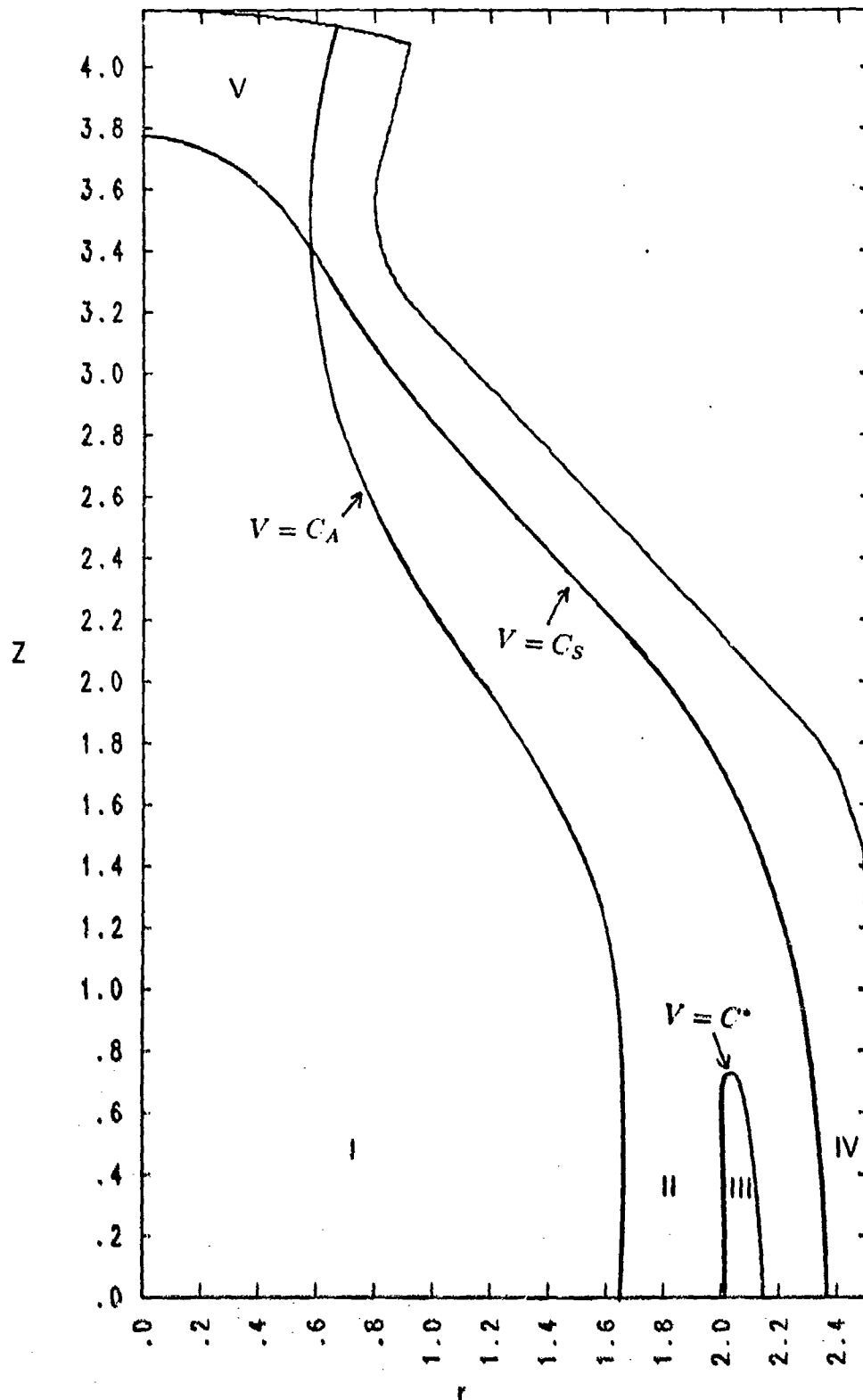
Fig. 39. Example of interlaced elliptic and hyperbolic regions in a magnetically confined plasma with a diffuse profile in a meridional magnetic nozzle.
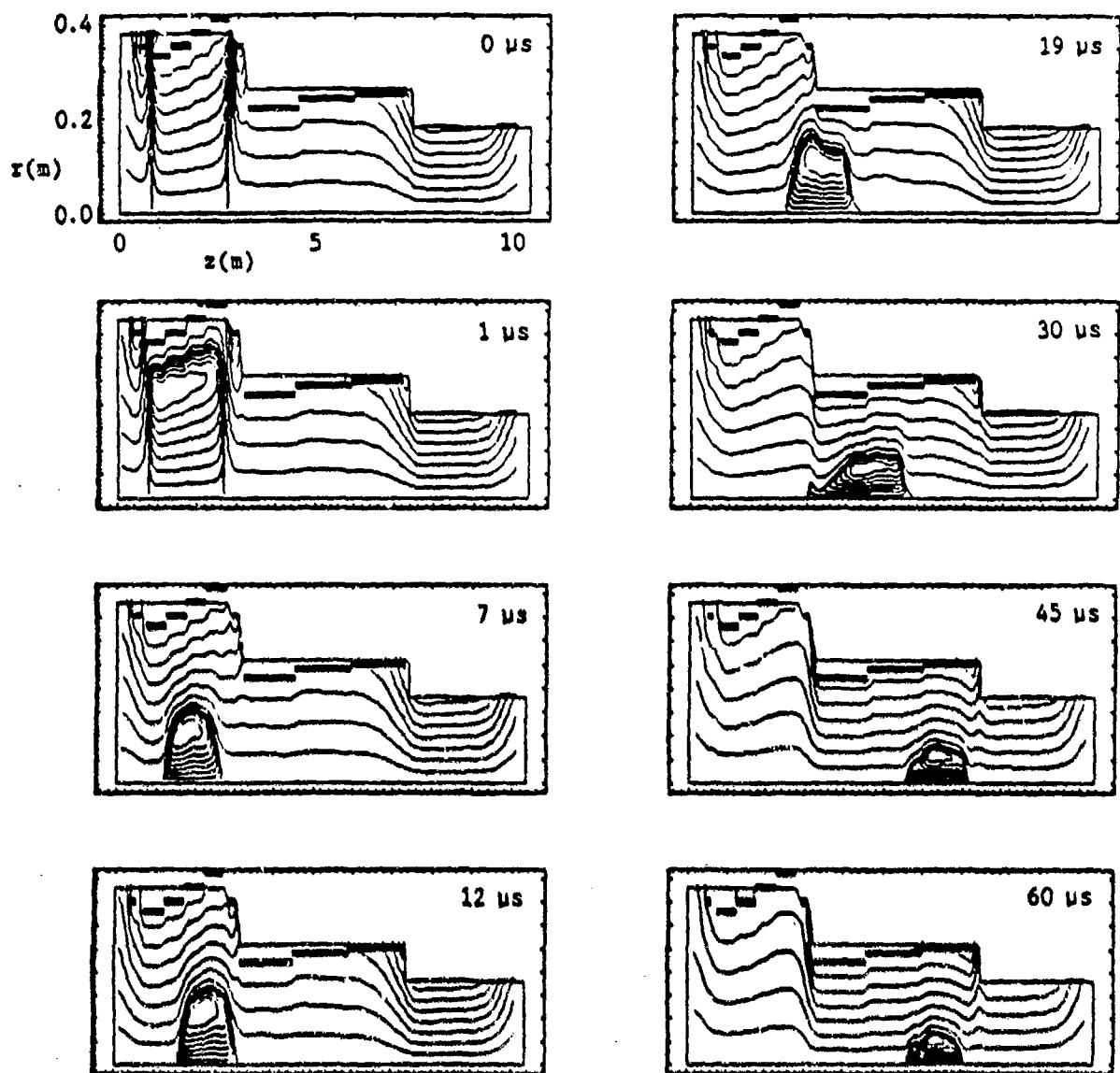
162

Fig. 40. FRC compression on FRX-C, 2-D MHD simulations, time evolution of flux surfaces $\psi(r, z)$.